Probing BSM Physics with CP-violation, Neutrinos and White Dwarfs

RAMIREZ-QUEZADA, MAURA,ELIZABETH

How to cite:

RAMIREZ-QUEZADA, MAURA,ELIZABETH (2021) *Probing BSM Physics with CP-violation, Neutrinos and White Dwarfs*, Durham theses, Durham University. Available at Durham E-Theses Online: http://etheses.dur.ac.uk/13928/

Probing BSM Physics with CP-violation, Neutrinos and White Dwarfs

Maura Elizabeth Ramírez Quezada

A Thesis presented for the degree of
Doctor of Philosophy

Institute for Particle Physics Phenomenology
Department of Physics
Durham University
United Kingdom

March 2021

Probing BSM Physics with CP-violation, Neutrinos and White Dwarfs

Maura Elizabeth Ramírez Quezada

Submitted for the degree of Doctor of Philosophy, March 2021

Abstract

While the Standard Model remains the best theory to describe elementary particles and their interactions, there are still some unresolved issues that cannot be addressed within its current framework.

Right handed neutrinos are introduced to the Standard Model to explain the observed active neutrino masses. If CP is violated during their radiative decays an asymmetry between two circularly–polarised photons can be generated. The CP asymmetry is somehow connected to circular polarisation. Therefore, observations of such polarised signal potentially lead to a measurement of the CP violation in the process.

Here, we provide the connection between these two asymmetries for both, Dirac and Majorana neutrinos. We then apply this formalism to a minimal seesaw model and give the CP asymmetry in terms of a series of Jarlskog-like parameter. We also provide the formalism to study the changes in the polarisation of photons at any energy, since the intensity of such circularly polarised signal could change as it propagates through the Universe.

Finally, we pay attention to the dark matter paradigm. We discuss the capture of dark matter in compact stellar objects as complementary to direct detection searches. We particularly work with white dwarfs (WD) since due to their abundance and high temperatures they one of the best observed compact objects proposed as cosmic laboratories for studying physical processes happening at very extreme conditions that cannot be achieved at terrestrial laboratories. Using an observed WD from the Messier 4 globular cluster, we set constraints on the DM interactions.

Contents

Declaration

The work in this thesis is based on research carried out at the Institute for Particle Physics Phenomenology, Department of Physics, University of Durham, England, United Kingdom. No part of this thesis has been submitted elsewhere for any other degree or qualification and it is all my own work unless referenced to the contrary in the text.

The following chapters in this work are based on joint research that have been published.

- Chapter 3 is based on “CP violation and circular polarisation in neutrino radiative decay” published in Journal of High Energy Physics [1]. This work was done in collaboration with S. Balaji and Y. Zhou. I calculated the kinetic terms in the loop for the transition dipole moment for the Yukawa model and cross-checked my results with another member of the project. All members of the project contributed to all aspects in the manuscript.

- Chapter 4 is based on “CP violation in the neutrino dipole moment” [2]. This work was done in collaboration with S. Balaji and Y. Zhou. I was involved in calculating all the loops, numerical results and performing the plots and cross checked my results with another member of the project. All authors contributed to all aspects in the manuscript.

- Chapter 2 and Chapter 5 contain work based on “Polarisation of high energy gamma-rays after scattering” published in Journal of Cosmology and Astroparticle Physics [3]. This work was done in collaboration with C. Boehm, Andres Olivares-del Campo and Y. Zhou. I was involved in the review, understanding and reproduction of previous works. I computed the general expressions of the A–matrix as well as the particular case of Compton Scattering and compared with another member of the project. I was involved in most of the analytical calculations and I reviewed and summarised all sources of circular polarisation.

- Chapter 6 is based on several referenced reviews and this work is still in progress. I reviewed all aspects of the white dwarfs such as EOS, inner structure, and observations. I also reviewed the discussion about the non-relativistic operators and form factors for carbon. I performed the capture rate (at the limit of zero temperature and at finite temperature) and evaporation rate analytically and numerically. I produced numerical results and some plots in the geometric and thin limits as well as including the complete treatment.

Acknowledgements

First and foremost, I would like to thank my PhD supervisors Celine Boehm and Silvia Pascoli for their support throughout my PhD. Additionally, a special thanks to Sandra Robles for providing her guidance encouragement and insightful discussions throughout my studies.

I would like to thank all my colleague for their insights and useful conversations, including Alexis Plascencia, Oscar Ochoa, Tommaso Boschi, Matheus Hoster, Andres Olivares–del Campo, Ryan Moodie, Elliott Reid, and last but not least my best IPPP amigo Joey Reiness. I am especially thankful to Shyam Balaji who has been of great support since we started working together and more than a colleague, he has become a very special friend of mine.

Thanks to all of my friends in Durham, Karen Gonzales, Carlos Ferrandon, Diana Martinez, Cesar Aguayo, Alma Vidal and my favourite boy Sebastian for always being there for me and make my days in Durham the best. A special thanks to the bad boys in Durham: Ariam Mora and Alejandro Galan who have been like family in this journey. Cheers to all those friends I have made all around the world, including Katarina, Jeremmie, Franco, Alberto, William Torres, Yu Alair and Camila. You guys made my days away from Durham really special.

Finally I want to thank my sisters Carola and Sara, and all my friends back in Mexico, Abraham, Cristhian, Hector, Wilmer, Chacalito, Dupret, Sandy, Pepe, Ana, Michelle, Ariadna and Jimena, because without all their support and help I wouldn't be here right now.

I gratefully acknowledge financial support from CONACyT (Mexican National Council for Science and Technology) throughout the whole period of my doctoral studies.

Logic will get you from A to Z; imagination will get you everywhere.

— Albert Einstein

Dedicated to

Carolina, Malena

and

Calcaneo

Chapter 1

Introduction

Everything we know about fundamental particles and their interactions in our Universe is best described by the Standard Model (SM), developed in the late 60s, right after the Higgs mechanism was introduced earlier in the 60s. Despite its remarkable success in describing almost all fundamental interactions, there is strong evidence that the SM of particle physics must be extended. In Sec. 1.1 we present an overview of the SM of particle physics. Sec. 1.2 is dedicated to the current challenges the SM is facing, such as providing an explanation for neutrino masses and dark matter. Finally, in Sec. 1.3 we motivate and outline this work.

1.1 The Standard Model of Particle Physics

The SM successfully describes particle properties and interactions (in particular the notions of electromagnetic, weak and strong forces) using the principles of gauge theory. It has been developed for several decades and remains the best model that we have to describe all subatomic processes. One might say that the very first element of the SM of particle physics was born during the late 20s when Dirac applied quantum field theory (QFT) to the electromagnetic interaction [4], establishing the well known Dirac equation. This achievement gave rise to the theory of Quantum electrodynamics (QED), which was further improved by Tomonga, Feynman and

Schwinger [5, 6, 7, 8, 9, 10]. The second element is a successful description of the electroweak (EW) interactions by Glashow, Weinberg and Salam in the 1960s who showed that EM and weak interactions[1] can be unified into a single electroweak theory [11, 12, 13]. The third element is a description of the strong forces which is not discussed in this work but can be found in Ref. [14].

The SM of particle physics is based on the symmetry group $SU(3)_C \otimes SU(2)_L \otimes U(1)_Y$ where $SU(3)_C$ corresponds to the strong interactions and the subscript C stands for colour. $SU(2)_L \otimes U(1)_Y$ corresponds to the electroweak interactions; the subscript L stands for left and the subscript Y for weak hypercharge. The particles mediating the interactions are called bosons: there are 8 bosons (the so-called gluons) associated with the strong force, 3 bosons (the $W^{\pm}$ and Z bosons) associated with the weak force and 1 boson (the photon) associated with the electromagnetic force. The photon is massless but the $W^{\pm}$ and Z bosons are massive particles [15, 16, 17, 18].

To account for the masses of the gauge bosons in the SM without violating gauge invariance, Guralnik, Hagen, & Kibble [19], Brout & Englert [20] and, Higgs [21] proposed a new mechanism: the so-called Englert-Brout-Kibble-Guralnik-Hagen-Higgs mechanism. The mechanism introduces a new particle field to the SM: the Higgs field, which acquires a non–zero vacuum expectation value because its energetically favourable according to the quartic potential. As a consequence, when the W and Z bosons interact with this field, they acquire a mass. We will discuss this in more detail in the next section. The complete SM Lagrangian in its very compact form is given as,

$$\begin{aligned}\mathcal{L}_{\mathrm{SM}} = &-\frac{1}{4}F_{\mu\nu}F^{\mu\nu} \\ &+ i\overline{\psi}\not{D}\psi \\ &+ i\overline{\psi}_i y_{ij}\psi_j\phi \\ &+ |D_\mu\phi|^2 - V(\phi) + h.c.,\end{aligned} \tag{1.1.1}$$

---

[1] The eponymous interaction proposed by Fermi in 1933 was a precursor of the weak interactions.

where $F_{\mu\nu}$ is the gauge field tensor, ψ represent fermion fields, ϕ is the Higgs field, D_μ the covariant derivative and y_{ij} the Yukawa couplings.

The first term in Eq. (1.1.1) describes the kinetic and self-interactions of the gauge bosons while the second term describes the kinetic terms of fermions and their interaction with gauge bosons. The third describes the interactions of the fermions with the Higgs field. The last term gives the kinetic and self-interactions of the Higgs boson.

1.1.1 Electroweak Spontaneous Symmetry Breaking

Now that we have discussed some of the most relevant aspects of the SM Lagrangian given in Eq. (1.1.1), we will discuss the Higgs mechanism in the EW sector.

The non–zero vacuum expectation of the Higgs field initiates Spontaneous Symmetry Breaking (SSB) of the electroweak sector,

$$SU(2)_L \bigotimes U(1)_Y \rightarrow SU(2)_{QED}. \tag{1.1.2}$$

The Lagrangian is

$$\mathcal{L} \subset -\frac{1}{4}(W^a_{\mu\nu})^2 - \frac{1}{4}B_{\mu\nu} + |D_\mu\phi|^2 - V(\phi) \tag{1.1.3}$$

with

$$\begin{aligned} B_{\mu\nu} &= \partial_\mu B_\nu - \partial_\nu B_\mu \\ W^a_{\mu\nu} &= \partial_\mu W^a_\nu - \partial_\nu W^a_\mu - g\epsilon^{abc}W^b_\mu W^c_\nu \end{aligned} \tag{1.1.4}$$

where B_μ is the hypercharge gauge boson; W^a_μ and g are the $SU(2)_L$ gauge boson and coupling, respectively; ϵ^{abc} is the Levi–Civita tensor. The covariant derivative is defined as,

$$D_\mu = \partial_\mu - igW^a_\mu\frac{1}{2}\sigma^a - ig'B_\mu Y_L \tag{1.1.5}$$

with σ^a being the Pauli matrices, g' the $U(1)_Y$ coupling and Y_L the weak hypercharge for left–handed (LH) fields. The form of the Higgs potential that leads to the SSB in Eq. (1.1.2) is

$$V(\phi) = -\mu^2|\phi|^2 + \lambda|\phi|^4. \tag{1.1.6}$$

This potential has a minimum at $|\phi| = \sqrt{\frac{\mu^2}{2\lambda}}$, and after symmetry breaking we can write the Higgs doublet in the form,

$$\phi = \exp\left(i\frac{\xi^a\sigma^2}{v}\right)\begin{pmatrix} 0 \\ \frac{v+h}{\sqrt{2}} \end{pmatrix} \tag{1.1.7}$$

where $v = \sqrt{\frac{\mu^2}{2\lambda}}$ and h, is the field associated with the Higgs boson. It is simpler to study this theory in unitary gauge, so we can set $\xi^a = 0$.

If we plug in the expression in Eq. (1.1.7), in the unitary gauge, into the covariant derivative of Eq. (1.1.3), we will obtain the mass terms associated with three massive gauge bosons

$$|D_\mu\phi|^2 = g^2\frac{v^2}{8^2}\left[(W_\mu^1)^2 + (W_\mu^2)^2 - \left(\frac{g'}{g}B_\mu - W_\mu^3\right)^2\right]. \tag{1.1.8}$$

When diagonalising the mass matrix, we obtain one massless eigenstate and one massive eigenstate as linear combination of the hypercharge gauge boson and one of the generators of $SU(2)$. These are the well–known massless photon A_μ and the Z_μ gauge boson

$$\begin{aligned} A_\mu &= \sin\theta_w W_\mu^3 + \cos\theta_w B_\mu\,, \\ Z_\mu &= \cos\theta_w W_\mu^3 - \sin\theta_w B_\mu\,, \end{aligned} \tag{1.1.9}$$

with $\tan\theta_w = g'/g$. Additionally, we also find the definition for the massive $W-$boson,

$$W_\mu^\pm = \frac{1}{\sqrt{2}}(W_\mu^1 \mp iW_\mu^2) \tag{1.1.10}$$

and the mass terms in the SM Lagrangian are given by

$$\mathcal{L} \subset -m_W^2 W^{+\mu}W_\mu^- - \frac{M_Z^2}{2}Z^\mu Z_\mu \tag{1.1.11}$$

Fermionic masses are also not allowed in the SM Lagrangian of Eq. (1.1.1), since

Field	$SU(3)_C$	$SU(2)_L$	$U(1)_Y$
Q_L	3	2	1/6
L_L	1	2	−1/2
e_R	1	1	−1
u_R	3	1	2/3
d_R	3	1	−1/3
H	1	2	1/2

Table 1.1: SM field content and their corresponding representation.

they break the gauge symmetry. However, the addition of the scalar field ϕ into the model will also generate the missing fermion mass terms. This will be discussed in the following section.

1.1.2 Fermion Masses

We shall now discuss how fermions in the SM of particle physics acquire their mass. There are three generations of SU(2) LH leptons and quarks in the SM,

$$L_L^\alpha = \begin{pmatrix} \nu_L^\alpha \\ \ell_L^\alpha \end{pmatrix}, \quad Q_L = \begin{pmatrix} u_L \\ d_L \end{pmatrix}, \begin{pmatrix} c_L \\ s_L \end{pmatrix}, \begin{pmatrix} t_L \\ b_L \end{pmatrix} \tag{1.1.12}$$

where $\alpha = e, \mu, \tau$. The right handed (RH) fermions are denoted in the following form,

$$\begin{aligned} &e_R = (e_R, \mu_R, \tau_R) \\ &u_R = (u_R, c_R, t_R) \qquad\qquad d_R = (d_R, s_R, b_R) \end{aligned} \tag{1.1.13}$$

LH and RH fermions present different hypercharge. Y_Q and Y_L denotes the LH fields' hypercharges, while Y_e, Y_u, and Y_d denote the RH fields' hypercharge. The field contents and their representation under the different gauge groups in the SM are shown in table 1.1, where the first two columns show the transformation properties under $SU(3)_C$ and $SU(2)_L$, while the last column shows the hypercharge of each field.

A lepton mass term in the SM Lagrangian would have the form $m_\alpha[\overline{\ell}_R^\alpha \ell_L^\alpha + \overline{\ell}_L^\alpha \ell_R^\alpha]$ where L and R stand for left–hand (LH) and right–hand (RH) helicities. Different helicities have different $SU(2)_L$ and $U(1)_Y$ gauge transformations. As a consequence, the explicit mass terms are forbidden in the SM Lagrangian since they violate chiral gauge symmetry. The resolution to this problem is achieved by means of the Higgs field and its interactions with fermions, known as *Yukawa interactions*. When the Higgs field acquires its vacuum expectation v, the Yukawa interactions lead to fermion mass terms as well as mixing between different generations in the SM Lagrangian of Eq. (1.1.1). For leptons, the Yukawa interaction is given as,

$$\mathcal{L}_{Y,\ell} = y_\ell \overline{L}^\alpha_L \phi e_R + h.c., \tag{1.1.14}$$

where y_ℓ is the Yukawa lepton coupling. This Lagrangian is $SU(2)$ and $U(1)$ invariant;[1] it generates the mass terms for leptons of the form $m_\ell = \frac{y_\ell}{\sqrt{2}}v$ after SSB, while neutrinos remain massless. In other words, there are no ν_R states in the SM, which is required to produce a ν mass term via an interaction with the Higgs field.

We need to adopt a slightly different approach to get the quark mass terms in the SM Lagrangian. We define Φ in terms of the Higgs field introduced previously, which is defined as $\Phi = i\sigma_2\phi^*$ with hypercharge $-1/2$ and transforms in the fundamental representation of $SU(2)$. Therefore, we can write a Yukawa term as,

$$\mathcal{L}_{Y,q} = y^d_{ij}\phi\overline{Q}^i_L\phi d^j_R + y^u_{ij}\overline{Q}^i_L\Phi u^j_R + h.c. \tag{1.1.15}$$

After SSB, the quark mass terms are

$$\mathcal{L}_{Y,q} = \frac{v}{\sqrt{2}}[\overline{d}_L\mathbf{y_d}d_R + \overline{u}_L\mathbf{y_u}u_R] + h.c. \tag{1.1.16}$$

where $u_{L,R} = u_{L,R}, c_{L,R}, t_{L,R}$ and $d_{L,R} = d_{L,R}, s_{L,R}, b_{L,R}$. $\mathbf{y_{u,d}}$ are mass matrices that need to be diagonalized by introducing two diagonal matrices M_u and M_d and two unitary matrices U_u and U_d such that[2]

$$\mathbf{y_{u,d}}\mathbf{y_{u,d}}^\dagger = U_{u,d}M^2_{u,d}U^\dagger_{u,d}. \tag{1.1.17}$$

---

[1] Both LH leptons and Higgs are $SU(2)$ doublets while the RH is a $SU(2)$ singlet. To see that the Lagrangian is also $U(1)$ invariant we need to sum up all the hypercharge, i.e. $-Y_L + Y_\phi + Y_e = 0$.

[2] The matrix $\mathbf{y_{u,d}}\mathbf{y_{u,d}}^\dagger$ is Hermitian and therefore has real eigenvalues.

For other unitary matrices $K_{u,d}$ we can generically write

$$\mathbf{y_{u,d}} = U_{u,d} M_{u,d} K^{\dagger}_{u,d}. \tag{1.1.18}$$

If we introduce this in the Lagrangian and additionally change the basis for the LH quarks $q_L \to U q_L$ and the RH quarks $q_R \to K q_R$, we are left only with the mass matrices M_u and M_d,[1]

$$\mathcal{L}_{Y,q} = m^d_j \overline{d}^j_L d^j_R + m^u_j \overline{u}^j_L u^j_R \tag{1.1.19}$$

where $m^j_{u,d}$ are diagonal elements of $\frac{v}{\sqrt{2}} M_{u,d}$. In the following section, we will discuss how this change of basis leads to mixing effects.

1.1.3 CKM Matrix

When the Higgs couples to quarks through Yukawa interactions and it acquires a vacuum expectation value we must introduce a change of basis for LH (RH) quarks $q_L \to U q_L$ ($q_R \to K q_R$) in order to obtain the diagonal mass matrix. As a result, the $W^{\pm}$ interactions couple to the physical q_L, leading to a mixing between families

$$\mathcal{L}_{kin} = \frac{-g}{\sqrt{2}} \overline{Q}^u_L \gamma^{\mu} W^+ V_{\mathrm{CKM}} Q^d_L + h.c \tag{1.1.20}$$

where $V_{\mathrm{CKM}} = U^{\dagger}_u U_d$ is known as the Cabbibo–Kobayashi–Maskawa (CKM) matrix [22]. The CKM matrix is a 3×3 unitary matrix that can be parameterized by three mixing angles and one phase [23],

$$V_{\mathrm{CKM}} = \begin{pmatrix} c_{12}c_{13} & s_{12}c_{13} & s_{13}e^{-i\delta} \\ -s_{12}c_{23} - c_{12}s_{23}s_{13}e^{i\delta} & c_{12}c_{23} - s_{12}s_{23}s_{13}e^{i\delta} & s_{23}c_{13} \\ s_{12}s_{23} - c_{12}c_{23}s_{13}e^{i\delta} & -c_{12}s_{23} - s_{12}c_{23}s_{13}e^{i\delta} & c_{23}c_{13} \end{pmatrix} \tag{1.1.21}$$

where $s_{ij} = \sin\theta_{ij}$, $c_{ij} = \cos\theta_{ij}$ corresponds to rotations in the ij–flavour planes and δ is the phase that accounts for CP–violation in the SM.[2]

---

[1] This is known as going to the mass basis.

[2] The necessary condition for CP invariance is that elements of the CKM matrix must be real. This is true for the three quark families only if $\delta = 0$ or $\delta = \pi$. If δ is not either of those values means that the CKM matrix is a source of CP–violation.

1.1.4 CP Violation in the SM

The study of CP violation in the SM dates back to the late 40s and early 50s when two supposedly different particles τ–meson and Θ-meson were observed to decay, via weak interactions, into three and two pions, respectively. [24]. The lifetime and mass of such particles were found to be identical, meaning they might be the same particle. However, the parity conservation in the decay process indicates that two pions would combine to produce a net parity of $+1$, and three pions would combine to have a net parity of -1 [25]. Therefore, if parity holds τ and Θ could not be the same particle. This is the so called *tau-theta puzzle*.

Around 1956, Chen-Ning Yang and Tsung-Dao suggested that parity might not hold in weak interactions in order to explain the tau-theta puzzle [26]. Among the several experiments their proposed, one of the simplest one was measurements on the beta decay of cobalt-60. This experiment was performed by Chien-Shiung Wu[1]. Wu observed that majority of emitted electrons went in one direction, showing an asymmetric behaviour. Thus proving that that parity is violated in weak subatomic interactions. Chen-Ning Yang and Tsung-Dao won the Nobel prize for such discovery, however Wu received public recognition only 21 years later, when she was awarded the Wolf prize.

Later in 1964, Cronin and Fitch decided to test P and C symmetries in Kaon decays. They discovered that P, C and CP symmetries are violated in such process [27]. It was not until 2001 when CP violation was discovered in B-meson decays by the Belle experiment [28] at the High Energy Accelerator Research Organisation (KEK) and the Babar experiment [29] at the National Accelerator Laboratory. Later on in 2010 LHCb experiment extends measurements of CP violation to much grater precision in the Large Hadron Collider (LHC) at CERN [30]. LHCb has measured the CKM mixing matrix elements and CP violation parameters in processes involving transitions of a b quark to a u or a c quark.

---

[1] She also received the help of Ernest Ambler, Ralph Hudson, Raymond Hayward and Dale Hoppes

In principle, the charge conjugation parity (CP) symmetry indicates that the laws of physics should be the same for matter and antimatter. However, assuming that the evolution of the Universe preserves the ratio between matter and antimatter components, the CP–symmetry must have been violated somehow to explain the predominance of matter over antimatter.

As discussed in the previous section, CP–violation appears in weak interactions in the SM. Unfortunately, the amount of asymmetry generated during such weak interactions is not enough to explain the observed matter–antimatter asymmetry. This strongly suggests that, besides weak interactions in the quark sector,[1] there must be additional sources of CP–violation, in physics beyond SM (BSM). This and some other SM challenges will be briefly discussed in the next section.

1.2 Physics Beyond the Standard Model

The SM of particle physics is not considered as the final theory of fundamental interactions. Instead, it is believed that there must be physics beyond the SM (BSM) and that the SM is only an effective theory below some cut-off scale. In the following, we briefly discuss some of the shortcomings of the SM that are relevant to this work. A more detailed discussion will be given in Chapter 2.

- **Neutrino masses.** Neutrino oscillation experiments have revealed that neutrinos are massive particles [31, 32], yet in the Standard Model they are predicted to be massless. The study of neutrino oscillations is a viable probe of BSM physics. Neutrino could be Dirac particles, therefore there could be a RH neutrino sate that does not interact with matter; this is known as a sterile neutrino. Neutrinos could also be Majorana particles, which implies that the neutrino is its own antiparticle. If this is the case, then introducing another Majorana heavy neutrino could explain the very low value of the neutrino

---

[1] CP violation can occur in the lepton sector and explain baryogenesis via leptogenesis.

masses compared to quarks and charged leptons via the seesaw mechanism. The decay of such a heavy particle could create CP violation large enough to explain the matter anti–matter asymmetry in the Universe.

- **CP–violation and Baryon Asymmetry.** Baryon asymmetry is characterised in terms of the baryon–to–photon ratio $\eta \sim 10^{-10}$ [33, 34]. The origin of such asymmetry is one of the most important questions in particle physics, and one of the conditions to produce such asymmetry is CP–violation. However, it is well established that CP-violation within the SM cannot explain why there is more matter than antimatter in our Universe. Hence, a new source of CP–violation is necessary to explain baryon asymmetry in the Universe.

- **Dark Matter.** Dark matter (DM) remains an unresolved mystery in cosmology and particle physics. There exists a body of evidence pointing towards the presence of some form of invisible matter in the Universe, for more detail see [35, 36, 37, 38, 39]. Neutrinos in the SM have all the essential characteristics for being a potential dark matter candidate: they are stable, neutral and without strong interactions. However, neutrino masses are so small that they would not be able to produce the observed number of large-scale-structures of our Universe in the simplest frameworks.

1.3 Motivation and Outline of this Thesis

This thesis is divided into two main subjects, namely polarisation of gamma rays and dark matter interactions. Firstly we will study the CP violation in radiative neutrino decays as a possible source of circularly polarised photons and the polarisation changes of such signals while propagating through the Universe. Secondly and last part of this work, we pay attention to constraints on dark matter interactions using compact stellar objects as complementary to DD experiments.

Observations of circular polarisation of gamma-rays provide a new way to search for BSM physics. This is because CP must be violated in order to generate a net circular polarisation. Electromagnetic or strong interactions are symmetric under C and P transformations, therefore they are also symmetric under CP. This means that they cannot generate a net circular polarisation. In general, we need processes that involve the interaction of asymmetric particles in order to obtain a net circular polarisation effect.

In particular if CP is violated during radiative neutrino decay $\nu_i \to \nu_f + \gamma_\lambda$, an asymmetry between two circularly–polarised photons can be generated. Therefore the circular polarisation of gamma–rays provides a potentially crucial probe to show the existence of CP violation in the neutrino sector.

A milestone in BSM physics is the evidence for DM. Although all the evidence stems from gravitational effects, the leading paradigm does assume that the DM has weak, yet not negligible, interactions with SM particles. Probing the existence of DM and its interactions with the visible sector is one of the biggest challenge contemporary physics faces. It involves cosmology, astrophysics, as well as particle physics.

There is a vast number of experiments currently searching for DM particles. In particular, direct detection (DD) experiments aim to observe nuclear recoils produced by DM particles scattering off target nuclei. During the past decade, significant progress has been achieved in DD searches. Experiments have reduced the background due to cosmic and gamma rays by shielding and placing experiments underground. However, background due to solar and atmospheric neutrinos is still a challenging problem in the sensitivity of the experiments [40]. Additionally, the sensitivity is limited by their threshold energy and target mass. Xenon1T has the best experiment sensitivity (for spin independent interactions), currently is up to a DM-proton cross section of $4.1 \times 10^{-47}\text{cm}^2$ for a DM mass around $30\,\text{GeV}$ [41].

Objects such as the Sun or planets cannot accelerate DM particles to relativistic velocities. Consequently, since DM particles are non-relativistic in the Galactic halo, most of the possible DM interactions with the matter in the Solar neighbourhood involve very small transferred momentum and low velocities. Therefore, DD experiments are limited to this non-relativistic regime, which makes it very hard to detect the DM and place constraints on momentum- or velocity-dependent DM-proton cross sections.

Finally, in the low mass regime of DM particles, the best constraints (below 5 GeV and up to 1.8 GeV) are given by Darkside [42]. At such low masses, the recoil energy produced is tiny and the neutrino floor becomes large, making the task of detection very difficult.

Due to their high densities, white dwarfs (WDs) are one of the best compact objects proposed as cosmic laboratories for studying physical processes happening at very extreme conditions that cannot be achieved at terrestrial laboratories. For instance, unlike DD experiments, DM particles close to WDs will be accelerated to high velocities due to the strong gravitational potential enabling us to probe velocity (momentum) dependent interactions. In addition, the low DM mass regime is not limited by a recoil threshold.

DM particles surrounding WDs may be captured when interacting with matter within the star. The capture will occur when the DM particle loses enough energy after scattering off a nucleus. This energy transferred to the nuclei in the capture and annihilation processes will lead to a rise in the star temperature. The heat induced in the WD creates an observational signal that we can use to set constraints on the interaction strength of DM particle(s) with nuclei.

In Chapter 2, a brief background is presented; a more detailed description of BSM physics related to neutrino masses and DM candidates is given. The discussion of radiative transfer of polarisation of low–energy polarised gamma-rays is also addressed, crucial for the understanding of their propagation through space once they are generated. Chapter 3 outlines the general connection between CP violation and circular polarisation for both Dirac and Majorana fermions, and can be used for any class of models that produce such radiative decays. The total CP violation is calculated based on a widely studied Yukawa interaction considered in both active and sterile neutrino radiative decay scenarios. In Chapter 4, the previous discussion is applied to a heavy neutrino radiatively decaying by means of SM interactions. In Chapter 5 we discuss the polarisation of high energy radiation after scattering off particles. After demonstrating the failure of geometric and low–energy QFT approaches, the transport formalism is established. This formalism is used to describe the change of high–energy photon polarisation when propagating through space or the atmosphere. Compton interactions are the primary focus, but the approach is general enough to describe the scattering of high energy photons off new particles or through new interactions. Finally, the conditions for a circularly–polarised γ–ray signal to keep the same level of circular polarisation as it propagates through its environment are discussed. Additionally, in the first part of Chapter 6, the study of the properties of white dwarfs, such as internal structure and equation of state, are summarised. In the second part, a discussion of the DM capture in WDs and calculation of bounds on DM interactions are extensively presented. Finally, we conclude in Chapter 7.

Chapter 2

Background

Polarisation of light is vital for the study of modern physics and BSM physics. For instance, linear and circular polarisation of the CMB could reveal more about the early Universe [43]; moreover, the observation and study of polarisation of electromagnetic waves can lead to hints of physics BSM [44]. Therefore, in the first part of this chapter, Sec. 2.1 and Sec. 2.2, a review of some of the topics on physics BSM is presented i.e. current status of neutrino physics and dark matter. Since circularly polarised photons can be changed when they propagate through the Universe, in the second part of this chapter, Sec. 2.3, the formalism for the study of circular polarisation in the classical regime (low–energy photons) is revisited; later on in this work such formalism will be generalised at any energies.

2.1 Relevant Aspects of Neutrino Physics

Neutrinos are spin 1/2 and electrically neutral particles which appear in three different species: ν_e (electron–type), ν_μ (muon–type) and ν_τ (tau–type)[2]. Due to gauge invariance neutrino mass terms cannot be included in the SM Lagrangian and as a

---

[2] Electron–type neutrinos are produced in nuclear beta decay, particularly in neutron decay processes $n \to p + e^- + \overline{\nu}_e$; they are also produced in muon decays $\mu^\pm \to e^\pm + \overline{\nu}_\mu(\nu_\mu) + \nu_e(\overline{\nu}_e)$. Muon–type neutrinos and anti-neutrinos are produced in muon decays and pion decays $\pi^\pm \to \mu^\pm + \nu_\mu(\overline{\nu}_\mu)$. Tau–type neutrinos are produced in $\tau^\pm$ decays.

consequence they are assumed to be massless. Nevertheless, neutrino experiments have shown that these particles possess very tiny masses since they can oscillate, after propagating a macroscopic distance, from one species to another $\nu_i \leftrightarrow \nu_j$. A leptonic mixing matrix will appear analogous to the CKM matrix discussed in Chapter 1. This gives rise to a leptonic charged current (CC) interaction of the form

$$\mathcal{L}_{CC} = \frac{g}{\sqrt{2}}(\overline{e}_L\, \overline{\mu}_L\, \overline{\tau}_L)\gamma^{\mu}\mathcal{U}_{\alpha\, i}\nu_i W^+_{\mu} + h.c. \tag{2.1.1}$$

with

$$\nu_\alpha = \mathcal{U}_{\alpha i}\nu_i \tag{2.1.2}$$

where $\alpha = e,\ \mu,\ \tau$ are the flavor eigenstates, $i = 1, 2, .., n$ are the mass eigenstates and $\mathcal{U}_{\alpha\, i}$ is a $3 \times n$ matrix that connects flavor states with mass states. This matrix was introduced by Ziro Maki, Masami Nakagawa and Shoichi Sakata in 1962 [45] to describe the neutrino oscillations. The idea of neutrino oscillation dates back to 1958 when Bruno Pontecorvo proposed the neutrino-antineutrino transition [46]. Nowadays the mixing matrix is known as the PMNS matrix.

For decades, studies of neutrinos have deepened our understanding of nature [47]. Although their very small but non-zero masses (for at least two of their generations) and lepton flavour mixing have been observed and verified by neutrino oscillation experiments, some fundamental questions about neutrinos such as their electromagnetic properties, CP violation, whether they are Dirac or Majorana fermions and if they have additional species existing in nature remain unknown.

2.1.1 Dirac vs Majorana Neutrinos

In this section we will address the discussion of neutrino masses. Since the nature of neutrinos is still an open question, the two possible Dirac and Majorana cases are discussed.

Dirac mass term

In order to generate a Dirac neutrino mass, it is necessary to introduce additional RH neutrino(s) ν_R to the SM Lagrangian. This will yield to neutrino mass terms through the Higgs mechanism, just like in the case of quarks and leptons.

RH neutrino fields are invariant under SM symmetries. They are singlets of – $SU(3)_C \otimes SU(2)_Y$ and have hypercharge $Y = 0$. Since they do not participate in weak interactions they are called sterile neutrinos. The number of sterile neutrinos that can be introduced to extend the SM is not constrained by the theory. In the simplest case where three sterile neutrinos, one for each flavor, are introduced to the SM, the extended Lagrangian mass term for leptons is now

$$\mathcal{L}_{\nu,Y} = -\overline{L}_L \mathbf{y}_\ell \phi e_R - \overline{L}_L \mathbf{y}_\nu \Phi \nu_R + h.c \tag{2.1.3}$$

with $\mathbf{y}_\nu$ a Yukawa matrix, $\overline{L}_L$ given by Eq. (1.1.12) and

$$\nu_R = \begin{pmatrix} \nu_{eR} \\ \nu_{\mu R} \\ \nu_{\tau R} \end{pmatrix} \tag{2.1.4}$$

The matrix $\mathbf{y}_\nu$ can be diagonalised in a similar way as for charged leptons, see chapter 1, and this is

$$V_L^{\nu,\ell\dagger} \mathbf{y}_{\nu,\ell} V_R^{\nu,\ell} = \mathbf{y}^\nu \tag{2.1.5}$$

$V_L^{\nu,\ell}$ and $V_R^{\nu,\ell}$ are 3×3 unitary matrices and the RHS is the diagonalised matrix $\mathbf{y}^\nu = y_{ij}^\nu \delta_{ij}$. From here we see that the change of basis for neutrinos is therefore $\nu_L' \to V_L^\dagger \nu_L$ and $\nu_R' \to V_R^\dagger \nu_R$. Hence when introducing this change of basis and the diagonalised mass matrix in Eq. (2.1.5) the neutrino Dirac masses terms are finally obtained in the Lagrangian given by

$$\mathcal{L}_{.mass} = \frac{1}{2}\bar{\ell}_{L\alpha} M_\ell \ell_{R\alpha} + \frac{1}{2}\overline{\nu}_L M_\nu \nu_R + h.c. \tag{2.1.6}$$

where M_ℓ is the diagonal mass matrix for charged leptons and

$$M_{\nu_i} = \frac{y_i^\nu v}{\sqrt{2}} \tag{2.1.7}$$

The mass terms of leptons in the Lagrangian, including neutrino masses, is given in Eq. (2.1.6). Following a similar approach of that for quarks in chapter 1, the change of basis for neutrinos made in this section generates the flavour mixing in the leptonic Lagrangian. It is straightforward to show that for three Dirac neutrinos the change of basis is therefore given as,

$$\mathcal{U}^D = V_L^{\ell\,\dagger} V_L^\nu . \tag{2.1.8}$$

This is the mixing matrix in the leptonic sector analogous to the CKM-matrix for the case of quarks. For Dirac neutrinos the mixing matrix depends on three mixing angles and one CP-violating phase. We will further discuss this at the end of this section.

Majorana mass term

In 1937 Majorana established that a massive neutral fermion can be described by a real wave equation [48]. This implies that the Majorana particle is its own antiparticle.[1] This led to the Majorana condition,

$$\nu = \ \nu^C \tag{2.1.9}$$

where the Majorana field is defined as $\nu = \nu_L + \nu_L^C$ and $\nu^C \equiv \mathcal{C}\,\overline{\nu}^T$, where $\mathcal{C}$ is the charge conjugation matrix.[2]

The Majorana mass term is obtained by substituting in Eq. (2.1.6) the RH neutrino ν_R by the charge conjugated field $\nu_L = \mathcal{C}\,\overline{\nu_L}^T$, which is indeed a RH chiral field. For one generation of Majorana neutrino, the Majorana Lagrangian is commonly written

---

[1] In the case in which particles and antiparticles were distinguishable, the wave function must be complex (Dirac nature).

[2] $\mathcal{C}\gamma_\mu^T\mathcal{C}^{-1} = -\gamma_\mu$.

as

$$\mathcal{L}^M = \frac{1}{2}\overline{\nu_L} i \overset{\leftrightarrow}{\not\partial} \nu_L - \frac{M}{2}\left(\overline{\nu_L}\mathcal{C}\overline{\nu_L}^T - \nu_L \mathcal{C}^\dagger \nu_L\right) \tag{2.1.10}$$

If now three generation of Majorana neutrinos are considered the Majorana mass term becomes

$$\mathcal{L} = \frac{1}{2}\sum_{\alpha\,,\beta} {\nu'}^T_{\alpha\, L}\mathcal{C}^\dagger M^L_{\alpha\beta}\nu'_{\beta\, L} \tag{2.1.11}$$

As in the case of Dirac neutrinos, it is necessary to diagonalise the complex symmetric matrix M^L. This, as usual, is achieved by introducing the 3×3 unitary matrix $V^n u_L$

$$(V^\nu_L)^T M^L V^\nu_L = M_\nu. \tag{2.1.12}$$

The diagonalisation is achieved by the change of basis $\nu' L \to V^\nu_L \to \nu_L$.[1] Using this, the Majorana mass term can be written as

$$\mathcal{L} = \frac{1}{2}\sum_{i=1}^{3} m_i \overline{\nu^C_{iL}}\nu_{iL} + h.c \tag{2.1.13}$$

As in the case of Dirac neutrinos, the leptonic Lagrangian with Majorana neutrinos can be written as in Eq. (2.1.1) with the Majorana mixing matrix $\mathcal{U}$. Nevertheless, there is an important difference compared to the Dirac mixing matrix. The Majorana mass term is not invariant under the global $U(1)$ symmetry. Therefore the physical CP–violating phases in the Majorana mixing matrix are three instead of one. The Majorana mixing matrix can be written in terms of the unitary Dirac mixing matrix in Eq. (2.1.8) and a diagonal matrix P_ν with two independent phases

$$\mathcal{U}^M = \mathcal{U}^D P_\nu \tag{2.1.14}$$

In the following section the discussion of the PMNS matrix parametrization is given in more detail.

---

[1] Here ν'_L corresponds to the LH flavour fields and ν_L to the fields with definite mass.

2.1.2 PMNS matrix

The PMNS matrix given in Eq. (2.1.8) and Eq. (2.1.14) for Dirac and Majorana neutrinos, can generically be written as

$$\mathcal{U}_{\alpha i} = P_{\ell,\alpha\alpha} V^{\ell\dagger}_{\alpha j} V^{\nu}_{j i} P_{\nu,ii} \tag{2.1.15}$$

where P_ℓ is a 3×3 phase matrix and P_ν a diagonal matrix, both introduced such that they reduce the number of phases in the PMNS matrix ($\mathcal{U}_{\rm PMNS}$). In the standard PDG parametrisation of the $\mathcal{U}_{\rm PMNS}$ [47], the matrix for three neutrinos is assumed to be unitary, i.e.

$$\mathcal{U}^\dagger\mathcal{U} = \mathbf{1} \;\rightarrow\; \sum_\alpha \mathcal{U}^*_{\alpha j}\mathcal{U}_{\alpha i} = \delta_{ij}, \tag{2.1.16}$$

hence there are three flavour mixing angles ($\theta_{12}\,,\theta_{13}\,,\theta_{23}$) and one (or three) CP–violating phase(s) corresponding to Dirac (or Majorana) nature of neutrinos. With this standard parametrisation the explicit form of Eq. (2.1.15) is

$$\begin{aligned}
\mathcal{U}_{\rm PMNS} &= \begin{pmatrix} 1 & 0 & 0 \\ 0 & c_{23} & s_{23} \\ 0 & -s_{23} & c_{23} \end{pmatrix}
\begin{pmatrix} c_{13} & 0 & s_{13}e^{-i\delta_\nu} \\ 0 & 1 & 0 \\ -s_{13}e^{i\delta_\nu} & 0 & c_{13} \end{pmatrix}
\begin{pmatrix} c_{12} & s_{12} & 0 \\ -s_{12} & c_{12} & 0 \\ 0 & 0 & 1 \end{pmatrix} P_\nu \\
&= \begin{pmatrix} c_{12}c_{13} & s_{12}c_{13} & s_{13}e^{-\delta_\nu} \\ -s_{12}c_{23} - c_{12}s_{13}s_{23}e^{\delta_\nu} & c_{12}c_{23} - s_{12}s_{13}s_{23}e^{\delta_\nu} & c_{13}s_{23} \\ s_{12}s_{23} - c_{12}s_{13}c_{23}e^{\delta_\nu} & -c_{12}s_{23} - s_{12}s_{13}c_{23}e^{\delta_\nu} & c_{13}c_{23} \end{pmatrix} P_\nu
\end{aligned} \tag{2.1.17}$$

where $c_{ij} \equiv \cos\theta_{ij}$ and $s_{ij} = \sin\theta_{ij}$. δ_ν is the CP–violating phase which is referred to as Dirac phase. Analogous to the quark case discussed in chapter 1 the mixing matrix of Dirac neutrinos depends on these four physical parameters. Therefore, the diagonal matrix P_ν will be simply a unit matrix. In the case where neutrinos are considered to be Majorana particles, the diagonal P_ν contains additional arbitrary phases (ρ and σ), called Majorana phases. As a consequence, the physical *CP*–violating phases in the Majorana mixing matrix are three instead of one. This is due to the fact that the Majorana mass term in Eq. (2.1.13) is not invariant under global $U(1)$ gauge transformations.

2.1.3 Theory of Neutrino Oscillation

Neutrino flavor oscillations are generated by the mixing of different massive neutrinos [46, 49]. The probability of the neutrino to oscillate in vacuum from one state to another will be discussed in this section [50].

A neutrino with flavor α created in a CC weak interaction process from a charged lepton ℓ_α is described by the flavour state, see Eq. (2.1.2),

$$|\nu_\alpha\rangle = \sum_i \mathcal{U}^*_{\alpha\, i}|\nu_i\rangle \tag{2.1.18}$$

The massive neutrino states evolve in time as plane waves,

$$|\nu_i(t)\rangle = e^{-iE_it}|\nu_i\rangle \tag{2.1.19}$$

where $E_i = \sqrt{m_i^2 + \vec{p}^2}$ is the massive neutrino energy. From Eq. (2.1.18) and Eq. (2.1.19) the time evolution of a neutrino state of flavour α is given as

$$|\nu_\alpha(t)\rangle = \sum_i \mathcal{U}^*_{\alpha\, i} e^{-iE_it}|\nu_i\rangle . \tag{2.1.20}$$

Using the unitarity relation, Eq. (2.1.16) we can instead write the mass states in terms of the flavor states as follows

$$|\nu_i\rangle = \sum_\alpha \mathcal{U}_{\alpha\, i}|\nu_\alpha\rangle \tag{2.1.21}$$

and this result can be introduced into Eq. (2.1.20) to obtain

$$|\nu_\alpha(t)\rangle = \sum_\beta \sum_i \mathcal{U}^*_{\alpha\, i} e^{-iE_it}\mathcal{U}_{\beta\, i}|\nu_\beta\rangle \tag{2.1.22}$$

this means that the superposition of massive neutrino states $|\nu_\alpha(t)\rangle$, where $|\nu_\alpha(0)\rangle = |\nu_\alpha\rangle$, becomes a superposition of different flavor states if neutrinos are mixed. The amplitude of $\nu_\alpha \to \nu_\beta$ transition as a function of time is given by

$$A_{\nu_\alpha\to\nu_\beta}(t) = \sum_i \mathcal{U}^*_{\alpha\, i}\mathcal{U}_{\beta\, i} e^{-iE_it} \tag{2.1.23}$$

and the transition probability is given by $P_{\nu_\alpha \to \nu_\beta}(t) = |A_{\nu_\alpha \leftrightarrow \nu_\beta}(t)|^2$

$$P_{\nu_\alpha \to \nu_\beta}(t) = \sum_i \sum_j \mathcal{U}^*_{\alpha\, i} \mathcal{U}_{\beta\, i} \mathcal{U}_{\alpha\, j} \mathcal{U}^*_{\beta\, j} e^{-i(E_i - E_j)t} \tag{2.1.24}$$

In the case of ultra-relativistic neutrinos $m_i << 1$, the energy–momentum relation $E_i = \sqrt{m_i^2 + \vec{p}^2}$ can be approximated by

$$E_i \sim E + \frac{m_i^2}{2E}, \quad \text{with} \quad E = |\vec{p}| \tag{2.1.25}$$

then, the probability can be written in terms of the neutrino squared–mass difference $\Delta m_{ij}^2 = m_i^2 - m_j^2$

$$P_{\nu_\alpha \to \nu_\beta}(t) = \sum_i \sum_j \mathcal{U}^*_{\alpha\, i} \mathcal{U}_{\beta\, i} \mathcal{U}_{\alpha\, j} \mathcal{U}^*_{\beta\, j} e^{-i \frac{\Delta m_{ij}^2 L}{2E}} \tag{2.1.26}$$

where we have approximated $t \sim L$ and L is the distance from the neutrino source to the detector. From Eq. (2.1.26) we can highlight several things

- Measurements of neutrino oscillations provide information on the values of the squared–mass difference Δm_{ij}^2 and the elements of the $\mathcal{U}_{\text{PMNS}}$ matrix.

- It is only possible to obtain values of the squared–differences but not the absolute values of neutrino masses, i. e. m_i or m_j.[1]

- The oscillation probability depends on the elements of the mixing matrix $\mathcal{U}_{\text{PMNS}}$ through

  $$\mathcal{U}^*_{\alpha\, i} \mathcal{U}_{\beta\, i} \mathcal{U}_{\alpha\, j} \mathcal{U}^*_{\beta\, j}. \tag{2.1.27}$$

  This quadratic product does not depend on the choice of parametrisation and is invariant under re-phasing transformations. This means that it is independent of any phases that can be factorised. Therefore in the case of Majorana neutrinos, neutrino oscillations are independent of the Majorana phases (ρ,σ) factorised in a diagonal matrix on the right, see Eq. (2.1.17). Consequently Majorana phases cannot be measured in neutrino oscillation experiments.

---

[1] From solar neutrino experiments we know $m_i > m_j$.

2.1.4 Type-I Seesaw Mechanism

The seesaw model is an extension to the SM of particle physics which introduce n RH neutrinos. This mechanism supplies with a very elegant way to explain the non-zero neutrino masses and their smallness with respect to other fermions in the SM [51]. The Lagrangian of the type-I seesaw model is given as [52, 53, 54],

$$\mathcal{L}_I = \frac{1}{2}\overline{N_I}\partial\!\!\!/ N_I - \mathbf{y}_{I\alpha}\overline{N_I}\Phi^\dagger L_\alpha - \frac{1}{2}\overline{N_I}M_{IJ}(N_{IJ})^C + h.c \tag{2.1.28}$$

M_{IJ} is a Majorana mass matrix of the fields N_I, $\mathbf{y}_{I\alpha}$ are the Yukawa couplings between the sterile neutrino field, the Higgs $\Phi = i\sigma_2\phi^*$ field and the leptons L, see Eq. (2.1.3).[1]

In this work we will work in the minimal type–I seesaw which corresponds to including only two RH neutrinos N_I $(I = 1, 2)$. When the Higgs field acquires a vacuum expectation, see section 1.1 and section 2.1.1, it generates a matrix of complex Dirac masses $(m_D)_{I\alpha}$ for LH and RH neutrinos, which is proportional to the Yukawa coupling,

$$(m_D)_{I\alpha} = \frac{\mathbf{y}_{I\alpha} v}{\sqrt{2}} \tag{2.1.29}$$

with $v = 245$GeV the Higgs vacuum expectation value. After SSB, the Lagrangian containing the neutrino mass terms can be written as,

$$\mathcal{L}_I^M \subset -\frac{1}{2}\left(\overline{\nu_{\alpha L}}^C \; \overline{N_I}\right)\begin{pmatrix} \mathbf{0}_{\alpha\beta} & (\mathbf{m_D^T})_{\alpha\mathbf{J}} \\ (\mathbf{m_D})_{\mathbf{I}\beta} & \mathbf{M_{IJ}} \end{pmatrix}\begin{pmatrix} \nu_\beta^L \\ N_J^C \end{pmatrix} + h.c \tag{2.1.30}$$

The mass matrix $\mathbf{M^N}$ corresponding to the minimal type-I seesaw is therefore a 5×5 matrix,

$$\mathbf{M^N} = \begin{pmatrix} \mathbf{0}_{\alpha\beta} & (\mathbf{m_D^T})_{\alpha\mathbf{J}} \\ (\mathbf{m_D})_{\mathbf{I}\beta} & \mathbf{M_{IJ}} \end{pmatrix} \tag{2.1.31}$$

This can be diagonalized as in section 2.1.1, with a unitary matrix. The diagonalized

---

[1] Here we have changed the notation from ν_R to N_I to indicate we are working with a heavy RH neutrino.

mass matrix reads

$$\mathbf{M^N{}_D} = \begin{pmatrix} m_i\delta_{ij} & 0 \\ 0 & M_I\delta_{IJ} \end{pmatrix} \tag{2.1.32}$$

where m_i stands for the three light neutrinos m_1, m_2, m_3 and M_I stands for the two heavy neutrinos $N_1\,, N_2$. In this thesis, we are considering the case where the RH neutrino masses are larger than the EW scale, this is the seesaw limit.

The Majorana mass matrix given in Eq. (2.1.31) can be taken as already diagonalized.

$$\mathbf{M^N} \to \mathbf{M^N} \approx \begin{pmatrix} \mathbf{m}_{\alpha\beta} & \mathbf{0} \\ \mathbf{0} & \mathbf{M_{IJ}} \end{pmatrix} \tag{2.1.33}$$

where the mass matrix of the light neutrinos is given as,

$$m_{\alpha\beta} = -(m_D)^T_{\alpha I} M^{-1}_{IJ} (m_D)_{J\beta} \tag{2.1.34}$$

at the seesaw limit, the heavy neutrino mass eigenvalues coincide with the RH neutrino asses at the Lagrangian level. Moreover, Eq. (2.1.34) indicates that in the type I seesaw, the masses of the active neutrinos are suppressed by M_I. For a more detailed review we refer the reader to [55, 56, 57]. The $m_{\alpha\beta}$ matrix can be diagonalized by means of a unitary matrix $\mathcal{U}$. This is further discussed in this work.

2.2 Relevant Aspects of Dark Matter

There exists strong evidence pointing towards the presence of dark matter (DM) in the Universe. However DM remains an unresolved mystery in cosmology and particle physics that the community actively is addressing [58, 59, 60].

The first evidence of DM, was found by Zwicky [35, 36] who, by observing the dynamics of cluster of galaxies concluded that, inside the cluster, a significant fraction of matter was invisible to us. Several years after this observation, another striking evidence for dark matter was found by, independently, Vera Rubin's and Albert Bosma's in the observation of the rotation of curves of galaxies [37, 38]. In fig. 2.1a

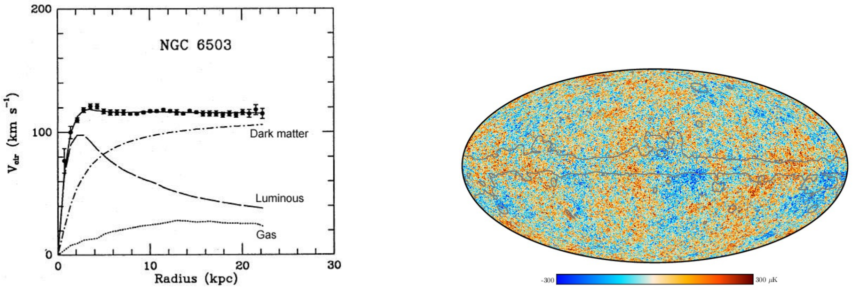

(a) (b)

Figure 2.1: 2.1a shows the rotation curves for NGC 6503 galaxy in function of the radial distribution. The dashed line correspond to the expected curve of rotation from visible matter. The dotted dashed line is the contribution from the DM halo, fig. taken from [63]. In 2.1b Temperature anisotropy of CMB from Planck collaboration. Fig. taken from [62]

an example of a rotation curve from the Galaxy NCG 6503 is shown. According to Newtonian dynamics, it is possible to establish a relation between the rotation velocity the stars within our galaxy and its mass distribution. Theoretically, the rotation velocity is expected to fall off with the distance according to $1/\sqrt{r}$. However Albert Bosma and Vera Rubin's observations shown a flat behaviour at large distances and so proving that the velocity remains constant at the edge of the visible galaxy.

Furthermore, simulations of the evolution of structure formation in the Universe, showed that the formation of galaxies could not happen if only ordinary matter is taken into account. A large amount of dark matter is required to explain observations of large-scale-structures [39]. Finally, analysis of the power spectrum of the Cosmic Microwave Background (CMB) gives information about the composition of the Universe, such as the abundance of baryons and dark matter. Measurements of the CMB by the Planck Satellite has reported $\Omega_{DM}h^2 = 0.120 \pm 0.001$, confirming that the Universe is composed of a large amount of dark matter[61, 62].

Since the very first evidence of the existence of DM, there has been great theoretical and experimental efforts to understand its nature. In the first part of this section, I briefly discuss some of the most important DM candidates. In the second part, I present the relevant DM experimental searches.

2.2.1 Dark Matter Candidates

Based on all the cosmological and astrophysical evidence, physicists have proposed several DM particle(s) candidates, which needs to be neutral, non-baryonic, non-relativistic, stable and collisionless.

One simple classification of DM is based on how relativistic they are when leaving thermal equilibrium in the early Universe. Hot DM (HDM) is still relativistic when decoupling and is in the range of up to a few tens of eV. It did not cluster to form clumps, instead galaxies formed only in super cluster regions where the matter distribution has locally collapsed [64]. Therefore HDM can only contribute to a small fraction of the total DM density. On the other hand cold DM (CDM) generally successfully explains the formation of large scale structure, producing numerical solutions in agreement with observations. However, it predicts too many substructures and possibly the wrong dark matter halo profile in observed dwarf galaxies [65]. Warm DM (WDM) could solve the CDM problems at small scales. WDM particles are usually relativistic at the time of their decoupling and become non relativistic afterwards.

The following list contains the most relevant DM particle candidates considered in this thesis.

- *SM neutrinos*

  Neutrinos have all the essential characteristics for being a potential DM candidate, such as being stable, neutral and without strong interactions. However, neutrino masses are so small that they would not be able to produce the observed large-scale-structures of our Universe in the simplest frameworks. Therefore, neutrinos cannot be a dominant component of DM. For a more complete review see Ref. [57].

- *Sterile neutrinos*

As originally proposed by Dodelson and Widrow [66], sterile neutrinos with a mass in the keV range are viable DM candidates. They are meant to be produced in the early Universe at very high temperatures and are usually referred to as WDM. For a complete review of sterile neutrinos in cosmology see Ref. [67].

Observational constraints on sterile neutrinos particle are placed from indirect detection through sterile neutrino decays ($\nu_N \to 3\nu$) [68] and loop mediated radiative decays $\nu_N \to \nu + \gamma$ [69]. The later is the main focus of this work and will be further discussed in chapter 3.

- *Weakly Interacting Massive Particle (WIMP)*

  Thermal WIMPs are produced and kinetically decouple in the early Universe after becoming non-relativistic. Because they are usually cold at decoupling, they are referred to as Cold DM. These hypothetical candidates are in the range of masses of tens of GeVs and are one of the best theoretically motivated candidates as their natural scale coincides with the scale of electroweak symmetry breaking (EWSB) in the thermal standard scenario. Within this classification, there are many DM-like WIMP particle candidates. We refer the reader to ref. [70] for a more complete review on WIMP particle candidates.

2.2.2 Searches for Dark Matter

In the following section, the techniques and current experiments searching for DM are briefly summarised. All experiments and techniques rely on the assumption that DM particles have a tiny interaction with SM particles.

- *Direct detection*

  These experiments are based on the hypothesis that DM particles interact weakly with SM particles, i.e. $\chi SM \to \chi SM$. Their aim is to measure the recoil energy generated after a DM particle scatters off a nucleus. Experiments are usually placed underground to avoid background such as cosmic rays. Some examples of direct detection experiments are, XENON1T [41, 71, 72], Lux[73], PandaX [74], and CRESST [75].

Such experiments have set limits in a wide range of DM masses, but the best constraint comes from XENON1T at a DM mass around 30 GeV and DM–nuclei cross section of $\sigma \sim 4.1 \times 10^{-47}\text{cm}^2$ [41].

- *Indirect detection*

  This type of experiment is based on the annihilation of DM particles to SM particles, i.e. $\chi\,\chi \to \overline{SM}\,SM$. Satellite and ground based telescopes are aiming to detect a signal on top of the background signal produced by well-known astrophysical processes. Examples of these experiments are CTA [76], IceCube [77], AMS [78], Fermi-LAT [79].

- *Collider searches*

  Similarly to direct and indirect detection, collider searches rely on the assumption that DM can be produced in SM particle collisions, i.e. $\overline{SM}\,SM \to \chi, \chi$. Just as neutrinos, the DM particle will not leave any particular signature in the detector. For more details on how collider searches work, see Ref. [80].

2.3 Theory of Radiative Transfer

Observation of gamma–rays from different sources in the Universe are key to searches for BSM physics. More specifically, the polarisation of these electromagnetic waves encodes important information on BSM interactions [44]. However, when propagating through our universe this information can be washed out due to further interaction with other kind of particles. It is thus necessary to establish a formalism that allows to understand and address such a problem.

The immediate solution comes from radiative transfer established by Chandrasekhar, who described the polarisation of starlight after scattering off dust particles in the atmosphere using a geometrical approach and introducing modified Stokes parameters, referred to as (I_l, I_r, U, V)[81]. His results for the radiative transfer are encapsulated in the so-called Phase–matrix (**P**–matrix) which describes the change in polarisation after scattering. In 1994 Kosowsky extended Chandrasekhar's formalism and described the polarisation of the Cosmological Microwave Background (CMB), as it propagates in an expanding (inhomogeneous) Universe using a QFT approach (see Ref. [82]).

Due to the nature of Rayleigh and Thomson scattering interactions, both Chandra–sekhar and Kosowsky concluded that, a low energy $(E_\gamma < m_e)$ circular polarisation signal cannot generate a linearly polarised component nor can it be produced by the scattering of a linear polarisation signal off cosmic material. Yet the intensity of a circularly polarised signal can change after scattering.

In this section we review the formalism introduced by Chandrasekhar to determine the polarisation of the visible light after Thomson or Rayleigh scattering. We also discuss possible sources of circularly polarised photons.

2.3.1 Electromagnetic Radiation and its Polarisation

The electric field $\vec{E}$ can be expressed as the linear combination of two perpendicular polarisation vectors $\vec{\epsilon}_l$ and $\vec{\epsilon}_r$,

$$\vec{E}(\mathbf{x}, t) = (E_r \; \vec{\epsilon}_r \; + \; E_l \; \vec{\epsilon}_l) e^{i(wt - \mathbf{k}\cdot\mathbf{x})} \,, \tag{2.3.1}$$

where $E_r = a_r e^{i\delta_r}$ and $E_l = a_l e^{i\delta_l}$ with $a_{l,r}$ being real and $\delta_{l,r}$ being the phases of $E_{l,r}$, respectively. From this definition, it follows that the two (orthogonal) vectors $\vec{\epsilon}_l$ and $\vec{\epsilon}_r$, which define the polarisation plane (see Fig. 2.2), can be written as [83]

$$\begin{aligned} \vec{\epsilon}_l(\mathbf{k}) =& \frac{1}{k_0 k_T}(k_x k_z, k_y k_z, -k_T^2) \,, \\ \vec{\epsilon}_r(\mathbf{k}) =& \frac{1}{k_T}(-k_y, k_x, 0) \;, \end{aligned} \tag{2.3.2}$$

where $\mathbf{k}$ refers to the 3-momentum of the propagating light $\mathbf{k} = (k_x, k_y, k_z)$ and $k_T = \sqrt{k_x^2 + k_y^2}$. When the two phases are the same $\delta_l = \delta_r = \delta$, the electric field is linearly polarised, and can be expressed as,

$$\vec{E}(\mathbf{x}, t) = (a_r\, \vec{\epsilon}_r \; + a_l\, \vec{\epsilon}_l\,)\; e^{i\delta} e^{i(wt - \mathbf{k}\cdot\mathbf{x})}\,. \tag{2.3.3}$$

When the phases differ by $\delta_l - \delta_r = \pm\pi/2$ and the amplitudes are the same ($a_r = a_l = a$), the electric field rotates around the propagation direction and the light is circularly polarised. The electric field then reads

$$\vec{E}(\mathbf{x}, t) = (\vec{\epsilon}_r \; \pm \; i\, \vec{\epsilon}_l)\; a\; e^{i\delta_r} e^{i(wt - \mathbf{k}\cdot\mathbf{x})}\,. \tag{2.3.4}$$

For convenience, we will define another set of perpendicular vectors $\vec{\epsilon}_\pm$ as a linear combination of $\vec{\epsilon}_{l,r}$, which can be written as

$$\vec{\epsilon}_\pm(k) = \frac{1}{\sqrt{2}}(\mp \vec{\epsilon}_l - i\, \vec{\epsilon}_r)\,, \tag{2.3.5}$$

where $\vec{\epsilon}_+$ and $\vec{\epsilon}_-$ describe photons with positive and negative helicity along the propagating direction respectively. The electric field in this “±" basis, reads as

$$\vec{E}(\mathbf{x}, t) = (E_+\, \vec{\epsilon}_+ \; + \; E_-\, \vec{\epsilon}_-)\; e^{i(wt - \mathbf{k}\cdot\mathbf{x})}\,, \tag{2.3.6}$$

where $E_\pm$ are given by

$$\begin{aligned} E_+ =& -\frac{a_l\, e^{i\delta_l} - i a_r\, e^{i\delta_r}}{\sqrt{2}}\,, \\ E_- =& \frac{a_l\, e^{i\delta_l} + i a_r\, e^{i\delta_r}}{\sqrt{2}}\,. \end{aligned} \tag{2.3.7}$$

Without loss of generality, one can always re-parametrise $E_\pm$ as $E_\pm = a_\pm e^{i\delta_\pm}$ with $a_\pm$ being absolute values in the ± basis and $\delta_\pm$ the associated phases. The (l, r) basis is more convenient to describe the linearly polarised light while the ± basis is more appropriate to describe circularly polarised light. We will use both in the following, depending on whether the emphasis is on circular or linear polarisation.

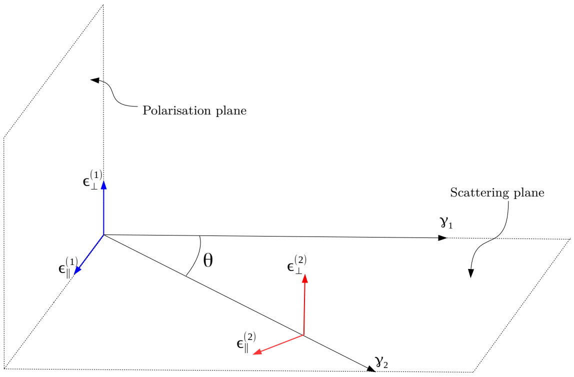

Figure 2.2: Illustration of the scattering plane formed by the incoming and outgoing photon directions. Before the scattering, the ϵ_r and ϵ_l vectors that define the polarisation plane are parallel and perpendicular to the scattering plane, so we denote them by $\epsilon_\perp^{(1)}$ and $\epsilon_{||}^{(1)}$ respectively. After the scattering, the polarisation plane (defined by $\epsilon_\perp^{(2)}$ and $\epsilon_{||}^{(2)}$) forms an angle θ with respect to the initial polarisation plane.

Stokes Parameters

One can describe the polarisation of light using four Stokes parameters. In the conventional formalism, the I–parameter measures the intensity of the polarisation signal, the Q– and U–parameters provide information regarding the linear polarisation of that signal and the V–parameter indicates whether the observed light is circularly polarised.

In the (l, r) basis, the Stokes parameters are defined by

$$\begin{aligned}
I &= |\vec{\epsilon}_l \cdot \vec{E}|^2 + |\vec{\epsilon}_r \cdot \vec{E}|^2 = a_l^2 + a_r^2 \,, \\
Q &= |\vec{\epsilon}_l \cdot \vec{E}|^2 - |\vec{\epsilon}_r \cdot \vec{E}|^2 = a_l^2 - a_r^2 \,, \\
U &= 2 \ \mathrm{Re}[(\vec{\epsilon}_r \cdot \vec{E})^* \times (\vec{\epsilon}_l \cdot \vec{E})] = 2 \ a_r \, a_l \cos(\delta_r - \delta_l) \,, \\
V &= -2 \ \mathrm{Im}[(\vec{\epsilon}_r \cdot \vec{E})^* \times (\vec{\epsilon}_l \cdot \vec{E})] = 2 \ a_r \, a_l \sin(\delta_r - \delta_l) \,, \qquad (2.3.8)
\end{aligned}$$

while in the ± basis (defined by Eq. (2.3.5)), the Stokes parameters read as

$$\begin{aligned}
I &= |\vec{\epsilon}_+ \cdot \vec{E}|^2 + |\vec{\epsilon}_- \cdot \vec{E}|^2 = a_+^2 + a_-^2 \,, \\
Q &= -2 \ \mathrm{Re}[(\vec{\epsilon}_+ \cdot \vec{E})^* \times (\vec{\epsilon}_- \cdot \vec{E})] = -2 \, a_+ \, a_- \cos(\delta_+ - \delta_-) \,,
\end{aligned}$$

$$
\begin{aligned}
U &= 2\,\mathrm{Im}[(\vec{\epsilon}_+ \cdot \vec{E})^* \times (\vec{\epsilon}_- \cdot \vec{E})] \;= 2\,a_+\,a_-\;\sin(\delta_+ - \delta_-)\,,\\
V &= |\vec{\epsilon}_+ \cdot \vec{E}|^2 - |\vec{\epsilon}_- \cdot \vec{E}|^2 \;= a_+^2 - a_-^2\,. \qquad (2.3.9)
\end{aligned}
$$

This last equality indicates that there is no net circular polarisation ($V = 0$) when the number of polarisation states are the same ($a_+^2 = a_-^2$).

Stokes Operator

To describe the change in polarisation and relate the Stokes parameters before and after scattering using Quantum principles, we first need to remind the reader of the definition of a photon quantum state. The latter reads as [84]

$$|\gamma^{(\alpha)}\rangle = a_r\,e^{i\theta_r}|\,\epsilon_r^{(\alpha)}\rangle \,+\, a_l\,e^{i\theta_l}|\,\epsilon_l^{(\alpha)}\rangle\,, \qquad (2.3.10)$$

where $|\epsilon_{r,l}^{(\alpha)}\rangle$ are the polarisation states and $\alpha = 1,2$ denotes the initial and final states, respectively. Let the operator for the Stokes parameters be $\hat{S} = (\hat{I}, \hat{Q}, \hat{U}, \hat{V})$, then the associated observables can be constructed using the relationship

$$S^{(\alpha)} \equiv \langle S^{(\alpha)}\rangle = \langle\gamma^{(\alpha)}\,|\,\hat{S}^{(\alpha)}\,|\,\gamma^{(\alpha)}\rangle\,, \qquad (2.3.11)$$

with $\hat{S}^{(\alpha)}$ being the Stokes operators for the initial or final states defined as

$$\hat{S}^{(\alpha)} = \mathbf{W}\,|\epsilon_j^{(\alpha)}\rangle\,\langle\epsilon_i^{(\alpha)}| \qquad (2.3.12)$$

with $i, j = r, l$ or $\pm$. In the (l, r) basis, the Stokes operator takes the form

$$\begin{bmatrix} \hat{I} \\ \hat{Q} \\ \hat{U} \\ \hat{V} \end{bmatrix}^{(\alpha)} = \underbrace{\begin{bmatrix} 1 & 0 & 0 & 1 \\ 1 & 0 & 0 & -1 \\ 0 & 1 & 1 & 0 \\ 0 & -i & i & 0 \end{bmatrix}}_{\mathbf{W}} \begin{bmatrix} |\epsilon_l\rangle\langle\epsilon_l| \\ |\epsilon_r\rangle\langle\epsilon_l| \\ |\epsilon_l\rangle\langle\epsilon_r| \\ |\epsilon_r\rangle\langle\epsilon_r| \end{bmatrix}^{(\alpha)}\,, \qquad (2.3.13)$$

which leads to the definitions in Eq. (2.3.8). In the ± basis, the Stokes operators take the form

$$\begin{bmatrix}\hat{I}\\ \hat{Q}\\ \hat{U}\\ \hat{V}\end{bmatrix}^{(\alpha)} = \underbrace{\begin{bmatrix}1 & 0 & 0 & 1\\ 0 & -1 & -1 & 0\\ 0 & i & -i & 0\\ 1 & 0 & 0 & -1\end{bmatrix}}_{\mathbf{W}} \begin{bmatrix}|\epsilon_+\rangle\langle\epsilon_+|\\ |\epsilon_+\rangle\langle\epsilon_-|\\ |\epsilon_-\rangle\langle\epsilon_+|\\ |\epsilon_-\rangle\langle\epsilon_-|\end{bmatrix}^{(\alpha)}, \tag{2.3.14}$$

leading to the definitions in Eq. (2.3.9).

2.3.2 Theory of Classic Radiative Transfer

Chandrasekhar was able to predict the polarisation of sunlight after scattering off dust particles [81] by using a geometrical description of the scattering and by introducing a modified set of Stokes parameters (I_l, I_r, U, V). Here, I_l, I_r are the intensity components $(I = I_l + I_r)$ of the signal in the scattering plane, which is defined by the $\epsilon_{l,r}$ vectors shown in Fig. 2.2. These vectors are themselves defined with respect to the $(\epsilon_{||}, \epsilon_{\perp})$ vectors that define the polarisation plane. One can also define $Q = I_l - I_r$, with $I_r = a_r^2$ and $I_l = a_l^2$.

The reason why Chandrasekhar could describe the radiative transfer using such a geometrical approach instead of Quantum Field Theory is that at low energy, the scattering changes the direction of the outgoing particles but has a negligible effect on the energy of the scattered particles. Hence, it is possible to express the radiative transfer in 2D using the one angle between the incident and outgoing photons (see Fig. 2.2). This makes the relation between the outgoing and incoming Stokes parameters extremely simple. In 3D, the same geometrical approach requires 4 angles. It is thus somewhat easier to first describe the scattering in 2D and then embed the result in 3D. The description of the radiative transfer in 2D is encapsulated in the so-called **R**–matrix whereas the 3D description is encapsulated in the **P**–matrix, and it can be summarised as,

$$\begin{bmatrix} I_l \\ I_r \\ U \\ V \end{bmatrix}^{(2)} = \mathbf{R} \begin{bmatrix} I_l \\ I_r \\ U \\ V \end{bmatrix}^{(1)} , \tag{2.3.15}$$

where the superscript (1) and (2) denote the parameters before and after scattering respectively. Since at low energy and in the scattering plane the photons are scattered with an angle θ in the l direction (see Fig. 2.2), one can deduce that $I_l^{(2)} = \cos^2\theta\, I_l^{(1)}$ and $I_r^{(2)} = I_r^{(1)}$. Therefore the **R**–matrix for Thomson scattering reads as,

$$\mathbf{R}_{\text{Chandrasekhar}} = \begin{bmatrix} \cos^2\theta & 0 & 0 & 0 \\ 0 & 1 & 0 & 0 \\ 0 & 0 & \cos\theta & 0 \\ 0 & 0 & 0 & \cos\theta \end{bmatrix} . \tag{2.3.16}$$

The **P**–matrix is then readily obtained by first rotating the plane defined by the incoming polarisation vectors by an angle $-\Phi_1$ and then rotating the outgoing direction by $\pi - \Phi_2$, as shown in Fig. 2.3b. This leads to the following relationship between the **P**– and the **R**–matrices [81]

$$\mathbf{P}_{\text{Chandrasekhar}} = \mathbf{L}(\pi - \Phi_2)\, \mathbf{R}_{\text{Chandrasekhar}}\, \mathbf{L}(-\Phi_1) , \tag{2.3.17}$$

where $\mathbf{L}(\Phi)$ is defined as,

$$\mathbf{L} = \begin{pmatrix} \cos^2\Phi & \sin^2\Phi & -\frac{1}{2}\sin 2\Phi & 0 \\ \sin^2\Phi & \cos^2\Phi & \frac{1}{2}\sin 2\Phi & 0 \\ \sin 2\Phi & -\sin 2\Phi & \cos 2\Phi & 0 \\ 0 & 0 & 0 & 1 \end{pmatrix} \tag{2.3.18}$$

and leads to the relation displayed in Appendix C.2 for the **P**–matrix, which eventually (see Appendix D and Fig. 2.3) leads to

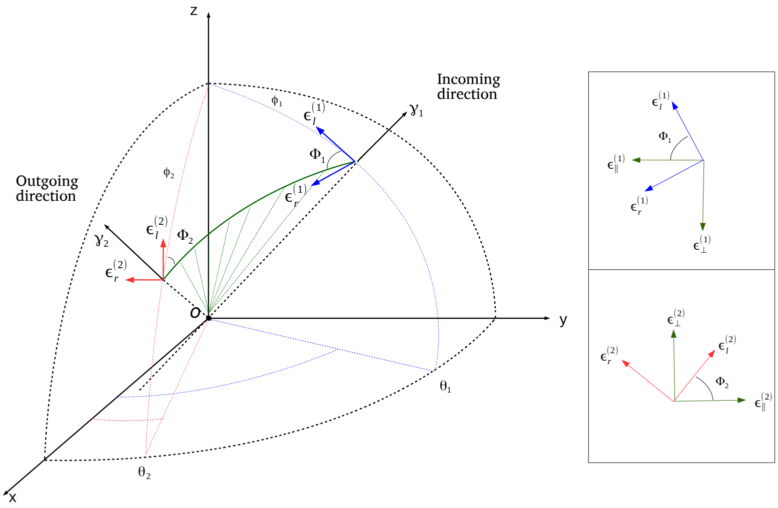

(a) (b)

Figure 2.3: In panel (a), we show the scattering plane in an absolute referential frame. The latter is defined by the scattering of an incoming photon off a particle located in O (see green vectors). One can associate a polarisation state for each incoming and outgoing particle, i.e. $(\epsilon_l^{(1)}, \epsilon_r^{(1)})$ and $(\epsilon_l^{(2)}, \epsilon_r^{(2)})$, noting that ϵ_l must be parallel (and ϵ_r perpendicular) to the plane formed by the z–axis and the corresponding photon direction. In this figure, $\Phi_{1,2}$ are the angles between the $\epsilon_l^{(1,2)}$ vector and the scattering plane respectively. In panel (b) we define, using the green colour, the parallel and perpendicular directions to the scattering plane as $\epsilon_{||,\perp}^{(1,2)}$. We show the two rotations that are needed to obtain the **P**–matrix, namely $\mathbf{L}(-\Phi_1)$ to rotate the $\epsilon_{l,r}^{(1)}$ to the $\epsilon_{||,\perp}^{(1)}$ basis and $\mathbf{L}(\pi - \Phi_2)$ to rotate the $\epsilon_{||,\perp}^{(2)}$ to $\epsilon_{l,r}^{(2)}$.

$$\mathbf{P}_{\text{Chandrasekhar}} = \begin{bmatrix} \mathbf{P_{11}} & \mu_2^2\, s_{12}^2 & \mathbf{P_{13}} & 0 \\ \mu_1^2\, s_{12}^2 & c_{12} & (\mu_1\, c_{12}\; s_{12}) & 0 \\ \mathbf{P_{31}} & -2(\mu_2\, c_{12}\, s_{12}) & \mathbf{P_{33}} & 0 \\ 0 & 0 & 0 & \mathbf{P_{44}} \end{bmatrix} \tag{2.3.19}$$

with

$$\begin{aligned} \mathbf{P_{11}} &= \left(\mu_1\, \mu_2\, c_{12} + \sqrt{1-\mu_1^2}\; \sqrt{1-\mu_2^2}\,\right)^2, \\ \mathbf{P_{13}} &= \tfrac{1}{2}\, \mu_2^2\, \mu_1\; \sin 2(\theta_2-\theta_1) + \mu_2 \sqrt{1-\mu_1^2}\; \sqrt{1-\mu_2^2}\, s_{12}, \\ \mathbf{P_{31}} &= -\tfrac{1}{2}\, \mu_2\, \mu_1^2\; \sin 2(\theta_2-\theta_1) - \mu_2 \sqrt{1-\mu_1^2}\; \sqrt{1-\mu_2^2}\, s_{12}, \\ \mathbf{P_{33}} &= \sqrt{1-\mu_1^2}\; \sqrt{1-\mu_2^2}\; c_{12} + \mu_1\, \mu_2\; \cos 2(\theta_2-\theta_1), \\ \mathbf{P_{44}} &= \sqrt{1-\mu_1^2}\; \sqrt{1-\mu_2^2}\; c_{12} + \mu_1\, \mu_2\,, \end{aligned} \tag{2.3.20}$$

and $s_{12} = \sin(\theta_2 - \theta_1)$, $c_{12} = \cos(\theta_2 - \theta_1)$, $\mu_{1,2} = \cos\phi_{1,2}$.

We note that it is actually possible to get both **R** and **P**–matrices without using geometrical arguments. Instead, one can use the definitions of the electric field in Eq. (2.3.1) and Stokes parameters in Eq. (2.3.8). This is demonstrated in Appendix C.1 where we substituted the polarisation vectors by their rest frame kinematics. This is important as this means that one should be able to use the definitions of the square matrix amplitude for Thomson interactions, which is given in terms of the polarisation vectors, and replace them by their kinematics to obtain the **P**–matrix. Indeed the square matrix amplitude for Thomson interactions reads as

$$|\mathcal{M}|^2 \;\propto\; \sum_{\lambda=r,l} \sum_{\beta=r,l} |\epsilon_\lambda^{(1)} \cdot \epsilon_\beta^{(2)}|^2 \tag{2.3.21}$$

where $\epsilon_{l,r}^{(1)}$ and $\epsilon_{l,r}^{(2)}$ are the polarisation vectors associated with the l, r directions in the scattering plane.

Since this amplitude essentially conveys the information about the intensity of the signal, one can write it as the following matrix:

$$\begin{bmatrix} I_l \\ I_r \end{bmatrix}^{(2)} = \begin{bmatrix} |\epsilon_l^{(1)} \cdot \epsilon_l^{(2)}|^2 & |\epsilon_l^{(1)} \cdot \epsilon_r^{(2)}|^2 \\ |\epsilon_r^{(1)} \cdot \epsilon_l^{(2)}|^2 & |\epsilon_r^{(1)} \cdot \epsilon_r^{(2)}|^2 \end{bmatrix} \begin{bmatrix} I_l \\ I_r \end{bmatrix}^{(1)} . \tag{2.3.22}$$

which after substitution (assuming electrons at rest) reads as

$$\begin{bmatrix} I_l \\ I_r \end{bmatrix}^{(2)} = \begin{bmatrix} \cos\theta^2 & 0 \\ 0 & 1 \end{bmatrix} \begin{bmatrix} I_l \\ I_r \end{bmatrix}^{(1)} . \tag{2.3.23}$$

Summing over all the elements to get the total intensity I, we obtain

$$|\mathcal{M}|^2 \quad \propto \quad 1 + \cos^2\theta \, , \tag{2.3.24}$$

which is indeed the square matrix element for the Thomson (i.e. low energy) interactions. The same exercise in 3D leads to the elements of the **P**–matrix as given by Chandrasekhar in [81] and eventually gives the following square matrix element

$$\begin{aligned} |\mathcal{M}|^2{}_{\text{Thomson}} \quad \equiv \quad & \frac{3}{4} \, \Big[1 + \mu_1^2 \, \mu_2^2 + (1 - \mu_1^2)(1 - \mu_2^2) \; c_{12} \\ & + 2\mu_1 \, \mu_2 \sqrt{(1 - \mu_1^2)} \sqrt{(1 - \mu_2^2)} \; c_{12} \Big] . \end{aligned} \tag{2.3.25}$$

which again leads to the well-known expression of the Thomson cross section in the electron rest frame, namely

$$|\mathcal{M}|^2{}_{\text{Thomson,rest}} \quad \equiv \quad 1 + \cos^2\phi_2 \, . \tag{2.3.26}$$

where ϕ_2 is the angle between the outgoing photon direction and the initial electron. There is therefore a strong connection between the **P**–matrix that Chandrasekhar obtained and the square matrix amplitude that one can derive using QFT.

It is possible to define the equivalent of the **R**–matrix and **P**–matrix in terms of the (I, Q, U, V) Stokes parameters. To avoid a possible confusion, we will denote by $\mathbf{R}'$ and $\mathbf{P}'$ the equivalent **R** and **P**–matrices obtained using the (I, Q, U, V) Stokes parameters. In other words,

$$\begin{bmatrix} I \\ Q \\ U \\ V \end{bmatrix}^{(2)} = \mathbf{R}' \;\; (\text{or} \;\; \mathbf{P}') \begin{bmatrix} I \\ Q \\ U \\ V \end{bmatrix}^{(1)} . \tag{2.3.27}$$

Using the definitions of the Stokes parameters in the ± basis, see Eq. (2.3.9), we obtain

$$\mathbf{R}' = \begin{pmatrix} 3+\cos 2\theta & -2\sin^2\theta & 0 & 0 \\ -2\sin^2\theta & 3+\cos 2\theta & 0 & 0 \\ 0 & 0 & 4\cos\theta & 0 \\ 0 & 0 & 0 & 4\cos\theta \end{pmatrix} \tag{2.3.28}$$

and

$$\mathbf{P}' = \begin{pmatrix} \mathbf{P'_{11}} & \mathbf{P'_{12}} & \mathbf{P'_{13}} & 0 \\ \mathbf{P'_{21}} & \mathbf{P'_{22}} & \mathbf{P'_{23}} & 0 \\ \mathbf{P'_{31}} & \mathbf{P'_{32}} & \mathbf{P'_{33}} & 0 \\ 0 & 0 & 0 & \mathbf{P'_{44}} \end{pmatrix} \tag{2.3.29}$$

with

$$\begin{aligned}
\mathbf{P'_{11}} &= \left(\mu_1^2\mu_2^2+1\right) c_{12}^2 + 2\sqrt{1-\mu_1^2}\sqrt{1-\mu_2^2}\;\mu_1\mu_2 c_{12} + (1-\mu_1^2)(1-\mu_2^2) + s_{12}^2\left(\mu_1^2+\mu_2^2\right) , \\
\mathbf{P'_{12}} &= \left(\mu_1^2\mu_2^2-1\right) c_{12} + 2\sqrt{1-\mu_1^2}\sqrt{1-\mu_2^2}\;\mu_1\mu_2 c_{12} + (1-\mu_1^2)(1-\mu_2^2) + s_{12}^2(\mu_1^2-\mu_2^2) , \\
\mathbf{P'_{13}} &= \; -2\,s_{12}\left(\sqrt{1-\mu_1^2}\sqrt{1-\mu_2^2}\;\mu_2 + c_{12}\mu_1\left(\mu_2^2-1\right)\right) , \\
\mathbf{P'_{21}} &= \left(\mu_1^2\mu_2^2-1\right) c_{12} + 2\sqrt{1-\mu_1^2}\sqrt{1-\mu_2^2}\;\mu_1\mu_2 c_{12} + (1-\mu_1^2)(1-\mu_2^2) + s_{12}^2\left(\mu_2^2-\mu_1^2\right) , \\
\mathbf{P'_{22}} &= \left(\mu_1^2\mu_2^2+1\right) c_{12} + 2\sqrt{1-\mu_1^2}\sqrt{1-\mu_2^2}\;\mu_1\mu_2 c_{12} + (1-\mu_1^2)(1-\mu_2^2) - s_{12}^2\left(\mu_1^2+\mu_2^2\right) , \\
\mathbf{P'_{23}} &= 2\,s_{12}(\sqrt{1-\mu_1^2}\sqrt{1-\mu_2^2}\;\mu_1 + c_{12}\mu_2\left(\mu_1^2+1\right)) , \\
\mathbf{P'_{31}} &= -\,2\,s_{12}\left(\sqrt{1-\mu_1^2}\sqrt{1-\mu_2^2}\;\mu_1 + c_{12}\left(\mu_1^2-1\right)\mu_2\right) , \\
\mathbf{P'_{32}} &= -\,2s_{12}\left(\sqrt{1-\mu_1^2}\sqrt{1-\mu_2^2}\;\mu_2 + c_{12}\left(\mu_2^2+1\right)\mu_1\right) ,
\end{aligned}$$

$$\mathbf{P}'_{33} = 2\left(\sqrt{1-\mu_1^2}\sqrt{1-\mu_2^2}\, c_{12} + \mu_1\mu_2 \cos 2(\theta_2-\theta_1)\right) ,$$
$$\mathbf{P}'_{44} = 2\left(c_{12}\sqrt{1-\mu_1^2}\sqrt{1-\mu_2^2} + \mu_1\mu_2\right) \tag{2.3.30}$$

with $s_{12} = \sin(\theta_2 - \theta_1)$, $c_{12} = \cos(\theta_2 - \theta_1)$, $\mu_1 = \cos\phi_1$ and $\mu_2 = \cos\phi_2$. The transformation from the $\mathbf{R}'$–matrix to the $\mathbf{P}'$–matrix is given in Appendix C.3.

2.3.3 Sources of Electromagnetic Radiation

Describing the propagation of polarised light is crucial to get information from our Universe. Such information could be about some of possible mechanisms that may give rise to a circular polarisation signal ($V \neq 0$). They are listed below.

- *Faraday Conversion*

  Circular polarisation can be generated by Faraday conversion of linear polarisation. This mechanism takes place when linearly polarised photons pass through a strong magnetic field. A phase shift is generated in the photon linear polarisation components, and eventually leads to a circular polarisation signal.

- *Bi-refringence*

  Another way to produce circular polarisation signals is through birefringence, see [85] for details. Birefringence occurs when a linear polarisation signal passes through a medium of aligned grains whose alignment twists along the line of sight. When the amount of linear polarisation is high (as this could occur for example in reflection nebulae), a high degree of circular polarisation could be produced [86].

- *Synchrotron emission*

  Synchrotron emission can emit polarised light [87, 88, 89, 90, 91, 92, 93, 94, 95, 96] and was proposed as a source of circular polarisation in e.g. Ref [97] and then developed by Legg [98]. This mechanism continues to be studied, in particular in light of the recent progress regarding strong magnetic fields as well as homogeneous and inhomogeneous magnetic fields see Ref. [99, 100, 101]. We note in addition that a circular polarisation signal may be of intrinsic origin [102, 103] (i.e. it could be generated in absence of Faraday conversion of linear polarisation in sites where there exists a large-scale magnetic field).

- *Parity-violating interactions and charge asymmetry*

  Circular polarisation could be produced in cosmic accelerators when Standard Model particles of the same charge (for example proton-proton) collide with each other and produce an excess of positive (negative) mesons and muons with respect to their negative (positive) counterparts [104], which eventually decay radiatively through parity-violating interactions. Electroweak (loop-induced) interactions of photons with the cosmological neutrino background could also create a circular polarisation signal [105], although the signal is expected to be very small. A circular polarisation signal could also be generated by beyond the Standard Model interactions, see for example [44, 85, 106, 107, 108, 109, 110, 111, 112, 113].

- *21 cm*

  Finally a circular polarisation signal is expected in conjunction with the 21 cm line [114]. The Hydrogen excitation that generates the circular polarisation signal is produced due to the interaction of the Hydrogen with the CMB quadrupole moment and could be measured in the future with an array of dipole antennas. Such a signal would indicate the existence of primordial gravitational waves [115].

Chapter 3

Neutrino Radiative Decay and Circular Polarisation

The electromagnetic dipole moments of neutrinos can be generated at various loop levels and radiative decays $\nu_{\mathbf{i}} \to \nu_{\mathbf{f}} + \gamma$ are induced by off-diagonal parts of the dipole moments [69, 116, 117, 118, 119, 120]. Charged current interaction contributions in the SM have previously been calculated at one-loop level in [69, 116, 117, 118, 119] and later studied in detail in [121, 122]. However, these contributions are tiny due to the large mass hierarchy between the active neutrinos and the W boson so there is currently no positive experimental indication in favour of their existence. Whilst neutrino radiative decays have been extensively studied for some mass regions of neutrinos, CP violation in these processes has not been studied for a more general spectrum of mass scales with very few exceptions e.g. [123]. Based on Ref. [1], we will study CP violation in radiative decays of both Dirac and Majorana neutrinos.

In Sec. 3.2, we outline the most general formalism of CP violation and circular polarisation in terms of form factors where the result is independent of the neutrino model or mass scale. In Sec. 3.3, we discuss CP violation based on a simplified neutrino model. We begin this section with a discussion about the size of CP asymmetry for the SM contribution and then consider how CP violation can be enhanced via new interactions. A comprehensive analytical calculation of CP asymmetry based on

Yukawa type BSM interactions is then performed. Finally, we summarise in Sec. 3.4

3.1 Introduction

Neutrino electromagnetic interactions provide a tantalising probe for physics beyond SM (BSM) (for a comprehensive review, see [124]). If more massive neutrinos exist, they may decay to lighter active neutrinos radiatively. These heavier neutrinos will consequently have a larger decay width due to the existence of such decay channels. Various hypothetical heavier neutrinos have been historically introduced, motivated by a combination of theoretical and phenomenological reasons. Some of the most famous ones are those introduced in the type-I seesaw mechanism [53, 125, 126, 127, 128, 129] proposed in order to address the origin of sub-eV left-handed neutrino masses. Additionally, phenomenological motivations have suggested keV sterile neutrinos as dark matter (DM) candidates to explain the detection of a 3.5 keV X-ray line in [130, 131] (for some representative reviews, see [132, 133, 134]). Very heavy DM was also proposed in order to explain the IceCube data [135, 136, 137, 138]. Radiative decays of such heavy particles may be more significant than those of active neutrinos due to their very large relative mass. Hence, radiative decay is typically a major channel of importance in detecting possible keV sterile neutrino DM.

A process involving neutrinos CP violation may exist. At low energy, neutrino oscillations provide the best way to clarify its existence in the neutrino sector. Combined analysis of current accelerator neutrino oscillation data [139] supports large CP violation in the appearance channel of neutrino oscillations [140, 141]. The next-generation neutrino oscillation experiments DUNE and T2HK are projected to observe CP violation in the near future [142, 143, 144]. At high energy, the most well-studied process involving CP violation is the very heavy right-handed neutrino decaying into SM leptons and the Higgs boson. This effect is the source of the so-called thermal leptogenesis phenomenon, which can explain the observed matter-antimatter asymmetry in our Universe [145]. On the other hand, if these heavy neutrinos have lighter masses, specifically around the GeV scale, CP violation may appear in right-handed neutrino oscillations, which provides an alternative mechanism for leptogenesis [146] (See [147, 148] for some reviews).

Recently, it was suggested in [44] that a net circular polarisation, specifically an asymmetry between two circularly polarised photons γ_+ and γ_-, can be generated if CP is violated in neutrino radiative decays. Therefore, the circular polarisation of photons provides a potentially crucial probe to prove the existence of CP violation in the neutrino and DM sectors. In this chapter we discuss a formulation introduced in [1] to describe both CP violation in neutrino radiative decays and also the resulting asymmetry between the produced photons γ_+ and γ_-.

3.2 Polarised Matrix Element

Assuming fermions are Dirac particles, the amplitude for the process $\nu_{\mathbf{i}} \to \nu_{\mathbf{f}} + \gamma_\pm$ is given by

$$i\mathcal{M}(\nu_{\mathbf{i}} \to \nu_{\mathbf{f}} + \gamma_\pm) = i\bar{u}(p_{\mathbf{f}})\Gamma^\mu_{\mathbf{fi}}(q^2)u(p_{\mathbf{i}})\varepsilon^*_{\pm,\mu}(q)\,. \tag{3.2.1}$$

Here, $u(p_{\mathbf{i}})$ and $u(p_{\mathbf{f}})$ are spinors for the initial $\nu_{\mathbf{i}}$ and final $\nu_{\mathbf{f}}$ state neutrinos respectively. By momentum conservation, the photon momentum is $q = p_{\mathbf{i}} - p_{\mathbf{f}}$. The spinors include the spin polarisation of the fermions, this will be discussed in more detail in the next subsection in a specified inertial reference frame. The transition form factor is then parametrised as per [118, 119, 120, 149]

$$\Gamma^\mu_{\mathbf{fi}}(q^2) = f^{\mathrm{Q}}_{\mathbf{fi}}(q^2)\gamma^\mu - f^{\mathrm{M}}_{\mathbf{fi}}(q^2)i\sigma^{\mu\nu}q_\nu + f^{\mathrm{E}}_{\mathbf{fi}}(q^2)\sigma^{\mu\nu}q_\nu\gamma_5 + f^{\mathrm{A}}_{\mathbf{fi}}(q^2)(q^2\gamma^\mu - q^\mu \not{q})\gamma_5\,. \tag{3.2.2}$$

We will not consider electrically charged neutrinos, namely we require that $f^Q = 0$. The modification to the result in the case of non-zero f^Q will be mentioned at the end of this section. By requiring the photon to be on-shell $q^2 = 0$ and choosing the Lorenz gauge $q \cdot \varepsilon_p = 0$, the anapole does not contribute. In this case, only the electromagnetic dipole moment contributes to the neutrino radiative decay. We then rewrite the form factor as

$$\Gamma^{\mu}_{\mathbf{fi}}(q^2) \;=\; i\sigma^{\mu\nu}q_{\nu}[f^{\mathrm{L}}_{\mathbf{fi}}(q^2)P_{\mathrm{L}} + f^{\mathrm{R}}_{\mathbf{fi}}(q^2)P_{\mathrm{R}}]\,, \tag{3.2.3}$$

where $f^{\mathrm{L,R}}_{\mathbf{fi}} = -f^{\mathrm{M}}_{\mathbf{fi}} \pm i f^{\mathrm{E}}_{\mathbf{fi}}$ and the chiral projection operators are defined as $P_{\mathrm{L,R}} = \frac{1}{2}(1 \mp \gamma_5)$. The decay widths for $\nu_{\mathbf{i}} \to \nu_{\mathbf{f}} + \gamma_{\pm}$ are then given by

$$\Gamma(\nu_{\mathbf{i}} \to \nu_{\mathbf{f}} + \gamma_{\pm}) \;=\; \frac{m_{\mathbf{i}}^2 - m_{\mathbf{f}}^2}{16\pi m_{\mathbf{i}}^3}|\mathcal{M}(\nu_{\mathbf{i}} \to \nu_{\mathbf{f}} + \gamma_{\pm})|^2\,. \tag{3.2.4}$$

The amplitudes $\mathcal{M}(\nu_{\mathbf{i}} \to \nu_{\mathbf{f}} + \gamma_{\pm})$ are directly correlated with the coefficients

$$\begin{aligned}
\mathcal{M}(\nu_{\mathbf{i}} \to \nu_{\mathbf{f}} + \gamma_{+}) &= +\sqrt{2} f^{\mathrm{L}}_{\mathbf{fi}}(m_{\mathbf{i}}^2 - m_{\mathbf{f}}^2)\,,\\
\mathcal{M}(\nu_{\mathbf{i}} \to \nu_{\mathbf{f}} + \gamma_{-}) &= -\sqrt{2} f^{\mathrm{R}}_{\mathbf{fi}}(m_{\mathbf{i}}^2 - m_{\mathbf{f}}^2)\,.
\end{aligned} \tag{3.2.5}$$

which are derived in detail in Appendix A. The sum of the decay widths for $\nu_{\mathbf{i}} \to \nu_{\mathbf{f}} + \gamma_{+}$ and $\nu_{\mathbf{i}} \to \nu_{\mathbf{f}} + \gamma_{-}$ yields the total radiative decay width $\Gamma(\nu_{\mathbf{i}} \to \nu_{\mathbf{f}} + \gamma)$.

Again, if we only consider radiative decay for an electrically neutral antineutrino, the amplitudes of radiative decay $\bar{\nu}_{\mathbf{i}} \to \bar{\nu}_{\mathbf{f}} + \gamma_{\pm}$ are then given by

$$i\mathcal{M}(\bar{\nu}_{\mathbf{i}} \to \bar{\nu}_{\mathbf{f}} + \gamma_{\pm}) = i\bar{v}(p_{\mathbf{i}})\bar{\Gamma}^{\mu}_{\mathbf{if}}(q^2)v(p_{\mathbf{f}})\varepsilon^{*}_{\pm,\mu}(q)\,, \tag{3.2.6}$$

where $v(p_{\mathbf{i}})$ and $v(p_{\mathbf{f}})$ are antineutrino spinors. The decay width for $\bar{\nu}_{\mathbf{i}} \to \bar{\nu}_{\mathbf{f},s'} + \gamma_{l}$ is

$$\Gamma(\bar{\nu}_{\mathbf{i}} \to \bar{\nu}_{\mathbf{f}} + \gamma_{\pm}) \;=\; \frac{m_{\mathbf{i}}^2 - m_{\mathbf{f}}^2}{16\pi m_{\mathbf{i}}^3}|\mathcal{M}(\bar{\nu}_{\mathbf{i}} \to \bar{\nu}_{\mathbf{f}} + \gamma_{\pm})|^2\,. \tag{3.2.7}$$

By parametrising the form factor in a similar form to before, we have

$$\bar{\Gamma}^{\mu}_{\mathbf{if}}(q^2) \;=\; i\sigma^{\mu\nu}q_{\nu}[\bar{f}^{\mathrm{L}}_{\mathbf{if}}(q^2)P_{\mathrm{L}} + \bar{f}^{\mathrm{R}}_{\mathbf{if}}(q^2)P_{\mathrm{R}}]\,, \tag{3.2.8}$$

with $\bar{f}^{\mathrm{L,R}}_{\mathbf{if}} = -\bar{f}^{\mathrm{M}}_{\mathbf{if}} \pm i\bar{f}^{\mathrm{E}}_{\mathbf{if}}$. Therefore, the amplitudes can be written in a similar fashion following Eq. (3.2.5), i.e. by replacing $f^{\mathrm{L}}_{\mathbf{fi}}$ and $f^{\mathrm{R}}_{\mathbf{fi}}$ by $\bar{f}^{\mathrm{L}}_{\mathbf{if}}$ and $\bar{f}^{\mathrm{R}}_{\mathbf{if}}$ respectively (see the proof in Appendix (A)). These formulae can be further simplified with the help of the *CPT* theorem, which is satisfied in all Lorentz invariant local quantum field theories with a Hermitian Hamiltonian. Due to *CPT* invariance, $\bar{\nu}_{\mathbf{i}} \to \bar{\nu}_{\mathbf{f}} + \gamma_{\mp}$ and $\nu_{\mathbf{f}} + \gamma_{\pm} \to \nu_{\mathbf{i}}$ have the same amplitude, and thus $\bar{f}^{\mathrm{M,E}}_{\mathbf{if}}(q^2) = -f^{\mathrm{M,E}}_{\mathbf{if}}(q^2)$ is satisfied

[124], leading to

$$\bar{f}^{\mathrm{L}}_{\mathbf{if}}(q^2) = -f^{\mathrm{L}}_{\mathbf{if}}(q^2)\,, \quad \bar{f}^{\mathrm{R}}_{\mathbf{if}}(q^2) = -f^{\mathrm{R}}_{\mathbf{if}}(q^2)\,. \tag{3.2.9}$$

Hence, amplitudes $\mathcal{M}(\bar{\nu}_{\mathbf{i}} \to \bar{\nu}_{\mathbf{f}} + \gamma_+)$ can be simplified to

$$\begin{aligned} \mathcal{M}(\bar{\nu}_{\mathbf{i}} \to \bar{\nu}_{\mathbf{f}} + \gamma_+) &= +\sqrt{2} f^{\mathrm{L}}_{\mathbf{if}}(m_{\mathbf{i}}^2 - m_{\mathbf{f}}^2)\,, \\ \mathcal{M}(\bar{\nu}_{\mathbf{i}} \to \bar{\nu}_{\mathbf{f}} + \gamma_-) &= -\sqrt{2} f^{\mathrm{R}}_{\mathbf{if}}(m_{\mathbf{i}}^2 - m_{\mathbf{f}}^2)\,. \end{aligned} \tag{3.2.10}$$

Physical neutrinos and antineutrinos are related by a CP transformation which interchanges particles with antiparticles and replaces momentum by its parity conjugate $\tilde{p} = (p_0, -\vec{p})$. The CP transformation reverses the momentum but preserves angular momentum. As a consequence, the polarisation is reversed. Performing a CP transformation for $\nu_{\mathbf{i}}(p_{\mathbf{i}}) \to \nu_{\mathbf{f}}(p_{\mathbf{f}}) + \gamma_{\pm}(q)$ gives rise to antineutrino channels with reversed 3D momentum and reversed photon polarisations in the final states $\bar{\nu}_{\mathbf{i}}(\tilde{p}_{\mathbf{i}}) \to \bar{\nu}_{\mathbf{f}}(\tilde{p}_{\mathbf{f}}) + \gamma_{\mp}(\tilde{q})$. Since the amplitude is parity-invariant, the amplitude of the process is equivalent to $\bar{\nu}_{\mathbf{i}}(p_{\mathbf{i}}) \to \bar{\nu}_{\mathbf{f}}(p_{\mathbf{f}}) + \gamma_{\mp}(q)$. Therefore, the radiative decay of antineutrinos can be represented as a CP conjugate of the decay of neutrinos

$$i\mathcal{M}(\bar{\nu}_{\mathbf{i}} \to \bar{\nu}_{\mathbf{f}} + \gamma_{\pm}) = i\mathcal{M}^{CP}(\nu_{\mathbf{i}} \to \nu_{\mathbf{f}} + \gamma_{\mp})\,. \tag{3.2.11}$$

In the case of CP conservation, both $f^{\mathrm{E}}_{\mathbf{if}}(q^2)$ and $f^{\mathrm{M}}_{\mathbf{if}}(q^2)$ are Hermitian i.e. $f^{\mathrm{M,E}}_{\mathbf{if}}(q^2) = [f^{\mathrm{M,E}}_{\mathbf{fi}}(q^2)]^*$. This leads to $f^{\mathrm{L,R}}_{\mathbf{if}}(q^2) = [f^{\mathrm{R,L}}_{\mathbf{fi}}(q^2)]^*$, namely, $\bar{f}^{\mathrm{L,R}}_{\mathbf{if}}(q^2) = -[f^{\mathrm{R,L}}_{\mathbf{fi}}(q^2)]^*$ [124, 150]. And eventually, we arrive at the identity

$$\Gamma(\nu_{\mathbf{i}} \to \nu_{\mathbf{f}} + \gamma_{\pm}) - \Gamma(\bar{\nu}_{\mathbf{i}} \to \bar{\nu}_{\mathbf{f}} + \gamma_{\mp}) \propto |\mathcal{M}(\nu_{\mathbf{i}} \to \nu_{\mathbf{f}} + \gamma_{\pm})|^2 - |\mathcal{M}^{CP}(\nu_{\mathbf{i}} \to \nu_{\mathbf{f}} + \gamma_{\pm})|^2 = 0\,. \tag{3.2.12}$$

However, a CP violating source in the interaction may contribute at loop level and break this equality.

3.2.1 Correlation Between CP Asymmetry and Circular Polarisation

We define the CP asymmetry between the radiative decay $\nu_{\mathbf{i}} \to \nu_{\mathbf{f}} + \gamma_+$ and its CP conjugate process $\bar{\nu}_{\mathbf{i}} \to \bar{\nu}_{\mathbf{f}} + \gamma_-$ as

$$\Delta_{CP,+} \;=\; \frac{\Gamma(\nu_{\mathbf{i}} \to \nu_{\mathbf{f}} + \gamma_+) - \Gamma(\bar{\nu}_{\mathbf{i}} \to \bar{\nu}_{\mathbf{f}} + \gamma_-)}{\Gamma(\nu_{\mathbf{i}} \to \nu_{\mathbf{f}} + \gamma) + \Gamma(\bar{\nu}_{\mathbf{i}} \to \bar{\nu}_{\mathbf{f}} + \gamma)}\,. \tag{3.2.13}$$

The CP asymmetry between $\nu_{\mathbf{i}} \to \nu_{\mathbf{f}} + \gamma_-$ and its CP conjugate process $\bar{\nu}_{\mathbf{i}} \to \bar{\nu}_{\mathbf{f}} + \gamma_+$, $\Delta_{CP,-}$, is defined by exchanging $+$ and $-$ signs. The photon polarisation independent CP asymmetry is obtained by summing $\Delta_{CP,+}$ and $\Delta_{CP,-}$ together which yields

$$\Delta_{CP} = \frac{\Gamma(\nu_{\mathbf{i}} \to \nu_{\mathbf{f}} + \gamma_+) - \Gamma(\bar{\nu}_{\mathbf{i}} \to \bar{\nu}_{\mathbf{f}} + \gamma_-) + \Gamma(\nu_{\mathbf{i}} \to \nu_{\mathbf{f}} + \gamma_-) - \Gamma(\bar{\nu}_{\mathbf{i}} \to \bar{\nu}_{\mathbf{f}} + \gamma_+)}{\Gamma(\nu_{\mathbf{i}} \to \nu_{\mathbf{f}} + \gamma) + \Gamma(\bar{\nu}_{\mathbf{i}} \to \bar{\nu}_{\mathbf{f}} + \gamma)}\,. \tag{3.2.14}$$

It is also convenient to define the asymmetry between the radiated photons γ_+ and γ_- as

$$\Delta_{+-} = \frac{\Gamma(\nu_{\mathbf{i}} \to \nu_{\mathbf{f}} + \gamma_+) + \Gamma(\bar{\nu}_{\mathbf{i}} \to \bar{\nu}_{\mathbf{f}} + \gamma_+) - \Gamma(\nu_{\mathbf{i}} \to \nu_{\mathbf{f}} + \gamma_-) - \Gamma(\bar{\nu}_{\mathbf{i}} \to \bar{\nu}_{\mathbf{f}} + \gamma_-)}{\Gamma(\nu_{\mathbf{i}} \to \nu_{\mathbf{f}} + \gamma) + \Gamma(\bar{\nu}_{\mathbf{i}} \to \bar{\nu}_{\mathbf{f}} + \gamma)}\,. \tag{3.2.15}$$

Given equal numbers for initial neutrinos and antineutrinos, Δ_{+-} represents the fraction $(\mathrm{N}_{\gamma_+} - \mathrm{N}_{\gamma_-})/(\mathrm{N}_{\gamma_+} + \mathrm{N}_{\gamma_-})$, where N_{γ_+} and N_{γ_-} are the number of polarised photons γ_+ and γ_- produced by the radiative decays respectively. It is this source that generates circular polarisation for the radiated photons giving rise to a non-zero Stokes parameter V.

Therefore, a non-zero Δ_{+-} is a source of circular polarisation for the photon produced by the radiative decay. Since the phase spaces are the same for neutrino and antineutrino channels, these formulae can be simplified to

$$\begin{aligned}
\Delta_{CP,+} &= \frac{|f^{\mathrm{L}}_{\mathbf{fi}}|^2 - |f^{\mathrm{R}}_{\mathbf{if}}|^2}{|f^{\mathrm{L}}_{\mathbf{fi}}|^2 + |f^{\mathrm{R}}_{\mathbf{fi}}|^2 + |f^{\mathrm{R}}_{\mathbf{if}}|^2 + |f^{\mathrm{L}}_{\mathbf{if}}|^2}\,,\\
\Delta_{CP,-} &= \frac{|f^{\mathrm{R}}_{\mathbf{fi}}|^2 - |f^{\mathrm{L}}_{\mathbf{if}}|^2}{|f^{\mathrm{L}}_{\mathbf{fi}}|^2 + |f^{\mathrm{R}}_{\mathbf{fi}}|^2 + |f^{\mathrm{R}}_{\mathbf{if}}|^2 + |f^{\mathrm{L}}_{\mathbf{if}}|^2}\,,
\end{aligned} \tag{3.2.16}$$

as well as

$$\begin{aligned}\Delta_{CP} &= \frac{|f^{\rm L}_{\bf fi}|^2+|f^{\rm R}_{\bf fi}|^2-|f^{\rm R}_{\bf if}|^2-|f^{\rm L}_{\bf if}|^2}{|f^{\rm L}_{\bf fi}|^2+|f^{\rm R}_{\bf fi}|^2+|f^{\rm R}_{\bf if}|^2+|f^{\rm L}_{\bf if}|^2}\,,\\ \Delta_{+-} &= \frac{|f^{\rm L}_{\bf fi}|^2-|f^{\rm R}_{\bf fi}|^2-|f^{\rm R}_{\bf if}|^2+|f^{\rm L}_{\bf if}|^2}{|f^{\rm L}_{\bf fi}|^2+|f^{\rm R}_{\bf fi}|^2+|f^{\rm R}_{\bf if}|^2+|f^{\rm L}_{\bf if}|^2}\,.\end{aligned} \tag{3.2.17}$$

The total CP asymmetry and the asymmetry between γ_+ and γ_- follows simple relations with $\Delta_{CP,+}$ and $\Delta_{CP,-}$ as

$$\begin{aligned}\Delta_{CP} &= \Delta_{CP,+}+\Delta_{CP,-}\,,\\ \Delta_{+-} &= \Delta_{CP,+}-\Delta_{CP,-}\,.\end{aligned} \tag{3.2.18}$$

Therefore, we arrive at an important result that the generation of circular polarisation is essentially dependent upon CP asymmetry between neutrino radiative decay and its CP conjugate process. Note that we have not included any details related to the Lagrangian or interactions yet. Given any neutral fermion, its radiative decay can always be parametrised by the electromagnetic dipole moments with coefficients $f^{\rm L}_{\bf fi}$ and $f^{\rm R}_{\bf fi}$ (as well as $\bar{f}^{\rm L}_{\bf if}$ and $\bar{f}^{\rm R}_{\bf if}$ for its antiparticle), we then arrive at the correlations between CP violation and circular polarisation in Eq. (3.2.18) with their definitions in Eqs. (3.2.16) and (3.2.17).

Another source of asymmetry between polarised photons is the existence of an initial number asymmetry between neutrinos and antineutrinos [44]. There may be some other CP violating sources in particle physics which can induce this condition [110]. On the other hand, this kind of asymmetry is more likely to be generated in extreme astrophysical environments. For example, in supernovae explosions, the asymmetry between sterile neutrinos and antineutrinos may be generated because of the different matter effects during neutrino and antineutrino propagation [151, 152]. In the rest of this paper, we will only consider circular polarisation directly produced by the CP violating decays between neutrinos and antineutrinos.

Now we may turn our attention to obtaining non-zero CP violation for the radiative decay. For $\nu_{\bf i} \to \nu_{\bf f} + \gamma_+$ and $\nu_{\bf i} \to \nu_{\bf f} + \gamma_-$, we parametrise the effective coefficients

$f_{\mathbf{fi}}^{\rm L}$ and $f_{\mathbf{fi}}^{\rm R}$, these should be obtained from the relevant loop calculations in the form

$$f_{\mathbf{fi}}^{\rm L} = \sum_l C_l K_l^{\rm L}\,, \quad f_{\mathbf{fi}}^{\rm R} = \sum_l C_l K_l^{\rm R}, \tag{3.2.19}$$

without loss of generality. Here, we have used l to classify the different categories of loop contributions. For each loop category l, C_l factorises out all coefficients of operators contributing to the diagram. $K_l^{\rm L}$ and $K_l^{\rm R}$ represents the pure loop kinematics after coefficients are extracted out. As a consequence, $\bar{f}_{\mathbf{if}}^{\rm L}$ and $\bar{f}_{\mathbf{if}}^{\rm R}$ (namely $-f_{\mathbf{if}}^{\rm L}$ and $-f_{\mathbf{if}}^{\rm R}$) corresponding to the effective parameters for $\bar{\nu}_{\mathbf{i}} \to \bar{\nu}_{\mathbf{f}} + \gamma_\pm$, can always be represented in the form [1]

$$f_{\mathbf{if}}^{\rm L} = \sum_l C_l^* K_l^{\rm R}\,, \quad f_{\mathbf{if}}^{\rm R} = \sum_l C_l^* K_l^{\rm L}\,. \tag{3.2.20}$$

The CP asymmetries with respect to the photon polarisations can then be simplified to

$$\begin{aligned}
\Delta_{CP,+} \propto |f_{\mathbf{fi}}^{\rm L}| - |f_{\mathbf{if}}^{\rm R}| &= -4 \sum_{l \neq l'} {\rm Im}(C_l C_{l'}^*) {\rm Im}(K_l^{\rm L} K_{l'}^{\rm L\,*})\,, \\
\Delta_{CP,-} \propto |f_{\mathbf{fi}}^{\rm R}| - |\bar{f}_{\mathbf{if}}^{\rm L}| &= -4 \sum_{l \neq l'} {\rm Im}(C_l C_{l'}^*) {\rm Im}(K_l^{\rm R} K_{l'}^{\rm R\,*})\,.
\end{aligned} \tag{3.2.21}$$

Therefore, a non-zero CP asymmetry is determined by non-vanishing ${\rm Im}(C_l C_{l'}^*)$ and non-vanishing ${\rm Im}(K_l^{\rm L} K_{l'}^{\rm L\,*})$ (or ${\rm Im}(K_l^{\rm R} K_{l'}^{\rm R\,*})$) from loops l and l'.

While the imaginary part of ${\rm Im}(C_l C_{l'}^*)$ is straightforwardly obtained from the relevant terms in the Lagrangian, the main task is to compute the imaginary parts of $K_l^{\rm L} K_{l'}^{\rm L\,*}$ and $K_l^{\rm R} K_{l'}^{\rm L\,*}$. In order to achieve non-zero values of these imaginary parts, one may apply the optical theorem which can be expressed as

$$ {\rm Im}\mathcal{M}(a \to b) = \frac{1}{2} \sum_c \int d\Pi_c\, \mathcal{M}^*(b \to c) \mathcal{M}(a \to c)\,, \tag{3.2.22}$$

---

[1] To clarify how this parametrisation is valid, we write out the subscripts explicitly, $f_{\mathbf{fi}}^{\rm L} = \sum_l (C_l)_{\mathbf{fi}} (K_l^{\rm L})_{\mathbf{fi}}$ and $f_{\mathbf{fi}}^{\rm R} = \sum_l (C_l)_{\mathbf{fi}} (K_l^{\rm R})_{\mathbf{fi}}$. Similarly, we can write out $f_{\mathbf{if}}^{\rm L} = \sum_l (C_l)_{\mathbf{if}} (K_l^{\rm L})_{\mathbf{if}}$ and $f_{\mathbf{if}}^{\rm R} = \sum_l (C_l)_{\mathbf{if}} (K_l^{\rm R})_{\mathbf{if}}$. One can simplify $f_{\mathbf{if}}^{\rm L}$ and $f_{\mathbf{if}}^{\rm R}$ in the following steps. 1) The coefficient $(C_l)_{\mathbf{if}}$ must be the complex conjugate of $(C_l)_{\mathbf{fi}}$ since both processes are CP conjugates of one another. 2) $(K_l^{\rm L})_{\mathbf{if}}$ and $(K_l^{\rm R})_{\mathbf{if}}$, as pure kinetic terms, must satisfy T parity, namely they must be invariant under the interchange of the initial and final state neutrinos $\nu_{\mathbf{i}} \leftrightarrow \nu_{\mathbf{f}}$, the chiralities must also be interchanged L ↔ R, namely, $(K_l^{\rm L})_{\mathbf{if}} = (K_l^{\rm R})_{\mathbf{fi}}$ and $(K_l^{\rm R})_{\mathbf{if}} = (K_l^{\rm L})_{\mathbf{fi}}$. Therefore, $f_{\mathbf{if}}^{\rm L}$ and $f_{\mathbf{if}}^{\rm R}$ can be re-written to be $f_{\mathbf{if}}^{\rm L} = \sum_l (C_l)_{\mathbf{fi}}^* (K_l^{\rm R})_{\mathbf{fi}}$ and $f_{\mathbf{if}}^{\rm R} = \sum_l (C_l)_{\mathbf{fi}}^* (K_l^{\rm L})_{\mathbf{fi}}$.

where the sum runs over all possible sets c of final-state particles [153]. Fixing $a = \nu_{\mathbf{i}}$ and $b = \nu_{\mathbf{f}} + \gamma$, c has to include an odd number of fermions plus arbitrary bosons. All particles heavier than $\nu_{\mathbf{i}}$ cannot be included in c since this would violate energy-momentum conservation. In other words, the RHS of Eq. (3.2.22) will be zero, meaning that $|M(a \to b)|^2$ is real. Therefore, if we want to generate an imaginary part in the radiative neutrino decay, this identity must be satisfied. In other words, the mass of the particle in the initial state a must be larger than the sum of the masses in the intermediate stat c.

In the next section, we will explicitly show how to derive a non-zero analytical result for $\mathrm{Im}(K_l^{\mathrm{R}} K_{l'}^{\mathrm{R}\,*})$ based on a simplified BSM model where $\mathrm{Im}(K_l^{\mathrm{L}} K_{l'}^{\mathrm{L}\,*})$ is negligibly small.

3.2.2 *CP* Asymmetry for Majorana Neutrino

The above discussion is only limited to Dirac neutrinos. However, neutrinos may also be Majorana particles i.e. where the neutrino is identical to the antineutrino but with potentially different kinematics. In this case, both the neutrino and antineutrino modes must be considered together. The amplitude is then given by $i\mathcal{M}^{\mathrm{M}}(\nu_{\mathbf{i}} \to \nu_{\mathbf{f}} + \gamma_{\pm}) = i\mathcal{M}(\nu_{\mathbf{i}} \to \nu_{\mathbf{f}} + \gamma_{\pm}) + i\mathcal{M}(\bar{\nu}_{\mathbf{i}} \to \bar{\nu}_{\mathbf{f}} + \gamma_{\pm})$. Taking the explicit formulas for the amplitudes given in Eq (3.2.5) and (3.2.10), we obtain results with definite spins in the initial and final states as

$$\begin{aligned}
\mathcal{M}^{\mathrm{M}}(\nu_{\mathbf{i}} \to \nu_{\mathbf{f}} + \gamma_{+}) &= +\sqrt{2}[f^{\mathrm{L}}_{\mathbf{fi}} - f^{\mathrm{L}}_{\mathbf{if}}](m_{\mathbf{i}}^2 - m_{\mathbf{f}}^2)\,, \\
\mathcal{M}^{\mathrm{M}}(\nu_{\mathbf{i}} \to \nu_{\mathbf{f}} + \gamma_{-}) &= -\sqrt{2}[f^{\mathrm{R}}_{\mathbf{fi}} - f^{\mathrm{R}}_{\mathbf{if}}](m_{\mathbf{i}}^2 - m_{\mathbf{f}}^2)\,, \qquad (3.2.23)
\end{aligned}$$

The decay width $\Gamma^{\mathrm{M}}(\nu_{\mathbf{i}} \to \nu_{\mathbf{f}} + \gamma_{\pm})$ is still written in the form shown in Eq. (3.2.4).

For Majorana fermions, the *CP* violation is identical to that obtained from *P* violation alone i.e. the *CP* asymmetry is essentially the same as the asymmetry between the two polarised photons $\Delta^{\rm M}_{+-}$

$$\Delta^{\rm M}_{CP,+} = -\Delta^{\rm M}_{CP,-} \equiv \Delta^{\rm M}_{+-} = \frac{\Gamma^{\rm M}(\nu_{\bf i} \to \nu_{\bf f} + \gamma_+) - \Gamma^{\rm M}(\nu_{\bf i} \to \nu_{\bf f} + \gamma_-)}{\Gamma^{\rm M}(\nu_{\bf i} \to \nu_{\bf f} + \gamma)} . \qquad (3.2.24)$$

The CP asymmetry without considering the polarisation of the radiated photon is zero, namely, $\Delta^{\rm M}_{CP} = \Delta^{\rm M}_{CP,+} + \Delta^{\rm M}_{CP,-} = 0$. With the help of Eq. (3.2.23), we can express $\Delta^{\rm M}_{+-}$ in the form of electromagnetc dipole parameters as

$$\Delta^{\rm M}_{+-} = \frac{|f^{\rm L}_{\bf fi} - f^{\rm L}_{\bf if}|^2 - |f^{\rm R}_{\bf fi} - f^{\rm R}_{\bf if}|^2}{|f^{\rm L}_{\bf fi} - f^{\rm L}_{\bf if}|^2 + |f^{\rm R}_{\bf fi} - f^{\rm R}_{\bf if}|^2} . \qquad (3.2.25)$$

We will not discuss the Majorana case further here since the asymmetries are similarly straightforward to obtain once coefficients of the transition dipole moment are ascertained.

At the end of this section, we comment on CP violation in electrically charged neutrino decay. In this scenario, the magnitudes of the neutrino and antineutrino decay modes are modified to

$$\begin{aligned}
\mathcal{M}(\nu_{\bf i} \to \nu_{\bf f} + \gamma_+) &= +\sqrt{2} f^{\rm L}_{\bf fi}(m^2_{\bf i} - m^2_{\bf f}) - \sqrt{2} f^{Q}_{\bf fi}(m_{\bf i} - m_{\bf f}) \,, \\
\mathcal{M}(\nu_{\bf i} \to \nu_{\bf f} + \gamma_-) &= -\sqrt{2} f^{\rm R}_{\bf fi}(m^2_{\bf i} - m^2_{\bf f}) + \sqrt{2} f^{Q}_{\bf fi}(m_{\bf i} - m_{\bf f}) \,, \\
\mathcal{M}(\bar\nu_{\bf i} \to \bar\nu_{\bf f} + \gamma_+) &= +\sqrt{2} f^{\rm L}_{\bf if}(m^2_{\bf i} - m^2_{\bf f}) - \sqrt{2} f^{Q}_{\bf if}(m_{\bf i} - m_{\bf f}) \,, \\
\mathcal{M}(\bar\nu_{\bf i} \to \bar\nu_{\bf f} + \gamma_-) &= -\sqrt{2} f^{\rm R}_{\bf if}(m^2_{\bf i} - m^2_{\bf f}) + \sqrt{2} f^{Q}_{\bf if}(m_{\bf i} - m_{\bf f}) \,, \qquad (3.2.26)
\end{aligned}$$

where, according to the CPT theorem, $\bar f^{Q}_{\bf if} = -f^{Q}_{\bf if}$ has been used. The modified amplitudes are equivalent to shifting coefficients $f^{\rm L}$ and $f^{\rm R}$ in Eqs. (3.2.5) and (3.2.10) to $f^{\rm L\prime} = f^{\rm L} - f^{Q}/(m_{\bf i} + m_{\bf f})$ and $f^{\rm R\prime} = f^{\rm R} - f^{Q}/(m_{\bf i} + m_{\bf f})$ respectively. CP asymmetries $\Delta_{CP,+}$, $\Delta_{CP,-}$, Δ_{CP} and the asymmetry between polarised photons Δ_{+-} (Dirac neutrino), as well as $\Delta^{\rm M}_{+-}$ (Majorana neutrino), are obtained following the same coefficient shifts.

3.3 *CP*-Violation in Neutrino Radiative Decay

Having provided a very general discussion on CP violation and circular polarisation for neutrino radiative decay in a mass scale and model independent way in the previous section, in the following sections, we will concentrate on a simplified example where a sterile neutrino radiatively decays $\nu_s \to \nu_i + \gamma$ and show how to obtain the exact form of the CP asymmetry and circular polarisation for the radiated photon. In this example, the initial and final state neutrinos are specified as $\nu_{\mathbf{i}} = \nu_s$ and $\nu_{\mathbf{f}} = \nu_i$ respectively. In this simplified case, we consider only one sterile neutrino generation and the three active neutrino generations with both ν_s and ν_i (for $i = 1, 2, 3$) being mass eigenstates. Extensions to multiple sterile neutrino generations are straightforward, and thus, will not be discussed here.

We will apply the above formulation in the following way. First, we estimate the size of CP violation from the SM contribution alone i.e. via the charged current interaction mediated by the W boson. Then, we consider the enhancement of CP violation by including BSM Yukawa interactions for sterile neutrinos. Such Yukawa interactions have a wide array of applications with theoretical and phenomenological utility which we will outline in the following section. Finally, we list the simplified analytical result for CP violation and circular polarisation generated from the decay at the end of this section.

3.3.1 Standard Model Contribution

It is well known that the radiative decay can happen via one-loop corrections induced by SM weak interactions with SM particles (specifically with charged lepton ℓ_α for $\alpha = e, \mu, \tau$ and the W boson) in the loop. The crucial operator is the charged-current interaction is

$$\mathcal{L}_{\text{c.c.}} = \sum_{\alpha=e,\mu,\tau} \sum_{m=1,2,3,s} \frac{g}{\sqrt{2}} U_{\alpha m}\, \bar{\ell}_\alpha \gamma^\mu P_{\text{L}} \nu_m W^-_\mu + \text{h.c.}\,, \tag{3.3.1}$$

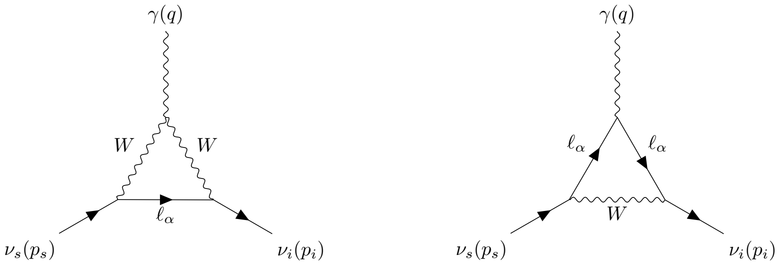

Figure 3.1: The Feynman diagrams for the one-loop Standard Model contributions from charged current interactions are shown above for radiative decay of a sterile neutrino. Diagrams involving unphysical Goldstone bosons and ghosts are omitted for the sake of brevity.

where g is the EW gauge coupling constant and $U_{\alpha m}$ represent the lepton flavour mixing. Here we have $m = i, s$ (where $i = 1, 2, 3$) representing the active light neutrino mass eigenstate ν_i and the sterile neutrino mass eigenstate ν_s.

The one-loop Feynman diagrams for the radiative decay via the SM charged current interaction are shown in Fig. 3.1 [1]. In the limit $m_s^2/m_W^2 \ll a_\alpha \equiv m_\alpha^2/m_W^2$, where m_α and m_W are the charged lepton and W boson masses respectively, we have the result for $\Gamma^{\mu}_{\mathbf{fi}}$ given as

$$\Gamma^{\mu}_{is} = \frac{ieG_{\mathrm{F}}\sigma^{\mu\nu}q_{\nu}}{4\pi^2\sqrt{2}} \sum_{\alpha=e,\mu,\tau} U^*_{\alpha i}U_{\alpha s}F_{\alpha}(m_s P_{\mathrm{R}} + m_i P_{\mathrm{L}})\,, \tag{3.3.2}$$

where F_α is a function obtained from the loop integrals and the Fermi constant is defined $G_{\mathrm{F}} = \dfrac{g^2}{4\sqrt{2}m_W^2}$. If $m_{\mathbf{i}}$ is much smaller than the charged lepton masses, we arrive at the classic result [69, 118]

$$F_\alpha = \frac{3}{4}\left(\frac{2-a_\alpha}{1-a_\alpha} - \frac{2a_\alpha}{(1-a_\alpha)^2} - \frac{2a_\alpha^2 \ln a_\alpha}{(1-a_\alpha)^3}\right) \approx \frac{3}{2} - \frac{3}{4}a_\alpha\,, \tag{3.3.3}$$

which is insensitive to neutrino masses. A more general neutrino mass-dependent result for F_α with $m_{\mathbf{i}}$, $m_{\mathbf{f}}$ up to the W boson mass has been given in [121, 122]. In general, for $m_{\mathbf{i}} < m_W$, there is not possible final states that can contribute to the

---

[1] In the Feynman gauge, additional diagrams involving unphysical Goldstone bosons and ghosts should also be included, note that these are not shown in the figure. In addition, the one-loop $\gamma - Z$ self-energy diagrams are essential to include to eliminate divergences in the presence of the sterile neutrino [154].

RHS of Eq. (3.2.22), and thus F_α is always positive.

From the above formulae, we obtain results for $f^{\rm L}_{\bf fi}$ and $f^{\rm R}_{\bf fi}$ given as

$$\begin{aligned} f^{\rm L}_{is} &= e\frac{g^2}{2}\frac{1}{16\pi^2 m_W^2}\sum_{\alpha=e,\mu,\tau} U^*_{\alpha i}U_{\alpha s}F_\alpha m_i\,, \\ f^{\rm R}_{is} &= e\frac{g^2}{2}\frac{1}{16\pi^2 m_W^2}\sum_{\alpha=e,\mu,\tau} U^*_{\alpha i}U_{\alpha s}F_\alpha m_s\,, \end{aligned} \tag{3.3.4}$$

factorising the SM contribution into a coefficient part and a purely kinetic part yields

$$f^{\rm L}_{{\bf fi},{\rm SM}} = \sum_\alpha C_\alpha K^{\rm L}_\alpha\,, \quad f^{\rm R}_{{\bf fi},{\rm SM}} = \sum_\alpha C_\alpha K^{\rm R}_\alpha \tag{3.3.5}$$

with

$$(C_\alpha)_{is} = e\frac{g^2}{2}U^*_{\alpha i}U_{\alpha s}\,, \tag{3.3.6}$$

and

$$(K^{\rm L}_\alpha)_{is} = \frac{1}{16\pi^2 m_W^2}F_\alpha m_i\,, \quad (K^{\rm R}_\alpha)_{is} = \frac{1}{16\pi^2 m_W^2}F_\alpha m_s\,, \tag{3.3.7}$$

with flavour index $\alpha = e,\mu,\tau$. Since F_α is real, both ${\rm Im}(K^{\rm L}_\alpha K^{{\rm L}*}_\beta)$ and ${\rm Im}(K^{\rm R}_\alpha K^{{\rm R}*}_\beta)$ vanish for any flavours $\alpha,\beta = e,\mu,\tau$. In addition, by interchanging $i \leftrightarrow s$ we notice that the one-loop SM contribution exactly satisfies $f^{\rm L}_{\bf fi} = \bar{f}^{\rm R}_{\bf if}$ and $f^{\rm R}_{\bf fi} = \bar{f}^{\rm L}_{\bf if}$. Therefore, there is no CP violation coming from these diagrams.

For a sterile neutrino with mass smaller than the W boson mass, we comment that a non-zero CP violation can in principle be obtained after considering higher-loop SM contributions. We analyse this by applying the optical theorem where Eq. (3.2.22) has to be satisfied n order to generate an imaginary part for the kinetic loop contribution. Again, we recall that we require on-shell intermediate states and the sum of their masses must be smaller than the sterile neutrino mass. Thus, only neutrinos and photons are left in the intermediate state c. There are typically three cases with intermediate states given by (a) $c = \nu_j + \gamma$ [1], (b) $\nu_j + \nu_k + \bar{\nu}_k$, and (c) $\nu_j + \alpha + \bar{\alpha}$ for $\alpha = e,\mu,\tau$. They correspond to four-, three- and two-loop diagrams

---

[1] CP violation for this case has been calculated in [123]

respectively. Case (c) applies only if $m_s > 2m_\alpha$, these contributions are in general very small. In order to obtain large CP violation, additional loop contributions from BSM have to be considered.

However, if the sterile neutrino is heavier than the W boson, an imaginary part can be obtained directly from the SM one-loop diagram, we will discuss this case in some of the following sections.

3.3.2 Enhancement by Beyond the Standard Model Physics

In order to enhance the CP violation in the radiative decay of the sterile neutrino, we include BSM contributions. We being by introducing two new particles, one fermion ψ and one scalar ϕ with opposite electric charges Q and $-Q$ respectively. Their couplings with neutrinos and the sterile neutrino are described by the following Yukawa interaction

$$-\mathcal{L}_{\rm BSM} \supset \sum_{m=1,2,3,s} \lambda_m \bar{\psi} \phi^* P_{\rm L} \nu_m + \lambda_m^* \bar{\nu}_m \phi P_{\rm R} \psi \,, \tag{3.3.8}$$

where λ_m, with $m = i, s$ (for $i = 1, 2, 3$), are complex coefficients to ν_i and ν_s, which are the active and sterile neutrino mass eigenstates respectively. Here, we only included one generation of ϕ and ψ respectively. The extension to more generations is straightforward and will be mentioned as necessary. Neither ψ or ϕ are supposed to be a specific DM candidate in this work and they can annihilate with their antiparticles due to their opposite electric charges.

The full amplitude including the BSM contribution for $\nu_s \to \nu_i + \gamma$ can then be written

$$\mathcal{M} = \sum_\alpha \mathcal{M}_\alpha^{\rm SM} + \sum_{l_{\rm BSM}} \mathcal{M}_{l_{\rm BSM}}^{\rm BSM} \,, \tag{3.3.9}$$

where we have flavour index $\alpha = e, \mu, \tau$ and $l_{\rm BSM}$ represents one-loop BSM contributions. Since $U(1)_Q$ is explicitly conserved and no electric charges are assigned for

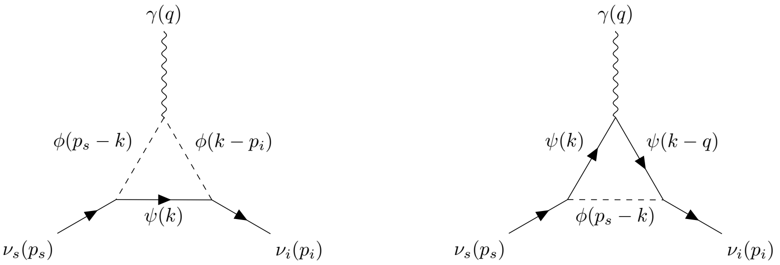

Figure 3.2: Feynman diagrams for the new physics one-loop contributions to the radiative decay of a sterile neutrino. We denote amplitudes for the two diagrams as $\mathcal{M}_1^{\rm BSM}$ and $\mathcal{M}_2^{\rm BSM}$. For $\mathcal{M}_1^{\rm BSM}$ we make the momenta assignments $p_1=p_s-k$, $p_2=k-p_i$ and for $\mathcal{M}_2^{\rm BSM}$, we assign $k'=k-q$. In both diagrams $p_s=p_i+q$.

neutrinos at tree level, they keep free of electric charges after loop corrections are included. Thus, radiative decays are induced only via the electromagnetic transition dipole moments. The coefficients $f^{\rm L}_{\mathbf{fi}}$, $f^{\rm R}_{\mathbf{fi}}$ and $f^{\rm L}_{\mathbf{if}}$, $f^{\rm R}_{\mathbf{if}}$, including BSM, are now written as

$$\begin{aligned} f^{\rm L}_{\mathbf{fi}} &= \sum_\alpha C_\alpha K^{\rm L}_\alpha + \sum_{l_{\rm BSM}} C_{l_{\rm BSM}} K^{\rm L}_{l_{\rm BSM}}\,, \qquad & f^{\rm R}_{\mathbf{fi}} &= \sum_\alpha C_\alpha K^{\rm R}_\alpha + \sum_{l_{\rm BSM}} C_{l_{\rm BSM}} K^{\rm R}_{l_{\rm BSM}}\,, \\ f^{\rm L}_{\mathbf{if}} &= \sum_\alpha C_\alpha K^{\rm R}_\alpha + \sum_{l_{\rm BSM}} C_{l_{\rm BSM}} K^{\rm R}_{l_{\rm BSM}}\,, \qquad & f^{\rm R}_{\mathbf{if}} &= \sum_\alpha C_\alpha K^{\rm L}_\alpha + \sum_{l_{\rm BSM}} C_{l_{\rm BSM}} K^{\rm L}_{l_{\rm BSM}}\,. \end{aligned} \tag{3.3.10}$$

From Eq. (3.3.10), we have the necessary expressions to compute the CP violation and asymmetry between the radiated photons γ_+ and γ_-. As an example, we take $\Delta_{CP,-}$ to demonstrate an explicit calculation. The definition of $\Delta_{CP,-}$ has been given in Eq. (3.2.16) where $\Delta_{CP,-} \propto |f^{\rm R}_{\mathbf{fi}}|^2 - |f^{\rm L}_{\mathbf{if}}|^2$. With the help of the parametrisation in Eq. (3.3.10) and assuming $|K^{\rm R}_l| = |\bar{K}^{\rm L}_l|$ for any loop l, we obtain

$$|f^{\rm R}_{\mathbf{fi}}|^2 - |f^{\rm L}_{\mathbf{if}}|^2 = -4\sum_{\alpha, l_{\rm BSM}} {\rm Im}(C_\alpha C^*_{l_{\rm BSM}}) {\rm Im}(K^{\rm R}_\alpha K^{{\rm R}\,*}_{l_{\rm BSM}}) - 2\sum_{l_{\rm BSM}\neq l'_{\rm BSM}} {\rm Im}(C_{l_{\rm BSM}} C^*_{l'_{\rm BSM}}) {\rm Im}(K^{\rm R}_{l_{\rm BSM}} K^{{\rm R}*}_{l'_{\rm BSM}}). \tag{3.3.11}$$

For the two BSM diagrams shown in Fig. 3.2, where a photon is radiated via the interaction between scalars ϕ and fermions ψ respectively, the amplitudes for

($\nu_s \to \nu_i + \gamma_-$) can be explicitly written as

$$i\mathcal{M}_1^{\rm BSM} = C_1 \int \frac{d^4k}{(2\pi)^4} \frac{\overline{u}(p_i) P_{\rm R}(\not{k} + m_\psi)(p_1 - p_2)^\mu P_{\rm L} u(p_s) \varepsilon^*_{-,\mu}(q)}{(k^2 - m_\psi^2 + i\epsilon)((k-p_s)^2 - m_\phi^2 + i\epsilon)((k-p_i)^2 - m_\phi^2 + i\epsilon)} \,,$$
$$i\mathcal{M}_2^{\rm BSM} = -C_2 \int \frac{d^4k}{(2\pi)^4} \frac{\overline{u}(p_i) P_{\rm R}(\not{k}' + m_\psi)\gamma^\mu(\not{k} + m_\psi) P_{\rm L} u(p_s) \varepsilon^*_{-,\mu}(q)}{((k-p_s)^2 - m_\phi^2 + i\epsilon)(k'^2 - m_\psi^2 + i\epsilon)(k^2 - m_\psi^2 + i\epsilon)} \,. \tag{3.3.12}$$

Where the coefficients $C_{l_{\rm BSM}}$ (for $l_{\rm BSM} = 1, 2$) are

$$C_1 \;=\; -C_2 = -Qe\lambda_s\lambda_i^* \,. \tag{3.3.13}$$

In this case, $\mathrm{Im}(C_1 C_2^*) = 0$ and the second part of Eq. (3.3.11) vanishes. On the other hand the imaginary part is given by

$$\mathrm{Im}(C_\alpha C_1^*) = -\mathrm{Im}(C_\alpha C_2^*) = -\frac{Q}{2} e^2 g^2\, \mathrm{Im}(U_{\alpha s} U_{\alpha i}^* \lambda_i \lambda_s^*) \,. \tag{3.3.14}$$

We now turn to the loop contributions. $\mathrm{Im}(K_1^{\rm R} K_2^{\rm R\,*})$ does not need to be calculated since $\mathrm{Im}(C_1 C_2^*)$ vanishes explicitly. Hence, the remaining term to be computed is $\mathrm{Im}(K_\alpha^{\rm R} K_{l_{\rm NP}}^{\rm R\,*})$. Furthermore, since the SM contributions are always real, $\mathrm{Im}(K_\alpha^{\rm R} K_{l_{\rm BSM}}^{\rm R\,*}) = -K_\alpha^{\rm R} \mathrm{Im}(K_{l_{\rm BSM}}^{\rm R})$.

In order to obtain CP violation between the radiative decay $\nu_s \to \nu_i + \gamma_-$ and its CP conjugate channel $\bar{\nu}_s \to \bar{\nu}_i + \gamma_+$ for a Dirac-type sterile neutrino, a non-vanishing imaginary part $\mathrm{Im}(K_{l_{\rm BSM}}^{\rm R})$ is required, this can be summarised

$$|f_{\bf fi}^{\rm R}|^2 - |f_{\bf if}^{\rm L}|^2 \;=\; +4 \sum_{\alpha, l_{\rm BSM}} \mathrm{Im}(C_\alpha C_{l_{\rm BSM}}^*) K_\alpha^{\rm R} \mathrm{Im}(K_{l_{\rm BSM}}^{\rm R}) \,. \tag{3.3.15}$$

Following a similar approach to determine CP violation between $\nu_s \to \nu_i + \gamma_+$ and its CP conjugate process $\bar{\nu}_s \to \bar{\nu}_i + \gamma_-$, we obtain

$$|f_{\bf fi}^{\rm L}|^2 - |f_{\bf if}^{\rm R}|^2 \;=\; +4 \sum_{\alpha, l_{\rm BSM}} \mathrm{Im}(C_\alpha C_{l_{\rm BSM}}^*) K_\alpha^{\rm L} \mathrm{Im}(K_{l_{\rm BSM}}^{\rm L}) \,. \tag{3.3.16}$$

Due to the optical theorem, non-zero $\mathrm{Im}(K_{l_{\rm BSM}}^{\rm L})$ and $\mathrm{Im}(K_{l_{\rm BSM}}^{\rm R})$ can only be achieved if the sterile neutrino mass is larger than the sum of the charged scalar and the charged fermion masses, $m_s > m_\phi + m_\psi$. In the remainder of this section, our aim will be to compute these quantities.

Here, the loop integrals for the relevant diagrams shown in Fig. 3.2 will be calculated. Starting from the general form of the amplitude for sterile neutrino radiative decay $\nu_s \to \nu_i + \gamma_\pm$ given in Eq. (3.2.1), we extract the purely kinetic terms $K^{\rm L}_{l_{\rm BSM}}$ and $K^{\rm R}_{l_{\rm BSM}}$ for $l_{\rm BSM} = 1, 2$ as [1]

$$\begin{aligned} K_1^{\rm L} &= \frac{m_i}{16\pi^2}\int_0^1 {\rm d}x{\rm d}y{\rm d}z \frac{\delta(x+y+z-1)\,z}{\Delta_{\phi\psi}(x,y,z)}\,, \\ K_1^{\rm R} &= \frac{m_s}{16\pi^2}\int_0^1 {\rm d}x{\rm d}y{\rm d}z \frac{\delta(x+y+z-1)\,y}{\Delta_{\phi\psi}(x,y,z)}\,, \\ K_2^{\rm L} &= \frac{m_i}{16\pi^2}\int_0^1 {\rm d}x{\rm d}y{\rm d}z \frac{\delta(x+y+z-1)\,xz}{\Delta_{\psi\phi}(x,y,z)}\,, \\ K_2^{\rm R} &= \frac{m_s}{16\pi^2}\int_0^1 {\rm d}x{\rm d}y{\rm d}z \frac{\delta(x+y+z-1)\,xy}{\Delta_{\psi\phi}(x,y,z)}\,, \end{aligned} \qquad (3.3.17)$$

where

$$\begin{aligned} \Delta_{\phi\psi}(x,y,z) &= m_\phi^2(1-x) + x m_\psi^2 - x(y m_s^2 + z m_i^2) \\ \Delta_{\psi\phi}(x,y,z) &= m_\psi^2(1-x) + x m_\phi^2 - x(y m_s^2 + z m_i^2)\,. \end{aligned} \qquad (3.3.18)$$

The above results are obtained without any approximations. In order to derive further simplified analytical formulae, we consider the large mass hierarchy between ν_s and ν_i where $m_i \ll m_s$, and may therefore take the limit $m_i \to 0$. In this case, $K^{\rm L}_{l_{\rm BSM}} = 0$ and after integrating over Feynman parameters z and x, $K^{\rm R}_{l_{\rm BSM}}$ can be written as

$$\begin{aligned} K_1^{\rm R} &= \frac{m_s}{16\pi^2}\int_0^1 {\rm d}y \frac{y}{m_s^2 y - m_\psi^2 + m_\phi^2}\log\left(\frac{\Delta_{\phi\psi}(y)}{m_\phi^2}\right)\,, \\ K_2^{\rm R} &= \frac{m_s}{16\pi^2}\left[\int_0^1 {\rm d}y \frac{-m_\psi^2 y}{(m_s^2 y + m_\psi^2 - m_\phi^2)^2}\log\left(\frac{\Delta_{\psi\phi}(y)}{m_\psi^2}\right) + \int_0^1 {\rm d}y \frac{y(y-1)}{m_s^2 y + m_\psi^2 - m_\phi^2}\right]\,, \end{aligned} \qquad (3.3.19)$$

---

[1] Here, $K^{\rm L}_{l_{\rm BSM}}$ and $K^{\rm R}_{l_{\rm BSM}}$ represent $(K^{\rm L}_{l_{\rm BSM}})_{is}$ and $(K^{\rm R}_{l_{\rm BSM}})_{is}$, respectively. Exchanging i with s, we obtain $(K^{\rm L}_{l_{\rm BSM}})_{si} = (K^{\rm R}_{l_{\rm BSM}})_{is}$ and $(K^{\rm R}_{l_{\rm BSM}})_{si} = 0$, this is compatible with our previous statement that $(K^{\rm L}_l)_{\bf if} = (K^{\rm R}_l)_{\bf fi}$ and $(K^{\rm R}_l)_{\bf if} = (K^{\rm L}_l)_{\bf fi}$.

where

$$\begin{aligned}\Delta_{\phi\psi}(y) &= y\left(m_s^2(y-1)+m_\phi^2\right)-m_\psi^2(y-1)\,,\\ \Delta_{\psi\phi}(y) &= y\left(m_s^2(y-1)+m_\psi^2\right)-m_\phi^2(y-1)\,.\end{aligned}\tag{3.3.20}$$

$K^{\rm R}_{l_{\rm BSM}}$ may have both real parts and imaginary parts. The real part ${\rm Re}(K^{\rm R}_{l_{\rm BSM}})$ is directly obtained by replacing $\Delta_{\phi\psi}$ and $\Delta_{\psi\phi}$ with there absolute values, therefore simple analytical expressions for ${\rm Re}(K^{\rm R}_{l_{\rm BSM}})$ are difficult to obtain. However, in the hierarchical case $m_s \gg m_\phi, m_\psi$ approximate analytical expressions can be derived by expanding in powers of m_ϕ^2/m_s^2 and m_ψ^2/m_s^2. Specifically, the leading-order results are given by

$$\begin{aligned}{\rm Re}(K_1^{\rm R}) &\approx \frac{1}{16\pi^2 m_s}\left[\log\left(\frac{m_s^2}{m_\phi^2}\right)-2\right]\,,\\ {\rm Re}(K_2^{\rm R}) &\approx \frac{1}{16\pi^2 m_s}\times\frac{-1}{2}\,.\end{aligned}\tag{3.3.21}$$

Since we are chiefly interested in the CP violating component, we will focus on how to obtain and simplify the imaginary parts of $K^{\rm R}_{l_{\rm BSM}}$.

Since $m_\phi^2, m_\psi^2 \geq 0$, the imaginary and thus CP violating component in Eq. (3.3.19) factorises when the argument of the logarithm is negative, by inspection we can see this occurs when

$$\begin{aligned}\Delta_{\phi\psi}(y) &< 0\,,\\ \Delta_{\psi\phi}(y) &< 0\,.\end{aligned}\tag{3.3.22}$$

Solutions at the boundaries of the CP violation conditions $\Delta_{\phi\psi}(y)=0$ and $\Delta_{\psi\phi}(y)=0$ are $y_{1,2}(m_\phi, m_\psi)$ and $y_{1,2}(m_\psi, m_\phi)$ respectively. Therefore the conditions in Eq. (3.3.22) in terms of y are fulfilled when $y_1(m_\phi, m_\psi) \leq y \leq y_2(m_\phi, m_\psi)$ and $y_1(m_\psi, m_\phi) \leq y \leq y_2(m_\psi, m_\phi)$ for the two diagrams respectively, where

$$\begin{aligned}y_{1,2}(m_\phi, m_\psi) &= \frac{1}{2}+\frac{m_\psi^2-m_\phi^2\mp\mu^2}{2m_s^2}\,,\\ y_{1,2}(m_\psi, m_\phi) &= \frac{1}{2}+\frac{m_\phi^2-m_\psi^2\mp\mu^2}{2m_s^2}\,,\end{aligned}\tag{3.3.23}$$

and μ^2 is defined as

$$\mu^2 = \sqrt{m_s^4 + m_\phi^4 + m_\psi^4 - 2m_s^2 m_\phi^2 - 2m_s^2 m_\psi^2 - 2m_\phi^2 m_\psi^2}\,. \tag{3.3.24}$$

It should be noted that in both cases $0 < y_1 < y_2 < 1$ is necessarily satisfied.

Hence, the imaginary component of Eq. (3.3.19) can now be written according to the complex logarithm definition as

$$\begin{aligned} \mathrm{Im}(K_1^{\mathrm{R}}) &= \frac{m_s}{16\pi^2} \times \pi \int_{y_1(m_\phi, m_\psi)}^{y_2(m_\phi, m_\psi)} \mathrm{d}y \frac{y}{m_s^2 y - m_\psi^2 + m_\phi^2}\,, \\ \mathrm{Im}(K_2^{\mathrm{R}}) &= \frac{m_s}{16\pi^2} \times \pi \int_{y_1(m_\psi, m_\phi)}^{y_2(m_\psi, m_\phi)} \mathrm{d}y \frac{-m_\psi^2 y}{(m_s^2 y + m_\psi^2 - m_\phi^2)^2}\,. \end{aligned} \tag{3.3.25}$$

Finally, integrating over the final Feynman parameter y leads to

$$\begin{aligned} \mathrm{Im}(K_1^{\mathrm{R}}) &= \frac{m_s}{16\pi^2}\frac{-\pi}{m_s^2}\left[\frac{\mu^2}{m_s^2} + \frac{m_\phi^2 - m_\psi^2}{m_s^2}\log\left(\frac{m_s^2 + m_\phi^2 - m_\psi^2 - \mu^2}{m_s^2 + m_\phi^2 - m_\psi^2 + \mu^2}\right)\right]\,, \\ \mathrm{Im}(K_2^{\mathrm{R}}) &= \frac{m_s}{16\pi^2}\frac{+\pi}{m_s^2}\left[\frac{\mu^2(m_\psi^2 - m_\phi^2)}{m_s^4} + \frac{m_\psi^2}{m_s^2}\log\left(\frac{m_s^2 + m_\psi^2 - m_\phi^2 - \mu^2}{m_s^2 + m_\psi^2 - m_\phi^2 + \mu^2}\right)\right]\,. \end{aligned} \tag{3.3.26}$$

The requirement $m_s > m_\phi + m_\psi$ leads to a positive μ^2. In the mass-degenerate limit $m_s = m_\phi + m_\psi$, $\mu^2 = 0$ and after some simplifications, it can be shown for this case that $\mathrm{Im}(K_1^{\mathrm{R}}) = \mathrm{Im}(K_2^{\mathrm{R}}) = 0$. In the massless limit $m_\phi, m_\psi \to 0$, these imaginary parts are approximately given by $\mathrm{Im}(K_1^{\mathrm{R}}) \to -1/(16\pi m_s)$ and $\mathrm{Im}(K_2^{\mathrm{R}}) \to 0$.

Since we need to compute $\Delta_{CP,-}$ to calculate CP violation, we apply Eq. (3.3.15), which in this example can be written explicitly as

$$f_{\mathbf{fi}}^{\mathrm{R}}|^2 - |f_{\mathbf{if}}^{\mathrm{L}}|^2 = +4\sum_\alpha \mathrm{Im}(C_\alpha C_1^*) K_\alpha^{\mathrm{R}}[\mathrm{Im}(K_1^{\mathrm{R}} - K_2^{\mathrm{R}})], \tag{3.3.27}$$

| therefore we obtain

$$|f_{\mathbf{fi}}^{\mathrm{R}}|^2 - |f_{\mathbf{if}}^{\mathrm{L}}|^2 = \frac{2\pi Q e^2 g^2}{(16\pi^2)^2 m_W^2}\sum_\alpha \mathrm{Im}(U_{\alpha s} U_{\alpha i}^* \lambda_i \lambda_s^*)\, F_\alpha\, I_{\phi\psi}\,. \tag{3.3.28}$$

For $\Delta_{CP,+}$, $|f_{\mathbf{fi}}^{\mathrm{R}}|^2 - |f_{\mathbf{if}}^{\mathrm{L}}|^2$ is obtained by multiplying by a factor m_i^2/m_s^2 which is strongly suppressed by the light active neutrino mass.

Here, we have defined $I_{\phi\psi}$, an order one normalised parameter which is defined via

$\mathrm{Im}(K_2^{\mathrm{R}} - K_1^{\mathrm{R}}) = \dfrac{m_s}{16\pi^2}\dfrac{\pi}{m_s^2} I_{\phi\psi}$ and explicitly given by

$$I_{\phi\psi} = \frac{\mu^2(m_s^2 + m_\psi^2 - m_\phi^2)}{m_s^4} + \frac{m_\phi^2 - m_\psi^2}{m_s^2}\log\left(\frac{m_s^2 + m_\phi^2 - m_\psi^2 - \mu^2}{m_s^2 + m_\phi^2 - m_\psi^2 + \mu^2}\right) + \frac{m_\psi^2}{m_s^2}\log\left(\frac{m_s^2 + m_\psi^2 - m_\phi^2 - \mu^2}{m_s^2 + m_\psi^2 - m_\phi^2 + \mu^2}\right) . \quad (3.3.29)$$

See Appendix B for more details regarding the calculation of the imaginary part of the loop diagrams.

In this example, we may safely ignore the $f_{\mathbf{fi}}^{\mathrm{L}}$ and $f_{\mathbf{if}}^{\mathrm{R}}$ terms since $f_{\mathbf{fi}}^{\mathrm{L}} \sim f_{\mathbf{if}}^{\mathrm{R}} \sim \frac{m_i}{m_s} f_{\mathbf{if}}^{\mathrm{L}} \sim \frac{m_i}{m_s} f_{\mathbf{fi}}^{\mathrm{R}}$, thus the asymmetries, defined in Eqs. (3.2.16) and (3.2.17) are approximately given by

$$-\Delta_{CP,-} \approx -\Delta_{CP} \approx \Delta_{+-} \approx \frac{|f_{\mathbf{if}}^{\mathrm{L}}|^2 - |f_{\mathbf{fi}}^{\mathrm{R}}|^2}{|f_{\mathbf{if}}^{\mathrm{L}}|^2 + |f_{\mathbf{fi}}^{\mathrm{R}}|^2} \quad (3.3.30)$$

and $\Delta_{CP,+}$ is negligibly small. This result works for the Dirac neutrino case. In the Majorana neutrino case, from Eq. (3.2.25), it is straightforward to apply a similar procedure and obtain

$$\Delta_{CP,+}^{\mathrm{M}} = -\Delta_{CP,-}^{\mathrm{M}} = \Delta_{+-}^{\mathrm{M}} \approx \frac{|f_{\mathbf{if}}^{\mathrm{L}}|^2 - |f_{\mathbf{fi}}^{\mathrm{R}}|^2}{|f_{\mathbf{if}}^{\mathrm{L}}|^2 + |f_{\mathbf{fi}}^{\mathrm{R}}|^2} \quad (3.3.31)$$

and $\Delta_{CP} = 0$. Regardless of whether the neutrinos are Dirac or Majorana particles $\Delta_{CP,-} \approx -\Delta_{+-}$ is satisfied. This is true in general if $f_{\mathbf{fi}}^{\mathrm{L}}, f_{\mathbf{if}}^{\mathrm{R}} \ll f_{\mathbf{if}}^{\mathrm{L}}, f_{\mathbf{fi}}^{\mathrm{R}}$.

3.4 Conclusion

Here we discussed a general framework for *CP* violation in neutrino radiative decays. *CP* violation in such processes produces an asymmetry between the circularly polarised radiated photons and provides an important source of net circular polarisation that can be observed in particle and astroparticle physics experiments.

It was discussed how to generate non-vanishing *CP* violation through a generic new physics Yukawa interaction extension consisting of electrically charged scalar and fermion states. Without introducing any source of electric charge for the neutrinos, these particles can decay only via the electromagnetic transition dipole moment. The explicit analytical result of CP violation for this model was derived and presented.

The formulation between CP violation in neutrino radiative decays and the neutrino electromagnetic dipole moment at the form factor level is developed for both Dirac and Majorana neutrinos. We observed the model-independent connection between the decays and photon circular polarisation produced by these processes and concluded that CP violation directly determines the circular polarisation. This fundamental result is applicable when determining circular polarisation for both Dirac and Majorana fermions and can be exported for use in any models that generate radiative decays of this type. Specifically in the Majorana neutrino case, the CP asymmetry is identical to the asymmetry of photon polarisations up to an overall sign difference.

Chapter 4

CP–Violation in Heavy Neutrino Radiative Decay

The formulation based on Chapter 2 has a wide array of possible applications. In this chapter, we will apply it to the minimal seesaw mechanism where right-handed neutrinos N_1 and N_2, with respective masses $M_1 < M_2$ much larger than the electroweak scale, are added to the SM in order to recover light active neutrino masses. In Section 4.2 a full one–loop computation of the neutrino radiative decay, in the context of Standard Model interactions, is performed in the Feynman gauge. In Section 4.2.1 we compute the CP violation generated by a required threshold condition for the neutrino masses along with non–vanishing CP violating phases in the lepton flavor mixing matrix. In Section 4.4 we discuss the extended parametrization of the flavor mixing matrix, including the heavy neutrinos N_1 and $N2$. We give the CP asymmetry in terms of a series of Jarlskog-like parameter. Finally, in Section 4.5 we present some numerical results on CP violation asymmetry with inputs of current neutrino oscillation data. We conclude in Section 4.6.

4.1 Introduction

The origin of finite but tiny neutrino masses is still unknown. The canonical seesaw mechanism [53, 125, 126, 127, 128, 129] and its numerous variations are proposed to solve this problem. The basic idea is that the small masses of left-handed neutrinos are attributed to the existence of much heavier right-handed Majorana neutrinos. The minimal seesaw model [155] is a simplified version of the canonical seesaw mechanism with only two right-handed neutrinos, which has been studied in depth [55]. See Sec. 2.1.4 in Chapter 2.

Neutrinos are usually considered as electrically neutral particles which do not participate in tree-level electromagnetic interactions. However, they may have electric and magnetic dipole moments appearing at loop level. A *transition* dipole moment between two different neutrino mass eigenstates can trigger a heavier neutrino radiatively decaying to a lighter neutrino through the release of a photon. In fact, if neutrinos are Majorana particles, the property that Majorana fermions are their own antiparticles implies that neutrinos have only a transitional component to their dipole moment [156].

A CP violating dipole moment has many interesting phenomenological applications. It may contribute to leptogenesis to explain the observed baryon-antibaryon asymmetry in our Universe [123]. It also provides a source of circular polarisation of photons in the sky for a suitable range of neutrino masses, [44].

In the present Chapter we apply the formalism introduced in Chapter 3. We focus on discussing CP violation in the neutrino dipole moment in right-handed neutrinos decays. We provide the one-loop calculation of the CP asymmetry of the neutrino transition dipole moment in full detail in the framework of the SM with the addition of $SU(2)_L$-singlet right-handed neutrinos.

4.2 One–loop Calculation of Neutrino Electromagnetic Form Factors

It is well known that the radiative decay can happen via one-loop corrections induced by SM weak interactions with SM particles in the loop.[1] We present below, the one-loop calculation of neutrino radiative decay $\nu_{\mathbf{i}} \to \nu_{\mathbf{f}}\, \gamma$ for massive neutrinos. The crucial operator for the charged-current interaction is,

$$\mathcal{L}_{\text{c.c.}} = \sum_{\alpha,m} \frac{g}{\sqrt{2}} \mathcal{U}_{\alpha m}\, \bar{\ell}_\alpha \gamma^\mu P_{\mathrm{L}} \nu_m W^-_\mu + \text{h.c.}\,, \tag{4.2.1}$$

where g is the electroweak (EW) gauge coupling constant, $\alpha = e,\ \mu,\ \tau$ represents the charged lepton flavours, m represents the three light neutrino mass eigenstates and $\mathcal{U}_{\alpha m}$ is the lepton flavour mixing matrix. In particular, $\nu_m = \nu_1\,, \nu_2\,, \nu_3$ corresponds to the three light neutrino mass eigenstates and $\nu_m = N_1, N_2, \ldots$ are the heavy neutrino mass eigenstates.

The one-loop Feynman diagrams for the radiative decay via the SM charged current interaction are shown in Fig. 4.1. The vertex functions of each proper vertex diagram in Fig.. 4.1are given by,

$$\begin{aligned}
\Gamma^{\mu,(1)}_{\mathbf{fi},\alpha} &= i\frac{eg^2}{2}\mathcal{U}_{\alpha\mathbf{i}}\mathcal{U}^*_{\alpha\mathbf{f}} \int d\mathbf{p} \frac{\gamma_\nu P_{\mathrm{L}}(\not{p}_{\mathbf{f}} - \not{p} + m_\alpha)\gamma^\mu(\not{p}_{\mathbf{i}} - \not{p} + m_\alpha)\gamma^\nu P_{\mathrm{L}}}{[(p_{\mathbf{f}} - p)^2 - m_\alpha^2][(p_{\mathbf{i}} - p)^2 - m_\alpha^2][p^2 - m_W^2]}\,,\\
\Gamma^{\mu,(2)}_{\mathbf{fi},\alpha} &= i\frac{eg^2}{2}\mathcal{U}_{\alpha\mathbf{i}}\mathcal{U}^*_{\alpha\mathbf{f}} \int d\mathbf{p} \frac{(m_{\mathbf{f}} P_{\mathrm{L}} - m_\alpha P_{\mathrm{R}})(\not{p}_{\mathbf{f}} - \not{p} + m_\alpha)\gamma^\mu(\not{p}_{\mathbf{i}} - \not{p} + m_\alpha)(m_\alpha P_{\mathrm{L}} - m_{\mathbf{i}} P_{\mathrm{R}})}{m_W^2[(p_{\mathbf{f}} - p)^2 - m_\alpha^2][(p_{\mathbf{i}} - p)^2 - m_\alpha^2][p^2 - m_W^2]}\,,\\
\Gamma^{\mu,(3)}_{\mathbf{fi},\alpha} &= i\frac{eg^2}{2}\mathcal{U}_{\alpha\mathbf{i}}\mathcal{U}^*_{\alpha\mathbf{f}} \int d\mathbf{p} \frac{\gamma_\rho P_{\mathrm{L}}(\not{p} + m_\alpha)\gamma_\nu P_{\mathrm{L}} V^{\mu\nu\rho}}{[(p_{\mathbf{f}} - p)^2 - m_W^2][(p_{\mathbf{i}} - p)^2 - m_W^2][p^2 - m_\alpha^2]}\,,\\
\Gamma^{\mu,(4)}_{\mathbf{fi},\alpha} &= i\frac{eg^2}{2}\mathcal{U}_{\alpha\mathbf{i}}\mathcal{U}^*_{\alpha\mathbf{f}} \int d\mathbf{p} \frac{(2p - p_{\mathbf{i}} - p_{\mathbf{f}})^\mu (m_{\mathbf{f}} P_{\mathrm{L}} - m_\alpha P_{\mathrm{R}})(\not{p} + m_\alpha)(m_\alpha P_{\mathrm{L}} - m_{\mathbf{i}} P_{\mathrm{R}})}{m_W^2[(p_{\mathbf{f}} - p)^2 - m_W^2][(p_{\mathbf{i}} - p)^2 - m_W^2][p^2 - m_\alpha^2]}\,,\\
\Gamma^{\mu,(5)}_{\mathbf{fi},\alpha} &= i\frac{eg^2}{2}\mathcal{U}_{\alpha\mathbf{i}}\mathcal{U}^*_{\alpha\mathbf{f}} \int d\mathbf{p} \frac{\gamma^\mu P_{\mathrm{L}}(\not{p} + m_\alpha)(m_\alpha P_{\mathrm{L}} - m_{\mathbf{i}} P_{\mathrm{R}})}{[(p_{\mathbf{f}} - p)^2 - m_W^2][(p_{\mathbf{i}} - p)^2 - m_W^2][p^2 - m_\alpha^2]}\,,\\
\Gamma^{\mu,(6)}_{\mathbf{fi},\alpha} &= i\frac{eg^2}{2}\mathcal{U}_{\alpha\mathbf{i}}\mathcal{U}^*_{\alpha\mathbf{f}} \int d\mathbf{p} \frac{(m_\alpha P_{\mathrm{R}} - m_{\mathbf{f}} P_{\mathrm{L}})(\not{p} + m_\alpha)\gamma^\mu P_{\mathrm{L}}}{[(p_{\mathbf{f}} - p)^2 - m_W^2][(p_{\mathbf{i}} - p)^2 - m_W^2][p^2 - m_\alpha^2]}\,,
\end{aligned} \tag{4.2.2}$$

---

[1] Specifically with charged lepton ℓ_α for $\alpha = e, \mu, \tau$ and the W boson.

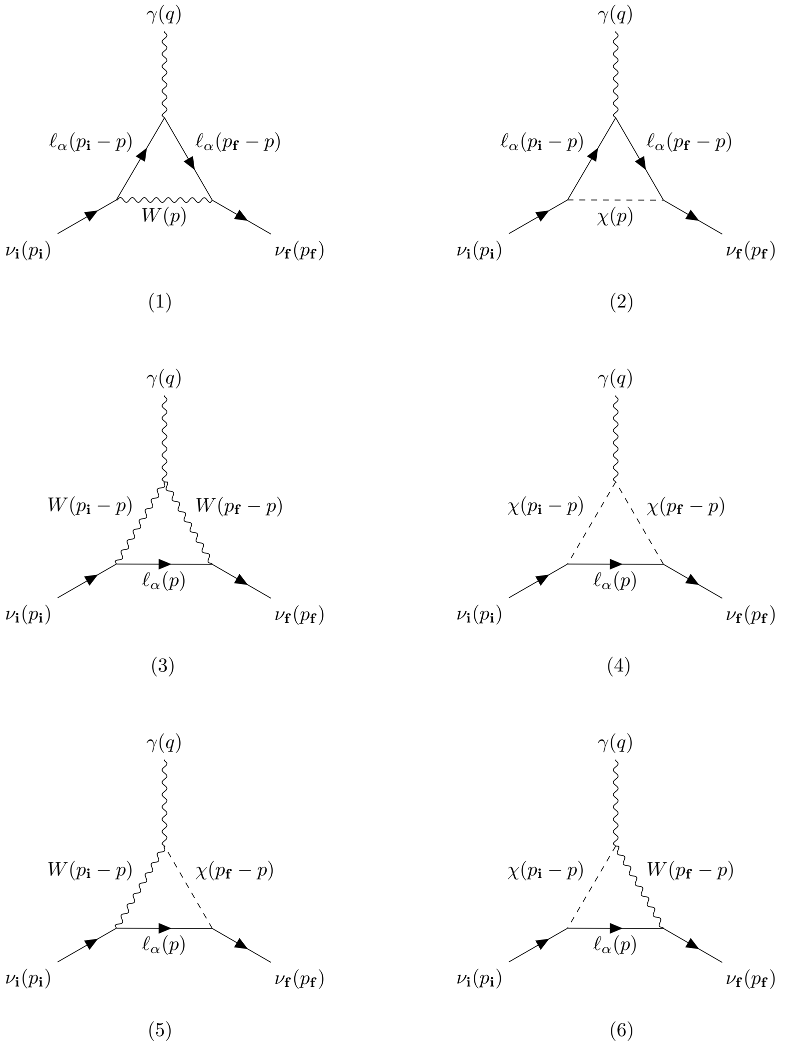

Figure 4.1: All Feynman diagrams contributing to the neutrino electromagnetic transition dipole moment, where χ is the charged Goldstone boson.

where $d\mathbf{p} \equiv \frac{\mathrm{d}^4 p}{(2\pi)^4}$ and,

$$V^{\mu\nu\rho} = g^{\mu\nu}(2p_\mathrm{i} - p - p_\mathrm{f})^\rho + g^{\rho\mu}(2p_\mathrm{f} - p - p_\mathrm{i})^\nu + g^{\nu\rho}(2p - p_\mathrm{i} - p_\mathrm{f})^\mu \,. \qquad (4.2.3)$$

A non-vanishing CP asymmetry requires two conditions; a CP contribution coming from coefficients of tree-level vertices and an imaginary part coming purely from loop kinematics [1]. The first condition is satisfied by the complex phases in the lepton flavor mixing matrix $\mathcal{U}$, this will be discussed in more detail in the following sections. In this section we focus on the second condition by computing the one-loop diagrams and deriving their imaginary part analytically.

We follow the standard procedure to integrate loop momenta with the help of Feynman parametrisation. Then, we apply the Gordon decomposition with chirality into consideration, and factorise dipole moment terms with coefficients as

$$\Gamma^{\mu}_{\mathbf{fi},\alpha} = \frac{eg^2}{4(4\pi)^2}\mathcal{U}_{\alpha\mathbf{i}}\mathcal{U}^*_{\alpha\mathbf{f}} i\sigma^{\mu\nu}q_{\nu}\int_0^1 \mathrm{d}x\mathrm{d}y\mathrm{d}z\,\delta(x+y+z-1)\sum_{k=1}^{6}\mathcal{P}^{(\mathrm{k})}, \quad (4.2.4)$$

where

$$\begin{aligned}
\mathcal{P}^{(1)} &= \frac{-2x(x+z)m_{\mathbf{i}}P_{\mathrm{R}} - 2x(x+y)m_{\mathbf{f}}P_{\mathrm{L}}}{\Delta_{\alpha W}(x,y,z)}, \\
\mathcal{P}^{(2)} &= \frac{[xzm_{\mathbf{f}}^2 - ((1-x)^2+xz)m_{\alpha}^2]m_{\mathbf{i}}P_{\mathrm{R}} + [xym_{\mathbf{i}}^2 - ((1-x)^2+xy)m_{\alpha}^2]m_{\mathbf{f}}P_{\mathrm{L}}}{m_W^2\Delta_{\alpha W}(x,y,z)}, \\
\mathcal{P}^{(3)} &= \frac{[(1-2x)z - 2(1-x)^2]m_{\mathbf{i}}P_{\mathrm{R}} + [(1-2x)y - 2(1-x)^2]m_{\mathbf{f}}P_{\mathrm{L}}}{\Delta_{W\alpha}(x,y,z)}, \\
\mathcal{P}^{(4)} &= \frac{[xzm_{\mathbf{f}}^2 - x(x+z)m_{\alpha}^2]m_{\mathbf{i}}P_{\mathrm{R}} + [xym_{\mathbf{i}}^2 - x(x+y)m_{\alpha}^2]m_{\mathbf{f}}P_{\mathrm{L}}}{m_W^2\Delta_{W\alpha}(x,y,z)}, \\
\mathcal{P}^{(5)} &= \frac{-zm_{\mathbf{i}}P_{\mathrm{R}}}{\Delta_{W\alpha}(x,y,z)}, \\
\mathcal{P}^{(6)} &= \frac{-ym_{\mathbf{f}}P_{\mathrm{L}}}{\Delta_{W\alpha}(x,y,z)}, \qquad (4.2.5)
\end{aligned}$$

and

$$\begin{aligned}
\Delta_{W\alpha}(x,y,z) &= m_W^2(1-x) + xm_{\alpha}^2 - x(ym_{\mathbf{i}}^2 + zm_{\mathbf{f}}^2) \\
\Delta_{\alpha W}(x,y,z) &= m_{\alpha}^2(1-x) + xm_W^2 - x(ym_{\mathbf{i}}^2 + zm_{\mathbf{f}}^2). \qquad (4.2.6)
\end{aligned}$$

Eq. (4.2.4) can be further simplified to

$$\Gamma^{\mu}_{\mathbf{fi},\alpha} = \frac{eG_{\mathrm{F}}}{4\sqrt{2}\pi^2}\mathcal{U}_{\alpha\mathbf{i}}\mathcal{U}^*_{\alpha\mathbf{f}} i\sigma^{\mu\nu}q_{\nu}(\mathcal{F}_{\mathbf{fi},\alpha}m_{\mathbf{i}}P_{\mathrm{R}} + \mathcal{F}_{\mathbf{if},\alpha}m_{\mathbf{f}}P_{\mathrm{L}}). \quad (4.2.7)$$

Here, $\mathcal{F}$ is derived from the sum of the integrals $\mathcal{P}^{(k)}$,

$$\begin{aligned}
\mathcal{F}_{\mathbf{fi},\alpha} = \int_0^1 \mathrm{d}x \Bigg\{ & \frac{\left(m_{\mathbf{i}}^2 - m_{\alpha}^2 - 2m_W^2\right)\left(m_{\alpha}^2 + m_{\mathbf{f}}^2x^2\right) + m_{\mathbf{fi},\alpha}^4 x}{\left(m_{\mathbf{i}}^2 - m_{\mathbf{f}}^2\right)^2 x} \log\left(\frac{m_{\alpha}^2 + \left(m_W^2 - m_{\alpha}^2 - m_{\mathbf{i}}^2\right)x + m_{\mathbf{i}}^2x^2}{m_{\alpha}^2 + \left(m_W^2 - m_{\alpha}^2 - m_{\mathbf{f}}^2\right)x + m_{\mathbf{f}}^2x^2}\right) \\
+ & \frac{\left(m_{\mathbf{i}}^2 - m_{\alpha}^2 - 2m_W^2\right)\left(m_{\alpha}^2 + m_{\mathbf{f}}^2(1-x)^2\right) + m_{\mathbf{fi},\alpha}^4(1-x)}{\left(m_{\mathbf{i}}^2 - m_{\mathbf{f}}^2\right)^2 x} \log\left(\frac{m_W^2 + \left(m_{\alpha}^2 - m_W^2 - m_{\mathbf{i}}^2\right)x + m_{\mathbf{i}}^2x^2}{m_W^2 + \left(m_{\alpha}^2 - m_W^2 - m_{\mathbf{f}}^2\right)x + m_{\mathbf{f}}^2x^2}\right)\Bigg\} \\
+ & \frac{m_{\mathbf{f}}^2 - m_{\alpha}^2 - 2m_W^2}{m_{\mathbf{i}}^2 - m_{\mathbf{f}}^2}, \qquad (4.2.8)
\end{aligned}$$

where $m^4_{\mathbf{fi},\alpha} = -(m^2_{\mathbf{i}} - m^2_\alpha - m^2_W)(m^2_{\mathbf{f}} + m^2_\alpha - 2m^2_W) + 2m^2_\alpha m^2_W$; the form of $\mathcal{F}_{\mathbf{if},\alpha}$ is obtained by exchanging $m_{\mathbf{i}}$ and $m_{\mathbf{f}}$. Therefore, we obtain the coefficients $f^{\rm L}_{\mathbf{fi}}$, $f^{\rm L}_{\mathbf{if}}$, $f^{\rm R}_{\mathbf{fi}}$ and $f^{\rm R}_{\mathbf{if}}$ as

$$\begin{aligned} f^{\rm L}_{\mathbf{fi}} &= \frac{eG_{\rm F}}{4\sqrt{2}\pi^2}\mathcal{U}_{\alpha\mathbf{i}}\mathcal{U}^*_{\alpha\mathbf{f}}\mathcal{F}_{\mathbf{if},\alpha}m_{\mathbf{f}}\,, \quad & f^{\rm R}_{\mathbf{fi}} &= \frac{eG_{\rm F}}{4\sqrt{2}\pi^2}\mathcal{U}_{\alpha\mathbf{i}}\mathcal{U}^*_{\alpha\mathbf{f}}\mathcal{F}_{\mathbf{fi},\alpha}m_{\mathbf{i}}\,, \\ f^{\rm L}_{\mathbf{if}} &= \frac{eG_{\rm F}}{4\sqrt{2}\pi^2}\mathcal{U}_{\alpha\mathbf{f}}\mathcal{U}^*_{\alpha\mathbf{i}}\mathcal{F}_{\mathbf{fi},\alpha}m_{\mathbf{i}}\,, \quad & f^{\rm R}_{\mathbf{if}} &= \frac{eG_{\rm F}}{4\sqrt{2}\pi^2}\mathcal{U}_{\alpha\mathbf{f}}\mathcal{U}^*_{\alpha\mathbf{i}}\mathcal{F}_{\mathbf{if},\alpha}m_{\mathbf{f}}\,, \end{aligned} \tag{4.2.9}$$

The integrals within $\mathcal{F}_{\mathbf{fi},\alpha}$ and $\mathcal{F}_{\mathbf{if},\alpha}$ in Eq. (4.2.8) can be further simplified in the limit of small neutrino masses, i.e., $m^2_{\mathbf{i}}, m^2_{\mathbf{f}} \ll m^2_\alpha, m^2_W$. In this case, the logarithm terms can be expanded in series of $m^2_{\mathbf{i}}$ and $m^2_{\mathbf{f}}$, and after a straightforward calculation, we prove that both $\mathcal{F}_{\mathbf{fi},\alpha}$ and $\mathcal{F}_{\mathbf{if},\alpha}$ are identical to $F(m^2_\alpha/m^2_W)$ in Eq. (3.3.3) which is the well-known result of loop factor obtained in the studies of neutrino dipole moment and radiative decays [69, 118].

4.2.1 Non-zero Imaginary Contribution

In this section, we outline how to obtain the non-zero imaginary parts for $\mathcal{F}_{\mathbf{fi},\alpha}$ and $\mathcal{F}_{\mathbf{if},\alpha}$ when neutrinos have large masses. From Eq. (4.2.8) we notice that the form of the integral include terms of the form $\int_0^1 {\rm d}x f(x)\log g(x)$, where $g(x)$ is not always positive in the domain $(0, 1)$. Instead, we can prove that there is an interval $(x_1, x_2) \subset (0, 1)$ where $g(x) < 0$ is satisfied, and x_1 and x_2 are solutions of $g(x) = 0$. The real and imaginary parts in the integration can then be split into,

$$\int_0^1 {\rm d}x f(x)\log g(x) = \int_0^1 {\rm d}x f(x)\log|g(x)| + i\pi\int_{x_1}^{x_2} {\rm d}x f(x)\,. \tag{4.2.10}$$

The imaginary part of $\int_{x_1}^{x_2} {\rm d}x f(x)$ can be obtained analytically [1].

$$\begin{aligned} {\rm Im}(\mathcal{F}_{\mathbf{fi},\alpha}) =& \pi\vartheta_{\mathbf{i}}\left\{\frac{m^2_{\mathbf{i}} - m^2_\alpha - 2m^2_W}{\left(m^2_{\mathbf{i}} - m^2_{\mathbf{f}}\right)^2}\left[-\mu^2_{\mathbf{i}}\frac{m^2_{\mathbf{f}}}{m^2_{\mathbf{i}}} + m^2_\alpha\log\left(\frac{m^2_{\mathbf{i}} + m^2_\alpha - m^2_W + \mu^2_{\mathbf{i}}}{m^2_{\mathbf{i}} + m^2_\alpha - m^2_W - \mu^2_{\mathbf{i}}}\right)\right]\right. \\ & \left. + \frac{\left(2m^2_{\mathbf{i}} - m^2_{\mathbf{f}} - m^2_\alpha - 2m^2_W\right)m^2_W}{\left(m^2_{\mathbf{i}} - m^2_{\mathbf{f}}\right)^2}\log\left(\frac{m^2_{\mathbf{i}} - m^2_\alpha + m^2_W + \mu^2_{\mathbf{i}}}{m^2_{\mathbf{i}} - m^2_\alpha + m^2_W - \mu^2_{\mathbf{i}}}\right)\right\} \end{aligned}$$

$$\begin{aligned} &+ \pi\vartheta_{\mathbf{f}}\left\{-\frac{m_{\mathbf{i}}^2 - m_\alpha^2 - 2m_W^2}{\left(m_{\mathbf{i}}^2 - m_{\mathbf{f}}^2\right)^2}\left[-\mu_{\mathbf{f}}^2 + m_\alpha^2 \log\left(\frac{m_{\mathbf{f}}^2 + m_\alpha^2 - m_W^2 + \mu_{\mathbf{f}}^2}{m_{\mathbf{f}}^2 + m_\alpha^2 - m_W^2 - \mu_{\mathbf{f}}^2}\right)\right]\right. \\ &\qquad \left. + \frac{\left(2m_{\mathbf{i}}^2 - m_{\mathbf{f}}^2 - m_\alpha^2 - 2m_W^2\right)m_W^2}{\left(m_{\mathbf{i}}^2 - m_{\mathbf{f}}^2\right)^2}\log\left(\frac{m_{\mathbf{f}}^2 - m_\alpha^2 + m_W^2 + \mu_{\mathbf{f}}^2}{m_{\mathbf{f}}^2 - m_\alpha^2 + m_W^2 - \mu_{\mathbf{f}}^2}\right)\right\}, \end{aligned} \tag{4.2.11}$$

where $\vartheta_{\mathbf{i},\mathbf{f}} = \vartheta(m_{\mathbf{i},\mathbf{f}} - m_W - m_\alpha)$ is the Heaviside step function, and

$$\begin{aligned} \mu_{\mathbf{i}}^2 &= \sqrt{m_{\mathbf{i}}^4 + m_\alpha^4 + m_W^4 - 2m_{\mathbf{i}}^2 m_\alpha^2 - 2m_{\mathbf{i}}^2 m_W^2 - 2m_\alpha^2 m_W^2}\,, \\ \mu_{\mathbf{f}}^2 &= \sqrt{m_{\mathbf{f}}^4 + m_\alpha^4 + m_W^4 - 2m_{\mathbf{f}}^2 m_\alpha^2 - 2m_{\mathbf{f}}^2 m_W^2 - 2m_\alpha^2 m_W^2}\,. \end{aligned} \tag{4.2.12}$$

Again, $\mathrm{Im}[\mathcal{F}_{\mathbf{if},\alpha}]$ is obtained from $\mathrm{Im}[\mathcal{F}_{\mathbf{fi},\alpha}]$ by exchanging $m_{\mathbf{i}}$ and $m_{\mathbf{f}}$. In order to generate a non-zero imaginary part in the loop integration, the threshold condition $m_{\mathbf{i}} > m_W + m_\alpha$ for the initial neutrino mass is required. In other words, the initial neutrino mass has to be larger than the sum of the W-boson and the charged lepton mass. There is a second contribution to the imaginary part of $\mathcal{F}_{\mathbf{fi},\alpha}$ if the neutrino in the final state satisfies the threshold condition, $m_{\mathbf{f}} > m_W + m_\alpha$. Due to sign difference it partly cancels with the first contribution.

4.3 *CP*-Asymmetry and Photon Polarisation

With the above results, we are now able to obtain the most general result of CP asymmetries in neutrino radiative decays. We will use the results of Section 3.2.1 in Chapter 3. Also see Ref. [1].

From Eq. 3.2.16, for Dirac neutrinos, we derive the CP asymmetry between $\nu_{\mathbf{i}} \to \nu_{\mathbf{f}}\gamma_+$ and $\bar{\nu}_{\mathbf{i}} \to \bar{\nu}_{\mathbf{f}}\gamma_-$ and that between $\nu_{\mathbf{i}} \to \nu_{\mathbf{f}}\gamma_-$ and $\bar{\nu}_{\mathbf{i}} \to \bar{\nu}_{\mathbf{f}}\gamma_+$. These are respectively given as,

$$\begin{aligned} \Delta_{CP,+}^{\mathrm{D}} &= \frac{-\sum_{\alpha,\beta}\mathcal{J}_{\alpha\beta}^{\mathbf{if}}\mathrm{Im}(\mathcal{F}_{\mathbf{if},\alpha}\mathcal{F}_{\mathbf{if},\beta}^*)m_{\mathbf{f}}^2}{\sum_{\alpha,\beta}\mathcal{R}_{\alpha\beta}^{\mathbf{if}}\left[\mathrm{Re}(\mathcal{F}_{\mathbf{fi},\alpha}\mathcal{F}_{\mathbf{fi},\beta}^*)m_{\mathbf{i}}^2 + \mathrm{Re}(\mathcal{F}_{\mathbf{if},\alpha}\mathcal{F}_{\mathbf{if},\beta}^*)m_{\mathbf{f}}^2\right]}\,, \\ \Delta_{CP,-}^{\mathrm{D}} &= \frac{-\sum_{\alpha,\beta}\mathcal{J}_{\alpha\beta}^{\mathbf{if}}\mathrm{Im}(\mathcal{F}_{\mathbf{fi},\alpha}\mathcal{F}_{\mathbf{fi},\beta}^*)m_{\mathbf{i}}^2}{\sum_{\alpha,\beta}\mathcal{R}_{\alpha\beta}^{\mathbf{if}}\left[\mathrm{Re}(\mathcal{F}_{\mathbf{fi},\alpha}\mathcal{F}_{\mathbf{fi},\beta}^*)m_{\mathbf{i}}^2 + \mathrm{Re}(\mathcal{F}_{\mathbf{if},\alpha}\mathcal{F}_{\mathbf{if},\beta}^*)m_{\mathbf{f}}^2\right]}\,. \end{aligned} \tag{4.3.1}$$

where α, β run for charged lepton flavours e, μ, τ and

$$\mathcal{J}^{\mathbf{if}}_{\alpha\beta} = \mathrm{Im}(\mathcal{U}_{\alpha\mathbf{i}}\mathcal{U}^*_{\alpha\mathbf{f}}\mathcal{U}^*_{\beta\mathbf{i}}\mathcal{U}_{\beta\mathbf{f}})\,, \qquad \mathcal{R}^{\mathbf{if}}_{\alpha\beta} = \mathrm{Re}(\mathcal{U}_{\alpha\mathbf{i}}\mathcal{U}^*_{\alpha\mathbf{f}}\mathcal{U}^*_{\beta\mathbf{i}}\mathcal{U}_{\beta\mathbf{f}})\,. \tag{4.3.2}$$

We have introduced a set of Jarlskog-like parameter $\mathcal{J}^{\mathbf{if}}_{\alpha\beta}$ to describe the CP violation from the vertex contribution. This parametrisation follows the famous definition of Jarlskog invariant used to describe CP violation in neutrino oscillations [157, 158]. The Jarlskog-like parameter are invariant under any phase rotation of charged leptons and neutrinos. If they vanish, no CP violation is generated in the neutrino transition dipole moment.

For Majorana neutrinos the relevant CP asymmetry, via Eq. (3.2.24) and Eq. (3.2.25), is given by,[1]

$$\Delta^{\mathrm{M}}_{+-} = \frac{\mathcal{J}^{\mathbf{if}}_{\alpha\beta}\left[\mathrm{Im}(\mathcal{F}_{\mathbf{fi},\alpha}\mathcal{F}^*_{\mathbf{fi},\beta})m^2_{\mathbf{i}} - \mathrm{Im}(\mathcal{F}_{\mathbf{if},\alpha}\mathcal{F}^*_{\mathbf{if},\beta})m^2_{\mathbf{f}}\right] - 2\mathcal{V}^{\mathbf{if}}_{\alpha\beta}\mathrm{Im}(\mathcal{F}_{\mathbf{fi},\alpha}\mathcal{F}^*_{\mathbf{if},\beta})m_{\mathbf{i}}m_{\mathbf{f}}}{\mathcal{R}^{\mathbf{if}}_{\alpha\beta}\left[\mathrm{Re}(\mathcal{F}_{\mathbf{fi},\alpha}\mathcal{F}^*_{\mathbf{fi},\beta})m^2_{\mathbf{i}} + \mathrm{Re}(\mathcal{F}_{\mathbf{if},\alpha}\mathcal{F}^*_{\mathbf{if},\beta})m^2_{\mathbf{f}}\right] - 2\mathcal{C}^{\mathbf{if}}_{\alpha\beta}\mathrm{Re}(\mathcal{F}_{\mathbf{fi},\alpha}\mathcal{F}^*_{\mathbf{if},\beta})m_{\mathbf{i}}m_{\mathbf{f}}}\,, \tag{4.3.3}$$

where

$$\mathcal{V}^{\mathbf{if}}_{\alpha\beta} = \mathrm{Im}(\mathcal{U}_{\alpha\mathbf{i}}\mathcal{U}^*_{\alpha\mathbf{f}}\mathcal{U}_{\beta\mathbf{i}}\mathcal{U}^*_{\beta\mathbf{f}})\,, \qquad \mathcal{C}^{\mathbf{if}}_{\alpha\beta} = \mathrm{Re}(\mathcal{U}_{\alpha\mathbf{i}}\mathcal{U}^*_{\alpha\mathbf{f}}\mathcal{U}_{\beta\mathbf{i}}\mathcal{U}^*_{\beta\mathbf{f}})\,. \tag{4.3.4}$$

$\mathcal{V}^{\mathbf{if}}_{\alpha\beta}$ is another type of Jarlskog-like parameter which appear only for Majorana neutrinos. It was first defined in the study of neutrino-antineutrino oscillations in the context of only three light neutrinos [158]. They are invariant under phase rotations for charged lepton but not for neutrinos.

4.4 *CP* violation in the Minimal Seesaw Model

In this section we consider the minimal seesaw model introduced in Sec. 2.1.4. We remind the reader that this mechanism consists of introducing only two RH neutrinos [155] in order to generate the tiny masses for LH neutrinos. We recall that the notation $\Delta_{CP} \equiv \Delta^M_{+-}$ for Majorana is used. We denote two RH neutrino mass

---

[1] We have to sum over lepton flavour $\alpha\,,\beta$ in the numerator and denominator.

eigenstates as N_I for $I = 1, 2$, with masses $M_1 < M_2$.

The minimal seesaw model predicts one massless neutrino $m_1 = 0$ in the normal mass ordering ($m_1 < m_2 < m_3$) and $m_3 = 0$ in the inverted mass ordering ($m_3 < m_2 < m_1$) schemes. In this work, we will only consider the the normal mass ordering. We take the best fit (in the 3σ ranges) of mass square differences in the normal ordering scheme [159].

$$\begin{aligned} m_2 &= \sqrt{\Delta m_{21}^2} = 8.60\ (8.24 \to 8.95)\ \text{meV}\,, \\ m_3 &= \sqrt{\Delta m_{31}^2} = 50.2\ (49.3 \to 51.2)\ \text{meV}\,. \end{aligned} \tag{4.4.1}$$

We recall once again the lepton charged-current interaction in Eq. (4.2.1). The three light neutrino mixing is represented by the first 3×3 submatrix of $\mathcal{U}$, i.e. $\mathcal{U}_{\alpha i}$ for $\alpha = e, \mu, \tau$ and $i = 1, 2, 3$. The parametrisation of this mixing submatrix is given in Eq. (2.1.17). The three mixing angles and the Dirac CP-violating phase for normal mass ordering are measured to be

$$\begin{aligned} \theta_{13} &= 8.61^\circ\ \ (8.22^\circ \to 8.99^\circ)\,, \\ \theta_{12} &= 33.82^\circ\ (31.61^\circ \to 36.27^\circ)\,, \\ \theta_{23} &= 48.3^\circ\ \ (40.8^\circ \to 51.3^\circ)\,, \\ \delta &= 222^\circ\ \ (141^\circ \to 370^\circ) \end{aligned} \tag{4.4.2}$$

at the best fit (in the 3σ ranges), where normal mass ordering has assumed. As we work in the minimal seesaw model, the lightest neutrino ν_1 is massless and only the second Majorana phase σ, in Eq. (2.1.17), is physical.

We account for the fraction of heavy neutrinos contributing to the flavour mixing $\mathcal{U}_{\alpha(I+3)}$, which we denote as $R_{\alpha I}$ from now on. $\mathcal{U}_{\alpha i}$ is only approximately equal to $U_{\alpha i}$, $\mathcal{U}_{\alpha i} = U_{\alpha i} + \mathcal{O}(RR^\dagger)$. $RR^\dagger$ is constrained to be maximally at milli-level [160]. Therefore, $\mathcal{U}_{\alpha i} \approx U_{\alpha i}$ is still a very good approximation. The charged-current interaction for leptons in the mass eigenstates is now written as

$$\mathcal{L}_{\text{c.c.}} = \sum_{\alpha=e,\mu,\tau} \frac{g}{\sqrt{2}}\, \bar{\ell}_\alpha \gamma^\mu P_{\text{L}} \Big(\sum_{i=1,2,3} U_{\alpha i}\nu_i + \sum_{I=1,2} R_{\alpha I} N_I \Big) W^-_\mu + \mathcal{O}(RR^\dagger) + \text{h.c.}. \tag{4.4.3}$$

The Yukawa coupling Y between lepton doublets and right-handed neutrinos are directly connected with R via $Y_{\alpha I} = R_{\alpha I} M_I / v_H$ [161]. The mixing between flavour states and heavy RH neutrinos are described by R. Following Casas-Ibarra parametrisation [162], R is given by

$$R_{\alpha I} \equiv \mathcal{U}_{\alpha(I+3)} = \sum_{i=1,2} U_{\alpha i} \Omega_{iI} \sqrt{\frac{m_{i+1}}{M_I}}\,. \tag{4.4.4}$$

Here, Ω is a 2×2 complex orthogonal matrix satisfying $\Omega^T \Omega = \Omega\Omega^T = 1$ and is parametrised as,

$$\Omega = \begin{pmatrix} \cos\omega & \sin\omega \\ -\zeta\sin\omega & \zeta\cos\omega \end{pmatrix}, \tag{4.4.5}$$

where ω is a complex parameter and $\zeta = \pm 1$. The two possible values of ζ correspond to two different distinct branches of Ω [163, 164]. In the whole model, three CP violating parameters are induced, δ, σ and $\text{Im}[\omega]$, if $\delta = 0$, $\sigma = 0$ or $\pi/2$ and $\text{Im}[\omega] = 0$, no CP violation can be generated.

The CP violation in the neutrino transition dipole moment can be checked by the study of the CP asymmetry of neutrino radiative decay. We can find three channels of interest, $\nu_i \to \nu_i\,\gamma$, $N_I \to \nu_i\,\gamma$ and $N_2 \to N_1\,\gamma$. For the first channel, since the light neutrinos have masses much smaller that the W boson, CP violation cannot be generated. The CP asymmetry for $N_I \to \nu_i\,\gamma$ is not negligible if $N_I$as a mass $M_I > m_W + m_e$. We sum over $i = 1, 2, 3$ together and calculate the overall CP asymmetry [cf. Eq. (4.3.3)]

$$\Delta_{CP}(N_I \to \nu\gamma) \quad = \quad \frac{\sum_i \sum_{\alpha,\beta} \mathcal{J}^{(I+3)i}_{\alpha\beta} \text{Im}(\mathcal{F}_{i(I+3),\alpha} \mathcal{F}^*_{i(I+3),\beta})}{\sum_i \sum_{\alpha,\beta} \mathcal{R}^{(I+3)i}_{\alpha\beta} \text{Re}(\mathcal{F}_{i(I+3),\alpha} \mathcal{F}^*_{i(I+3),\beta})}\,. \tag{4.4.6}$$

This parameter is tiny, numerically confirmed to be maximally $\lesssim 10^{-17}$. The reason why it is so small can be understood as follows. Since m_i is negligible, $\mathcal{F}_{i(I+3),\alpha} =$

$\mathcal{F}_{1(I+3),\alpha}$, and $\Delta_{CP}(N_I \to \nu\gamma) \propto \sum_{i,\alpha,\beta} \mathcal{J}_{\alpha\beta}^{(I+3)i} = \sum_{i,\alpha,\beta} \mathrm{Im}(\mathcal{U}_{\alpha(I+3)}\mathcal{U}_{\alpha i}^{*}\mathcal{U}_{\beta(I+3)}^{*}\mathcal{U}_{\beta i}) \approx \sum_{i,\alpha} \mathrm{Im}(\mathcal{U}_{\alpha(I+3)}\mathcal{U}_{\alpha(I+3)}^{*}) = 0$.

Finally, we focus on the CP asymmetry in $N_2 \to N_1\gamma$, which is given by

$$\Delta_{CP} = \frac{\mathcal{J}_{\alpha\beta}^{54}\left[\mathrm{Im}(\mathcal{F}_{45,\alpha}\mathcal{F}_{45,\beta}^{*})M_2^2 - \mathrm{Im}(\mathcal{F}_{54,\alpha}\mathcal{F}_{54,\beta}^{*})M_1^2\right] - 2\mathcal{V}_{\alpha\beta}^{54}\mathrm{Im}(\mathcal{F}_{45,\alpha}\mathcal{F}_{54,\beta}^{*})M_2M_1}{\mathcal{R}_{\alpha\beta}^{54}\left[\mathrm{Re}(\mathcal{F}_{45,\alpha}\mathcal{F}_{45,\beta}^{*})M_2^2 + \mathrm{Re}(\mathcal{F}_{54,\alpha}\mathcal{F}_{54,\beta}^{*})M_1^2\right] - 2\mathcal{C}_{\alpha\beta}^{54}\mathrm{Re}(\mathcal{F}_{45,\alpha}\mathcal{F}_{54,\beta}^{*})M_2M_1}. \tag{4.4.7}$$

Here, $\mathcal{C}_{\alpha\beta}^{\mathbf{if}}$ and $\mathcal{V}_{\alpha\beta}^{\mathbf{if}}$ were defined in Eq. (4.3.4) and the Jarlskog-like parameter are given by $\mathcal{J}_{\alpha\beta}^{54} = \mathrm{Im}(R_{\alpha 2}R_{\alpha 1}^{*}R_{\beta 2}^{*}R_{\beta 1})$ and $\mathcal{V}_{\alpha\beta}^{54} = \mathrm{Im}(R_{\alpha 2}R_{\alpha 1}^{*}R_{\beta 2}R_{\beta 1}^{*})$.

4.5 Neutrino Phenomenology

In the present section we discuss the behaviour of the CP asymmetry in $N_2 \to N_1\gamma$ as a function of the RH neutrino mass M_2, see Fig. 4.2. We notice that the CP asymmetry of this channel is much larger than that in $N_I \to \nu\gamma$. In this figure, we vary M_2 from 0.1 to 10 TeV and consider three benchmark scenarios where the mass ratio M_1/M_2 is fixed to 0.2, 0.5 and 0.8 respectively. In all plots, we fix $\zeta = 1$ and the Majorana phase $\sigma = \pi/2$. Therefore, no Majorana-type CP violation is induced. We use the best-fit oscillation data as inputs which include a large CP violating value for δ. In the top panel, we fix ω to be real, $\omega = 5$. Therefore, δ is the only source of CP violation. We note that a large CP asymmetry ratio $|\Delta_{CP}| \sim 10^{-5}$-$10^{-3}$ is generated. Peaks of $|\Delta_{CP}|$ are generated due to the enhancement in the log term of $\mathrm{Im}(\mathcal{F}_{\mathbf{fi},\alpha})$ around $M_2 \approx m_W$ (cf. Eq.(4.2.11)). Sharp changes refer to cancellations occurring in Δ_{CP} due to the selected values of inputs. In the bottom panel, $\omega = 5-5i$, both δ and ω contribute to the CP violation. The constraints on $|RR^{\dagger}|$ from the non-unitarity effect has been included [160].

We also show the branching ratio $\mathcal{B}(N_2 \to N_1\gamma) = \Gamma(N_2 \to N_1\gamma)/\Gamma_{N_2}$. In the total decay width Γ_{N_2}, we include five main decay channels $N_2 \to \ell^- W_{L,T}^{+}$, $\nu Z_{L,T}$ and νH [165]. Although the CP asymmetry is large, the branching ratio is suppressed as shown in the right panel of Fig. 4.2, leading to very small $\Delta_{CP} \times \mathcal{B}$.

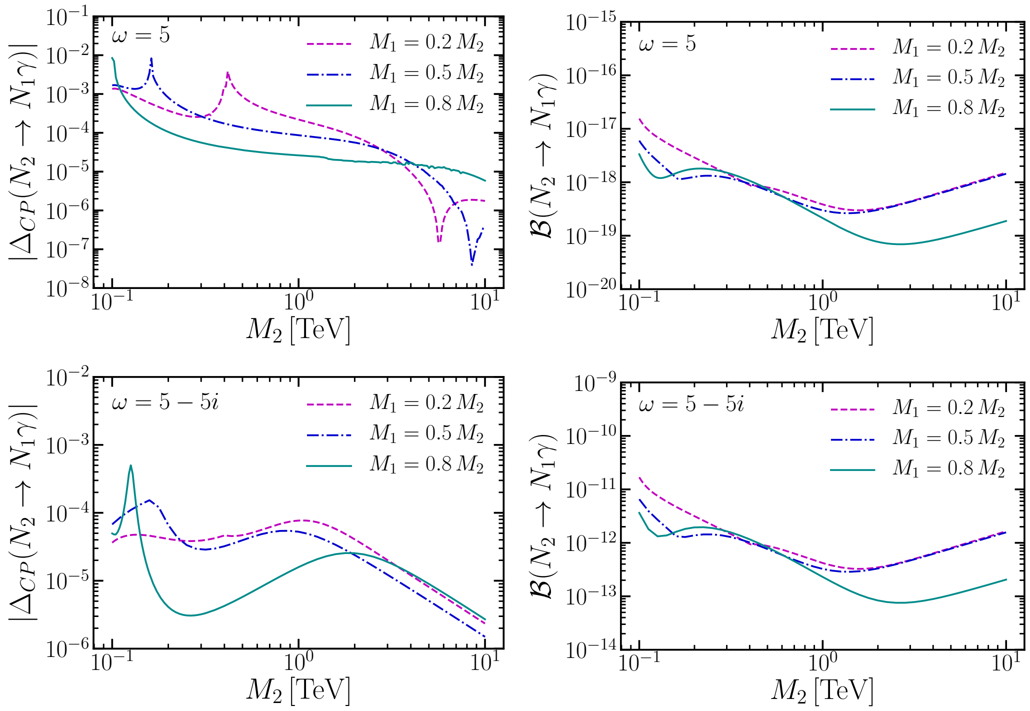

Figure 4.2: The CP asymmetry (left panel) and branching ratio (right panel) for the radiative decay process $N_2 \to N_1\gamma$ as a function of the heavy neutrino mass M_2. Four different benchmarks for the lightest right-handed neutrino $M_1 = 0.2M_2, 0.5M_2, 0.8M_2$ are considered as per the respective plot legends. Values of ω are fixed at $\omega = 5$ (top panel) and $5 - 5i$ (bottom panel), respectively. In all cases, we use the best-fit oscillation data as inputs while we set $\zeta = 1$ with a Majorana phase $\sigma = \pi/2$.

We note that there is particularly interesting phenomenology for $\omega = 5 - 5i$ as the branching ratio is greatly enhanced when assigning an imaginary part to ω. This is because the mixing R is enhanced by $\sin\omega$ and $\cos\omega$, which are both $\sim e^{|\mathrm{Im}[\omega]|}$. One can further increase the branching ratio to be much larger than 10^{-13} by enlarging the imaginary part of ω, hence the combination $\Delta_{CP} \times \mathcal{B}$ is also enhanced. Another feature of the right panels is that, in spite of the different orders of magnitude, the shape profiles of the curves are almost the same between $\omega = 5$ and $5 - 5i$. This is because the inclusion of an imaginary part for ω simply changes the size of $R_{\alpha I}$ but rarely changes the correlation between the decay width and right-handed neutrino masses.

In Fig. 4.3 we show a numerical scan performed for M_2 in the same range. We sample M_2 logarithmically in the range [0.1, 10] TeV and the ratio M_1/M_2 in the range [0.1, 1). The blue points refer to purely real ω randomly sampled from $[0, 2\pi)$. In this case, only two of the CP violating phases δ and σ contribute to the CP violation. The CP asymmetry Δ_{CP} shows a roughly linear correlation with M_2^{-1}. Most points of Δ_{CP} are located in the regimes $(10^{-3},\ 10^{-5})$ for $M_2 \simeq 0.1$ TeV, $(10^{-4},\ 10^{-6})$ for $M_2 \simeq 1$ TeV and $(10^{-5},\ 10^{-7})$ for $M_2 \simeq 10$ TeV. However, the branching ratio of the decay is tiny, between $(10^{-20}, 10^{-15})$, which makes the CP asymmetry unobservable in experiments. For the red points, we allow an imaginary part for ω as well, namely, $\mathrm{Im}[\omega] \in [-5, 5]$. A CP asymmetry of order one is then easily achieved. The branching ratio of the radiative decay can maximally reach $\sim 10^{-11}$. We have also checked that the combination $\Delta_{CP} \times \mathcal{B}$ can maximally reach 4×10^{-15}. Note that considering a larger imaginary part of ω could further enhance the branching ratio and $\Delta_{CP} \times \mathcal{B}$. However, as this process happens at one loop and there are constraints on the non-unitary effect, the branching ratio is always suppressed by $(16\pi^2)^{-2}|RR^\dagger|^2/|RR^\dagger|$. By taking $RR^\dagger \sim 10^{-3}$, we obtain a branching ratio which maximally reaches $\sim 10^{-7}$ and is therefore challenging to probe in future experiments.

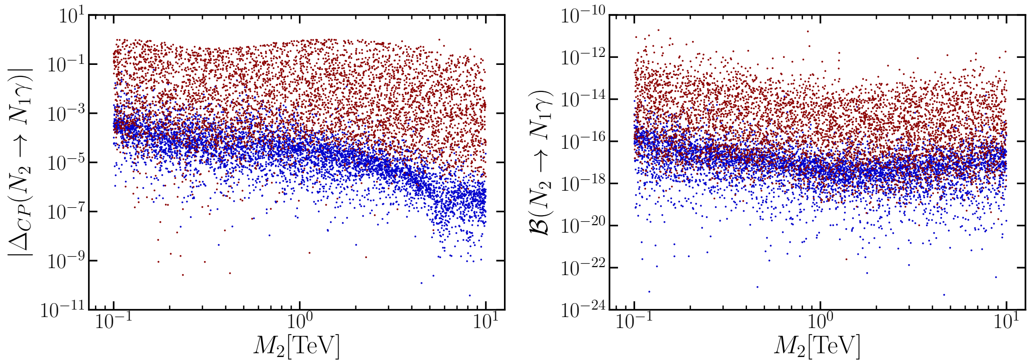

Figure 4.3: The CP asymmetry parameter Δ_{CP} (left) and branching ratio (right) scanned in the region M_2 in $[0.1, 10]$ TeV and the ratio M_1/M_2 in $[0.1,\ 1)$, where both masses are scanned in the logarithmic scale. The red region refers to $\omega = [0, 2\pi] + i[-5, 5]$ while the blue region is the smaller $\omega = [0, 2\pi]$. All oscillation parameters are scanned in the 3σ ranges, $\omega = [0, 2\pi]$ and $\zeta = +1$ are used. The scan performed for the $\zeta = -1$ branch gives the same distribution and is thus omitted.

4.6 Conclusion

We study the CP violation in the neutrino electromagnetic dipole moment. A full one-loop calculation of the transition dipole moment is performed in the context of the Standard Model with an arbitrary number of right-handed singlet neutrinos. The CP asymmetry is analytically derived in terms of the leptonic mixing matrix accounting for heavy neutrino mass eigenstates. A detailed explanation of how to generate a non-vanishing CP asymmetry in the neutrino transition dipole moment is provided. This requires a threshold condition for the initial neutrino mass being larger than the sum of W-boson mass and the charged leptons running in the loop and a CP violating phase in the lepton flavour mixing matrix. The threshold condition is necessary to generate a non-zero imaginary part for the loop function. An analytical formulation of this loop integral imaginary component is then derived. The lepton flavour mixing for vertex contributions has been parametrised in terms of Jarlskog-like parameter. For Majorana particles, the CP asymmetry is identical to the asymmetry of circularly-polarised photons released from the radiative decay.

The formulation is then applied to a minimal seesaw model where two right-handed neutrinos N_1 and N_2 are introduced with the mass ordering $M_1 < M_2$. A complete study of CP asymmetry in all radiative decay channels was performed, where the mass range 0.1 TeV $< M_2 <$ 10 TeV is considered. The CP asymmetry in $N_{1,2} \to \nu\gamma$ is very small, maximally reaching 10^{-17}. In the $N_2 \to N_1\gamma$ channel, the CP asymmetry is significantly enhanced, with Δ_{CP} achieving 10^{-5}-10^{-3}, even with the Dirac phase δ being the only source of CP violation. There is a significant correlation between the CP violation in radiative decay and that coming from oscillation experiments. We performed a parameter scan of the CP asymmetry with oscillation data in 3σ ranges taken as inputs and found that the CP asymmetry can maximally reach order one.

Chapter 5

Change in the Polarisation of Gamma Rays

The measurement of polarisation of light is a cornerstone of modern astrophysics. Observations of both linear and circular polarisation have been used to understand the nature of astrophysical sources emitting electromagnetic radiation [43, 166, 167]. Hence, it is important to describe any possible polarisation changes of gamma-rays propagation due to fundamental interactions. This change can be understood as follows. Photons have two helicity states. Each of them are associated with one circular polarisation state (refer to as LH and RH in the following); if one helicity state dominates over the other a net circular polarisation is realised. If however the number of photons with ± helicity state is the same, there is no net circular polarisation. The photon interactions which change the number of photon polarisation states can thus change the fraction of net circular polarisation. They can also change the properties of linearly polarised light.

So far the literature has focused on the polarisation of visible light and mm radiation (see Chapter 2), and there are some efforts to describe the polarisation of X-ray radiation [43]. However, such formalism breaks down for high–energy gamma–rays polarisation. Therefore, in this chapter we will describe how the polarisation of these high energy ($\sqrt{s} \geq m_e$) electromagnetic signals changes as they propagate through space. We derive the formalism for such studies assuming generic interactions and eventually focus on Compton interactions.

5.1 Introduction

Electromagnetic interactions at high energy ($\sqrt{s} > m_e$) are described by the Compton scattering cross section in the high energy regime (which is different from the Klein-Nishima regime) and critically includes helicity-flip processes such as $e^-_R\gamma_L \to e^-_L\gamma_R$. In this regime, the (classical) radiative transfer approach is no longer appropriate since it assumes that the scattering only changes the direction of the outgoing photons and ignores significant transfer of energy or flip of the helicity configuration of the particles involved. The QFT approach that Kosowsky developed is more suited to describe the nature of the interactions. Thus, the correct formalism has to be a mixed of the two; i.e., one needs to embed the QFT formulation in a radiative transfer framework. Here we develop such a formalism and show how to recast Chandrasekhar's low energy **P**–matrix in terms of the (QFT) scattering matrix amplitude elements, thus addressing an important gap in the literature. This formalism is general enough to be applied in a different context, including for example to describe the evolution of the Stokes parameters after the light scatters off generic new particles.

5.2 High Energy Description of Polarisation of Gamma Rays

One can generalise the geometrical formalism proposed by Chandrasekhar and understand it in a more fundamental way by using Quantum Field Theory (QFT). In the following, we show how to relate the Stokes parameters to the scattering matrix amplitude $\mathcal{M}$ associated with microscopic interactions.

5.2.1 Generalisation of the Phase–Matrix

Now that we have defined the Stokes operators, we can relate them to scattering matrix amplitudes. In the remainder of the paper we will focus on Compton interactions but we are keeping the formalism general enough so that it can be applied to any light scattering process at any energy, that is $\mathcal{M}(X\,\gamma_i \rightarrow X\,\gamma_{i'}) \equiv M_{i'i}$, with X being the particle the photon scatters off (e.g. an electron in the case of Thomson or Compton scatterings). The outgoing polarisation state ($|\epsilon^{(2)}_{i'}\rangle$) is related to the initial polarisation state ($|\epsilon^{(1)}_{i}\rangle$) by the matrix element $M_{i'i} \equiv \langle\epsilon^{(2)}_{i'}|\epsilon^{(1)}_{i}\rangle$ where i, i' refers to the (l, r) or the ± basis, leading to

$$|\epsilon^{(2)}_{j'}\rangle\langle\epsilon^{(2)}_{i'}| = M_{i'i}\, M^*_{j'j}\, |\epsilon^{(1)}_{j}\rangle\langle\epsilon^{(1)}_{i}|\,. \tag{5.2.1}$$

Using Eq.(2.3.12) and Eq.(5.2.1), we then obtain

$$\hat{S}^{(2)} = \mathbf{W}\, |\epsilon^{(2)}_{j'}\rangle\langle\epsilon^{(2)}_{i'}| = \mathbf{W}\, M_{i'i}\, M^*_{j'j} |\,\epsilon^{(1)}_{j}\rangle\langle\epsilon^{(1)}_{i}| \;=\; \mathbf{W}\, M_{i'i}\, M^*_{j'j}\, \mathbf{W}^{-1}\; \hat{S}^{(1)}, \tag{5.2.2}$$

which we will write in the following as

$$\hat{S}^{(2)} = \mathbf{A'}_{i'ij'j}\; \hat{S}^{(1)} \tag{5.2.3}$$

with $i'ij'j$ indices that refer to the different polarisation of the photons in the initial and final states. We can now express the $\mathbf{A'}_{i'ij'j}$ matrix in the (l, r) basis, that is

$$\begin{bmatrix}\hat{I}\\ \hat{Q}\\ \hat{U}\\ \hat{V}\end{bmatrix}^{(2)} = \underbrace{\mathbf{W}\begin{bmatrix} M_{ll}M^*_{ll} & M_{ll}M^*_{lr} & M_{lr}M^*_{ll} & M_{lr}M^*_{lr}\\ M_{ll}M^*_{rl} & M_{ll}M^*_{rr} & M_{lr}M^*_{rl} & M_{lr}M^*_{rr}\\ M_{rl}M^*_{ll} & M_{rl}M^*_{lr} & M_{rr}M^*_{ll} & M_{rr}M^*_{lr}\\ M_{rl}M^*_{rl} & M_{rl}M^*_{rr} & M_{rr}M^*_{rl} & M_{rr}M^*_{rr}\end{bmatrix}\mathbf{W}^{-1}}_{\mathbf{A'}} \begin{bmatrix}\hat{I}\\ \hat{Q}\\ \hat{U}\\ \hat{V}\end{bmatrix}^{(1)} . \tag{5.2.4}$$

or, in the ± basis,

$$\begin{bmatrix}\hat{I}\\ \hat{Q}\\ \hat{U}\\ \hat{V}\end{bmatrix}^{(2)} = \underbrace{\mathbf{W}\begin{bmatrix} M_{++}M^*_{++} & M_{+-}M^*_{++} & M_{++}M^*_{+-} & M_{+-}M^*_{+-}\\ M_{-+}M^*_{++} & M_{--}M^*_{++} & M_{-+}M^*_{+-} & M_{--}M^*_{+-}\\ M_{++}M^*_{-+} & M_{+-}M^*_{-+} & M_{++}M^*_{--} & M_{+-}M^*_{--}\\ M_{-+}M^*_{-+} & M_{--}M^*_{-+} & M_{-+}M^*_{--} & M_{--}M^*_{--}\end{bmatrix}\mathbf{W}^{-1}}_{\mathbf{A}'} \begin{bmatrix}\hat{I}\\ \hat{Q}\\ \hat{U}\\ \hat{V}\end{bmatrix}^{(1)} . \tag{5.2.5}$$

5.2.2 A'-Matrix Definition in the ± Basis

Replacing the **W** matrix by Eq. (2.3.14), we find that the $\mathbf{A}'$–matrix takes the following form in the ± basis

$$\begin{bmatrix}\hat{I}\\ \hat{Q}\\ \hat{U}\\ \hat{V}\end{bmatrix}^{(2)} = \begin{bmatrix} \mathbf{A}'_{11} & \mathbf{A}'_{12} & \mathbf{A}'_{13} & \mathbf{A}'_{14}\\ \mathbf{A}'_{21} & \mathbf{A}'_{22} & \mathbf{A}'_{23} & \mathbf{A}'_{24}\\ \mathbf{A}'_{31} & \mathbf{A}'_{32} & \mathbf{A}'_{33} & \mathbf{A}'_{34}\\ \mathbf{A}'_{41} & \mathbf{A}'_{42} & \mathbf{A}'_{43} & \mathbf{A}'_{44}\end{bmatrix} \begin{bmatrix}\hat{I}\\ \hat{Q}\\ \hat{U}\\ \hat{V}\end{bmatrix}^{(1)} , \tag{5.2.6}$$

with

$$\begin{aligned}
\mathbf{A}'_{11} &= \tfrac{1}{2}\Big(|M_{++}|^2 + |M_{+-}|^2 + |M_{-+}|^2 + |M_{--}|^2\Big)\\
\mathbf{A}'_{31} &= \mathrm{Im}(M_{+-}M^*_{--} + M_{++}M^*_{-+})\\
\mathbf{A}'_{12} &= -\mathrm{Re}\,(M_{--}M^*_{-+} + M_{+-}M^*_{++})\\
\mathbf{A}'_{32} &= \mathrm{Im}(M_{--}M^*_{++} + M_{-+}M^*_{+-})\\
\mathbf{A}'_{13} &= \mathrm{Im}\,(M_{--}M^*_{-+} + M_{+-}M^*_{++})\\
\mathbf{A}'_{33} &= \mathrm{Re}\,(M_{++}M^*_{--} - M_{+-}M^*_{-+})\\
\mathbf{A}'_{14} &= \tfrac{1}{2}\Big(|M_{++}|^2 + |M_{-+}|^2 - |M_{+-}|^2 - |M_{--}|^2\Big)\\
\mathbf{A}'_{34} &= \mathrm{Im}(M_{++}M^*_{-+} + M_{--}M^*_{+-})\\
\mathbf{A}'_{21} &= -\mathrm{Re}\,(M_{++}M^*_{-+} + M_{--}M^*_{+-})\\
\mathbf{A}'_{41} &= \tfrac{1}{2}\Big(|M_{++}|^2 + |M_{+-}|^2 - |M_{-+}|^2 - |M_{--}|^2\Big)
\end{aligned}$$

$$\begin{aligned}
\mathbf{A'}_{22} &= \mathrm{Re}\,(M_{--}M^{*}_{++} + M_{-+}M^{*}_{+-}) \\
\mathbf{A'}_{42} &= \mathrm{Re}\,(M_{--}M^{*}_{-+} - M_{+-}M^{*}_{++}) \\
\mathbf{A'}_{23} &= \mathrm{Im}(M_{++}M^{*}_{--} + M_{-+}M^{*}_{+-}) \\
\mathbf{A'}_{43} &= \mathrm{Im}(M_{-+}M^{*}_{--} + M_{+-}M^{*}_{++}) \\
\mathbf{A'}_{24} &= \mathrm{Re}\,(M_{--}M^{*}_{+-} - M_{++}M^{*}_{-+}) \\
\mathbf{A'}_{44} &= \tfrac{1}{2}\Big(|M_{++}|^2 + |M_{--}|^2 - |M_{+-}|^2 - |M_{-+}|^2\Big)
\end{aligned} \tag{5.2.7}$$

5.2.3 A'-matrix Definition in (l, r) Basis

In the (l, r) basis, the $\mathbf{A'}$–matrix reads as

$$\begin{aligned}
\mathbf{A'}_{11} &= \tfrac{1}{2}\Big(|M_{ll}|^2 + |M_{lr}|^2 + |M_{rl}|^2 + |M_{rr}|^2\Big) & \mathbf{A'}_{31} &= \mathrm{Re}(M_{ll}M^{*}_{rl} + M_{lr}M^{*}_{rr}) \\
\mathbf{A'}_{12} &= \tfrac{1}{2}\Big(|M_{ll}|^2 - |M_{lr}|^2 + |M_{rl}|^2 - |M_{rr}|^2\Big) & \mathbf{A'}_{32} &= \mathrm{Re}(M_{ll}M^{*}_{rl} - M_{lr}M^{*}_{rr}) \\
\mathbf{A'}_{13} &= \mathrm{Re}\,(M_{ll}M^{*}_{lr} + M_{rl}M^{*}_{rr}) & \mathbf{A'}_{33} &= \mathrm{Re}\,(M_{ll}M^{*}_{rr} - M_{lr}M^{*}_{rl}) \\
\mathbf{A'}_{14} &= -\mathrm{Im}(M_{ll}M^{*}_{lr} + M_{rl}M^{*}_{rr}) & \mathbf{A'}_{34} &= -\mathrm{Im}(M_{ll}M^{*}_{rr} + M_{rl}M^{*}_{lr}) \\
\mathbf{A'}_{21} &= \tfrac{1}{2}\Big(|M_{ll}|^2 + |M_{lr}|^2 - |M_{rl}|^2 - |M_{rr}|^2\Big) & \mathbf{A'}_{41} &= \mathrm{Im}(M_{ll}M^{*}_{rl} + M_{lr}M^{*}_{rr}) \\
\mathbf{A'}_{22} &= \tfrac{1}{2}\Big(|M_{ll}|^2 - |M_{lr}|^2 - |M_{rl}|^2 + |M_{rr}|^2\Big) & \mathbf{A'}_{42} &= \mathrm{Im}(M_{ll}M^{*}_{rl} + M_{rr}M^{*}_{lr}) \\
\mathbf{A'}_{23} &= \mathrm{Re}(M_{ll}M^{*}_{lr} - M_{rl}M^{*}_{rr}) & \mathbf{A'}_{43} &= \mathrm{Im}(M_{ll}M^{*}_{rr} + M_{lr}M^{*}_{rl}) \\
\mathbf{A'}_{24} &= -\mathrm{Im}\,(M_{ll}M^{*}_{lr} - M_{rl}M^{*}_{rr}) & \mathbf{A'}_{44} &= \mathrm{Re}(M_{rr}M^{*}_{ll} - M_{rl}M^{*}_{lr})\,.
\end{aligned} \tag{5.2.8}$$

5.2.4 Relationship Between the Initial and Final Chandrasekhar Stokes Parameters

To compare our results with that of Chandrasekhar, one needs to perform the following transformation

$$\begin{bmatrix} \hat{I}_l \\ \hat{I}_r \\ \hat{U} \\ \hat{V} \end{bmatrix} = \mathbf{C} \begin{bmatrix} \hat{I} \\ \hat{Q} \\ \hat{U} \\ \hat{V} \end{bmatrix} \text{, with } \mathbf{C} = \begin{bmatrix} \frac{1}{2} & \frac{1}{2} & 0 & 0 \\ \frac{1}{2} & -\frac{1}{2} & 0 & 0 \\ 0 & 0 & 1 & 0 \\ 0 & 0 & 0 & 1 \end{bmatrix} . \tag{5.2.9}$$

This transformation is only valid in the (l, r) basis where we can decompose the intensity I in terms of I_l and I_r. Using this transformation, the change in the modified Stokes parameters after scattering reads as

$$\begin{bmatrix} \hat{I}_l \\ \hat{I}_r \\ \hat{U} \\ \hat{V} \end{bmatrix}^{(2)} = \underbrace{\mathbf{C}\ \mathbf{A}'\ \mathbf{C}^{-1}}_{\mathbf{A}} \begin{bmatrix} \hat{I}_l \\ \hat{I}_r \\ \hat{U} \\ \hat{V} \end{bmatrix}^{(1)} \tag{5.2.10}$$

with

$$\mathbf{A} = \begin{bmatrix} M_{ll}M_{ll}^* & M_{lr}M_{lr}^* & \mathbf{A}_{13} & \mathbf{A}_{14} \\ M_{rl}M_{rl}^* & M_{rr}M_{rr}^* & \mathbf{A}_{23} & \mathbf{A}_{24} \\ M_{ll}M_{rl}^* + M_{rl}M_{ll}^* & M_{lr}M_{ll}^* + M_{rr}M_{lr}^* & \mathbf{A}_{33} & \mathbf{A}_{34} \\ -i(M_{ll}M_{rl}^* - M_{rl}M_{ll}^*) & -i(M_{lr}M_{ll}^* - M_{rr}M_{lr}^*) & \mathbf{A}_{43} & \mathbf{A}_{44} \end{bmatrix} \tag{5.2.11}$$

and

$$\begin{aligned}
\mathbf{A}_{13} &= \frac{1}{2}(M_{ll}M_{lr}^* + M_{lr}M_{ll}^*) \\
\mathbf{A}_{14} &= \frac{1}{2}i(M_{ll}M_{lr}^* - M_{lr}M_{ll}^*) \\
\mathbf{A}_{23} &= \frac{1}{2}(M_{rl}M_{rr}^* + M_{rr}M_{rl}^*) \\
\mathbf{A}_{24} &= \frac{1}{2}i(M_{rl}M_{rr}^* - M_{rr}M_{rl}^*) \\
\mathbf{A}_{33} &= \frac{1}{2}(M_{ll}M_{rr}^* + M_{lr}M_{rl}^* + M_{rl}M_{lr}^* + M_{rr}M_{ll}^*) \,, \\
\mathbf{A}_{34} &= \frac{1}{2}i(M_{ll}M_{rr}^* - M_{lr}M_{rl}^* + M_{rl}M_{lr}^* - M_{rr}M_{ll}^*) \,, \\
\mathbf{A}_{43} &= -\frac{1}{2}i(M_{ll}M_{rr}^* + M_{lr}M_{rl}^* - M_{rl}M_{lr}^* - M_{rr}M_{ll}^*) \,, \\
\mathbf{A}_{44} &= \frac{1}{2}(M_{ll}M_{rr}^* - M_{lr}M_{rl}^* - M_{rl}M_{lr}^* + M_{rr}M_{ll}^*) \,.
\end{aligned} \tag{5.2.12}$$

We note that, at low energy, the above expression can be used to derive both **P** and **R**–matrices, depending on the choice of kinematics. Using the rest frame kinematics leads to the expression of the **R**–matrix while the fixed frame kinematics (see Eq. (5.2.10)) leads to the **P**–matrix. Finally we have checked that these expressions are consistent with Chandrasekhar's definitions of the **R** and **P** matrices in the case of Thomson interactions in Appendix C.4.

5.3 Compton Interactions

We are now equipped to determine the change in polarisation of γ-rays after they scatter off electrons, whatever the energy regime (and in particular when the initial energy exceeds the electron mass, that is $\sqrt{s} > m_e$). Our formalism is general enough to study dark photon scattering off electrons or photon scattering off Beyond Standard Model particles. Unlike Thomson interactions which do not flip the spin of the electron, Compton interactions can affect both the photon polarisation and the electron spin configuration due to the energies at play. As a result, we expect the relation between the outgoing and incoming Stokes parameters to be much more complex than in the case of Thomson interactions, and to depend on both the momentum and energy of the incoming particles.

We note that other works have attempted to describe the change in linear polarisation of high energy gamma-rays after scattering. However there are a number of issues. For example, Ref. [168] uses Chandrasekhar's geometrical approach to describe the scattering of X-rays and gamma–rays but the geometrical approach does not capture the complexity of Compton scattering interactions at high energy (in particular the presence of helicity-flip processes). The Klein—Nishina formula has also been used in [169] to describe the linear polarisation of high energy gamma-rays but it is only valid when the electrons are strictly at rest and thus does only apply in very specific circumstances. Finally, other works have used the photon density matrix to describe the process of polarisation transfer [170, 171, 172] but have not folded in the information about the cross section which is critical at high energy ($\sqrt{s} > m_e$). The formalism that we have developed thus aims to provide a consistent treatment of polarisation after scattering, whatever the energy regime one is considering.

In the previous section, we have defined the **R**–matrix in the (l, r) basis and showed how to convert it in the ± basis. Defining the **R**–matrix in the (l, r) basis was straightforward because at low energy, the scattering only induces a change in the photon direction (i.e. $I_l^{(2)} = \cos^2\theta \, I_l^{(1)}$ and $I_r^{(2)} = I_r^{(1)}$). However at high energies, the effect of the scattering is much more complex and one needs to account for helicity-flip processes. This means that i) one needs to use a QFT approach and ii) the $\mathbf{R}'$–matrix in the ± basis gives more information about the physical process than the $\mathbf{R}'$–matrix in the (l, r) basis.

For clarity, we remind the reader of our notations:

- **$\mathbf{A}'$–matrix**: This the most generic relation between the incoming and outgoing (I, Q, U, V) parameters. It is valid for any photon energy and scattering off any type of particle and can be computed using both the ± and the (l, r) photon helicity states (see Eq. (5.2.5) and Eq. (5.2.4) respectively).

- **A–matrix**: Similarly, the **A**–matrix is the most generic relation between the incoming and scattered (I_l, I_r, U, V) parameters. Due to the definition of the modified Stokes parameters, the **A**-matrix is only expressed in terms of the (l, r) photon polarisation states.

- **$\mathbf{R}'$–matrix and $\mathbf{P}'$–matrix**: These are the $\mathbf{A}'$-matrices expressed in the rest-frame (scattering plane) and fixed frame kinematics (3D plane) respectively.

- **R–matrix and P–matrix**: These are the **A**-matrices expressed in the rest-frame (scattering plane) and fixed frame kinematics (3D plane) respectively.

5.3.1 The Phase–Matrix for Compton Interactions

We can now determine how the Stokes parameters change after γ-rays scatter off electrons by inserting the Compton scattering matrix elements in Eq. (5.2.3). Using the definitions $M_{i'i} \equiv \mathcal{M}(e_\alpha \gamma_i \to e_\beta \gamma'_i)$ (where $\alpha, \beta = \pm$ denote the electron spin configurations) and

$$M_{i'i} M^*_{j'j} \equiv \frac{1}{2} \sum_{\alpha,\beta=\pm} \mathcal{M}(e_\alpha \gamma_i \to e_\beta \gamma'_i)\, \mathcal{M}^*(e_\alpha \gamma_j \to e_\beta \gamma'_j) \tag{5.3.1}$$

we find that the $\mathbf{A}'$–matrix simplifies to

$$\mathbf{A}' = \begin{bmatrix} \mathbf{A}'_{11} & \mathbf{A}'_{12} & 0 & 0 \\ \mathbf{A}'_{21} & \mathbf{A}'_{22} & 0 & 0 \\ 0 & 0 & \mathbf{A}'_{33} & 0 \\ 0 & 0 & 0 & \mathbf{A}'_{44} \end{bmatrix} \tag{5.3.2}$$

with

$$\begin{aligned}
\mathbf{A}'_{11} &= 2 \left(\frac{p_1 \cdot k_1}{p_1 \cdot k_2} + \frac{p_1 \cdot k_2}{p_1 \cdot k_1} \right) + 4\, m_e^2 \left(\frac{1}{p_1 \cdot k_1} - \frac{1}{p_1 \cdot k_2} \right) + 2\, m_e^4 \left(\frac{1}{p_1 \cdot k_1} - \frac{1}{p_1 \cdot k_2} \right)^2 , \\
\mathbf{A}'_{12} &= \mathbf{A}'_{21} = 4\, m_e^2 \left(\frac{1}{p_1 \cdot k_1} - \frac{1}{p_1 \cdot k_2} \right) + 2\, m_e^4 \left(\frac{1}{p_1 \cdot k_1} - \frac{1}{p_1 \cdot k_2} \right)^2 , \\
\mathbf{A}'_{22} &= 2 \,+\, 2 \left(1 + m_e^2 \left(\frac{1}{p_1 \cdot k_1} - \frac{1}{p_1 \cdot k_2} \right) \right)^2 , \\
\mathbf{A}'_{33} &= 4 \,+ 4\, m_e^2 \left(\frac{1}{p_1 \cdot k_1} - \frac{1}{p_1 \cdot k_2} \right) , \\
\mathbf{A}'_{44} &= 2 \left(\frac{p_1 \cdot k_1}{p_1 \cdot k_2} + \frac{p_1 \cdot k_2}{p_1 \cdot k_1} \right) + 2\, m_e^2 \left(\frac{p_1 \cdot k_1}{p_1 \cdot k_2} + \frac{p_1 \cdot k_2}{p_1 \cdot k_1} \right) \left(\frac{1}{p_1 \cdot k_1} - \frac{1}{p_1 \cdot k_2} \right) ,
\end{aligned} \tag{5.3.3}$$

where p_1 is the 4–momentum of the incoming electron and k_1, k_2 are the 4–momentum of the incoming and outgoing photons respectively.

R′ and P′–Matrices for Compton Interactions

We can now express the $\mathbf{R}'$ and $\mathbf{P}'$–matrices for Compton scattering by taking the appropriate kinematic limit. In the rest frame of the electron, the $\mathbf{R}'$-matrix reads as

$$\mathbf{R}' = \frac{2}{m_e}\begin{bmatrix} \mathbf{R'_{11}} & -m_e \sin^2\theta & 0 & 0 \\ -m_e \sin^2\theta & m_e(1+\cos^2\theta) & 0 & 0 \\ 0 & 0 & 2m_e \cos\theta & 0 \\ 0 & 0 & 0 & \mathbf{R'_{44}} \end{bmatrix} \tag{5.3.4}$$

with $\mathbf{R'_{11}} = \Delta E_\gamma(1-\cos\theta) + m_e(1+\cos^2\theta)$, $\mathbf{R'_{44}} = [2m_e + \Delta E_\gamma(1-\cos\theta)]\cos\theta$ and $\Delta E_\gamma \equiv (E_{\gamma,1} - E_{\gamma,2})$. The angle θ is the angle between the incoming and outgoing photons. Here $E_{\gamma,1}$ and $E_{\gamma,2}$ are the energies of the incoming and outgoing photons, respectively.

R and P – Matrices for Compton Interactions

Similarly we can find the **R**–matrix using the expression of the **A**–matrix in the (l, r) basis, that is

$$\mathbf{A} = \begin{bmatrix} \mathbf{A}_{11} & \mathbf{A}_{12} & 0 & 0 \\ \mathbf{A}_{21} & \mathbf{A}_{22} & 0 & 0 \\ 0 & 0 & \mathbf{A}_{33} & 0 \\ 0 & 0 & 0 & \mathbf{A}_{44} \end{bmatrix} \tag{5.3.5}$$

with

$$\begin{aligned} \mathbf{A}_{11} &= 4 + \frac{2\,m_e^2\,(p_1{\cdot}k_1 - p_1{\cdot}k_2)\left(m_e^2\,(p_1{\cdot}k_1 - p_1{\cdot}k_2)\,-\,2\,p_1{\cdot}k_1\,p_1{\cdot}k_2\right)}{(p_1{\cdot}k_1)^2(p_1{\cdot}k_2)^2}, \\ \mathbf{A}_{12} = \mathbf{A}_{21} &= \frac{2\,m_e^2\,(p_1{\cdot}k_1 - p_1{\cdot}k_2)\left(m_e^2\,(p_1{\cdot}k_1 - p_1{\cdot}k_2)\,-\,2\,p_1{\cdot}k_1\,p_1{\cdot}k_2\right)}{(p_1{\cdot}k_1)^2\,(p_1{\cdot}k_2)^2}, \\ \mathbf{A}_{22} &= \frac{2}{(p_1{\cdot}k_1)^2(p_1{\cdot}k_2)^2}\left[m_e^4\,(p_1{\cdot}k_1 - p_1{\cdot}k_2)^2 + 2m_e^2\,p_1{\cdot}k_1\,p_1{\cdot}k_2\,(p_1{\cdot}k_2 - p_1{\cdot}k_1)\right. \\ &\qquad\qquad \left. + p_1{\cdot}k_1\,p_1{\cdot}k_2\left(p_1{\cdot}k_1{}^2 + p_1{\cdot}k_2{}^2\right)\right], \\ \mathbf{A}_{33} &= \frac{2\left((p_1{\cdot}k_1)^2 + (p_1{\cdot}k_2)^2\right)\left(m_e^2\,(p_1{\cdot}k_2 - p_1{\cdot}k_1) + p_1{\cdot}k_1\,p_1{\cdot}k_2\right)}{(p_1{\cdot}k_1)^2(p_1{\cdot}k_2)^2}, \\ \mathbf{A}_{44} &= 4\,+4\,m_e^2\left(\frac{1}{p_1{\cdot}k_1} - \frac{1}{p_1{\cdot}k_2}\right). \end{aligned} \tag{5.3.6}$$

The **R**–matrix then reads as

$$\begin{bmatrix} \hat{I}_l \\ \hat{I}_r \\ \hat{U} \\ \hat{V} \end{bmatrix}^{(2)} = \begin{bmatrix} \mathbf{R}_{11} & \mathbf{R}_{12} & 0 & 0 \\ \mathbf{R}_{21} & \mathbf{R}_{22} & 0 & 0 \\ 0 & 0 & \mathbf{R}_{33} & 0 \\ 0 & 0 & 0 & \mathbf{R}_{44} \end{bmatrix} \begin{bmatrix} \hat{I}_l \\ \hat{I}_r \\ \hat{U} \\ \hat{V} \end{bmatrix}^{(1)} \tag{5.3.7}$$

with

$$\begin{aligned} \mathbf{R}_{11} &= \tfrac{1}{2}\left(\mathbf{A}_{11}+\mathbf{A}_{12}+\mathbf{A}_{21}+\mathbf{A}_{22}\right) & \mathbf{R}_{12} &= \tfrac{1}{2}\left(\mathbf{A}_{11}-\mathbf{A}_{12}+\mathbf{A}_{21}-\mathbf{A}_{22}\right) \\ \mathbf{R}_{21} &= \tfrac{1}{2}\left(\mathbf{A}_{11}+\mathbf{A}_{12}-\mathbf{A}_{21}-\mathbf{A}_{22}\right) & \mathbf{R}_{33} &= \mathbf{A}_{33} \\ \mathbf{R}_{22} &= \tfrac{1}{2}\left(\mathbf{A}_{11}-\mathbf{A}_{12}-\mathbf{A}_{21}+\mathbf{A}_{22}\right) & \mathbf{R}_{44} &= \mathbf{A}_{44} \end{aligned} \tag{5.3.8}$$

which leads in the rest frame of the electron (see Appendix D)

$$\mathbf{R} = \frac{2}{m_e} \begin{bmatrix} \sin^2\frac{\theta}{2}\,\Delta E_\gamma + 2m_e\,\cos^2\theta & \sin^2\frac{\theta}{2}\,\Delta E_\gamma & 0 & 0 \\ \sin^2\frac{\theta}{2}\,\Delta E_\gamma & \sin^2\frac{\theta}{2}\,\Delta E_\gamma + 2m_e & 0 & 0 \\ 0 & 0 & 2m_e\,\cos\theta & 0 \\ 0 & 0 & 0 & \mathbf{R_{44}} \end{bmatrix} \tag{5.3.9}$$

with $\mathbf{R_{44}} = \left[2m_e + \Delta E_\gamma\left(1-\cos\theta\right)\right]\cos\theta$.

The expression of the **P**-matrix for Compton scattering (3D, fixed frame) is too long to be given in this Chapter.

As one can see, the expression of the **R**-matrix now involves ΔE_γ and a less straightforward combination of the scattering angle which is not just purely a geometrical factor. Using Eq. (5.3.9) (as well as the expression of the **P**–matrix) and taking the low energy limit ($E_{\gamma,1} \simeq E_{\gamma,2} \ll m_e$), we could verify that we recover the same **R** and **P** –matrices as in [81] (see Eq. (2.3.16)), thus confirming that using a QFT approach and taking different kinematics is indeed an alternative to Chandrasekhar's geometrical approach for deriving the **P** –matrix. The novelty of this technique though is that it allows us to compute the relationship between the Stokes (or modified Stokes) parameters – before and after scattering – whatever the incident photon energy, interaction and type of scattering material (i.e. whether the particles belong to the Standard Model or to some extensions).

Scattering with Unpolarised Electrons

Now that we have described how the polarisation of high energy photons could change after scattering, we can focus on either linear or circular polarisation. Circular polarisation is given by the V parameters and, like observed by Chandrasekhar for Rayleigh scattering, we note that in the rest frame, there is no transfer from linear to circular polarisation and vice versa even for high energy photons. Indeed under these conditions, $\mathbf{A}'_{44}$ (and therefore $\mathbf{R}'_{44}$) is secluded. In other words, a net circular polarisation signal cannot be converted into a linear polarisation signal and vice versa. This means that no circular polarisation signal can be created by the scattering of linearly polarised light (i.e. $V^{(2)} \neq 0$ requires that $V^{(1)} \neq 0$) and implies that a change in circular polarisation can only occur if there is a change in the number of photons with a given polarisation state. These results have also been checked using a different approach to calculate the scattering amplitude based on its decomposition in terms of different photon polarisations. We refer the reader to Appendix E for further details.

With the formalism given in this chapter, we can study the change of polarisation when high energy γ–rays hit electrons. Since ${\mathbf{A}'}_{i4,i\neq 4} = 0$ (i.e. there is no transfer of polarisation from linear to circular polarisation and vice versa), a possible change in the magnitude of the circular polarisation signal after scattering, $V^{(2)} \neq V^{(1)}$, has to reflect the number of photons whose polarisation state is changed by the scattering process. If the scattering is as likely to change the photon polarisation as to maintain it, we would expect no net circular polarisation – that is $V^{(2)} = 0$ – regardless of the initial net polarisation. Therefore the change in net circular polarisation (Δ_V) can be formulated in terms of the scattering matrix amplitudes, as [1]

---

[1] Here, the subscripted signs ± refers to the photon polarisation state, i.e. $e\gamma_i \rightarrow e\gamma_j$, where $i, j = \pm$.

$$\Delta_V = \frac{|\mathcal{M}_{++}|^2 + |\mathcal{M}_{--}|^2 - |\mathcal{M}_{+-}|^2 - |\mathcal{M}_{-+}|^2}{|\mathcal{M}_{++}|^2 + |\mathcal{M}_{--}|^2 + |\mathcal{M}_{+-}|^2 + |\mathcal{M}_{-+}|^2} = \frac{\mathbf{A'}_{44}}{\mathbf{A'}_{11}}\,, \tag{5.3.10}$$

where

$$\begin{aligned} |\mathcal{M}_{\pm\pm}|^2 = {} & 2\left(\frac{p_1{\cdot}k_1}{p_1{\cdot}k_2} + \frac{p_1{\cdot}k_2}{p_1{\cdot}k_1}\right) + m_e^2\left(2 + \frac{p_1{\cdot}k_1}{p_1{\cdot}k_2} + \frac{p_1{\cdot}k_2}{p_1{\cdot}k_1}\right) \times \\ & \times \left(\frac{1}{p_1{\cdot}k_1} - \frac{1}{p_1{\cdot}k_2}\right) + m_e^4\left(\frac{1}{p_1{\cdot}k_1} - \frac{1}{p_1{\cdot}k_2}\right)^2 \end{aligned}$$

$$|\mathcal{M}_{\pm\mp}|^2 = m_e^2\left(2 - \frac{p_1{\cdot}k_1}{p_1{\cdot}k_2} - \frac{p_1{\cdot}k_2}{p_1{\cdot}k_1}\right)\left(\frac{1}{p_1{\cdot}k_1} - \frac{1}{p_1{\cdot}k_2}\right) + m_e^4\left(\frac{1}{p_1{\cdot}k_1} - \frac{1}{p_1{\cdot}k_2}\right)^2 . \tag{5.3.11}$$

From this expression, one readily sees that the value of Δ_V is limited to the range $[-1, 1]$ and different values can be interpreted as follows.

- $\Delta_V = 1$: There is no change in the initial value of the V parameter (i.e., no change in the amount of circular polarisation left after scattering).
- $0 < \Delta_V < 1$: The initial circular polarisation is partly washed out by the scattering.
- $\Delta_V = 0$: Any net circular polarisation will be erased completely after one single scattering.
- $-1 < \Delta_V < 0$: The sign of the circular polarisation is changed and most polarisation states have flipped.
- $\Delta_V = -1$: All polarisation states have flipped ($V^{(2)} = -V^{(1)}$).

A similar information can be defined in terms of the total cross section corresponding to each amplitude (see Appendix F for details). We can now determine how likely a net circular polarisation signal is expected to change after Compton scattering as a function of the incoming and outgoing kinematics. In Fig. 5.1 we present the

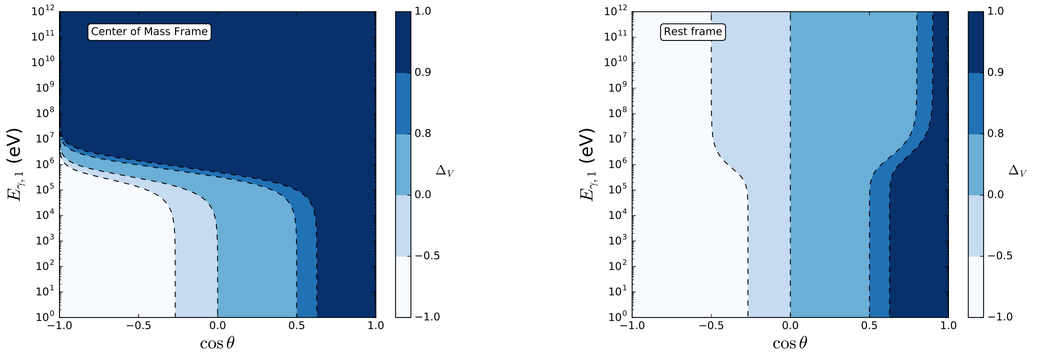

(a) Centre of Mass Frame (b) Rest Frame

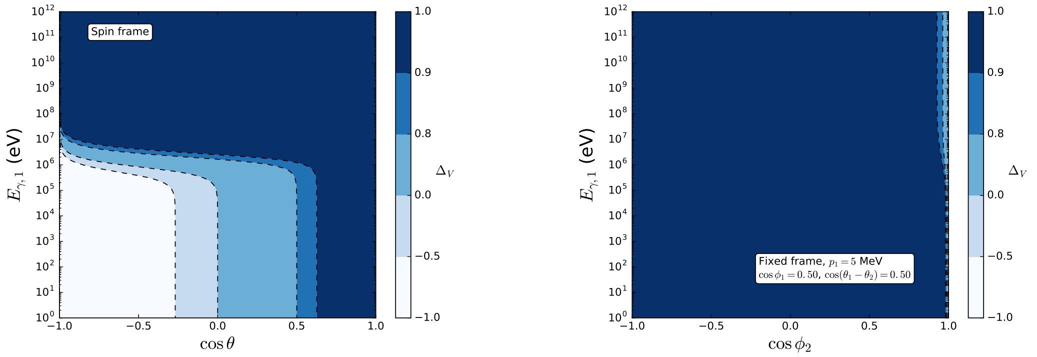

(c) Spin Frame (d) Fixed Frame

Figure 5.1: The change of net circular polarisation after a single $e-\gamma$ scattering in (a) the centre of mass frame, (b) the electron rest frame, (c) the spin frame, and (d) the fixed frame. In the former three frames, we choose the incoming photon energy $E_{\gamma,1}$ and the angle between outgoing and incoming photons θ as variables. In the last frame, the incoming photon energy $E_{\gamma,1}$ and the angle between outgoing photon and incoming electron are chosen as variables.

asymmetry Δ_V defined in Eq. (5.3.10) as a function of the incoming photon energy and the angle between the incoming and outgoing photon (θ). The results are shown in the centre of mass frame (COM), the rest frame, the spin frame and the fixed frame. The rest frame is very useful for energetic photons propagating through a medium and scattering with very low energy (background) electrons. The spin frame is a new frame that we define in this Chapter to reflect the fact that for incoming and outgoing electrons travelling in the $\mp z$, the spinor definitions that we are using to calculate the matrix amplitude correspond to the spin eigenstates of the electrons. The results in this frame thus match the result in the COM frame. The fixed frame gives the most general description of electron photon scattering. The only constraint is that the momentum of the incoming electron is fixed along the $+z$ direction. This gives us more freedom about the angular configuration of the scattering. In this frame, it is not very intuitive to show Δ_V as a function of θ so we will present it as a function of the angle between the outgoing photon and the incoming electron (i.e., ϕ_2), as in Fig. 5.1d. In this figure, we have fixed the incoming electron momentum at $p_1 = 5$ MeV, as well as the angles $\phi_1 = \theta_1 - \theta_2 = \pi/3$, where ϕ_1 is the angle between incoming electron and photon and $\theta_1 - \theta_2$ is the difference of the angles of the incoming and outgoing photons projected on the plane perpendicular to the z direction. Note that this plot is just shown as an example, more results for the fixed frame can be found in Appendix F.1. The polarisation behaviour is dependent on all these kinetic variables. If one of them changes, Δ_V changes quite a bit too. For more information about how Δ_V varies in the different frames of reference, we refer the reader to Appendix D.

A common feature among the first three frames is that, for a low energy incoming photon, $E_{\gamma,1} \ll m_e$, the asymmetry Δ_V crucially depends on the direction of the outgoing photon after scattering. The fixed frame does not follow this feature simply because we have assumed a relativistic incoming electron by fixing p_1 at 5 MeV. If the incoming electron is non-relativistic (as can be seen in the appendix F.1) we get similar results as in the other frames.

In the high energy regime of the incoming photon ($E_{\gamma,1} \gg m_e$), Compton scattering preserves the polarisation states of most of the outgoing photons regardless of the direction of the incoming photon. However, this is not true in the rest frame (Fig. 5.1b), where Δ_V strongly depends on the scattering direction of the outgoing photon with respect to the incoming photon and is independent on the incoming photon energy. When the initial electron is at rest, the only way that a "$+/-$" polarised photon can conserve angular momentum requires the photon to be scattered in the forward direction. Otherwise, it would have to flip its polarisation. On the contrary, when the electron has some initial energy, (like in the spin or COM frames for $E_{\gamma,1} \gg m_e$), the photon can scatter in any direction while keeping its initial polarisation without violating angular momentum conservation. One common feature of all the frames in this regime is that the change of the net polarisation no longer depends on the incoming photon energy. However, when the energy of the incoming photon is around or slightly above the electron mass, the value of Δ_V then becomes strongly frame dependent.

5.4 Boltzmann–Like Equation for Polarisation

Now that we know how the Stokes parameters are modified after scattering, see Eq. (5.3.9), we can study their evolution as light propagates through space. This is possible by using the Boltzmann equation. The general form of the Boltzmann equation is

$$\frac{dn}{dt} = C[n]\,, \tag{5.4.1}$$

where n is the phase space photon distribution function and C is the collisional term, i.e., a functional of the photon distribution function n describing the scattering of the photon with any other particles ψ in the medium. The latter reads as

$$\begin{aligned} C[n] = \int d\mathbf{p}_1\ d\mathbf{p}_2\ d\mathbf{k}_2\ \ |\mathcal{M}(\psi\gamma \to \psi\gamma)|^2\ (2\pi)^4 \times \\ \times\, \delta^4(p_1 + k_1 - p_2 - k_2)[n_\psi(\mathbf{p}_2)n_\gamma(\mathbf{k}_2) - n_\psi(\mathbf{p}_1)n_\gamma(\mathbf{k}_1)], \end{aligned} \tag{5.4.2}$$

where $p_{1(2)} \equiv (E_{\psi,1(2)},\ \mathbf{p}_{1(2)})$ is the four-momentum of the incoming (outgoing) particle ψ in the medium, $k_{1(2)} \equiv (E_{\gamma,1(2)},\ \mathbf{k}_{1(2)})$ is the four-momentum of the incoming (outgoing) photon, $d\mathbf{k}_2 \equiv \dfrac{d^3\mathbf{k}_2}{(2\pi)^3 2E_{\gamma,2}}$, $d\mathbf{p}_{1(2)} \equiv \dfrac{d^3\mathbf{p}_{1(2)}}{(2\pi)^3}\dfrac{m_\psi}{E_{\psi,1(2)}}$, $n_{\psi,\gamma}$ is the distribution function of the particles ψ and γ respectively, and $|\mathcal{M}(\psi\gamma \to \psi\gamma)|^2$ is the squared scattering matrix amplitude. In the current form, this equation is for any particle physics process involving photon scattering.

5.4.1 Boltzmann Formalism for Generic Interactions

In order to study the evolution of the polarisation, we need to relate the photon energy distribution to the Stokes parameters. In Eq. (2.3.14), we saw that the Stokes parameters could be expressed in terms of the different photon states. The next step is to relate them to the density matrix. Combining Eq. (2.3.14) with the definition of density matrix

$$\rho_{ij} = \frac{|\epsilon_i\rangle\langle\epsilon_j|}{\mathrm{Tr}(\rho)}, \tag{5.4.3}$$

where $i, j = \{l, r\}$ or $\{+, -\}$, and making use of

$$\langle S\rangle = \mathrm{Tr}(\rho\hat{S})\,, \tag{5.4.4}$$

with $S = I, Q, U, V$, the Stokes parameters in the ± basis can be expressed as

$$\begin{aligned}
\langle I\rangle &= \rho_{++} + \rho_{--}\,,\\
\langle Q\rangle &= \,-\left(\rho_{+-} + \rho_{-+}\right)\,,\\
\langle U\rangle &= i\left(\rho_{+-} - \rho_{-+}\right)\,,\\
\langle V\rangle &= \rho_{++} - \rho_{--}
\end{aligned} \tag{5.4.5}$$

To continue further, we need to define the time evolution of the different matrix density elements. This can be done by expressing the photon number operator $\mathcal{D}_{ij}(\mathbf{k}) \equiv a_i^\dagger(\mathbf{k})a_j(\mathbf{k})$ in terms of the density matrix associated with the different photon polarisation states [82]. Making use of the relation

$$\langle\mathcal{D}_{ij}\rangle = (2\pi)^3\delta(0)2k^0\rho_{ij}(\mathbf{k}) \tag{5.4.6}$$

and assuming that the collision time scale is smaller than the time scale for the variation of the density matrix (which is true for weak scale processes), we can then express the density matrix in terms of the photon number operator [173]

$$(2\pi)^3\delta(0)2E_k\frac{d}{dt}\rho_{ij}(\mathbf{k}) = -\frac{1}{2}\int_{-\infty}^{\infty} dt\langle[H_I^0(t),[H_I^0(0),\mathcal{D}_{ij}^0(\mathbf{k})]]\rangle\,, \tag{5.4.7}$$

where H_I^0 is the interaction Hamiltonian to first order.

Assuming that most of the particles in space are not polarised since there is no left/right asymmetry, Eq. (5.4.7) can be rewritten as

$$\begin{aligned}
2E_{\gamma,1}\frac{d}{dt}\rho_{ij}(\mathbf{k}_1) = -\frac{1}{4}\int d\mathbf{p}_1\ d\mathbf{p}_2\ d\mathbf{k}_2\ (2\pi)^4\ \delta^4(p_2+k_2-p_1-k_1)\ \ M_{\alpha\alpha'}M^*_{\beta'\beta} \\
\times\left[n_\psi(\mathbf{p}_1)\delta_{\beta\alpha'}(\delta_{i\alpha}\rho_{\beta'j}(\mathbf{k}_1)+\delta_{j\beta'}\rho_{i\alpha}(\mathbf{k}_1)) - 2n_\psi(\mathbf{p}_2)\delta_{i\alpha}\delta_{j\beta'}\rho_{\alpha'\beta}(\mathbf{k}_2)\right],
\end{aligned} \tag{5.4.8}$$

where $M_{\alpha\alpha'} \equiv \mathcal{M}(\psi\gamma_\alpha \to \psi\gamma_{\alpha'})$ with $\alpha, \alpha' = \pm$ being different polarisation states of the photon. This eventually leads to

$$\begin{aligned}
\frac{d}{dt}\rho_{++}(\mathbf{k}_1) = -\frac{1}{8E_{\gamma,1}}\int & d\mathbf{p}_1 d\mathbf{p}_2 d\mathbf{k}_2 (2\pi)^4\delta^4(p_2+k_2-p_1-k_1) \\
& \times\Big(2|M_{++}|^2[n_\psi(\mathbf{p}_1)\rho_{++}(\mathbf{k}_1) - n_\psi(\mathbf{p}_2)\rho_{++}(\mathbf{k}_2)] \\
& + 2|M_{+-}|^2[n_\psi(\mathbf{p}_1)\rho_{++}(\mathbf{k}_1) - n_\psi(\mathbf{p}_2)\rho_{--}(\mathbf{k}_2)] \\
& + n_\psi(\mathbf{p}_1)\left(\rho_{-+}(\mathbf{k}_1)\left(M_{++}M^*_{-+} + M_{+-}M^*_{--}\right)\right. \\
& \left. + \rho_{+-}(\mathbf{k}_1)\left(M_{-+}M^*_{++} + M_{--}M^*_{+-}\right)\right) \\
& - 2n_\psi(\mathbf{p}_2)[M_{++}M^*_{+-}\rho_{+-}(\mathbf{k}_2) + M_{+-}M^*_{++}\rho_{-+}(\mathbf{k}_2)]\Big), \\
\frac{d}{dt}\rho_{--}(\mathbf{k}_1) = -\frac{1}{8E_{\gamma,1}}\int & d\mathbf{p}_1 d\mathbf{p}_2 d\mathbf{k}_2 (2\pi)^4\delta^4(p_2+k_2-p_1-k_1) \\
& \times\Big(2|M_{-+}|^2\left[n_\psi(\mathbf{p}_1)\rho_{--}(\mathbf{k}_1) - n_\psi(\mathbf{p}_2)\rho_{++}(\mathbf{k}_2)\right] \\
& + 2|M_{--}|^2\left[n_\psi(\mathbf{p}_1)\rho_{--}(\mathbf{k}_1) - n_\psi(\mathbf{p}_2)\rho_{--}(\mathbf{k}_2)\right] \\
& + n_\psi(\mathbf{p}_1)\left(\rho_{+-}(\mathbf{k}_1)\left(M_{-+}M^*_{++} + M_{--}M^*_{+-}\right)\right. \\
& \left. + \rho_{-+}(\mathbf{k}_1)\left(M_{++}M^*_{-+} + M_{+-}M^*_{--}\right)\right) \\
& - 2n_\psi(\mathbf{p}_2)[M_{-+}M^*_{--}\rho_{+-}(\mathbf{k}_2) + M_{--}M^*_{-+}\rho_{-+}(\mathbf{k}_2)]\Big), \\
\frac{d}{dt}\rho_{+-}(\mathbf{k}_1) = -\frac{1}{8E_{\gamma,1}m_\psi^2}\int & d\mathbf{p}_1 d\mathbf{p}_2 d\mathbf{k}_2 (2\pi)^4\delta^4(p_2+k_2-p_1-k_1)\times, \\
& \times\Big(n_\psi(\mathbf{p}_1)\left[\,\rho_{+-}(\mathbf{k}_1)(|M_{++}|^2 + |M_{-+}|^2 + |M_{+-}|^2 + |M_{--}|^2)\right. \\
& \left. + (\rho_{++}(\mathbf{k}_1) + \rho_{--}(\mathbf{k}_1))(M_{++}M^*_{-+} + M_{+-}M^*_{--})\,\right] \\
& - 2n_\psi(\mathbf{p}_2)[M_{++}M^*_{-+}\rho_{++}(\mathbf{k}_2) + M_{+-}M^*_{--}\rho_{--}(\mathbf{k}_2) \\
& + M_{+-}M^*_{-+}\rho_{-+}(\mathbf{k}_2) + M_{++}M^*_{--}\rho_{+-}(\mathbf{k}_2)]\Big),
\end{aligned}$$

$$
\begin{aligned}
\frac{d}{dt}\rho_{-+}(\mathbf{k}_1) = -\frac{1}{8E_{\gamma,1}m_\psi^2}\int & d\mathbf{p}_1 d\mathbf{p}_2 d\mathbf{k}_2 (2\pi)^4\delta^4(p_2+k_2-p_1-k_1) \\
& \times \Big(n_\psi(\mathbf{p}_1)\Big[\rho_{-+}(\mathbf{k}_1)(|M_{++}|^2+|M_{-+}|^2+|M_{+-}|^2+|M_{--}|^2) \\
& +(\rho_{++}(\mathbf{k}_1)+\rho_{--}(\mathbf{k}_1))(M_{-+}M^*_{++}+M_{--}M^*_{+-})] \\
& -2n_\psi(\mathbf{p}_2)[M_{-+}M^*_{++}\rho_{++}(\mathbf{k}_2)+M_{--}M^*_{+-}\rho_{--}(\mathbf{k}_2) \\
& +M_{-+}M^*_{+-}\rho_{+-}(\mathbf{k}_2)+M_{--}M^*_{++}\rho_{-+}(\mathbf{k}_2)]\Big)\,. \qquad (5.4.9)
\end{aligned}
$$

Expressing the scattering matrix elements in terms of the $\mathbf{A}'$–matrix elements, we then get

$$
\begin{aligned}
|M_{++}|^2 &= \tfrac{1}{2}\left(\mathbf{A'}_{11}+\mathbf{A'}_{14}+\mathbf{A'}_{41}+\mathbf{A'}_{44}\right) \\
M_{++}M^*_{-+} &= \tfrac{1}{2}\left(-\mathbf{A'}_{21}-\mathbf{A'}_{24}+i\mathbf{A'}_{31}+i\mathbf{A'}_{34}\right) \\
|M_{+-}|^2 &= \tfrac{1}{2}\left(\mathbf{A'}_{11}-\mathbf{A'}_{14}+\mathbf{A'}_{41}-\mathbf{A'}_{44}\right) \\
M_{--}M^*_{+-} &= \tfrac{1}{2}\left(-\mathbf{A'}_{21}+\mathbf{A'}_{24}-i\mathbf{A'}_{31}+i\mathbf{A'}_{34}\right) \\
|M_{-+}|^2 &= \tfrac{1}{2}\left(\mathbf{A'}_{11}+\mathbf{A'}_{14}-\mathbf{A'}_{41}-\mathbf{A'}_{44}\right) \\
M_{++}M^*_{+-} &= \tfrac{1}{2}\left(-\mathbf{A'}_{12}-i\mathbf{A'}_{13}-\mathbf{A'}_{42}-i\mathbf{A'}_{43}\right) \\
|M_{--}|^2 &= \tfrac{1}{2}\left(\mathbf{A'}_{11}-\mathbf{A'}_{14}-\mathbf{A'}_{41}+\mathbf{A'}_{44}\right) \\
M_{-+}M^*_{+-} &= \tfrac{1}{2}\left(\mathbf{A'}_{22}+i\mathbf{A'}_{23}+i\mathbf{A'}_{32}-\mathbf{A'}_{33}\right) \\
M_{++}M^*_{--} &= \tfrac{1}{2}\left(\mathbf{A'}_{22}+i\mathbf{A'}_{23}+\mathbf{A'}_{33}-i\mathbf{A'}_{32}\right) \\
M_{-+}M^*_{--} &= \tfrac{1}{2}\left(-\mathbf{A'}_{12}+\mathbf{A'}_{42}-i\mathbf{A'}_{13}+i\mathbf{A'}_{43}\right) \qquad (5.4.10)
\end{aligned}
$$

Therefore, using Eqs. ((5.4.5)) and ((5.4.9)), we obtain the time evolution of the Stokes parameters, namely

$$
\begin{aligned}
\frac{d}{dt}I(\mathbf{k}_1) = -\frac{m_\psi^2}{8\pi E_{\psi,1}E_{\gamma,1}E_{\psi,2}}\int_0^\infty dE_{\gamma,2}E_{\gamma,2}\int\frac{d\Omega}{4\pi}\delta\left(E_{\psi,2}+E_{\gamma,2}-E_{\psi,1}-E_{\psi,1}\right)\times \\
\times\Bigg[\Big(n_{\psi,1}I(\mathbf{k}_1)-n_{\psi,2}I(\mathbf{k}_2)\Big)\mathbf{A'}_{11} \\
+\,n_{\psi,1}\Big(V(\mathbf{k}_1)\mathbf{A'}_{41}+Q(\mathbf{k}_1)\mathbf{A'}_{21}-U(\mathbf{k}_1)\mathbf{A'}_{31}\Big)
\end{aligned}
$$

$$
\begin{aligned}
&\qquad\qquad - n_{\psi,2}\Big(V(\mathbf{k}_2)\mathbf{A'}_{14} + Q(\mathbf{k}_2)\mathbf{A'}_{12} - U(\mathbf{k}_2)\mathbf{A'}_{13}\Big)\Bigg]\\
\frac{d}{dt}Q(\mathbf{k}_1) &= -\frac{m_\psi^2}{8\pi E_{\psi,1}E_{\gamma,1}E_{\psi,2}}\int_0^\infty dE_{\gamma,2}E_{\gamma,2}\int\frac{d\Omega}{4\pi}\delta\left(E_{\psi,2}+E_{\gamma,2}-E_{\psi,1}-E_{\psi,1}\right)\times\\
&\quad\times\Bigg[\Big(n_{\psi,1}I(\mathbf{k}_1) - n_{\psi,2}I(\mathbf{k}_2)\Big)\mathbf{A'}_{21} + n_{\psi,1}Q(\mathbf{k}_1)\mathbf{A'}_{11}\\
&\qquad - n_{\psi,2}\Big(V(\mathbf{k}_2)\mathbf{A'}_{24} + Q(\mathbf{k}_2)\mathbf{A'}_{22} - U(\mathbf{k}_2)\mathbf{A'}_{23}\Big)\Bigg]\\
\frac{d}{dt}U(\mathbf{k}_1) &= -\frac{m_\psi^2}{8\pi E_{\psi,1}E_{\gamma,1}E_{\psi,2}}\int_0^\infty dE_{\gamma,2}E_{\gamma,2}\int\frac{d\Omega}{4\pi}\delta\left(E_{\psi,2}+E_{\gamma,2}-E_{\psi,1}-E_{\psi,1}\right)\\
&\quad\times\Bigg[-\Big(n_{\psi,1}I(\mathbf{k}_1) - n_{\psi,2}I(\mathbf{k}_2)\Big)\mathbf{A'}_{31} + n_{\psi,1}U(\mathbf{k}_1)\mathbf{A'}_{11}\\
&\qquad + n_{\psi,2}\Big(V(\mathbf{k}_2)\mathbf{A'}_{34} + Q(\mathbf{k}_2)\mathbf{A'}_{32} - U(\mathbf{k}_2)\mathbf{A'}_{33}\Big)\Bigg]\\
\frac{d}{dt}V(\mathbf{k}_1) &= -\frac{m_\psi^2}{8\pi E_{\psi,1}E_{\gamma,1}E_{\psi,2}}\int_0^\infty dE_{\gamma,2}E_{\gamma,2}\int\frac{d\Omega}{4\pi}\delta\left(E_{\psi,2}+E_{\gamma,2}-E_{\psi,1}-E_{\psi,1}\right)\\
&\quad\times\Bigg[\Big(n_{\psi,1}I(\mathbf{k}_1) - n_{\psi,2}I(\mathbf{k}_2)\Big)\mathbf{A'}_{41} + n_{\psi,1}V(\mathbf{k}_1)\mathbf{A'}_{11}\\
&\qquad - n_{\psi,2}\Big(V(\mathbf{k}_2)\mathbf{A'}_{44} + Q(\mathbf{k}_2)\mathbf{A'}_{42} - U(\mathbf{k}_2)\mathbf{A'}_{43}\Big)\Bigg] \qquad (5.4.11)
\end{aligned}
$$

where $\mathbf{p}_2 = \mathbf{p}_1 + \mathbf{k}_1 - \mathbf{k}_2$ and where it is assumed that the particles in the medium follow a thermal Maxwell-Boltzmann distribution so that $n_{\psi,1(2)} \equiv n_{\psi,1(2)}(\mathbf{x}) = \int \frac{d^3\mathbf{p}_{1(2)}}{(2\pi)^3} f_\psi(\mathbf{x}, \mathbf{p}_{1(2)})$. We are now ready to compute the time evolution of the circular polarisation component by inputting the appropriate electron densities and $\mathbf{A}'$–matrix elements. This has been done for low energy photons in [174].

5.4.2 Boltzmann Formalism for Photo – Electron Scattering

For the study of more than one process we now apply the Boltzmann formalism to the photon-electron scattering. Using the general results in Eq. (5.4.11) and Eq. (5.3.2) the Boltzmann equation for photon-electron scattering simplifies and can then be expressed in terms of the $\mathbf{A}'$–matrix elements. Consequently, for the specific case of Compton scattering, we get

$$
\begin{aligned}
\frac{d}{dt} I(\mathbf{k}_1) = &- \frac{m_e^2}{8\pi E_{e,1} E_{\gamma,1} E_{e,2}} \int_0^\infty dE_{\gamma,2} E_{\gamma,2} \int \frac{d\Omega}{4\pi} \delta \Big(E_{e,2} + E_{\gamma,2} - E_{e,1} - E_{e,1} \Big) \\
&\times \Bigg[\Big(n_{e,1} I(\mathbf{k}_1) - n_{e,2} I(\mathbf{k}_2) \Big) \mathbf{A}'_{11} + \Big(n_{e,1} Q(\mathbf{k}_1) - n_{e,2} Q(\mathbf{k}_2) \Big) \mathbf{A}'_{12} \Bigg] , \\
\frac{d}{dt} Q(\mathbf{k}_1) = &- \frac{m_e^2}{8\pi E_{e,1} E_{\gamma,1} E_{e,2}} \int_0^\infty dE_{\gamma,2} E_{\gamma,2} \int \frac{d\Omega}{4\pi} \delta \Big(E_{e,2} + E_{\gamma,2} - E_{e,1} - E_{e,1} \Big) \\
&\times \Bigg[\Big(n_{e,1} I(\mathbf{k}_1) - n_{e,2} I(\mathbf{k}_2) \Big) \mathbf{A}'_{12} + n_{e,1} Q(\mathbf{k}_1) \mathbf{A}'_{11} - n_{e,2} Q(\mathbf{k}_2) \mathbf{A}'_{22} \Bigg] , \\
\frac{d}{dt} U(\mathbf{k}_1) = &- \frac{m_e^2}{8\pi E_{e,1} E_{\gamma,1} E_{e,2}} \int_0^\infty dE_{\gamma,2} E_{\gamma,2} \int \frac{d\Omega}{4\pi} \delta \Big(E_{e,2} + E_{\gamma,2} - E_{e,1} - E_{e,1} \Big) \\
&\times \Big[n_{e,1} U(\mathbf{k}_1) \mathbf{A}'_{11} - n_{e,2} U(\mathbf{k}_2) \mathbf{A}'_{33} \Big] , \\
\frac{d}{dt} V(\mathbf{k}_1) = &- \frac{m_e^2}{8\pi E_{e,1} E_{\gamma,1} E_{e,2}} \int_0^\infty dE_{\gamma,2} E_{\gamma,2} \int \frac{d\Omega}{4\pi} \delta \Big(E_{e,2} + E_{\gamma,2} - E_{e,1} - E_{e,1} \Big) \\
&\times \Big[n_{e,1} V(\mathbf{k}_1) \mathbf{A}'_{11} - n_{e,2} V(\mathbf{k}_2) \mathbf{A}'_{44} \Big] , \qquad (5.4.12)
\end{aligned}
$$

where $c_2 \equiv \cos 2\phi_2$ and $c_1 \equiv \cos 2\phi_1$ and the explicit form of the $\mathbf{A}'$–matrix elements are given by Eq. (5.3.3).

We note that the evolution of the intensity $I(\mathbf{k}_1)$ and linear polarisation parameter $Q(\mathbf{k}_1)$ are independent of the evolution of the $U(\mathbf{k}_1)$ and $V(\mathbf{k}_1)$ parameters. Consequently, for Compton scattering, there is no conversion between circular and linear polarisation over time as expected.

5.5 Conclusion

The formalism developed in this work provides with a powerful tool to study the changes in circular polarisation as light propagates through any type of medium. This implies that observations of circularly polarised light can be used to deepen our understanding of the nature of dark matter or other theories beyond the Standard Model.

As it is expected, the $\mathbf{A}'$–matrix elements at high energy (Eq. (5.3.2)) are significantly different from the ones at low energy. Some of the elements which were vanishing in the low energy limit do not vanish at high energy. Furthermore, unlike in the low energy case, the change of the Stokes parameters after scattering also depends on the photon energies in the initial and final states. The relationship between the Stokes parameters before and after scattering is therefore more complex at high energy than at low energy. Nevertheless, just like for the interactions at low energies, circular polarisation is secluded. Consequently, if the V-parameter changes after scattering, this means that a number of photons with a given helicity state were converted into photons with the opposite helicity. Therefore, if one kind of circular polarisation dominates over the other one, we will be able to observe a net circular polarisation signal i.e. $\Delta_V \neq 0$.

We also determine the conditions for which a net circular polarisation signal would be preserved after scattering at low/high energies. This was done in four different frames: centre of mass frame, rest frame, spin frame and fixed frame. We observed that, for the first three frames mentioned before, a common characteristic is that for low energy incoming photon, the change on the net circular polarisation depends on the scattering direction. The fixed frame does not have this characteristic because the incoming electron is relativistic. On the other hand, for high energies of the incoming photon in the centre of mass and spin frame, the circular polarisation is conserved independently of the scattering direction. This is not true for the rest frame, where the change in the net circular polarisation depends on the scattering direction of the outgoing photon. The only way the polarisation changes in this frame is when the photon scatters in the forward direction.

To complement this work, we developed a general formalism to study the time evolution of the Stokes parameters in the (I, Q, U, V) basis in terms of the scattering matrix elements. For the particular case of Compton scattering, we found that the time evolution of the V–parameter is independent of the other Stokes parameters. This means that even after multiple scatterings, while the amount of circular polarisation might change (i.e., the difference between left or right helicity states), circularly polarised light will never become linearly polarised or vice versa.

Chapter 6

Capture of Dark Matter in White Dwarfs

In this chapter, we will discuss the DM capture mechanism in stars [60]. We will apply this formalism to the case of DM captured in white dwarfs (WDs). In Sec. 6.2 we will provide a complete discussion on the physics of WDs such as their composition and equation of state (EoS). In Sec. 6.3 we will introduce the DM capture rate formalism. We also estimate the effects of evaporation for low DM masses in Sec. 6.4. Finally in Sec. 6.5, we turn our attention to setting constraints on DM interactions.

6.1 Introduction

Compact stellar objects such as WDs generate a very strong gravitational potential. Hence, the flux of DM particles in the neighbourhood of the stars will be gravitationally pulled towards the star increasing the scattering probability of DM particles off stellar targets such as nucleons, nuclei or leptons. If DM particles lose enough energy, they will not be able to escape the star. The captured DM will concentrate in the centre of the star where further annihilation provides extra heating that could affect the WD luminosity. Therefore, observations of WDs lead to new ways to place limits on the strength of DM interactions.

Dark matter capture in stars was first introduced by William H. Press and David N. Spergel [175]. They calculated the capture rate of DM in the Sun to account for the observed solar neutrino discrepancy. Later the formalism was improved by Andrew Gould who computed the capture rate for a generic spherical object and then applied this calculation to DM capture in the Sun and in the Earth [176, 177].

The capture probability for a DM particle passing through the Sun, or the Earth, is very small compared to that of a DM particle passing through a compact stellar object. This is because the gravitational potential of the Sun and the Earth is several orders of magnitude weaker than that of a compact star. Due to this fact, later work has focused on the capture of DM in compact objects such as neutron stars (NSs) to probe the particle properties of DM [178, 179, 180]. NSs are the smallest and densest stars known in the Universe which could make difficult observations of their thermal emissions [180]. To place limits on DM interactions using NSs, it is necessary to observe sufficiently old, isolated, and nearby stars. The detection of the thermal emission of a NS due to maximal DM capture in the star might be possible with forthcoming infrared telescopes [181].

On the other hand, as we shall see in sec. 6.2, WDs are very well observed and studied compact stellar objects. Due to the vast number of observations, their high densities and the better understanding we have of their inner structure, WDs are promising probes to set constraints on the DM scattering cross section. The capture rate of DM particles in WDs has been already explored, see e.g. Refs. [182, 183]. However, relativistic effects due to the star compactness and inner structure have been neglected.

Here, we adapt the treatment of the capture process, established in Ref. [184] for the Sun and later improved in Ref. [60] for NSs, to DM capture in WDs. To obtain more realistic estimates of the capture rate, first we discuss the physics of such stars i.e. their composition and inner structure in the following section.

6.2 White Dwarfs

There are three possible final states for a star when collapsing gravitationally; the precise evolutionary path a star follows primarily depends on its mass at birth. Massive stars (mass $\sim 10 - 29\,\mathrm{M}_\odot$) will become either neutron stars or black holes. Around 90% of all stars in the Galaxy, with masses $M_\star \lesssim 8 - 10\,M_\odot$, will become white dwarfs.

Compact stars differ from normal stars in two aspects: (1) Fusion does not occur anymore. Consequently, there is no outward thermal pressure, in the particular case of WDs the only support against gravitational collapse is the pressure generated by highly degenerate electrons. (2) They are extremely small, therefore they generate a much stronger gravitational field.

In the following, we will discuss some physical aspects that are useful for the computation of the capture rate of DM in WDs.

6.2.1 Composition

WDs are compact objects with extremely high energy densities ($\sim 10^6\mathrm{kg/m}^3$). According to observations [185, 186, 187], a typical WD is about $0.6\mathrm{M}_\odot$, with an surface temperature of the order of 10^4 K and a radius of the order of that of the Earth. At the extremely high densities found in WDs, electrons are highly degenerate [188] so that, because of Pauli's principle, an electron degeneracy pressure arises, which supports WDs against gravitational collapse. Therefore, electrons determine the equation of state (EoS) and the internal structure of white dwarfs. When the WD mass exceeds the so called Chandrasekhar limit $M_{\mathrm{CH}} \sim 1.4\mathrm{M}_\odot$[189], the electron degeneracy pressure becomes insufficient to support WDs against gravitational collapse. Below this limit, the WD will remain stable; however, if the WD mass becomes greater than M_{CH}, the star will further collapse into a different type of stellar remnant such as NSs or BHs. Massive WDs with mass around $\sim 1.33\mathrm{M}_\odot$ have been observed [190]. Such WDs generate a significantly strong gravitational field so that general relativistic (GR) effects become relevant for the study of their structure and evolution, see Fig. 6.1.

Most WDs are thought to be composed of carbon and oxygen, nonetheless observations show that WDs possess also an atmosphere either H–dominant or He–dominant. The envelope account for 1% of the fraction of the total mass. Typically the atmosphere is composed of a maximum amount of helium around $10^{-2}M_\star$ and a maximum mass of hydrogen around $10^{-4}M_\star$ [191]. There are other (less abundant) types of WDs where the dominant element in the envelope is different from Hydrogen and Helium. We will discuss this in more detail in section 6.2.4.

WDs are born at very high temperatures and they require several billions of years to cool down. Hence, observations of the coldest WDs contain information of the early stages of our Galaxy. Moreover, their extremely high densities cannot be reproduced at terrestrial laboratories becoming “physics laboratories” for matter in extreme environments.

6.2.2 Equation of State

Equations that relate thermodynamic properties, such as temperature, pressure and density, of a system are called equations of state. We use this set of equations to describe the properties of matter in the interior of stars. In this section, we discuss the ideal and Salpeter equations of state of a WD. In both approaches we assume that a WD is made of only one element.

Ideal Equation of State

In the classical approach the WD EoS is obtained by considering WD matter consisting of electrons and nuclei of atomic weight A and atomic charge Z. Additionally, given that in the WD interior electrons are highly degenerate it is a good first approximation to consider the matter at absolute zero temperature.

In this first approach, not only the effects of temperature are neglected, but also interactions among electrons and nuclei are not taken into account and the main molecular weight $\mu_e = A/Z$ is considered as constant. As a result, the EoS given by the parametric forms of the total energy density $\epsilon(\xi)$ and pressure $p(\xi)$ receive only two contributions: $\epsilon_{\rm n}$ and ϵ_e which are respectively the nucleon and electron energy density contributions. For non interacting electrons of number density $n_e = n_{\rm n}/\mu_e$, these contributions are defined as,

$$\epsilon_{\rm n}(\xi) = \epsilon_0 \frac{M_u \mu_e}{3m_e} \sinh^3 \frac{\xi}{4}, \tag{6.2.1}$$

with M_u the atomic mass unit, and

$$\epsilon_e(\xi) = \frac{\epsilon_0}{8} \left[\frac{1}{4}(\sinh \xi - \xi) - \frac{8}{3} \sinh^3 \frac{\xi}{4} \right], \tag{6.2.2}$$

where we have used $\xi = 4 \sinh^{-1} x$, $\epsilon_0 = \frac{m_e^4 c^5}{\pi^2 \hbar^3}$, $x = p_F/m_e c$ and p_F is the electron Fermi momentum.

The internal pressure of the WD is given by the changes in the Helmholtz free energy $F(T, E)$. Considering the limit of zero temperature we have,

$$p = -\frac{1}{4\pi r_e^2 a_0^3} \frac{dE}{dr_e}, \tag{6.2.3}$$

where $E = \epsilon/n_e$, the pressure in the classical approach without temperature dependence and electromagnetic interaction corrections is given by

$$p(\xi) = \frac{\epsilon_0}{96} \left[\sinh \xi - 8 \sinh \frac{\xi}{2} + 3\xi \right]. \tag{6.2.4}$$

Salpeter Equation of State

In Ref. [192], Salpeter introduced several corrections to the classical approach discussed above. He principally relaxed the assumption of non-interacting electrons and introduced corrections to the electron energy due to the electrostatic potential, which is the most important correction to the EoS. A uniformly negatively charged spherical cell of radius $r_e a_0$, with a positively charged ion at the centre, is assumed in this treatment, where a_0 is the Bohr radius and r_e the classical electron radius. This is the so called Wigner–Seitz (WS) cell. Additional corrections were discussed in his work such as the ions not being rigid in the WS cell, and self interactions but he concluded that they are not relevant at high densities. We now list all the corrections introduced to the EoS in Ref. [192].

1. Coulomb effects: As stated before, the electron-proton lattice is assumed to be the Wigner-Seitz cell approximation. When relaxing the assumption of non-interacting electrons, we consider interactions among electrons in the cell as well as with the positive ion. However, the electrostatic interaction among different cells remains neglected. The corresponding corrections terms to the total energy density ϵ are,

   a) Classical Coulomb effect, which accounts for the electrostatic interaction between electrons and ions,

   $$\epsilon_{\mathrm{C}}(\xi) = -\frac{32K}{3}\frac{9}{10}\left(\frac{4}{9\pi}\right)^{1/3}\alpha Z^{2/3}\sinh^4\frac{\xi}{4}. \tag{6.2.5}$$

   with $K = \frac{\pi m_e^4 c^5}{4\hbar^3}$, m_e the electron mass and α the fine-structure constant.

   b) The Thomas-Fermi correction. This correction accounts for a deviation of the electron charge distribution from uniformity and is given by,

   $$\epsilon_{TF}(\xi) = -\frac{32K}{3}\frac{162}{175}\left(\frac{4}{9\pi}\right)^{2/3}\alpha^2 Z^{4/3}\cosh\frac{\xi}{4}\sinh^3\frac{\xi}{4}. \tag{6.2.6}$$

   c) Exchange Energy. This contribution accounts for the fact that electrons are indistinguishable and it is necessary to consider electron interactions via the transverse electromagnetic field. To evaluate this correction, the influence of the ionic charge on the electron's charge distribution is omitted,

   $$\epsilon_{\mathrm{ex}} = -\frac{3}{128\pi}\alpha\,\frac{32K}{3}\left[18 + 12\xi\sinh\frac{\xi}{2} - 3\xi^2 - 16\cosh\frac{\xi}{2} - 2\cosh\xi\right]. \tag{6.2.7}$$

d) Correlation energy. This is the next term for the interaction energy between electrons. The correlation energy correction accounts for how affected is an electron due to the presence of others

$$\epsilon_{\mathrm{corr}} = \frac{32K}{3}\alpha^2 \sinh^3\frac{\xi}{4}\left(-0.0277 + 0.031\log_e\left[\frac{\alpha}{\sinh\frac{\xi}{4}}\right]\right). \tag{6.2.8}$$

2. Ion motion: estimation of the zero-point energy of the actual motion of the ions produced by another ions as well as electrons. The computation is based on the motion of a single ion at a time. However, this contribution is not relevant for large nuclei and low density. The Coulomb effects due to electrons predominate.

3. Other corrections: These are some types of corrections which are small or even absent.

   a) Self-energy term. It is expected that the Fermi gas of electrons affects the self–energy of an individual electron. This comes from the virtual emission of a photon accompanied by the recoil of the electron and followed by the re–absorption of the photon.

   b) Absence of corrections due to a potential gradient. Besides the electric field due to individual nuclei in the star, as described in item 1, there is a macroscopic electrostatic field through the spherically symmetric star $\phi(r)$. However, when calculating the total energy density ϵ, electrons were considered free. This is, the potential ϕ created by the macroscopic electric field was neglected.

   c) Effect of the potential. If on the contrary, a constant potential $\phi(r) = \phi_0$ is introduced in each region of the star, it can be demonstrated that the EoS is unaffected by the numerical value of ϕ_0. However, if we are dealing with a Lorentz invariant scalar potential V instead of an electrostatic potential ϕ_0, in the definition of x and energy density ϵ, the electron mass would be replaced by $(m_e + Vc^{-2})$.

4. Restrictions on Z (atomic charge) and A (atomic mass). So far these quantities have been considered as constant and independent of the electron number density. However, even at zero temperature reactions such as inverse β–decay can occur if the density is high enough. Such reactions, change the electron per nucleon fraction, and thus affect the EoS. Salpeter briefly discuss this correction indicating that values for Z and A as continuous functions of the density have to be derived.

The inclusion of electrostatic contributions in the EoS, results in a more realistic approach, since they account for interactions among electrons and nuclei. The total energy density for a non-ideal gas is therefore,

$$\epsilon(\xi) = \epsilon_{\rm n}(\xi) + \epsilon_{\rm e}(\xi) + \epsilon_{\rm c}(\xi) + \epsilon_{\rm TF}(\xi) + \epsilon_{\rm ex}(\xi) + \epsilon_{\rm corr}(\xi). \tag{6.2.9}$$

Using Eq. (6.2.3), the corresponding pressure corrections due to Coulomb effects are,

$$\begin{aligned}
P_{\rm C} &= -\frac{16}{5}K\alpha Z^{2/3}\left(\frac{4}{9\pi}\right)^{1/3}\sinh^4\frac{\xi}{4}, \\
P_{\rm TF} &= -\frac{576}{175}K\alpha^2 Z^{4/3}\left(\frac{4}{9\pi}\right)^{2/3}\sinh^4\frac{\xi}{4}\tanh\frac{\xi}{4}, \\
P_{\rm ex} &= -\frac{\alpha}{2\pi}K\left[\cosh\xi + 8\cosh\frac{\xi}{2} - 6\xi\sinh\frac{\xi}{2} + \frac{3}{2}\xi^2\right. \\
&\qquad \left. -9 - \frac{4}{3}\tanh\frac{\xi}{4}\left(\sinh\xi - 2\sinh\frac{\xi}{2} - 3\xi\cosh\frac{\xi}{2} + 3\xi\right)\right], \\
P_{\rm corr} &= -\frac{32}{9}0.0311K\alpha^2\sinh^3\frac{\xi}{4}.
\end{aligned} \tag{6.2.10}$$

6.2.3 Internal Structure

Coupling the classical form of the equation of hydrostatic equilibrium and the mass equation given by,

$$\frac{dP}{dr} = -\frac{GM(r)\epsilon(r)}{c^2r^2}, \tag{6.2.11}$$

$$\frac{dM}{dr} = \frac{4\pi r^2\epsilon(r)}{c^2}, \tag{6.2.12}$$

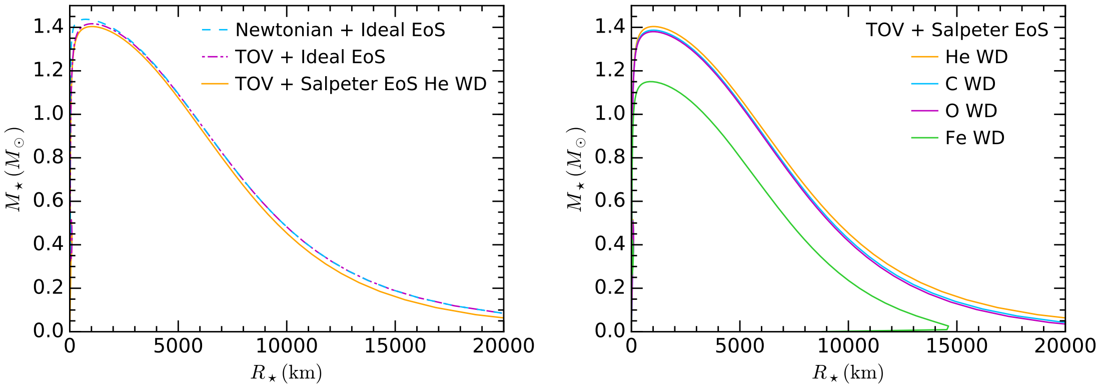

Figure 6.1: Mass radius relation for white dwarfs calculated with the ideal and the Salpeter equations of state for different chemical compositions.

to the EoS $p = p(\epsilon)$ given by the parametric forms of the energy density $\epsilon(\xi)$ and pressure $p(\xi)$ of a degenerate Fermi gas, we obtain the pressure and mass at different shells of the stellar interior.

If the star is very compact, then relativistic effects have to be taken into account. Hence, the Newtonian expression for the equation of hydrostatic equilibrium is replaced by its GR counterpart, the Tolman–Oppenheimer–Volkoff (TOV) equation. The compact object is in gravitational equilibrium due to the balance of the internal pressure support against the gravitational field of the star. The TOV equation is derived from the Einstein's field equation,

$$G_{\alpha\beta} + \Lambda_{\alpha\beta} = \frac{8\pi G}{c^4} T_{\alpha\beta}. \tag{6.2.13}$$

In this equation, $G_{\alpha\beta}$ is the Einstein curvature tensor and $\Lambda_{\alpha\beta}$ the cosmological constant that can be ignored at galactic scales. For a non-rotating spherical compact object, we use the Schwarschild metric given in spherical coordinates,

$$g_{\mu\nu}(r) = \mathrm{diag}(e^{\nu(r)}, -e^{\lambda(r)}, -r^2, -r^2\sin^2\theta). \tag{6.2.14}$$

And the principal task is to find the form of the $\nu(r)$ and $\lambda(r)$ functions so that we can determine the TOV equation. In the process of finding the latter we also obtain

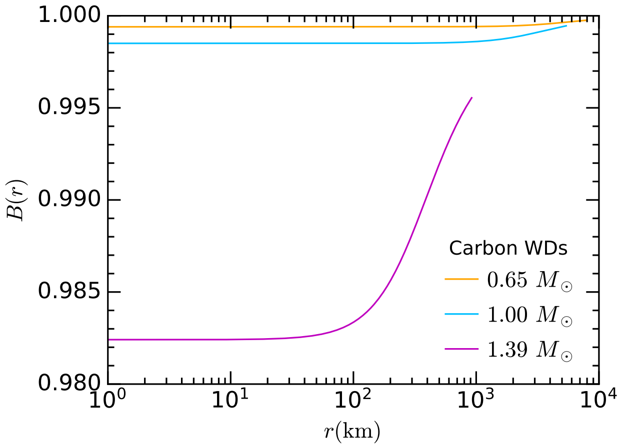

Figure 6.2: B radial profile for carbon WDs of $0.65\mathrm{M}_\odot$, $1\mathrm{M}_\odot$ and $1.4\mathrm{M}_\odot$ with Salpeter EoS.

the following relation[1]

$$\frac{d}{dr}B(r) = \frac{\frac{8\pi G}{c^4}rP(r) + \frac{2GM(r)}{c^2r^2}}{1-\frac{2GM(r)}{c^2r}}B(r). \tag{6.2.15}$$

Contrary to NSs, GR corrections encoded in $B(r)$ for a WD of mass $1\mathrm{M}_\odot$ or even a WD as massive as $1.4\mathrm{M}_\odot$ are always close to 1 which means that the relativistic effects due to the compactness of the star can be safely neglected, see Fig. 6.2.

Finally, the TOV equation is given by,

$$\frac{dP(r)}{dr} = -\frac{G\epsilon(r)M(r)}{r^2}\left[1+\frac{P(r)}{c^2\epsilon(r)}\right]\left[1+\frac{4\pi r^3}{c^2M(r)}P(r)\right]\left[1-\frac{2M(r)}{c^2r}\right]^{-1}. \tag{6.2.16}$$

In the left panel of Fig. 6.1, the mass radius relation for WDs of any composition with $\mu_e = 2$ is obtained. To illustrate the effect of including GR corrections we couple the ideal EoS to the classical form of the equation of hydrostatic equilibrium (dashed blue line), and to the TOV equation (dashed-dotted magenta line). Finally, we couple the Salpeter EoS for He WDs to the TOV equation (orange solid line). We notice that for massive WDs relativistic effects are significant. On the other hand, Coulomb corrections are significant for less dense WDs.

---

[1] On the surface of a compact object of mass $M_\star$ and radius $R_\star$ it is easy to show that

$$B(R_\star) = 1 - \frac{2GM_\star}{c^2R_\star}.$$

.

The right panel of Fig. 6.1 shows the mass radius relation for WDs made of different elements: helium (He), carbon (C), oxygen (O) and iron (Fe). For all cases the relation was determined using the TOV equations with Salpeter EoS. For a WD composed of heavy elements the energy density is higher. Hence, the negative contributions to the energy density and pressure from electron interactions with electrons and ions are higher than for lighter elements. As a consequence for a Fe WD, the maximum mass the star can achieve is significantly below the Chandrasekhar mass limit, contrary to WDs made of lighter elements [193].

6.2.4 WD Observations

Most WDs are thought to be composed of carbon and oxygen. Spectroscopy shows that their emitted light comes from an atmosphere which is either H– or He– rich. The dominant element is usually 1000 times more abundant than all the other elements. Due to the high surface gravity, heavy elements are on the core and lighter elements on the top.

Since electrons have a large mean free path due to the Fermi sea, there is high conductivity [194]. Therefore, the core of a WD is considered to have a uniform temperature. The core is covered by non degenerate outer layers in "radiative equilibrium" and there is an energy flux carried outward by the diffusion of photons from the outer layers [195]. If we know the temperature gradient, is possible to find the surface effective temperature T_{eff} in terms of the core temperature T_c. The luminosity L, of a WD with mass $M_\star$ and radius $R_\star$, is related to the core temperature T_c by [196, 197][1],

$$L = 5.7 \times 10^5 \mathrm{erg\,s}^{-1} \frac{\mu}{\mu_e^2} \frac{1}{Z(1+X_h)} \frac{M_\star}{M\odot} \left(\frac{T_c}{K}\right)^{3.5} . \tag{6.2.17}$$

Notice that this result is similar to $L = 4\pi\sigma_B R_\star^2 T_{eff}^4$ which is the luminosity for a black body, where σ_B, is the Stefan–Boltzmann constant. However, Eq. (6.2.17)

---

[1] Note that in Eq. (4.1.3) and Eq. (4.1.10) of Reference [196] factors of $1/K^{-3.5}$ and $1/K^{1.5}$, respectively, are missing and have been added here. The later can be checked in Ref. [197].

Type	Spectrum
DA	Only Balmer emission lines (H), no He or metals
DB	He I lines, no H or metals
DC	Continuous
DO	He II strong, He I or H present
DZ	Metal lines only, no H or He lines
DQ	Carbon features, atomic or molecular

Table 6.1: White dwarfs spectral classification. The letter "D" in these designation stands for "degenerate" in the original classification [201].

involves the temperature of the core T_c instead of the observable temperature of the surface T_{eff}. This suggest that the observed temperature, known as effective temperature, is related to the core temperature by

$$T_c^{7/2} = \frac{4\pi\sigma_B R_\star^2}{5.7\times 10^5 \mathrm{erg\,s}^{-1}} \frac{\mu_e^2}{\mu} Z(1+X_h) \frac{M_\odot}{M_\star} \frac{T_{eff}^4}{K^{-7/2}}, \tag{6.2.18}$$

where μ is the mean molecular weight and $\mu_e = Y_e^{-1}$ with Y_e the mean number of electrons per nucleon. In the latter expression, Z stands for the fractional abundance of elements heavier than hydrogen and helium and X_h is the fractional abundance of hydrogen [198]. For more details, we refer the reader to Appendix G.

Spectral Types.

Colour photometry is the observed correlation between the colour of the star and the strength of specific absorption lines which leads to a classification scheme into spectral types. Additionally, each spectral type corresponds to a certain range of colour temperature; hotter stars are bluer and cooler stars are redder. The spectral energy distribution is determined by 1) the temperature structure, characterised by the effective temperature T_{eff}, 2) the pressure stratification, determined by the surface gravity g and the chemical composition of the atmosphere layers. The classification criteria for major spectral types are listed in Table 6.1 [199, 200].

Observations and Abundances.

WD mass distributions can be found in the literature. For instance, in refs. [185] and [190], the authors presented the mass distribution for all pure DA WDs detected in the Sloan Digital Sky Survey (SDSS) data release 10,[1] as well as DB WDs and compared them with Monte Carlo simulations. The mass distribution for DAs with $T_{eff} \geq 13000\,\mathrm{K}$ and DBs with $T_{eff} \geq 16000\,\mathrm{K}$ have a maximum around $M_\star = 0.624\mathrm{M}_\odot$. Additionally observed WD mass distribution samples from SDSS and Gaia local 20 pc surveys were explored [186, 202]. The samples are restricted to $16000 < T_{eff}(\mathrm{K}) < 22000$, $16 < g(mag) < 18.5$ and to single non-magnetic WDs. The simulations of the local 20 pc predict a larger maximum mass ($M_\star = 0.702\mathrm{M}_\odot$) in comparison to the SDSS ($M_\star = 0.642\mathrm{M}_\odot$), this is in agreement with observations. However, in both samples, simulations predicted a larger number of WDs. Probably causes are, binary evolution, neglect of magnetic white dwarfs (SDSS), and unidentified faint massive objects (20 pc sample). It is expected that most of these uncertainties will be improved by Gaia [203].

6.3 Capture Rate

When DM particles are gravitationally attracted to WDs, the probability they scatter with the constituents of the stellar matter increases. These interactions can provoke that DM particles lose enough energy so they become gravitationally bound to the star. In principle, DM can scatter off nuclei and electrons of the stellar matter. In this work, we only consider DM scattering off nuclei. We first pay attention to the capture rate in the optically thin limit. Further considerations such as the star opacity will be reviewed later in the section.

The rate at which DM particles are captured into massive objects such as planets or the Sun after a single scattering, was derived by Gould in Ref. [176, 177]. Later, this computation was improved in Ref. [184], including velocity and momentum dependent DM-nucleus interactions, the inner structure and the opacity of the Sun. Recently, the capture rate formalism for compact stars has been improved, including

---

[1] The Sloan Digital Sky Survey or SDSS is a major multi-spectral imaging and spectroscopic redshift survey.

among other effects GR corrections, see Ref. [60]. In order to include GR effects due to the compactness of the star, the Schwarzschild metric, Eq. (6.2.14), was used on the star surface, and the TOV equations inside, Eq. (6.2.16). Following the formalism given by Gould, the authors arrived to a capture rate that accounts for relativistic effects induced by the compact star on the DM flux. Relativistic corrections to the capture rate are encoded in $B(r)$ given in Eq. (6.2.15). In a NS $B(r)$ varies in the range of $0.2 - 0.7$ [60] which indicates that relativistic effects are not negligible. Conversely, as shown in Fig. 6.2, even for the heaviest WD $B(r)$ remains approximately constant and very close to 1. Consequently, in order to calculate the capture rate in WDs, it is safe to follow the non-relativistic approach for the Sun given in Ref. [184].

To derive the capture rate, we consider the number of DM particles per unit time crossing a spherical surface of radius r and thickness dr,

$$\frac{dN}{dt} = 2\pi \frac{\rho_\chi}{m_\chi} \frac{f(u)du}{u} \frac{JdJ}{m_\chi^2}, \tag{6.3.1}$$

where J is the DM angular momentum with a maximum given by $J_{clas}^{max} = m_\chi v_e(r) r$. Here, ρ_χ is the local DM density, m_χ is the DM mass, $v_e(r)$ is the star escape velocity and $f(u)$ is the DM velocity distribution assumed to be Maxwell–Boltzmann and, in the limit of $T_\star \to 0$, where $T_\star$ is the temperature of the isothermal region (core temperature T_c), it reads,

$$\lim_{T_\star \to 0} f(u)du = \frac{u}{v_d v_\star} \sqrt{\frac{3}{2\pi}} \left[e^{-\frac{3}{2v_d^2}(u-v_\star)^2} - e^{-\frac{3}{2v_d^2}(u+v_\star)^2} \right] du, \tag{6.3.2}$$

where u stands for the DM velocity far away from the star, $v_\star$ is the WD velocity relative to the Galactic rest frame and v_d is the Galactic halo velocity dispersion.

In order to obtain the differential capture rate, the number of DM particles entering the star has to be multiplied by the scattering rate $\Omega^-(w)$, see Sec. 6.3.1. Finally, after integrating over the DM momentum J, the differential capture rate is given by,

$$\frac{dC}{dr} = 4\pi r^2 \frac{\rho_\chi}{m_\chi} \frac{w}{u} f(u) du \Omega^-(w), \tag{6.3.3}$$

where $\dot{r} = \vec{w}$ indicates the DM velocity once it has fallen close to the star and,

$$w^2 = u^2 + v_e(r)^2. \tag{6.3.4}$$

The WD escape velocity is defined as,

$$v_e^2(r) = 1 - B(r). \tag{6.3.5}$$

The differential capture rate in Eq. (6.3.3) has two main components, one from astrophysics and the other from particle physics. On the astrophysics side, we have the DM flux $(\rho_\chi/m_\chi)(f(u)du/u)$. On the other hand, the particle physics description is encoded in the $\Omega^-(w)$ function defined as the DM interaction rate i.e. the rate at which DM scatters off stellar matter, see Sec. 6.3.1 for details.

The expression for the capture rate is,

$$C = \int_0^{R_\star} 4\pi r^2 \frac{\rho_\chi}{m_\chi} \frac{w}{u} f(u) du \Omega^-(w). \tag{6.3.6}$$

This definition differs from that given in Ref. [60] by the $B(r)$ term in the denominator.

6.3.1 Interaction Rate

The next step in the computation of the capture rate is to evaluate the interaction rate, $\Omega^-(w)$, which is given as a function of the differential scattering cross section. A DM particle will be captured in the WD if its final velocity, after scattering off stellar matter, results less than or equal to the escape velocity. Otherwise the rate will correspond to particles escaping the star after scattering. Then, the DM interaction rate is given by,

$$\Omega^-(\omega) = \int_0^{v_e} dv\, R^-(\omega \to v), \tag{6.3.7}$$

where R^- is the DM differential interaction rate.

The differential interaction rate $R^-(w \to v)$ indicates the rate at which a DM particle with velocity w scatters off a nucleus to a final velocity v. In the lab frame, this rate is given by the product of the differential cross section, $d\sigma/dv$, the Maxwell-Boltzmann number density and the relative velocity between a DM particle with velocity w and a nucleus of velocity v_T [204],

$$dR = \frac{d\sigma_{T\chi}}{dv}(v_T^2 + w^2 + 2v_T w\cos\theta)^{1/2}\frac{2}{\pi^{1/2}}n_T(r)\kappa^3 v_T^2 e^{-\kappa^2 v_T^2}\theta(1-|\cos\theta|)dv_T\, d\cos\theta, \tag{6.3.8}$$

where θ is the lab frame angle between the direction of the incoming and outgoing DM particle, n_T is the target nucleus number density and $\kappa^2 = m_T/2T_\star$, where $T_\star$ is the nuclei temperature and m_T the nucleus mass. This can be rewritten in the centre of mass (com) frame, as a function of s and t which are respectively the velocity of the centre of mass and the velocity of the DM particle before the collision in the centre of mass frame. Therefore, w and v_T should be written in terms of the s and t velocities, this can be done using the following relations,

$$\begin{aligned} w &= s + t, \\ (1+\mu)s &= |\mu w + v_T|, \\ (1+\mu)t &= |w - v_T|, \end{aligned} \tag{6.3.9}$$

where $\mu = m_\chi/m_T$, $\mu_\pm = (\mu \pm 1)/2$. The nucleus velocity written as a function of s and t is determined by combining the last two expressions in Eq. (6.3.9),

$$v_T^2 = 2\mu\mu_+ t^2 + 2\mu_+ s^2 - \mu w^2, \tag{6.3.10}$$

and Eq. (6.3.8) in the com reads,

$$dR = \frac{32\mu_+^4}{\pi^{1/2}}\kappa^3 n_T(r)\frac{t^2 s}{w}e^{-\kappa^2 v_T^2}\frac{d\sigma_{T\chi}}{dv}\Theta(w - |s-t|)\Theta(s+t-w)ds dt, \tag{6.3.11}$$

where we have substituted $d\cos\theta = \frac{4\mu_+^2 t}{wu}dt$ and $v_T dv_T = 2\mu_+ s ds$. The differential DM-nucleus cross section in the com frame can be expressed as,

$$\frac{d\sigma_{T\chi}}{dv} = \frac{d\sigma_{T\chi}}{d\cos\theta_{cm}}\frac{d\cos\theta_{cm}}{dv}, \tag{6.3.12}$$

where the angle θ_{cm} is recast in terms of the variables s and t by finding the angle between t and t', where the latter is the DM velocity in the com frame after scattering. Therefore, $\cos\theta_{cm}$ is given by,

$$\cos\theta_{cm} \equiv \cos(\theta_{st} \pm \theta_{st'}) = \cos\theta_{st'}\cos\theta_{st} + \sin\theta_{st'}\sin\theta_{st}\sin\phi_{st'}, \tag{6.3.13}$$

$\theta_{st'(st)}$ is the angle between $t'(t)$ and s. $\phi_{st'}$ is the azimuthal angle of the DM speed after the scattering. From Eq. (6.3.9)

$$\cos\theta_{st'} = \frac{v^2 - s^2 - t^2}{2st} \rightarrow \frac{d\cos\theta_{st'}}{dv} = \frac{v}{st}. \tag{6.3.14}$$

Finally the differential interaction rate is given by [204],

$$\begin{aligned} R(w \to v) = \int_0^\infty ds \int_0^\infty dt \frac{32\mu_+^4}{\sqrt{\pi}}\kappa^3 n_T(r)\frac{d\sigma_{T\chi}}{d\cos\theta}\frac{vt}{w}e^{-\kappa^2 v_T^2} \\ \times\, \Theta(t+s-w)\Theta(w-|t-s|)\Theta(v-|s-t|)\Theta(s+t-v), \end{aligned} \tag{6.3.15}$$

where $\Theta(v-|s-t|)\Theta(s+t-v)$ are introduced to account for $\cos\theta_{st'} = \pm 1$ in Eq. (6.3.14).

As a first approximation, we can take the $T_\star \to 0$ limit, since the thermal motion of the nuclei is negligible in the capture process. Following Ref. [184] one arrives to [177],

$$R^-(w \to v) = \frac{4\mu_+^2}{\mu w} n_T(r)\frac{d\sigma_{T\chi}}{d\cos\theta}\,\Theta\left(v - w\frac{|\mu_-|}{\mu_+}\right). \tag{6.3.16}$$

Plugging this expression into Eq. (6.3.7), the DM interaction rate is then given by,

$$\Omega^-(w) \;=\; \frac{4\mu_+^2}{\mu w} n_T(r)\int_{w\frac{|\mu_-|}{\mu_+}}^{v_e} dv v \frac{d\sigma_{T\chi}}{d\cos\theta}\Big(q_{tr}, w\Big). \tag{6.3.17}$$

The transfer momentum is given by,

$$q_{tr}^2 = (1 - \cos\theta_{\rm cm})v_r^2\frac{2m_\chi^2}{(1+\mu)^2}. \tag{6.3.18}$$

From Eq. (6.3.9), we rewrite the relative velocity as $v_r^2 = t^2(1+\mu)^2$, leading to

$$q_{tr} = (1 - \cos\theta_{cm})2m_\chi^2 t^2. \tag{6.3.19}$$

From Eq. (6.3.9) and Eq. (6.3.13), and averaging over the azimuthal angle of DM speed after scattering, q_{tr} reads,

$$q_{tr}^2 = 2m_\chi^2 t^2 \left(1 - \frac{(s^2+t^2-v^2)(s^2+t^2-w^2)}{4s^2t^2}\right). \tag{6.3.20}$$

Assuming the target velocity is zero, we arrive to

$$q_{tr}^2 = m_\chi^2 \frac{w^2-v^2}{\mu}. \tag{6.3.21}$$

Before computing the capture rate in the optically thin limit, it is worth to define a natural limit for this rate. This is the geometric limit which corresponds to the case where DM capture occurs on the surface of the star. The capture rate cannot exceed this limit. The geometric limit of the capture rate in Eq. (6.3.6) takes the following form,

$$C_{geom} = \frac{\pi R_\star^2 \rho_\chi}{3v_\star m_\chi}\left[(3v_{esc}^2(R_\star) + 3v_\star^2 + v_d^2)\mathrm{erf}\left(\sqrt{\frac{3}{2}}\frac{v_\star}{v_d}\right) + \sqrt{\frac{6}{\pi}}v_\star v_d e^{-\frac{3v_\star^2}{2v_d^2}}\right]. \tag{6.3.22}$$

It is obtained by assuming the maximum interaction rate i.e. $\Omega^- \to 1$. In this limit, the DM capture rate is proportional to $1/m_\chi$ and it is independent of the DM-proton cross section. Fig. 6.3 shows the capture rate in the geometric limit for WDs made of different elements (He, C, O and Fe) in terms of their radius ($R_\star$) and their masses ($M_\star$). We see that there is a maximum capture rate for He, C and O WDs with $R_\star \simeq 6 \times 10^3\,\mathrm{km}$ and $M_\star = 0.85\,\mathrm{M}_\odot$. The maximum in the geometric limit is due to the mass radius relationship. In other words the escape velocity is suppressed in lighter WDs due to a larger radius which reduces the capture rate.

The geometric limit in Eq.(6.3.22) is unique for all the star constituents, however the saturation limit, will be different for every species. It restricts the value of the capture rate at large cross sections, however, contrary to the geometric limit, the interaction rate is different from 1. For WDs made of only one element, the saturation limit is given by,

$$C_{sat} = \pi R_\star^2 \frac{\rho_\chi}{m_\chi}\int_0^{v_e\sqrt{\mu}/|\mu_-|} du f(u) \frac{4\mu_+^2}{\mu}\int_{w\frac{|\mu_-|}{\mu_+}}^{v_e} dv v \frac{d\sigma_{T\chi}}{d\cos\theta}(q_{tr}, w, v)\Bigg|_{r=R\star}, \tag{6.3.23}$$

we refer the readers to Ref. [184] for details.

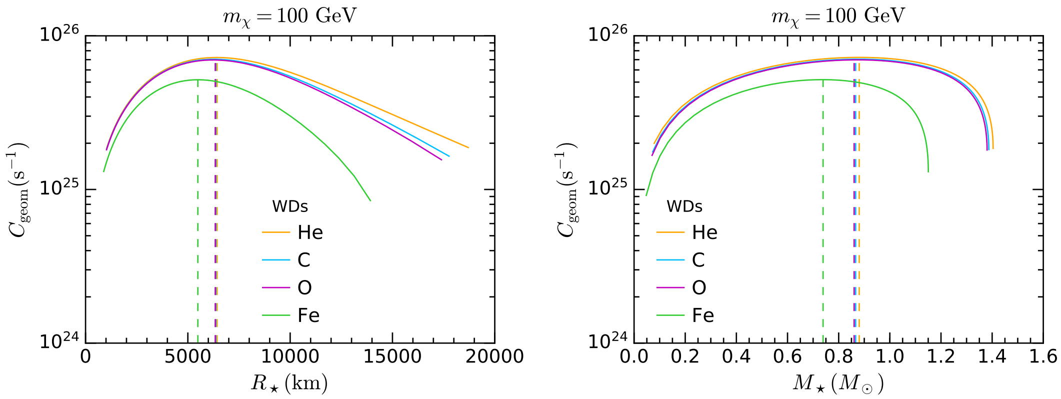

Figure 6.3: Capture rate in the geometric limit for different WDs as a function of $R_\star$ (left) and $M_\star$ (right).

6.3.2 EFT operators in the non-relativistic limit

In this section we will consider generic fermionic DM interactions with ordinary matter. Such interactions are described by means of dimension 6 Effective Field Theory (EFT) operators [205, 206]. At high–energy, the operators are given in terms of quarks and gluons [206]. In table 6.2, we show 5 of the 10 dimension 6 operators. These are spin independent (SI). We only use SI operators because we are assuming carbon-12 WDs, which has nuclear spin zero. However, if DM and the targets are not relativistic, the interactions will happen at very low energies. Hence, we should calculate the EFT operators in the non-relativistic limit. Therefore, we now go from quark–gluon to nucleon level operators by calculating the matrix element $\langle N|\bar{q}q|N\rangle$.

By expanding the Dirac spinor functions in their non relativistic limits and evaluating the matrix element $\langle \chi, N|D_i|N, \chi\rangle$, where D_i corresponds to the operators given in Table 6.2, we determine low energy operators at nucleon level. In the fourth column we show the respective DM–proton scattering cross–sections in the non-relativistic limit with $\mu = m_\chi/m_N$. These operators are a linear combination of the following non-relativistic (NR) operators [208],

$$\begin{aligned} O_1 &= \mathbb{1}, & O_{10} &= i(\vec{s}_N \cdot \vec{q}_{tr}), \\ O_8 &= \vec{s}_\chi \cdot \vec{w}^\perp, & O_{11} &= i(\vec{s}_\chi \cdot \vec{q}_{tr}), \\ O_9 &= i\vec{s}_\chi \cdot (\vec{s}_N \times \vec{q}_{tr}), & O_{12} &= \vec{w}^\perp \cdot (\vec{s}_\chi \times \vec{s}_N), \end{aligned} \tag{6.3.24}$$

Name	Operator	Coupling	$\frac{d\sigma}{d\cos\theta}(w^2, q_{tr}^2)$
D1	$\bar{\chi}\chi\,\bar{q}q$	y_q/Λ^2	$\frac{(c_N^S)^2}{\Lambda^4}\frac{m_\chi^2}{2\pi(\mu+1)^2}$
D2	$\bar{\chi}\gamma^5\chi\,\bar{q}q$	iy_q/Λ^2	$\frac{(c_N^S)^2}{\Lambda^4}\frac{q_{tr}^2}{8\pi(\mu+1)^2}$
D5	$\bar{\chi}\gamma_\mu\chi\,\bar{q}\gamma^\mu q$	$1/\Lambda^2$	$\frac{(c_N^V)^2}{\Lambda^4}\frac{m_\chi^2}{2\pi(\mu+1)^2}$
D6	$\bar{\chi}\gamma_\mu\gamma^5\chi\,\bar{q}\gamma^\mu q$	$1/\Lambda^2$	$\frac{(c_N^V)^2}{\Lambda^4}\frac{4m_\chi^2 w^2+\left(\mu^2-2\mu-1\right)q_{tr}^2}{8\pi(\mu+1)^2}$
D10	$\bar{\chi}\sigma_{\mu\nu}\gamma^5\chi\,\bar{q}\sigma^{\mu\nu}q$	i/Λ^2	$\frac{(c_N^T)^2}{\Lambda^4}\frac{8m_\chi^2 w^2-\left(\mu^2+4\mu+1\right)q_{tr}^2}{2\pi(\mu+1)^2}$

Table 6.2: EFT operators [206] with spin-independent interactions and differential cross sections for the scattering of Dirac DM off a nucleon $N = p, n$. Here, μ stands for $\mu = m_\chi/m_N$. Here, q_{tr} and w are defined for nucleons. The effective couplings for each operator are given as a function of the quark Yukawa coupling, y_q, and the cutoff scale, Λ. The fourth column shows the differential cross section at low energy [207].

Name	NR limit
D1	$\frac{c_N^S}{\Lambda^2}(4m_N m_\chi O_1)$
D2	$\frac{c_N^S}{\Lambda^2}(-4m_N O_{11})$
D5	$\frac{c_N^V}{\Lambda^2}(4m_N m_\chi O_1)$
D6	$\frac{c_N^V}{\Lambda^2}8m_\chi(m_N O_8 + O_9)$
D10	$\frac{c_N^T}{\Lambda^2}8(m_\chi O_{11} - m_N O_{10} - 4m_\chi m_N O_{12})$

Table 6.3: EFT operators [206] with spin-independent interactions and differential cross sections for the scattering of Dirac DM off a nucleon $N = p, n$ in terms of the non-relativistic (NR) operators [208].

where $\vec{s}_N$ and $\vec{s}_\chi$ are the nucleon and DM spin, respectively and the perpendicular DM relative velocity is defined as $w^\perp = \vec{w} - q^2/2\mu_N$ with μ_N the DM-nucleon reduced mass. In Table 6.3 we show the SI EFT operators in terms of the NR operators given in Eq. (6.3.24). The coefficients for the differential cross sections in Table 6.2 read,

$$c_N^S = \frac{\sqrt{2}\,m_N}{v}\left[\sum_{q=u,d,s} f_{T_q}^{(N)} + \frac{2}{9} f_{T_G}^{(N)}\right], \tag{6.3.25}$$

$$c_N^V = 3, \tag{6.3.26}$$

$$c_N^T = \sum_{q=u,d,s} \delta_q^{(N)}, \tag{6.3.27}$$

where $v = 246$ GeV is the EW vacuum expectation value, $f_{T_q}^{(N)}$, $f_{T_G}^{(N)}$ and $\delta_q^{(N)}$ are the hadronic matrix elements, determined either experimentally or by lattice QCD simulations. Note that $f_{T_G}^{(N)} = 1 - \sum_{q=u,d,s} f_{T_q}^{(N)}$. The values of the hadronic matrix elements for protons are listed in Table 6.4.

q	$f_{T_q}^{(p)}$	$\delta_q^{(p)}$	$f_{T_q}^{(n)}$	$\delta_q^{(n)}$
u	0.0153	0.840	0.0110	-0.230
d	0.0191	-0.230	0.0273	0.840
s	0.0447	-0.046	0.0447	-0.046

Table 6.4: Hadronic matrix elements for nucleons [209].

To compute the corresponding DM-nucleus cross section we follow Ref. [208],

$$\frac{d\sigma_{T\chi}}{d\cos\theta} = \frac{1}{32\pi} \frac{\overline{|\mathcal{M}_T|}^2}{(m_\chi + m_T)^2}\,. \tag{6.3.28}$$

The DM-nucleus average matrix elements depend on the momentum transferred q_{tr} and in some cases on the relative velocity $v_r = |\vec{w} - \vec{v}_T|$ between the DM and the nucleus through the following expression

$$\overline{|\mathcal{M}_T|}^2 = \frac{m_T^2}{m_N^2} \sum_{N,N',i,j} C_i^N C_j^{N'} F_{ij}^{NN'}(q_{tr}^2), \tag{6.3.29}$$

where the C_i^N coefficients correspond to the NR operator O_i prefactors in the right column of Table 6.3. Note that q_{tr} and w are defined with respect to the nucleus. $F_{ij}^{NN'}$ are the form factors in terms of the transferred momentum q_{tr}, $N, N' = p, n$ and i, j indicates NR operators in the right column of Table 6.3. The form factors $F_{ij}^{NN'}(q_{tr}^2)$ are given in terms of the isoscalar (0) and isovector (1) basis F_{ij}^{ab}, whose non-zero elements for carbon–12 are a function of [210],

$$\begin{aligned} F_M^{00} &= 0.565882 e^{-2y}(2.25 - y)^2 \\ F_{\Phi''}^{00} &= 0.0480805 e^{-2y} \\ F_{M\Phi''}^{00} &= e^{-2y}(-0.371134 + 0.16498y), \end{aligned} \tag{6.3.30}$$

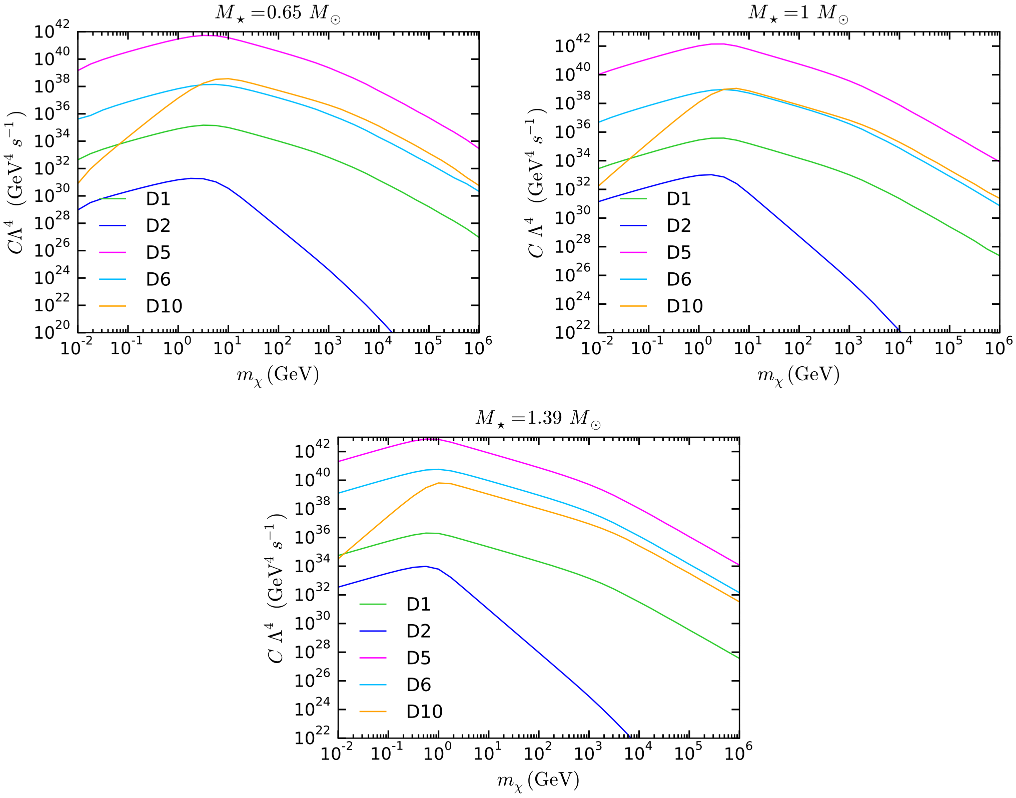

Figure 6.4: Capture rate as function of the DM mass in the optical thin limit for the SI EFT operator D1 (green), D2 (blue), D5 (magenta), D6 (light blue) and D10 (orange) given in Table 6.2. The capture is computed in the carbon WDs in Table 6.5.

where $y = (bq_{tr}/2)^2$ with $b = \sqrt{41.467/(45A^{-1/3} - 25A^{-2/3})}\,\mathrm{fm}$ and A the atomic mass of the target. The relations between the nuclear response functions F_{ij}^{ab} and $F_{ij}^{NN'}$ are given in Ref. [205]. E.g. F_{ij}^{00} is,

$$F_{ij}^{00} = \frac{1}{4}\left(F_{ij}^{pp} + F_{ij}^{nn} + F_{ij}^{pn} + F_{ij}^{np}\right). \tag{6.3.31}$$

In Fig. 6.4 we compare the capture rate in the optically thin limit for the SI EFT operators, D1 (green), D2 (blue), D5 (magenta), D6 (light blue) and D10 (orange) given in Table 6.3, for the 3 carbon WDs with Salpeter EoS in Table 6.5, we assume dispersion velocity $v_d = 270\,\mathrm{kms}^{-1}$ and star velocity $v_\star = 220\,\mathrm{kms}^{-1}$ and a DM density $\rho_\chi = 0.4\,\mathrm{GeV\,cm}^{-3}$. We notice that, for DM masses above $\sim 10^3\,\mathrm{GeV}$, the capture rate is suppressed for all operators. This is because we have assumed capture of DM after a single scattering. Such assumption breaks down for massive

DM particles which require more than one scattering in order to be captured [182]. On the other hand, the suppression at low masses comes from the form factor and its dependence on the transferred momentum q_{tr}^2, being the operator D10 the most deflected. As expected, the capture rate is more suppressed for less massive WDs due to their weaker gravitational potential. The capture rate for D2 is more suppressed, at large DM masses, with respect to the other operators since the interaction of the DM with the nucleon is only momentum transfer dependent.

6.3.3 White Dwarf Opacity

Another physical consideration we have to account for is the star opacity. The DM flux of particles passing through the WD can be significantly reduced at deeper layers. Recall we have neglected corrections due to multi–scattering. Therefore, in order to incorporate the opacity of the WD into the capture rate computation, we follow the approach outlined in Ref. [60] for single scattering which calculates an optical factor eta,

$$\eta = e^{-\tau_\chi}, \tag{6.3.32}$$

which is given in terms of an optical depth τ_χ calculated along the DM orbit inside the star instead of assuming that DM particles follow a linear trajectory [184]. The optical depth indicates how transparent is the stellar matter to DM particles, in a certain position within the star. The optical factor removes DM particles from the incoming flux once they are captured.

The integral of the interaction rate along the path a DM particle follows until is captured is the optical depth,

$$\tau_\chi(r) = \int_\gamma \frac{d\tau}{dr}\Omega^-(r)dr, \tag{6.3.33}$$

where γ is the DM path and τ is the proper time. DM particles travelling towards the star can follow two possible paths in order to reach a point x over a shell of radius r within the star. The first path corresponds to the optical depth τ_χ^- and it goes from the WD surface to x, without passing the perihelion. The second path corresponds to the optical depth τ_χ^+ and goes from the WD surface to the perihelion and then to the point x. These two possible optical depths are,

$$\begin{aligned}
\tau_\chi^-(r) &= \int_r^{R_\star} \frac{dx}{\sqrt{1-\frac{J^2}{J_{max}(x)^2}}} \frac{\Omega^-(x)}{\sqrt{B(x)(1-B(x))}}, && (6.3.34)\\
\tau_\chi^+(r) &= \tau_\chi^-(r_{min}) + 2\int_{r_{min}}^{r} \frac{dx}{\sqrt{1-\frac{J^2}{J_{max}(x)^2}}} \frac{\Omega^-(x)}{\sqrt{B(x)(1-B(x))}}, && (6.3.35)
\end{aligned}$$

where $J(r)$ is the DM angular momentum and it can be written in terms of the maximum angular momentum,

$$J(r) = yJ_{max}(r), \;\; 0 \leqslant y \leqslant 1, \tag{6.3.36}$$

with

$$J_{max}(r) = m_\chi r\sqrt{\frac{1-B(r)}{B(r)}}. \tag{6.3.37}$$

For each angular momentum J and position r there is a perihelion, which is denoted by r_{min}. Hence we solve $yJ_{max}(r) = J_{max}(r_{min})$ in order to find the perihelion in function of y and r.

The optical depth can be written in terms of $yJ_{max}(r)$ instead, this would lead to

$$\begin{aligned}
\tau_\chi^-(r,y) &= \int_r^{R_\star} \frac{dx}{\sqrt{1-y^2\frac{J_{max}(r)^2}{J_{max}(x)^2}}} \frac{\Omega^-(x)}{\sqrt{B(x)(1-B(x))}}, && (6.3.38)\\
\tau_\chi^+(r,y) &= \tau_\chi^-(r_{min},y) + 2\int_{r_{min}}^{r} \frac{dx}{\sqrt{1-y^2\frac{J_{max}(r)^2}{J_{max}(x)^2}}} \frac{\Omega^-(x)}{\sqrt{B(x)(1-B(x))}}. && (6.3.39)
\end{aligned}$$

Averaging over the two possible trajectories, the total optical depth factor is

$$\eta(r) = \frac{1}{2}[\eta_-(r,y) + \eta_+(r,y)]. \tag{6.3.40}$$

When calculating the differential capture rate in Eq. (6.3.6) an integral over J was performed. Therefore, we average the optical depth factor over the DM angular

EoS	**WD$_1$**	**WD$_2$**	**WD$_3$**
ρ_c [kg m^{-3}]	4.77×10^9	3.37×10^{10}	3.29×10^{13}
P_c [Pa]	2.79×10^{22}	4.70×10^{23}	5.10×10^{27}
$M_\star$ [M$_\odot$]	0.65	1.00	1.39
$R_\star$ [km]	7.98×10^3	5.40×10^3	9.19×10^2

Table 6.5: Three different configurations of the Salpeter EoS for carbon white dwarfs, where ρ_c and P_c are respectively the star density and pressure in the core.

momentum, J, distribution,

$$\eta(r) = \frac{1}{2}\int_0^1 \frac{y dy}{1-y^2}[\eta_-(r,y) + \eta_+(r,y)]. \tag{6.3.41}$$

Introducing Eq. (6.3.41) into Eq. (6.3.6), the complete expression for the capture rate reads,

$$C = \frac{\rho_\chi}{m_\chi}\int_0^{R_\star} 4\pi r^2 \eta(r) n_T(r) \int_0^\infty du \frac{w}{u_\chi} f_{\rm MB}(u_\chi) \frac{4\mu_+^2}{\mu w}\int_{w\frac{|\mu_-|}{\mu_+}}^{v_e} dv v \frac{d\sigma_{T\chi}}{d\cos\theta}. \tag{6.3.42}$$

In Fig. 6.5 we show the complete expression of the DM capture rate for single scattering, Eq. (6.3.42), as a function of the DM-proton cross section (solid lines) that we assume to be constant for $m_\chi = 100\,$GeV. We have taken into account the three carbon WD configurations, shown in Table 6.5, for three different SI EFT operators, D1 (blue), D2 (magenta), and D10 (orange), given in Table 6.2. The optically thin limit that neglects the opacity of the star, is represented as dot–dashed lines and the geometric limit as brown dashed lines. Notice that the optically thin limit is a good approximation for small DM-proton scattering cross sections. Observe that for larger cross sections the capture rate is suppressed due to the optical depth factor η and approaches asymptotically to the geometric limit. Thus, Eq. (6.3.42) realises the transition between the optically thin limit and the optically thick (geometric). In all WDs, this transition happens around $\sigma_{th} \sim 10^{-43}\,$cm^2 D2 and D10 operators. On the other hand, D1 approaches to the geometric limit around $\sigma_{th} \sim 10^{-42}\,$cm^2 in the lighter WDs (see top panels) and around $\sigma_{th} \sim 10^{-43}\,$cm^2 in the heaviest WD (bottom panel).

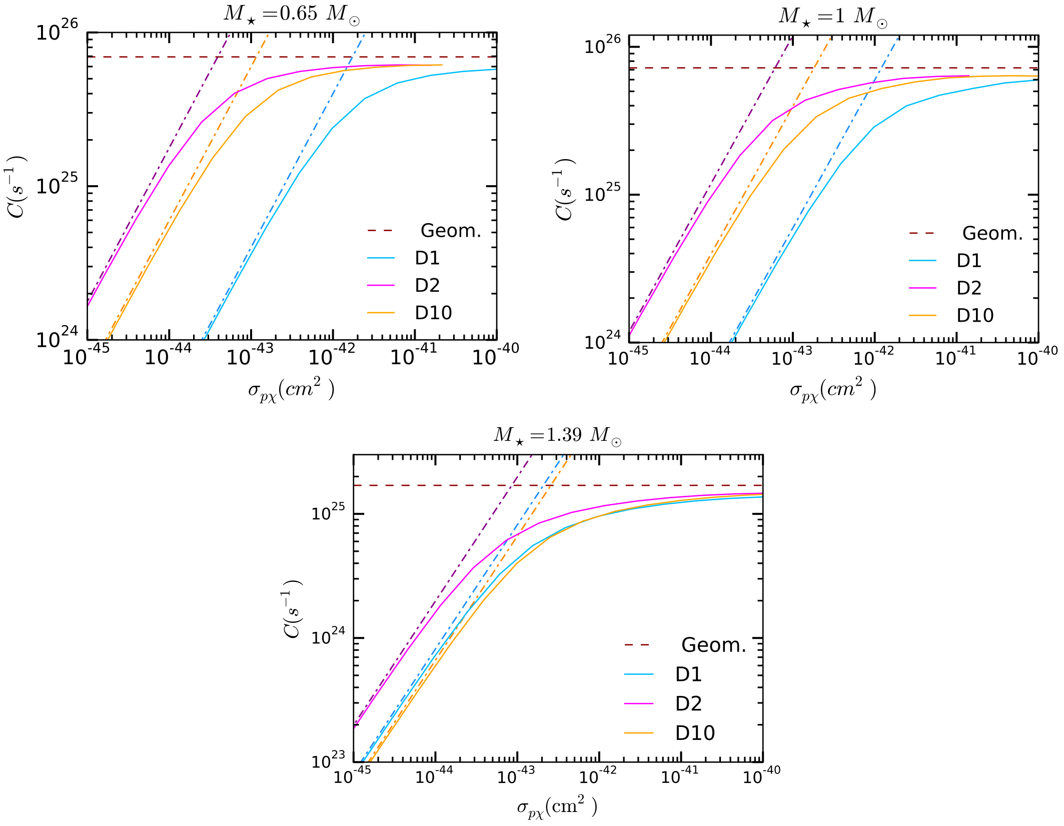

Figure 6.5: Capture rate as a function of the DM–proton cross section for a DM of $m_\chi = 100$GeV the SI EFT operator D1 (blue), D2 (magenta), and D10 (orange) given in Table 6.2. Dashed brown lines denote the geometric limit, dot–dashed lines correspond to the optically thin limit and solid lines include the effect of the star opacity.

6.3.4 Temperature effects

To account for the temperature effects on the capture rate, we use the complete form of the DM velocity distribution function given by,

$$f(u)du = \frac{u}{v_\star}\sqrt{\frac{3}{2\pi(v_d^2 + 3T_\star\mu/m_\chi)}}\left[e^{\frac{-3(u-v_\star)^2}{(v_d^2+3T\mu/m_\chi)}} - e^{\frac{-3(u+v_\star)^2}{(v_d^2+3T\mu/m_\chi)}}\right]. \tag{6.3.43}$$

As mentioned above, the interaction rate also depends on the star temperature and its form is given in Eq. (6.3.15). Hence, we compute the temperature dependent capture rate for the SI EFT operators in Table 6.2. The geometric limit is obtained by substituting in the Eq. (6.3.22)

$$v_d \to \sqrt{v_d^2 + 3T_\star/m_T}. \tag{6.3.44}$$

We computed the capture rate including temperature effects for different WDs with $T = 10^5$ K. In the left panel of Fig. 6.6 we present the ratio of the finite temperature capture rate to the zero temperature limit for a WD of $M_\star = 0.49\mathrm{M}_\odot$. The right panel shows the same for a WD of $M_\star = 1.38\mathrm{M}_\odot$. The capture rates where computed for $\Lambda = 1$ for all operators in Table 6.2. The vertical brown dashed line indicates the mass at which evaporation becomes relevant (see Section 6.4). We observe that the effects of the temperature are more noticeable below this mass while for larger mass range the zero temperature limit capture rate is accurate.

6.4 Evaporation

In the region of low DM masses, there is another phenomena we should take into account; this is called evaporation. This process is the opposite to DM capture. It happens when a captured DM particle scatters off nuclei and gains energy and as a consequence, the DM escapes the star.

The evaporation rate was first described in Ref. [211] and later improved in [212] for the Sun. The physics of WDs is very different from that of the Sun. The

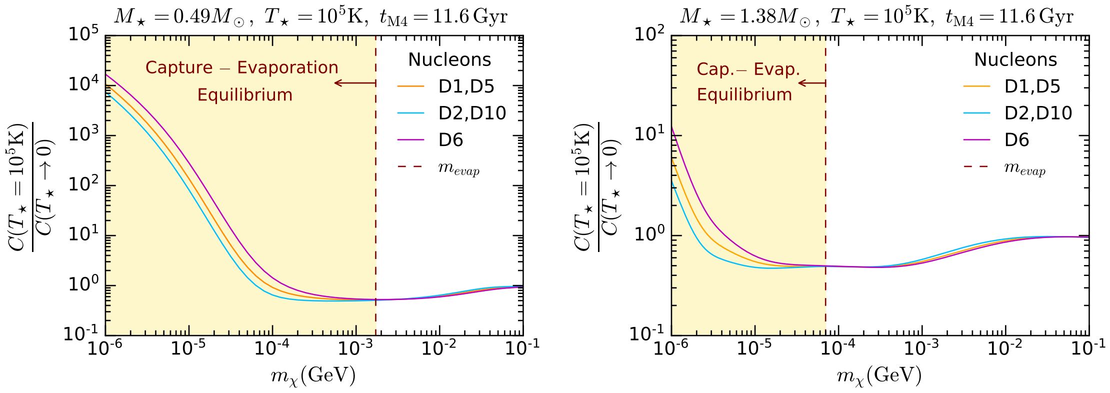

Figure 6.6: Finite temperature effects on the capture rate for carbon targets, for two WDs in the globular cluster M4, $M_\star = 0.49\text{M}_\odot$ (left) and $M_\star = 1.38\text{M}_\odot$ (right). The DM mass range where capture and evaporation are expected to be in equilibrium is shaded in yellow. The dashed brown line corresponds to the evaporation mass.

principal differences come from the fact that in the Sun fusion still happens in the core releasing energy that keeps the core hot. The outer layers are heated by energy transferred from the core, therefore a temperature gradient exist between the core and the outer layers. On the contrary, in WDs, which are stellar remnants, fusion is a dead process and the only source of thermal energy is the internal energy of the ions. When WDs are formed they still are among the hottest stars in the Universe, all the heat in their interior is trapped and only the heat in their outer layers can escape into space in form of radiation. Since there are no active fusion processes the star gradually cools down. As degenerate electrons are excellent heat conductors and the cooling process is very slow, the core temperature is considered to be constant.

In order to estimate the DM evaporation rate in a WD the DM population in the star is required. This is obtained from DM energy transport, see Ref. [213, 214, 215]. Assuming that DM particles do not interact among them, DM thermalisation is usually split in two regimes: local and global.

When thermalisation is local (LTE), DM particles scatter very often so they are in local thermodynamic equilibrium with the stellar matter. As a consequence, DM particles in this regime will reflect the local temperature at every point in the star.

The corresponding DM number density for LTE is given by,

$$n_{\mathrm{LTE}}(r) = n_{\mathrm{LTE}}(0)\left(\frac{T_\star(r)}{T_c}\right)^{3/2} e^{-\int_0^r \frac{\alpha(r')\frac{dT_\star(r')}{dr'}+m_\chi\frac{d\phi(r')}{dr'}}{T_\star(r')}dr'}, \tag{6.4.1}$$

where $\phi(r)$ is the local value of the gravitational potential and α is the thermal diffusivity. The LTE DM number density is a function of the temperature gradient in the core and the thermal diffusivity of the star α. The latter, in the case of the Sun, varies throughout the star according to the relative abundances of the different atomic nuclei. In the case of a WD, the heat escapes very slowly and the temperature is taken to be constant. If the WD is considered made of only one element i.e. carbon, the thermal diffusivity will also be constant across the star.

In the case of global thermalisation, DM particles are isothermically (iso) distributed and consequently they reflect an overall temperature. The number density of DM captured in a compact object by the effect of gravity in this regime is given by,

$$n_{iso}(r) = \frac{e^{-m_\chi\phi(r)/T_\chi}}{\int_0^{R_\star} dr 4\pi r^2 e^{-m_\chi\phi(r)/T_\chi}}. \tag{6.4.2}$$

DM particles cluster stronger in the core of the star, assuming a spherically symmetric mass distribution and a uniform density the form of $\phi(r)$ under such symmetry leads to,

$$n_{iso}(r) = \frac{e^{-r^2/r_\chi^2}}{\int_0^{R_\star} dr 4\pi r^2 e^{-r^2/r_\chi^2}}, \tag{6.4.3}$$

where

$$r_\chi = \sqrt{\frac{3T_c}{2\pi G\rho_c m_\chi}}, \tag{6.4.4}$$

is known as the DM length scale. It is the radius of the DM distribution within the star. This number is usually compared with the inner scattering distance $\ell_\chi = [n_T(r)\langle\sigma_{T\chi}\rangle]^{-1}$. This comparison is given by the Kundsen number $K = \ell_\chi/r_\chi$. Based on the results of Ref. [176], we define,

$$f(K) = \frac{1}{1+\frac{K^2}{K_0^2}}, \tag{6.4.5}$$

where $K_0 \approx 0.4$ (for the Sun) is the crossing point from local to global regimes . The

DM velocity distribution within the star, is given by

$$f_{evap}(v) = [1 - f(K)]n_{iso}(r)e^{-\frac{m_\chi v^2}{2T_\chi}} + f(K)n_{LTE}(r)e^{-\frac{m_\chi v^2}{2T(r)}}. \tag{6.4.6}$$

From Eq. (6.4.5) we observe that when $K < 1$ DM is in the LTE regime, while $K > 1$ corresponds to the isothermal regimen.

Similarly to the capture rate, the evaporation rate is defined as,

$$E = \int_0^{R_\star} dr 4\pi r^2 \eta(r) \int_0^{v_e(r)} f_{evap}(w)\Omega^+(w)dw. \tag{6.4.7}$$

Here we are using the $\eta(r)$ for evaporation, which now depends on the star temperature, see Ref. [184] for details and $\Omega^+(w)$ is the rate at which DM escapes the star and is given by

$$\Omega^+(w) = \int_{v_e}^\infty R^+(w \to v), \tag{6.4.8}$$

and R^+ is the rate at which a DM particle with velocity w scatters to a final velocity v larger than the WD escape velocity. This is calculated as in Eq. (6.3.15), however, we cannot take the $T_\star \to 0$ limit since for evaporation the nuclei temperature is not negligible anymore because it affects the kinematics. In order to calculate numerically the differential interaction rate for evaporation we make a change of variables, e.g. $s + t = x$ and $t - s = y$,

$$R^+(w \to v) = \frac{8\mu_+^4}{\sqrt{\pi}} \frac{v}{w} n_T(r) \int_0^\infty \mathrm{d}x \int_{-\infty}^\infty dy \kappa^3 (y + x) e^{-\kappa^2 v_T^2} \frac{d\sigma_{T\chi}}{d\cos\theta} \Theta(x - w)\Theta(v - |y|), \tag{6.4.9}$$

where now we have $v_T^2 = \frac{1}{2}\mu\mu_+(x+y)^2 + \frac{\mu_+}{2}(x-y)^2 - \mu w^2$.

Since the WD core temperature is expected to be constant, to estimate the evaporation rate we have considered only the isothermal DM number density (global regime). In other words we have taken the $f(K) \to 0$ limit in the velocity distribution function.

We can estimate the number of DM particles N accumulated in a WD by solving the following equation,

$$\frac{dN}{dt} = C - EN, \tag{6.4.10}$$

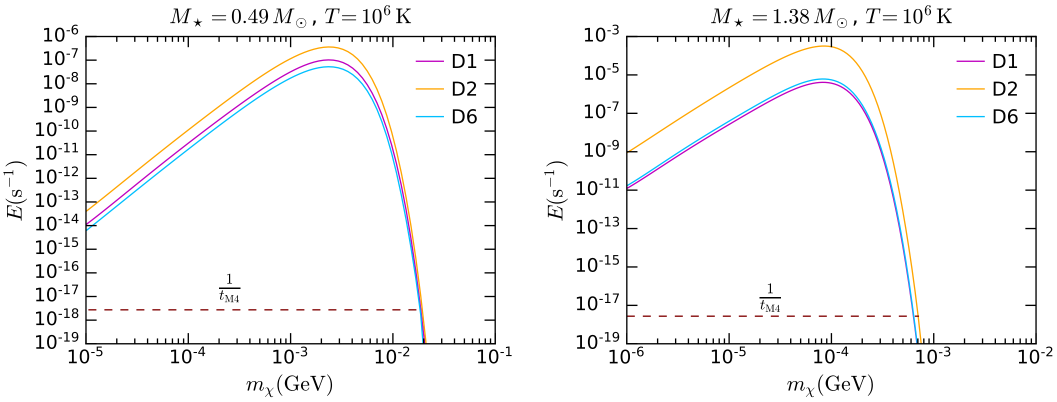

Figure 6.7: Evaporation rate as a function of the DM mass for operators D1, D2 and D6. The brown dashed line indicates the inverse of the estimated age of M4.

where C and E are respectively the capture and evaporation rate; we have ignored the effects of annihilation. Considering the capture and evaporation rate as constant over time, the total number of DM particles is given by,

$$N(t_\star) = Ct_\star \left(\frac{1 - e^{-Et_\star}}{Et_\star} \right) . \tag{6.4.11}$$

If evaporation is negligible, all particles are captured after scattering off nuclei and the DM population would be given by $Ct_\star$. On the contrary, when evaporation is relevant, the DM population in the WD is reduced by the factor,

$$\left(\frac{1 - e^{-Et_\star}}{Et_\star} \right) . \tag{6.4.12}$$

In Fig. 6.7 shows the evaporation rate as function of the DM mass for two WDs in the globular cluster M4 with $M_\star = 0.49\,\mathrm{M}_\odot$ (left) and $M_\star = 1.38\,\mathrm{M}_\odot$(right), $T \approx 10^6\,\mathrm{K}$, for the operators D1 (magenta), D2 (orange) and D6 (blue). As mentioned above, the factor in Eq. (6.4.12) quantifies the impact of the evaporation process on the number of accreted DM particles. When $E(m_\chi)t \to \infty$ this term tends to zero which means that all captured DM escapes the star. When $E(m_\chi)t_\star \gtrsim 1$ the number of DM particles in the WD is reduced significantly. Therefore, we define the evaporation mass as the DM mass for which $E(m_{evap})t_\star \sim 1$, see the dashed brown line where we have assumed $t_\star = t_{\mathrm{M4}}$ ($t_{\mathrm{M4}} \sim 11.6\,\mathrm{Gyr}$ [216]). We find $m_{evap} \sim$ 19MeV and

$m_{evap} \sim 0.7$MeV for the WD of $M_\star = 0.49\,\mathrm{M}_\odot$ and $M_\star = 1.38\,\mathrm{M}_\odot$, respectively. The evaporation mass in the heavier star is smaller, therefore massive WDs would allow us to set constraints on the interactions of sub-GeV DM.

6.5 Limits on DM-nucleon Interactions

In this section we will use the capture rate in the optically thin limit to set constraints on DM–nucleon interactions. As it can be seen in Eq. (6.3.6) and Fig. 6.5 in this limit the capture rate is proportional to the DM–proton cross section. In this limit, we should not use cross sections that exceed the threshold cross section σ_{th}, which is given by the intersection of the optically thin limit and the geometric limit.

Several works have compared the luminosity due to the capture and further annihilation of DM particles in WDs, with the observed luminosity in order to derive constraints on the DM scattering cross section [217, 218, 219]. In those analyses, it was assumed that DM particles were captured after a single scattering. Recently, multi–scattering was implemented in the capture rate calculation [182] and limits on DM interactions for massive DM particles were improved [183].

DM captured in the WD core self annihilates. Hence, the number of DM particles in the WD core, in the absence of evaporation, is defined as,

$$\frac{dN}{dt} = C - A, \tag{6.5.1}$$

here A is the annihilation rate given by,

$$A = \frac{1}{2}\frac{N^2\langle\sigma_{ann}v\rangle}{\frac{4}{3}\pi r_\chi^3}, \tag{6.5.2}$$

where r_χ is given in Eq. (6.4.4), N is the total number of DM in the WD and $\langle\sigma_{ann}v\rangle$ is the thermally averaged annihilation cross section. We assume equilibrium between DM capture and annihilation processes since in WDs the time-scale for this to happen is very short (of the order of one year) [217]. When the capture and annihilation rates are in equilibrium ($C = A$) Eq. (6.5.1) will be equal to zero. Therefore we can assume that the captured DM is instantly converted into additional star luminosity [217]. Such luminosity contribution due to DM capture and immediate DM self-annihilation is given by,

$$L_{DM} = m_\chi C. \tag{6.5.3}$$

Using the fact that the observed WD luminosity should be greater than or equal to the DM contribution, we can calculate upper limits on the DM-nucleon cross section.

6.5.1 Comparison with previous work

In Ref. [183] WDs observed in the closest globular cluster M4 [216] (about 1.9 kpc [220]) were used to derive constraints on the DM–proton cross section. These WDs were selected since they are old compact stars. Their cooling age is estimated by means of observations of their temperature and luminosity as well as theoretical WD luminosity functions. WDs in the M4 globular cluster are cool enough to actually observe effects arising from captured DM. Furthermore, if DM is present in M4, the expected DM density is very large when compared to the DM density in the Solar vicinity which enhances the capture rate. Using a Navarro-Frenk-White profile to model the DM halo, the DM density in M4 at the largest radius within which the WD data was taken $r_{max} = 2.3\,\mathrm{pc}$, is estimated to be $\rho_\chi = 798\,\mathrm{GeVcm}^{-3}$ for a contracted halo and $\rho_\chi = 532\,\mathrm{GeVcm}^{-3}$ for an uncontracted halo [219]. To compare our results with the bound derived in Ref. [183], we use a WD with the same characteristics as the authors considered, namely made of carbon, $R_\star \sim 9 \times 10^3\,\mathrm{km}$ and $L \sim 2.5 \times 10^{31}\,\mathrm{GeV\,s^{-1}}$.

In order to model the inner structure of the WD, we use the Salpeter EoS coupled to the TOV equation Eq. (6.2.16) and the mass equation Eq. (6.2.12). To solve this system of equations an additional parameter is necessary, the central density $\rho(0) = \rho_c$ that gives the estimated radius of the star. For the above mentioned WD we find that $\rho_c = 1.99 \times 10^9\,\mathrm{kg\,m^{-3}}$ and $M_\star = 0.49\,\mathrm{M}_\odot$. In this process we obtain the radial profiles for the number density of the targets and the escape velocity. We are now able to compute the capture rate in the optically thin limit given in Eq. (6.3.6). We derive an upper bound on the DM–cross section by imposing the observed luminosity must be greater than the contribution from DM capture and further annihilation. The bounds are determined for the two DM profiles (contracted and uncontracted). Note that for WDs in M4 the exact values of the star and DM dispersion velocities are unknown but the star velocity is assumed to be $v_\star = 20\,\mathrm{km\,s^{-1}}$ and the dispersion velocity is found to be not greater than $v_d = 8\,\mathrm{km\,s^{-1}}$ [219].[1]

In Fig. 6.8 we compare bounds for the scalar operator D1 calculated using our approach (light green band), see Sec. 6.3 with the result from Ref. [183] (grey line) and a heavier M4 WD (light blue band). It is evident that in the range of large DM masses ($m_\chi \gtrsim 10^5\,\mathrm{GeV}$) it is necessary to consider multi–scattering. We have improved Ref. [183] computations by introducing the inner structure of the M4 WD. In addition, in the DM-nucleus cross section we have included the response function for carbon–12 [210], to properly describe the inner structure of the nucleus. The simplifying assumptions made in Ref. [183] overestimate the WD upper bound by around 1.5 order of magnitude, using the same WD, in the $m_\chi \gtrsim 10\,\mathrm{GeV}$, while in the sub-GeV regime the difference is about one order of magnitude. Notice also that for $m_\chi \lesssim 19\,\mathrm{MeV}$ the evaporation processes are relevant and reduce the DM population available for annihilation within the star. Hence we cannot derive limits in this DM mass region. In addition, we have taken into account the uncertainty in the DM density in M4, which gives slightly different bounds on the DM interactions. For comparison, we also show limits from the leading direct detection (DD) experiments, such as DarkSide-50 [42], Xenon1T [41, 71, 72], projected sensitivities from SuperCDMS SNOLAB Ge/Si [221], CDEX-1T [222], and Darwin [223], as well as the neutrino coherent scattering background for Xenon

---

[1] The DM velocity dispersion in the M4 cluster is estimated by integrating the hydrostatic equation, Eq. (6.2.11), assuming the contracted (uncontracted) DM profile.

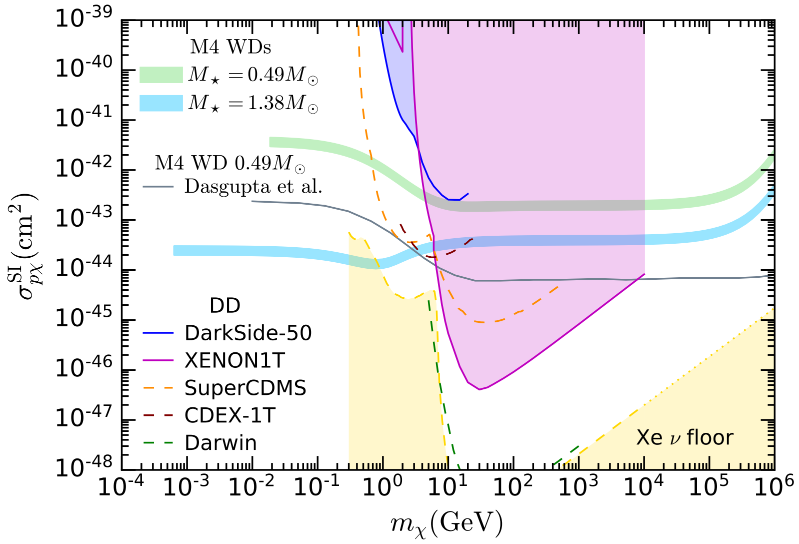

Figure 6.8: Spin independent DM-proton cross section, $\sigma^{SI}_{p\chi}$, as a function of the DM mass. The grey line corresponds to the Dasgupta et al. limit on $\sigma^{SI}_{p\chi}$ [183], while the light blue band denotes the bound calculated for the operator D1 using the scalar our approach for the capture rate computation in the optically thin limit and DM density in M4 for an uncontracted ($\rho_\chi = 532\,\mathrm{GeV\,cm^{-3}}$) and a contracted ($\rho_\chi = 798\,\mathrm{GeV\,cm^{-3}}$) halo [219]. The light green band denotes the limit placed with a heavier M4 WD. DD limits from DarkSide-50 [42], Xenon1T [41, 71, 72], projected sensitivities from SuperCDMS SNOLAB Ge/Si [221], CDEX-1T [222], and Darwin [223], as well as the neutrino coherent scattering background for xenon detectors [40] are shown for comparison.

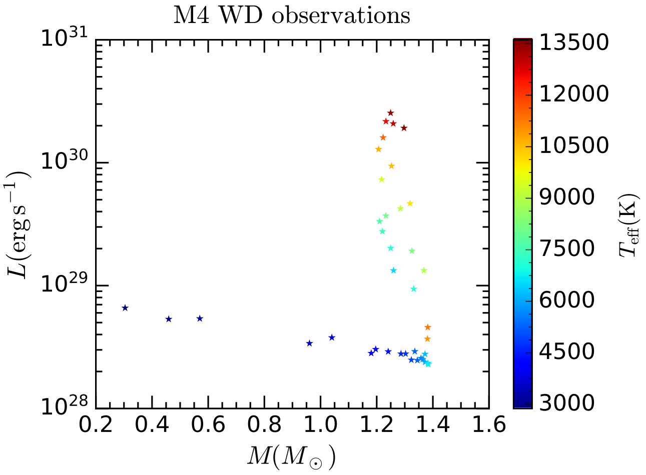

Figure 6.9: Luminosity vs mass for WDs observed in the M4 globular cluster [219].

detectors [40]. Notice that upper bounds from WDs are orders of magnitude stronger in the low DM mass regime in comparison with constraints from current and future direct detection experiments. Observe that in the DM mass region around $0.1-10\,\mathrm{GeV}$ there is a significant change in the order of magnitude of the DM-proton cross section. This is because of the DM-target dependence on the form factor and the DM-nucleon and DM-target mass ratios. For small DM masses $m_\chi << m_p$, the DM cross section is dominated by the proton/target mass ratio and it behaves as if it were independent of the DM mass. The region above $10\,\mathrm{GeV}$ corresponds to the limit of $m_\chi >> m_T$, where the DM mass dependence approximately cancels out. Therefore in these two limits, $m_\chi << m_p$ and $m_\chi >> m_T$, the DM-proton cross section is approximately independent of the DM mass, while in between these two extreme cases, the DM mass is comparable to either the proton or the target mass, making its contribution significant.

In this work we follow the approach from Ref. [219], rather than Ref. [183], to set constraints on DM interactions. This is because observed luminosities and effective temperatures are correlated quantities, $L = 4\pi K_B R_\star^2 T_{eff}^4$. Therefore, bounds derived from L vs $R_\star$ in Fig. 6.8 are misleading (light green band and green line [183]). The heavier the WD the higher the DM capture rate which enhances the DM contribution to the star luminosity. Furthermore, massive WDs cool down faster than lighter

WDs. As a result, the heaviest WD with the lowest observed luminosity, which for M4 corresponds to a WD with mass $M_\star = 1.38\,\mathrm{M}_\odot$ and $L \sim 2.5 \times 10^{28}\,\mathrm{ergs\,s^{-1}}$ (see Fig. 6.9), set an upper limit on L_{DM}. In addition in Ref. [183] a luminosity that does not correspond to a WD of radius $R_\star \sim 9 \times 10^3\,\mathrm{km}$ as reported in Ref. [219] was used, see Fig. 6.9.

Finally, using the above mentioned WD, we find an improved upper bound on the cross section for the scalar operator D1 (see light blue band). Observe that constraints in the sub-GeV DM region are improved by around 2 orders of magnitude for DM capture rate and one order of magnitude above $\sim 10\,\mathrm{GeV}$. Furthermore, due to the DM evaporation mass reported in the previous section for this WD ($m_{evap} = 0.7\,\mathrm{MeV}$) is possible to set constraints on the interactions of even lighter DM.

6.5.2 Results

In this section we use the WDs observed in the M4 globular cluster [216] to estimate bounds on the cutoff scale of the SI EFT operators. We assume the WDs are made of carbon and that the DM is captured in the star after a single scattering.[1] Constraints on these DM models have been obtained recently using NSs and considering DM interactions with nucleons and electrons [207, 224, 225]. Here we will assume the DM interacts only with carbon nuclei.

In order to set limits on the cutoff scale of the operators in Table 6.2, we assume the observed WD luminosity should be greater than or equal to the luminosity from DM contributions from DM capture and further annihilation in the WD core, see Eq. (6.5.3). Here L corresponds to the observed luminosity of the WDs in the M4 globular cluster reported in Ref. [219].

In Fig. 6.10 we show limits on the cutoff scale, Λ, for the operators given in Table 6.2 using a WD of $M_\star = 1.38\,\mathrm{M}_\odot$ instead the one used in Ref. [183]. We

---

[1] Which is not true for DM masses above 10^5 GeV, where multi–scattering needs to be considered in the capture rate computation.

also show bounds on Λ calculated with the most stringent DD limits on the DM-proton cross section and sensitivity projections from future experiments in Fig. 6.8. The brown vertical line indicates the evaporation DM mass; in the yellow region ($m_{eva} \lesssim 0.7\,\mathrm{MeV}$) capture and evaporation are in equilibrium, hence the limits in this region are not valid. Notice that the bound on Λ for the operator D1 is about 1.5 orders of magnitude suppressed with respect to D5. The suppression comes from the Yukawa couplings in D1 which are not present in D5. The operator D2 is even more suppressed in the regime of large DM masses due to the cross section dependence on the momentum transfer. Operators D6 and D10 are velocity and momentum dependent and their constraints on Λ are similar for large DM masses. Notice that in the low mass region D10 is suppressed several orders of magnitude since, unlike D6, the momentum transfer component in the DM-nucleon cross section contributes negatively to the total cross section. If DM is present in M4, DM captured in WDs provide the strongest upper limit in the low mass region, $m_\chi \lesssim 10\,\mathrm{GeV}$, for the 5 SI EFT operators compared to current and future DD experiments. For D1 and D5 Xenon1T and the future Darwin experiments outperform the WD limit in the intermediate region, $m_\chi \gtrsim 10\,\mathrm{GeV}$, Darwing would be able to place the strongest bounds in this mass region, while the current leading bounds are set by XENON1T. On the contrary, for operators D2, D6 and D10, DM captured in WDs overcomes the velocity and momentum suppression that hampers terrestrial experiments, giving the strongest bounds in both, low and large, DM mass regimes. Note also that for D6 and D10, the future Darwin experiment might be able to set stronger bounds on the cutoff Λ in the region $\sim 10 - 10^3\,\mathrm{GeV}$. For heavy DM ($m_\chi \gtrsim 10^5\,\mathrm{GeV}$) multiple scattering is not accounted for in Fig. 6.10.

6.6 Conclusions

Due to their high gravitational potential and vast number of observations, white dwarfs are one of the best compact stellar objects to set bounds on DM interactions

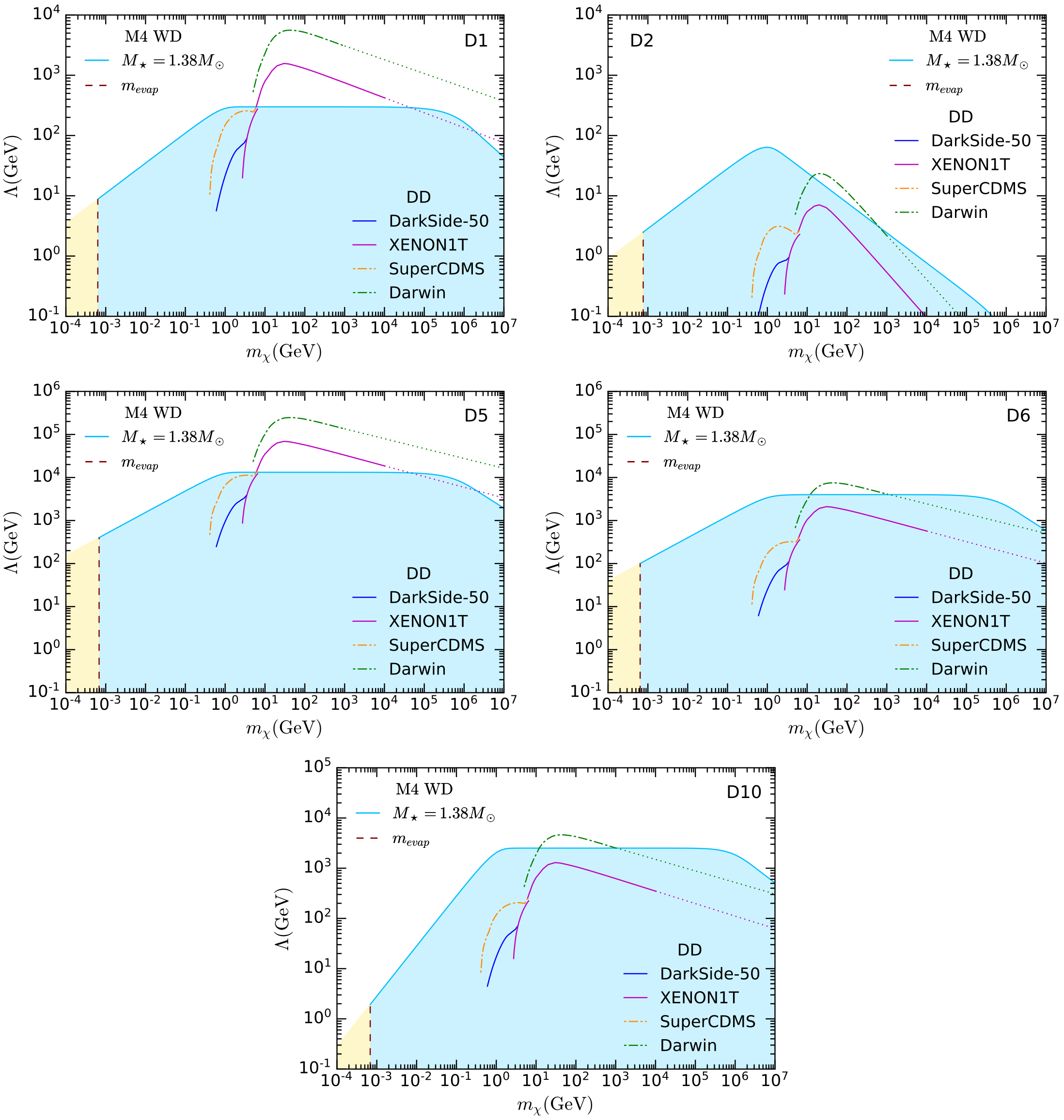

Figure 6.10: Limits on the cutoff scale Λ as a function of the DM mass for the different operators given in Table 6.2. Limits are calculated using the same WD as in Fig. 6.8 and $\rho_\chi = 798\,\mathrm{GeV\,cm^{-3}}$ (contracted halo) [219]. DD limits from DarkSide-50 [42], Xenon1T [41, 71, 72], projected sensitivities from SuperCDMS SNOLAB Ge/Si [221], CDEX-1T [222], and Darwin [223] are shown for comparison.

with ordinary matter. DM captured in WDs can increase the star temperature, as a consequence a fraction of the observed luminosity might come from the DM capture and annihilation processes. In order to observe such effects coming from accretion of DM in the core, the star has to be old enough i.e. should have cooled down. Here we have improved the capture rate calculation for WDs, using the recent treatment for the DM capture rate computation given in Ref. [60]. We have incorporated the inner structure of the WD by coupling the EoS with the TOV equation, Eq. (6.2.16) as well as the star opacity and a more realistic DM-nucleus scattering cross section by including the nuclear response functions for carbon–12 given in Ref. [210].

Most WDs are mainly made of carbon nuclei and degenerate electrons. In this work we have considered only DM interactions with nuclei. This simplifies in some aspects the discussion given in Ref. [60] and allows us to use the non-relativistic treatment in Ref. [184] since nucleons are not degenerate in WDs. To explore the impact of the WD configuration on the capture rate, we assumed different WDs made of only one element. We found a WD configuration, made of either helium, carbon or oxygen, with mass around $0.85\,\mathrm{M}_\odot$ for which the DM capture rate in the geometric limit is maximum. Then, we assumed three hypothetical WDs made only of carbon in order to compute the capture in the optically thin limit and including the star opacity.

In order to set constraints on the DM–proton scattering cross section, we used WDs observed in the M4 globular cluster. We follow the discussion in Ref. [183] and compare their results with those obtained using the formalism given in this work. Despite the discrepancy between the two approaches due to more realistic considerations, i.e. inner structure of the WD, and the response function in the DM-nucleus interactions, we find that in any case WDs would provide significantly more constraining power than current Earth–based experiments in the regime of low and large DM masses in regions with a high DM density. Although in our formalism it is necessary to implement multi–scattering in the large DM regime i.e. $m_\chi \gtrsim 10^5\,\mathrm{GeV}$.

We have then used an Effective Field Theory approach to describe the interactions between fermionic DM and nuclei and calculated bounds on the cutoff scale of spin-independent operators. We have found that if DM is present in M4, DM captured in WDs places the strongest bound on velocity and momentum independent DM-nucleon interactions in the low mass regime, while Xenon1T is more stringent above $m_\chi \gtrsim 10\,\mathrm{GeV}$. For DM interactions with momentum and velocity dependence, DM captured in WDs places the strongest constraints on the whole DM mass region where the EFT is valid. Summing up, WDs can be a complementary probe to direct detection experiments, improving constraints on the low DM mass region and on velocity– momentum dependent DM-interactions. Observations of these stars may shed some light on the nature of DM particles.

Chapter 7

Conclusions

The Standard Model of particle physics is the best available theory describing the most elementary components of our Universe and their interactions. However, there is strong evidence that indicates it is not the ultimate theory and it requires new physics in order to provide a complete description of nature. In this thesis we have discussed different alternatives to probe physics beyond the Standard Model.

In the radiative decay of neutral fermions, CP violation can produce an asymmetry between circularly polarised directions of radiated photons giving rise to a net circular polarisation in particle and astroparticle physics observables. In Chapter 3 we discussed how CP asymmetry and circular polarisation are connected. Then we showed the formalism for analytical calculations of the CP asymmetry using a simplified neutrino model.

Assuming neutrinos as Dirac and later as Majorana particles, we computed the CP asymmetry given in terms of electromagnetic dipole moments. We found that the generation of circular polarisation is essentially dependent upon CP asymmetry between neutrino radiative decay and its CP conjugate process. We discussed the CP violation within the SM framework and then how there is no CP violation coming from these diagrams. In order to obtain a non-vanishing CP violation we introduced a new generic Yukawa interaction consisting of electrically charged scalar and fermion states. We extensively discussed how CP violation in the radiative decay of a massive neutrino can be enhanced by means of such a new interaction. These results can be applied to any models where radiative decays of this type take place. Therefore, observations of circular polarisation in future telescopes are a useful probe of new physics.

In Chapter 4 we discussed the CP violation in the neutrino transition electromagnetic dipole moment within the SM framework. We introduced two RH neutrinos N_1 and N_2, with masses $M_1 < M_2$. We then, presented the generic full one-loop calculation of the neutrino electromagnetic form factors corresponding to three channels of interest: $\nu_i \to \nu_j \, \gamma$, $N_I \to \nu_j \, \gamma$ and $N_2 \to N_1 \, \gamma$. We gave analytical expressions for the CP violation and obtained the CP asymmetry for the last two channels only. This is because the condition for CP violation is such that the mass of the decaying particle has to be larger than the W boson mass i.e. $N_I > m_W$. Hence, for the first channel, CP violation vanishes due to the light neutrinos masses $m_i << m_W$.

For the numerical computation of the CP asymmetry, we considered a mass range of $0.1\,\text{TeV} < M_2 < 10\,\text{TeV}$. We found that the CP asymmetry for the $N_I \to \nu \, \gamma$ process is very tiny, reaching a value of the order of 10^{-17}. On the other hand, in the decay process $N_2 \to N_1 \, \gamma$, CP asymmetry is enhanced reaching values of the order of magnitude of 10^{-5} to 10^{-3}. By performing a scan, using the 3σ ranges, of the CP asymmetry we found that CP asymmetry can reach values of order one.

In order to study BSM physics via such neutrino radiative decays it is necessary that we can observe the signal of circularly polarised photons produced in these processes. Nonetheless, such signal could be washed out during propagation through the Universe, by scattering off various intermediate particles. In Chapter 5 we studied the propagation of energetic gamma-rays and the change on their net polarisation.

We generalised the radiative transfer formalism introduced by Chandrasekhar to any type of photon interaction at any energy. Roughly, this was done by writing the **P**–matrix, describing the changes on polarisation, in terms of the scattering amplitude. We then applied our results to the specific case of Compton scattering where we observed that the parameter V related to the circular polarisation was excluded. This is because in Compton scattering, circular polarisation cannot change to linear polarisation and vice versa. Instead the circularly polarised signal could be attenuated by an asymmetry between the two kind of polarisations. We finally computed the conditions in which a circularly polarised signal is conserved after scattering for different frames of reference. We found different results for each case one, in the low and high energy regimes. Finally, for completeness, we perform a general formalism to study the time evolution of the circular polarisation in a generic scattering process and then applied it to the particular case of Compton scattering.

This work is of great importance, since it could provide a way to search for new interactions. In this work we particularly used Compton scattering, however the formalism is general enough to compute the **P**–matrix for photons scattering off, for instance, Axions or Axion-like particles (ALP). This might not only change the photon polarisation while propagation, but it could also be a source of circular polarisation itself [226].

In Chapter 6 we derived constraints on dark matter interactions using white dwarfs. Due to their strong gravitational field and low temperatures, old compact stars such as neutron stars or white dwarfs are the best objects to set bounds on DM interactions. The accretion and annihilation of DM in these objects can increase the star temperature affecting their observed luminosity.

In this work we have adapted the treatment of the DM capture given in Ref. [60] and used the non-relativistic approach of Ref. [184]. We assumed three hypothetical WDs made of carbon in order to compute the capture rate in the optically thin limit and including the star opacity in the zero temperature approximation. We have used an Effective Field Theory (EFT) approach to describe fermionic DM interactions with ordinary matter. We also considered finite temperature effects on the capture rate and estimated the evaporation rate for WDs observed in the M4 globular cluster. We found that the effects of the temperature in the capture rate are significant in the very low mass regimen where DM evaporation takes place. The latter was found to be $m_{evap} = 0.7\,\mathrm{MeV}$ for a WD of $M_\star = 1.38\,\mathrm{M}_\odot$ in M4.

Finally, we derived bounds on the scale cutoff of spin-independent EFT operators. If DM is present in M4 DM captured in WDs will place the strongest bounds for sub-GeV with scalar, vector and tensor DM interactions as well as DM interactions with momentum and velocity dependence.

Appendix A

Polarisation-dependent amplitudes

We may derive the amplitudes of neutrino and antineutrino radiative decays specifying the photon polarisation in the final state, $\mathcal{M}(\nu_{\mathbf{i}} \to \nu_{\mathbf{f}} + \gamma_{\pm})$ and $\mathcal{M}(\bar{\nu}_{\mathbf{i}} \to \bar{\nu}_{\mathbf{f}} + \gamma_{\pm})$. We apply the chiral representation, where the γ matrices are given by

$$\gamma^{\mu} = \begin{pmatrix} 0 & \sigma^{\mu} \\ \bar{\sigma}^{\mu} & 0 \end{pmatrix}, \quad \gamma_5 \equiv i\gamma^0\gamma^1\gamma^2\gamma^3 = \begin{pmatrix} -\mathbf{1} & 0 \\ 0 & \mathbf{1} \end{pmatrix}, \tag{A.0.1}$$

$$\sigma^{\mu\nu} = \frac{i}{2}[\gamma^{\mu}, \gamma^{\nu}], \quad P_{\mathrm{L,R}} = \frac{1 \mp \gamma_5}{2}, \tag{A.0.2}$$

and $\sigma^{\mu} = (\mathbf{1}, \sigma^1, \sigma^2, \sigma^3)$ and $\bar{\sigma}^{\mu} = (\mathbf{1}, -\sigma^1, -\sigma^2, -\sigma^3)$ and σ^i are Pauli matrices. Given momentum $p = (p_0, \vec{p})$, the normalised particle and antiparticle Dirac spinors are represented by

$$u_S(p) = \begin{pmatrix} \sqrt{p \cdot \sigma}\ \xi_S \\ \sqrt{p \cdot \bar{\sigma}}\ \xi_S \end{pmatrix}, \quad v_S(p) = \begin{pmatrix} \sqrt{p \cdot \sigma}\ \eta_S \\ \sqrt{-p \cdot \bar{\sigma}}\ \eta_S \end{pmatrix}, \tag{A.0.3}$$

where ξ_S and η_S are two-component spinors normalised to unity. Here, we include the polarisation index S for two independent spinors.

To simplify the derivation, we prefer to work in the rest frame. Frame-independent results can be obtained straightforwardly from this case. In the rest frame, the initial sterile neutrino $\nu_{\mathbf{i}}$ is at rest $p_{\mathbf{i}}^{\mu} = (m_{\mathbf{i}}, 0, 0, 0)^T$, and the photon is released in the $+z$ direction with momentum $q^{\mu} = (q, 0, 0, q)^T$. Conservation of momentum requires $p_{\mathbf{f}}^{\mu} = (E_{\mathbf{f}}, 0, 0, -q)^T$ with $q = (m_{\mathbf{i}}^2 - m_{\mathbf{f}}^2)/(2m_{\mathbf{i}})$ and $E_{\mathbf{f}} = (m_{\mathbf{i}}^2 + m_{\mathbf{f}}^2)/(2m_{\mathbf{i}})$. In this frame, S denotes spin along the $+z$ direction i.e. S_z, which takes values $\pm\frac{1}{2}$. This geometry is shown in Fig. A.1.

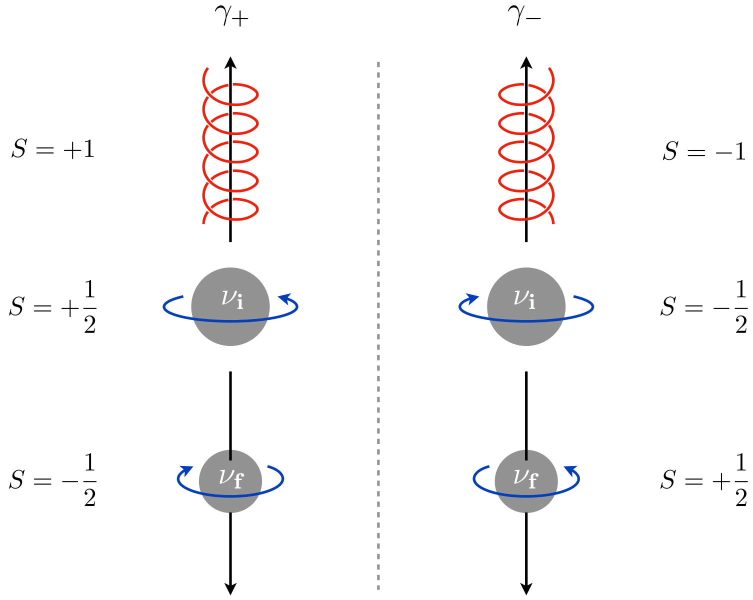

Figure A.1: Polarisation for neutrino radiative decay in the rest frame.

The angular momentum along the z direction is conserved $S_z(\nu_{\mathbf{i}}) = S_z(\nu_{\mathbf{f}}) + S_z(\gamma)$. For a fermion, $S_z = \pm 1/2$ and for a massless photon, $S_z = \pm 1$. Given the initial state $\nu_{\mathbf{i}}$ with spin $S_z(\nu_{\mathbf{i}}) = +1/2(-1/2)$, the only solution for spins in final states is $S_z(\nu_{\mathbf{f}}) = -1/2(+1/2)$ and $S_z(\gamma) = +1(-1)$. In other words, the released photon is the right-handed γ_+ (left-handed γ_-).

For the photon moving in the $+z$ direction, the polarisation vectors are as defined in [153]

$$\varepsilon_+^{\mu} = \frac{1}{\sqrt{2}}(0, 1, i, 0)\,, \quad \varepsilon_-^{\mu} = \frac{1}{\sqrt{2}}(0, 1, -i, 0) \tag{A.0.4}$$

correspond to spin $S_z = +1$ and -1, respectively [1].

---

[1] Here we apply the convention in the textbook [153]. The definition of ϵ_+ in this convention has a sign difference from the one shown in [44]. Using the convention in [44] leads to a sign

In this frame, for the neutrino $\nu_{\mathbf{f}}$ moving in the $-z$ direction, the spinors $u_S(p)$ and $v_S(p)$ with spin $\pm\frac{1}{2}$ are simplified to

$$
\begin{aligned}
u_{+\frac{1}{2}}(p_{\mathbf{f}}) &= \begin{pmatrix} \sqrt{E+q}\ \xi_{+\frac{1}{2}} \\ \sqrt{E-q}\ \xi_{+\frac{1}{2}} \end{pmatrix}, \qquad u_{-\frac{1}{2}}(p_{\mathbf{f}}) = \begin{pmatrix} \sqrt{E-q}\ \xi_{-\frac{1}{2}} \\ \sqrt{E+q}\ \xi_{-\frac{1}{2}} \end{pmatrix}, \\
v_{+\frac{1}{2}}(p_{\mathbf{f}}) &= \begin{pmatrix} \sqrt{E+q}\ \eta_{+\frac{1}{2}} \\ -\sqrt{E-q}\ \eta_{+\frac{1}{2}} \end{pmatrix}, \quad v_{-\frac{1}{2}}(p_{\mathbf{f}}) = \begin{pmatrix} \sqrt{E-q}\ \eta_{-\frac{1}{2}} \\ -\sqrt{E+q}\ \eta_{-\frac{1}{2}} \end{pmatrix}, \qquad \text{(A.0.5)}
\end{aligned}
$$

with

$$
\xi_{+\frac{1}{2}} = \eta_{-\frac{1}{2}} = \begin{pmatrix} 1 \\ 0 \end{pmatrix}, \quad \xi_{-\frac{1}{2}} = \eta_{+\frac{1}{2}} = \begin{pmatrix} 0 \\ 1 \end{pmatrix}. \qquad \text{(A.0.6)}
$$

In the massless case, $u_{+\frac{1}{2}}$ and $u_{-\frac{1}{2}}$ are purely left- and right-handed respectively (because we have assumed $\nu_{\mathbf{f}}$ is moving in the $-z$ direction). Spinors for initial neutrino $\nu_{\mathbf{i}}$ and antineutrino $\bar{\nu}_{\mathbf{i}}$ are given by

$$
\begin{aligned}
u_{+\frac{1}{2}}(p_{\mathbf{i}}) &= \sqrt{E} \begin{pmatrix} \xi_{+\frac{1}{2}} \\ \xi_{+\frac{1}{2}} \end{pmatrix}, \qquad u_{-\frac{1}{2}}(p_{\mathbf{i}}) = \sqrt{E} \begin{pmatrix} \xi_{-\frac{1}{2}} \\ \xi_{-\frac{1}{2}} \end{pmatrix}, \\
v_{+\frac{1}{2}}(p_{\mathbf{i}}) &= \sqrt{E} \begin{pmatrix} \eta_{+\frac{1}{2}} \\ -\eta_{+\frac{1}{2}} \end{pmatrix}, \quad v_{-\frac{1}{2}}(p_{\mathbf{i}}) = \sqrt{E} \begin{pmatrix} \eta_{-\frac{1}{2}} \\ -\eta_{-\frac{1}{2}} \end{pmatrix}, \qquad \text{(A.0.7)}
\end{aligned}
$$

The amplitudes with definite spins in the initial and final states are then given by

$$
\begin{aligned}
\mathcal{M}(\nu_{\mathbf{i},+\frac{1}{2}} \to \nu_{\mathbf{f},-\frac{1}{2}} + \gamma_+) &= +\sqrt{2} f^{\mathrm{L}}_{\mathbf{fi}} (m_{\mathbf{i}}^2 - m_{\mathbf{f}}^2), \\
\mathcal{M}(\nu_{\mathbf{i},-\frac{1}{2}} \to \nu_{\mathbf{f},+\frac{1}{2}} + \gamma_-) &= -\sqrt{2} f^{\mathrm{R}}_{\mathbf{fi}} (m_{\mathbf{i}}^2 - m_{\mathbf{f}}^2), \\
\mathcal{M}(\bar{\nu}_{\mathbf{i},+\frac{1}{2}} \to \bar{\nu}_{\mathbf{f},-\frac{1}{2}} + \gamma_+) &= -\sqrt{2} f^{\mathrm{L}}_{\mathbf{if}} (m_{\mathbf{i}}^2 - m_{\mathbf{f}}^2), \\
\mathcal{M}(\bar{\nu}_{\mathbf{i},-\frac{1}{2}} \to \bar{\nu}_{\mathbf{f},+\frac{1}{2}} + \gamma_-) &= +\sqrt{2} f^{\mathrm{R}}_{\mathbf{if}} (m_{\mathbf{i}}^2 - m_{\mathbf{f}}^2), \qquad \text{(A.0.8)}
\end{aligned}
$$

Here, $\nu_{\mathbf{i},+\frac{1}{2}} \to \nu_{\mathbf{f},-\frac{1}{2}} + \gamma_+$ and $\bar{\nu}_{\mathbf{i},-\frac{1}{2}} \to \bar{\nu}_{\mathbf{f},+\frac{1}{2}} + \gamma_-$ are CP conjugates, while $\nu_{\mathbf{i},-\frac{1}{2}} \to \nu_{\mathbf{f},+\frac{1}{2}} + \gamma_-$ and $\bar{\nu}_{\mathbf{i},+\frac{1}{2}} \to \bar{\nu}_{\mathbf{f},-\frac{1}{2}} + \gamma_+$ are CP conjugates. The other channels have vanishing amplitudes, consistent with angular momentum conservation.

---

difference for $i\mathcal{M}(\nu_{\mathbf{i},+\frac{1}{2}} \to \nu_{\mathbf{f},-\frac{1}{2}} + \gamma_+)$ and $i\mathcal{M}(\bar{\nu}_{\mathbf{i},+\frac{1}{2}} \to \bar{\nu}_{\mathbf{f},-\frac{1}{2}} + \gamma_+)$ in Eqs. (3.2.5) and (3.2.10) and $i\mathcal{M}^{\mathrm{M}}(\nu_{\mathbf{i},+\frac{1}{2}} \to \nu_{\mathbf{f},-\frac{1}{2}} + \gamma_+)$ in Eq. (3.2.23).

We can generalise the result in Eq. (A.0.8) to any inertial reference frame via spatial rotations and Lorentz boosts. These transformations change spins for fermions but leave photon polarisation invariant. Eventually, we obtain the Lorentz-invariant amplitudes $\mathcal{M}(\nu_{\mathbf{i}} \to \nu_{\mathbf{f}} + \gamma_{\pm})$ and $\mathcal{M}(\bar{\nu}_{\mathbf{i}} \to \bar{\nu}_{\mathbf{f}} + \gamma_{\pm})$ taking the same result as Eq. (A.0.8) in any reference frame. Using the CPT-invariance property, namely, $\bar{f}_{\mathbf{if}}^{\mathrm{R,L}} = -f_{\mathbf{if}}^{\mathrm{R,L}}$, we eventually arrive at Eqs. (3.2.5) and (3.2.10). These are the most general results independent of either particle model or reference frame.

Appendix B

Derivation of imaginary parts of the loop integrals

The two NP contributions to the sterile neutrino radiative decay given by the new proposed interactions are shown in Fig. 3.2. In order to compute their respective matrix elements, we use the couplings of the new particles ϕ and ψ with neutrinos and sterile neutrinos shown in Section 3.3.2.

In general, we have

$$i\mathcal{M}(\nu_s \to \nu_i + \gamma_\pm) = i\overline{u}(p_i)\Gamma^\mu_{is}(q^2)u(p_s)\varepsilon^*_{\pm,\mu}(q) \tag{B.0.1}$$

and the matrix elements for each loop contribution, $\mathcal{M}_j \equiv \mathcal{M}_j(\nu_s \to \nu_i + \gamma_\pm)$, shown in Fig. 3.2 take the form

$$\begin{aligned} i\mathcal{M}_1 &= -Qe\lambda_s\lambda_i^*\times \\ &\times \int \frac{d^4k}{(2\pi)^4}\frac{\overline{u}(p_i)P_\mathrm{R}(\not{k}+m_\psi)(p_1-p_2)^\mu P_\mathrm{L}u(p_s)\varepsilon^*_{\pm,\mu}(q)}{(k^2-m_\psi^2+i\epsilon)((k-p_s)^2-m_\phi^2+i\epsilon)((k-p_i)^2-m_\phi^2+i\epsilon)}\,, \\ i\mathcal{M}_2 &= +Qe\lambda_s\lambda_i^*\times \\ &\times \int \frac{d^4k}{(2\pi)^4}\frac{\overline{u}(p_i)P_\mathrm{R}(\not{k}'+m_\psi)\gamma^\mu(\not{k}+m_\psi)P_\mathrm{L}u(p_s)\varepsilon^*_{\pm,\mu}(q)}{((k-p_s)^2-m_\phi^2+i\epsilon)(k'^2-m_\psi^2+i\epsilon)(k^2-m_\psi^2+i\epsilon)}\,. \end{aligned} \tag{B.0.2}$$

Due to the projection operators, the matrix elements reduce to

$$\begin{aligned}
i\mathcal{M}_1 &= -Qe\lambda_s\lambda_i^* \int \frac{d^4k}{(2\pi)^4} \frac{\overline{u}(p_i)\not{k}(p_1-p_2)^\mu P_{\mathrm{L}} u(p_s)\varepsilon^*_{\pm,\mu}(q)}{(k^2-m_\psi^2+i\epsilon)((k-p_s)^2-m_\phi^2+i\epsilon)((k-p_i)^2-m_\phi^2+i\epsilon)} \\
i\mathcal{M}_2 &= +Qe\lambda_s\lambda_i^* \int \frac{d^4k}{(2\pi)^4} \frac{\overline{u}(p_i)\not{k}'\gamma^\mu\not{k} P_{\mathrm{L}} u(p_s)\varepsilon^*_{\pm,\mu}(q)}{((k-p_s)^2-m_\phi^2+i\epsilon)(k'^2-m_\psi^2+i\epsilon)(k^2-m_\psi^2+i\epsilon)} \, .
\end{aligned} \tag{B.0.3}$$

In order to perform dimensional regularisation to Eq. (B.0.3), we must substitute the denominator with the relevant Feynman parameters, therefore, we perform the loop momentum shifts $\ell = k - (xp_s + zp_i)$ and $\ell = k - (xp_s + zq)$ for the two diagrams respectively. This leads to

$$\begin{aligned}
i\mathcal{M}_1 &= -Qe\lambda_s\lambda_i^* \int \frac{d^d\ell}{(2\pi)^d} \int dxdydz\delta(x+y+z-1)\times \\
&\quad \times \frac{\overline{u}(p_i)[-2\ell^\mu\not{\ell} + (p_s+p_i)^\mu(\not{p}_s y + \not{p}_i z) - 2(p_s y + p_i z)^\mu(\not{p}_s y + \not{p}_i z)] P_{\mathrm{L}} u(p_s)\varepsilon^*_{\pm,\mu}(q)}{(\ell^2 - \Delta_{\phi\psi}(x,y,z))^3} \, , \\
i\mathcal{M}_2 &= +Qe\lambda_s\lambda_i^* \int \frac{d^d\ell}{(2\pi)^d} \int dxdydz\delta(x+y+z-1)\times \\
&\quad \times \frac{\overline{u}(p_i)[\not{\ell}\gamma^\mu\not{\ell} + (\not{q}(z-1) + \not{p}_s x)\gamma^\mu(\not{q}z + \not{p}_s x)] P_{\mathrm{L}} u(p_s)\varepsilon^*_{\pm,\mu}(q)}{(\ell^2 - \Delta_{\psi\phi}(x,y,z))^3} \, ,
\end{aligned} \tag{B.0.4}$$

where $\Delta_{\phi\psi}(x,y,z)$ and $\Delta_{\psi\phi}(x,y,z)$ have been defined in Eq. (3.3.18). We ignore linear terms of ℓ since these terms vanish after integration. We use the following results from [153] for d-dimensional integrals over ℓ in Minkowski space

$$\begin{aligned}
\int \frac{d^d\ell}{(2\pi)^d} \frac{1}{(\ell^2-\Delta)^n} &= \frac{(-1)^n}{(4\pi)^{d/2}} \frac{\Gamma(n-d/2)}{\Gamma(n)} \left(\frac{1}{\Delta}\right)^{n-\frac{d}{2}} \\
\int \frac{d^d\ell}{(2\pi)^d} \frac{\ell^\alpha\ell^\beta}{(\ell^2-\Delta)^n} &= i\frac{(-1)^{n-1}}{(4\pi)^{d/2}} \frac{g^{\alpha\beta}}{2} \frac{\Gamma(n-d/2-1)}{\Gamma(n)} \left(\frac{1}{\Delta}\right)^{n-\frac{d}{2}-1} \, .
\end{aligned} \tag{B.0.5}$$

After dimensional regularisation, we set $d = 4 - \epsilon$, therefore the amplitudes acquire the following general form

$$\begin{aligned}
i\mathcal{M}_1 = \frac{-iQe\lambda_s\lambda_i^*}{(4\pi)^2} \int dxdydz\delta(x+y+z-1)\overline{u}(p_i) \Bigg[\left(-\frac{2}{\epsilon} + \log\frac{\Delta_{\phi\psi}(x,y,z)}{4\pi} + \gamma_\epsilon + \mathcal{O}(\epsilon) \right) \gamma^\mu \\
- \frac{(p_s+p_i)^\mu(\not{p}_s y + \not{p}_i z) - 2(p_s y + p_i z)^\mu(\not{p}_s y + \not{p}_i z)]}{\Delta_{\phi\psi}(x,y,z)} \Bigg] P_{\mathrm{L}} u(p_s)\varepsilon^*_{\pm,\mu}(q),
\end{aligned}$$

$$i\mathcal{M}_2 = \frac{iQe\lambda_s\lambda_i^*}{(4\pi)^2}\int dxdydz\delta(x+y+z-1)\overline{u}(p_i)\Bigg[\bigg(-\frac{2}{\epsilon}+1+\log\frac{\Delta_{\psi\phi}(x,y,z)}{4\pi}+\gamma_\epsilon+\mathcal{O}(\epsilon)\bigg)\gamma^\mu - \frac{(\not{q}(z-1)+\not{p}_s x)\gamma^\mu(\not{q}z+\not{p}_s x)}{\Delta_{\psi\phi}(x,y,z)}\Bigg] P_{\rm L}u(p_s)\varepsilon^*_{\pm,\mu}(q). \tag{B.0.6}$$

We simplify the above expressions by making use of the following identities

$$\begin{aligned}
\overline{u}(p_i)(p_s+p_i)^\mu P_{\rm L}u(p_s) &= \overline{u}(p_i)[\gamma^\mu(m_sP_{\rm R}+m_iP_{\rm L})+i\sigma^{\mu\nu}q_\nu P_{\rm L}]u(p_s)\,,\\
\overline{u}(p_i)(\not{p}_s+\not{p}_i)\gamma^\mu P_{\rm L}u(p_s) &= \overline{u}(p_i)[2m_i\gamma^\mu P_{\rm L}+i\sigma^{\mu\nu}q_\nu P_{\rm L}+q^\mu P_{\rm L}]u(p_s)\,,\\
\overline{u}(p_i)\gamma^\mu(\not{p}_s+\not{p}_i)P_{\rm L}u(p_s) &= \overline{u}(p_i)[2m_s\gamma^\mu P_{\rm R}+i\sigma^{\mu\nu}q_\nu P_{\rm L}-q^\mu P_{\rm L}]u(p_s)\,.
\end{aligned} \tag{B.0.7}$$

Finally, applying the Ward identity $q^\mu\mathcal{M}_\mu = 0$ and ignoring terms proportional to γ^μ, since these are simply vertex corrections to the overall electric charge[1], we only need to consider the tensor-like terms within Γ^μ_{is} to determine the form factor resulting from these diagrams. These are given by

$$\begin{aligned}
\Gamma^\mu_{is,1} &= -\frac{Qe\lambda_s\lambda_i^*}{(4\pi)^2}i\sigma^{\mu\nu}q_\nu\int_0^1 {\rm d}x{\rm d}y{\rm d}z\delta(x+y+z-1)\frac{(m_syP_{\rm R}+m_izP_{\rm L})}{\Delta_{\phi\psi}(x,y,z)}\\
\Gamma^\mu_{is,2} &= +\frac{Qe\lambda_s\lambda_i^*}{(4\pi)^2}i\sigma^{\mu\nu}q_\nu\int_0^1 {\rm d}x{\rm d}y{\rm d}z\delta(x+y+z-1)\frac{(m_sxyP_{\rm R}+m_ixzP_{\rm L})}{\Delta_{\psi\phi}(x,y,z)}\,.
\end{aligned} \tag{B.0.8}$$

Setting $m_i \to 0$ for the active neutrino mass in Eq. (B.0.8) and integrating over z yields

$$\begin{aligned}
\Gamma^\mu_{is,1} &= \frac{C_1}{(4\pi)^2}i\sigma^{\mu\nu}q_\nu\int_0^1\int_0^{1-y}{\rm d}x{\rm d}y\frac{m_syP_{\rm R}}{m_\phi^2(1-x)+xm_\psi^2-xym_s^2}\\
\Gamma^\mu_{is,2} &= \frac{C_2}{(4\pi)^2}i\sigma^{\mu\nu}q_\nu\int_0^1\int_0^{1-y}{\rm d}x{\rm d}y\frac{m_sxyP_{\rm R}}{m_\psi^2(1-x)+xm_\phi^2-xym_s^2}\,.
\end{aligned} \tag{B.0.9}$$

From these last expressions, we can identify the factors $K^{\rm L}_{1,2}$ and $K^{\rm R}_{1,2}$ given in Eq. (3.3.17) and then integrate over the remaining Feynman parameters x and y as shown in Eq. (3.3.19).

---

[1] Notice that when both contributions are added the divergent terms cancel out.

Appendix C

Low energy regimen: Phase matrix derivation

In this appendix, we briefly review the change of photon polarisation during Thomson scattering. Most of the result are well-known and are convenient to be compared with our results of scattering in the high energy limit.

C.1 Deriving the Thomson P–matrix directly from the Stokes parameters

For the Thomson scattering, the **P**–matrix can be directly obtained by following the original definition of Stokes parameters. Applying the formula in Eq. (2.3.8) to Stokes parameters for both incoming photon and outgoing photon, we obtain

$$\begin{aligned}
I_l^{(2)} &= (\vec{\epsilon_l}^{(2)} \cdot \vec{\epsilon_r}^{(1)})^2 a_r^2 + (\vec{\epsilon_l}^{(2)} \cdot \vec{\epsilon_l}^{(1)})^2 a_l^2 + 2 a_r\, a_l \cos(\delta_l - \delta_r)(\vec{\epsilon_l}^{(2)} \cdot \vec{\epsilon_r}^{(1)})(\vec{\epsilon_l}^{(2)} \cdot \vec{\epsilon_l}^{(1)}), \\
&= (\vec{\epsilon_l}^{(2)} \cdot \vec{\epsilon_r}^{(1)})^2\ I_r^{(1)} + (\vec{\epsilon_l}^{(2)} \cdot \vec{\epsilon_l}^{(1)})^2\ I_l^{(1)} + (\vec{\epsilon_l}^{(2)} \cdot \vec{\epsilon_r}^{(1)})(\vec{\epsilon_l}^{(2)} \cdot \vec{\epsilon_l}^{(1)})\ U^{(1)},
\end{aligned}$$

$$\begin{aligned}
I_r^{(2)} &= (\vec{\epsilon_r}^{(2)} \cdot \vec{\epsilon_r}^{(1)})^2 a_r^2 + (\vec{\epsilon_r}^{(2)} \cdot \vec{\epsilon_l}^{(1)})^2 a_l^2 + 2 a_r\, a_l \cos(\delta_l - \delta_r)(\vec{\epsilon_l}^{(2)} \cdot \vec{\epsilon_r}^{(1)})(\vec{\epsilon_r}^{(2)} \cdot \vec{\epsilon_l}^{(1)}), \\
&= (\vec{\epsilon_r}^{(2)} \cdot \vec{\epsilon_r}^{(1)})^2\ I_r^{(1)} + (\vec{\epsilon_r}^{(2)} \cdot \vec{\epsilon_l}^{(1)})^2\ I_l^{(1)} + (\vec{\epsilon_l}^{(2)} \cdot \vec{\epsilon_r}^{(1)})(\vec{\epsilon_r}^{(2)} \cdot \vec{\epsilon_l}^{(1)})\ U^{(1)},
\end{aligned}$$

$$\begin{aligned}
U^{(2)} &= 2(\vec{\epsilon}_r^{(2)} \cdot \vec{\epsilon}_r^{(1)})(\vec{\epsilon}_l^{(2)} \cdot \vec{\epsilon}_r^{(1)})a_r^2 + 2(\vec{\epsilon}_r^{(2)} \cdot \vec{\epsilon}_l^{(1)})(\vec{\epsilon}_l^{(2)} \cdot \vec{\epsilon}_l^{(1)})a_l^2 \\
&\quad +2a_r\, a_l \cos(\delta_l - \delta_r) \left[(\vec{\epsilon}_r^{(2)} \cdot \vec{\epsilon}_r^{(1)})(\vec{\epsilon}_l^{(2)} \cdot \vec{\epsilon}_l^{(1)}) - (\vec{\epsilon}_r^{(2)} \cdot \vec{\epsilon}_l^{(1)})(\vec{\epsilon}_l^{(2)} \cdot \vec{\epsilon}_r^{(1)})\right] \\
&= 2(\vec{\epsilon}_r^{(2)} \cdot \vec{\epsilon}_r^{(1)})(\vec{\epsilon}_l^{(2)} \cdot \vec{\epsilon}_r^{(1)})\; I_r^{(1)} \;+2(\vec{\epsilon}_r^{(2)} \cdot \vec{\epsilon}_l^{(1)})(\vec{\epsilon}_l^{(2)} \cdot \vec{\epsilon}_l^{(1)})\; I_l^{(1)} \\
&\quad + \left[(\vec{\epsilon}_r^{(2)} \cdot \vec{\epsilon}_r^{(1)})(\vec{\epsilon}_l^{(2)} \cdot \vec{\epsilon}_l^{(1)}) + (\vec{\epsilon}_r^{(2)} \cdot \vec{\epsilon}_l^{(1)})(\vec{\epsilon}_l^{(2)} \cdot \vec{\epsilon}_r^{(1)})\right] U^{(1)},
\end{aligned}$$

$$\begin{aligned}
V^{(2)} &= 2a_r\, a_l \sin(\delta_l - \delta_r) \left[(\vec{\epsilon}_r^{(2)} \cdot\ \vec{\epsilon}_r^{(1)})(\vec{\epsilon}_l^{(2)} \cdot \vec{\epsilon}_l^{(1)}) - (\vec{\epsilon}_r^{(2)} \cdot \vec{\epsilon}_l^{(1)})(\vec{\epsilon}_l^{(2)} \cdot \vec{\epsilon}_r^{(1)})\right] \\
&= \left[(\vec{\epsilon}_r^{(2)} \cdot \vec{\epsilon}_r^{(1)})(\vec{\epsilon}_l^{(2)} \cdot \vec{\epsilon}_l^{(1)}) - (\vec{\epsilon}_r^{(2)} \cdot \vec{\epsilon}_l^{(1)})(\vec{\epsilon}_l^{(2)} \cdot \vec{\epsilon}_r^{(1)})\right] V^{(1)}\,. \qquad \text{(C.1.1)}
\end{aligned}$$

From these relations, one obtains the following expression for the **P**–matrix in terms of the photon polarisation vectors

$$\mathbf{P} = \begin{bmatrix}
(\vec{\epsilon}_l^{(2)} \cdot \vec{\epsilon}_l^{(1)})^2 & (\vec{\epsilon}_l^{(2)} \cdot \vec{\epsilon}_r^{(1)})^2 & (\vec{\epsilon}_l^{(2)} \cdot \vec{\epsilon}_r^{(1)})(\vec{\epsilon}_l^{(2)} \cdot \vec{\epsilon}_l^{(1)}) & 0 \\
(\vec{\epsilon}_r^{(2)} \cdot \vec{\epsilon}_l^{(1)})^2 & (\vec{\epsilon}_r^{(2)} \cdot \vec{\epsilon}_r^{(1)})^2 & (\vec{\epsilon}_r^{(2)} \cdot \vec{\epsilon}_r^{(1)})(\vec{\epsilon}_r^{(2)} \cdot \vec{\epsilon}_l^{(1)}) & 0 \\
(\vec{\epsilon}_r^{(2)} \cdot \vec{\epsilon}_l^{(1)})(\vec{\epsilon}_l^{(2)} \cdot \vec{\epsilon}_l^{(1)}) & (\vec{\epsilon}_r^{(2)} \cdot \vec{\epsilon}_r^{(1)})(\vec{\epsilon}_l^{(2)} \cdot \vec{\epsilon}_r^{(1)}) & \mathbf{P}_{33} & 0 \\
0 & 0 & 0 & \mathbf{P}_{44}
\end{bmatrix} \qquad \text{(C.1.2)}$$

with

$$\begin{aligned}
\mathbf{P}_{33} &= \left[(\vec{\epsilon}_r^{(2)} \cdot\ \vec{\epsilon}_r^{(1)})(\vec{\epsilon}_l^{(2)} \cdot\ \vec{\epsilon}_l^{(1)})\ +\ (\vec{\epsilon}_r^{(2)} \cdot\ \vec{\epsilon}_l^{(1)})(\vec{\epsilon}_l^{(2)} \cdot\ \vec{\epsilon}_r^{(1)})\right], \\
\mathbf{P}_{44} &= \left[(\vec{\epsilon}_r^{(2)} \cdot\ \vec{\epsilon}_r^{(1)})(\vec{\epsilon}_l^{(2)} \cdot\ \vec{\epsilon}_l^{(1)})\ -\ (\vec{\epsilon}_r^{(2)} \cdot\ \vec{\epsilon}_l^{(1)})(\vec{\epsilon}_l^{(2)} \cdot\ \vec{\epsilon}_r^{(1)})\right]. \qquad \text{(C.1.3)}
\end{aligned}$$

One can recover Chandrasekhar's expression for the **P**–matrix in Eq. (2.3.19) by substituting the 3D kinematics in a general (fixed) frame, see Appendix D for the dot products between the incoming (1) and outgoing (2) polarisation vectors, namely

$$\begin{aligned}
\vec{\epsilon}_l^{(2)} \cdot\ \vec{\epsilon}_l^{(1)} &= \sin\phi_1 \sin\phi_2 + \cos\phi_1 \cos\phi_2 \cos(\theta_2 - \theta_1)\,, \\
\vec{\epsilon}_r^{(2)} \cdot\ \vec{\epsilon}_r^{(1)} &= \cos(\theta_2 - \theta_1)\,, \\
\vec{\epsilon}_l^{(2)} \cdot\ \vec{\epsilon}_r^{(1)} &= \cos\phi_2 \sin(\theta_2 - \theta_1)\,, \\
\vec{\epsilon}_r^{(2)} \cdot\ \vec{\epsilon}_l^{(1)} &= -\cos\phi_1 \sin(\theta_2 - \theta_1)\,\cdot \qquad \text{(C.1.4)}
\end{aligned}$$

C.2 P–matrix for Thomson interactions

Using the expression of the **R**–matrix as shown in Eq. (2.3.16), we obtain the following $\mathbf{P}_{\text{Chandrasekhar}}$–matrix elements

$$\begin{aligned}
\mathbf{P}_{11} &= (\cos\theta\cos\Phi_1\cos\Phi_2 - \sin\Phi_1\sin\Phi_2)^2 \\
\mathbf{P}_{12} &= (\cos\Phi_1\sin\Phi_2 + \cos\theta\sin\Phi_1\cos\Phi_2)^2 \\
\mathbf{P}_{13} &= \tfrac{1}{2}\left(-\cos^2\theta\sin2\Phi_1\cos^2\Phi_2 - \cos\theta\cos2\Phi_1\sin2\Phi_2 + \sin2\Phi_1\sin^2\Phi_2\right) \\
\mathbf{P}_{21} &= (\cos\theta\cos\Phi_1\sin\Phi_2 + \sin\Phi_1\cos\Phi_2)^2 \\
\mathbf{P}_{22} &= (\cos\Phi_1\cos\Phi_2 - \cos\theta\sin\Phi_1\sin\Phi_2)^2 \\
\mathbf{P}_{23} &= \tfrac{1}{2}\left(\sin2\Phi_1\left(\cos^2\Phi_2 - \cos^2\theta\sin^2\Phi_2\right) + \cos\theta\cos2\Phi_1\sin2\Phi_2\right) \\
\mathbf{P}_{31} &= \sin2\Phi_2\left(\cos^2\theta\cos^2\Phi_1 - \sin^2\Phi_1\right) + \cos\theta\sin2\Phi_1\cos2\Phi_2 \\
\mathbf{P}_{32} &= \sin2\Phi_2\left(\cos^2\theta\sin^2\Phi_1 - \cos^2\Phi_1\right) - \cos\theta\sin2\Phi_1\cos2\Phi_2 \\
\mathbf{P}_{33} &= \cos\theta\cos2\Phi_1\cos2\Phi_2 - 2\left(1+\cos^2\theta\right)\sin\Phi_1\cos\Phi_1\sin\Phi_2\cos\Phi_2
\end{aligned} \tag{C.2.1}$$

C.3 P′–matrix for Thomson interactions

The $\mathbf{P}'$–matrix denotes the **P**–matrix in the (I, Q, U, V) basis. Considering a rotation of the plane defined by the incoming polarisation vectors by an angle Φ_1 and a rotation for the final photon with another angle Φ_2, the $\mathbf{P}'$ follows the transformation

$$\mathbf{P}' = \mathbf{L}'(\pi - \Phi_2)\ \mathbf{R}'\ \mathbf{L}'(-\Phi_1)\,, \tag{C.3.1}$$

where $\mathbf{L}'(\Phi)$ takes a different form from $\mathbf{L}(\Phi)$ in Eq. (2.3.18),

$$\mathbf{L}'(\Phi) = \begin{pmatrix} 1 & 0 & 0 & 0 \\ 0 & \cos2\Phi & \sin2\Phi & 0 \\ 0 & -\sin2\Phi & \cos2\Phi & 0 \\ 0 & 0 & 0 & 1 \end{pmatrix}. \tag{C.3.2}$$

This eventually leads to the following $\mathbf{P}'$–matrix elements

$$\begin{array}{ll}
\mathbf{P}'_{11}=\mathbf{R}'_{11} & \mathbf{P}'_{31}=\mathbf{R}'_{31}c_{\Phi_2}+\mathbf{R}'_{21}s_{\Phi_2} \\
\mathbf{P}'_{32}=c_{\Phi_1}\Big(\mathbf{R}'_{32}c_{\Phi_2}+\mathbf{R}'_{22}s_{\Phi_2}\Big)+s_{\Phi_1}\Big(\mathbf{R}'_{33}c_{\Phi_2}+\mathbf{R}'_{23}s_{\Phi_2}\Big) & \mathbf{P}'_{12}=\mathbf{R}'_{12}c_{\Phi_1}+\mathbf{R}'_{13}s_{\Phi_1} \\
\mathbf{P}'_{33}=c_{\Phi_1}\Big(\mathbf{R}'_{33}c_{\Phi_2}+\mathbf{R}'_{23}s_{\Phi_2}\Big)-s_{\Phi_1}\Big(\mathbf{R}'_{32}c_{\Phi_2}+\mathbf{R}'_{22}s_{\Phi_2}\Big) & \mathbf{P}'_{13}=\mathbf{R}'_{13}c_{\Phi_1}-\mathbf{R}'_{12}s_{\Phi_1} \\
\mathbf{P}'_{14}=\mathbf{R}'_{14} & \mathbf{P}'_{34}=\mathbf{R}'_{34}c_{\Phi_2}+\mathbf{R}'_{24}s_{\Phi_2} \\
\mathbf{P}'_{21}=\mathbf{R}'_{21}c_{\Phi_2}-\mathbf{R}'_{31}s_{\Phi_2} & \mathbf{P}'_{41}=\mathbf{R}'_{41} \\
\mathbf{P}'_{22}=c_{\Phi_1}\Big(\mathbf{R}'_{22}c_{\Phi_2}-\mathbf{R}'_{32}s_{\Phi_2}\Big)+s_{\Phi_1}\Big(\mathbf{R}'_{23}c_{\Phi_2}-\mathbf{R}'_{33}s_{\Phi_2}\Big) & \mathbf{P}'_{42}=\mathbf{R}'_{42}c_{\Phi_1}+\mathbf{R}'_{43}s_{\Phi_1}\,, \\
\mathbf{P}'_{23}=s_{\Phi_1}\Big(\mathbf{R}'_{32}s_{\Phi_2}-\mathbf{R}'_{22}c_{\Phi_2}\Big)+c_{\Phi_1}\Big(\mathbf{R}'_{23}c_{\Phi_2}-\mathbf{R}'_{33}s_{\Phi_2}\Big) & \mathbf{P}'_{43}=\mathbf{R}'_{43}c_{\Phi_1}-\mathbf{R}'_{42}s_{\Phi_1}\,, \\
\mathbf{P}'_{24}=\mathbf{R}'_{24}c_{\Phi_2}-\mathbf{R}'_{34}s_{\Phi_2}\,, & \mathbf{P}'_{44}=\mathbf{R}'_{44}
\end{array} \qquad \text{(C.3.3)}$$

with $c_{\Phi_1}\equiv\cos(2\Phi_1)$, $c_{\Phi_2}\equiv\cos(2\Phi_2)$, $s_{\Phi_1}\equiv\sin(2\Phi_1)$, $s_{\Phi_2}\equiv\sin(2\Phi_2)$.

C.4 Deriving the P–matrix using the Quantum formalism

We can now compare both the geometrical formalism derived by Chandrasekhar and our quantum formalism by studying the special case of Thomson interactions. We first need to replace each of the matrix amplitude elements, as defined in Eq.(5.2.11), in the quantum formalism by their QFT definition. Without loss of generality, the matrix elements for Thomson scattering can be parameterized as

$$M_{i'i} \;=\; M_{\mu\nu}\;\epsilon_i^{(1)\mu}\,\epsilon_{i'}^{*(2)\nu}\,, \qquad \text{(C.4.1)}$$

where μ,ν are Lorentz indices, in the Lorentz gauge $\epsilon_i=(0,\vec{\epsilon_i})$ and $M_{\mu\nu}$ the polarisation vector-independent amplitude associated with each Feynman diagram. The amplitude squared for Thomson scattering is given by

$$M_{i'i}\,M^*_{j'j}=\sum_{\lambda=s,t,st}\Big(M_{\mu\nu}\,M^*_{\mu'\nu'}\Big)_\lambda\;\epsilon_i^{(1)\mu}\epsilon_{i'}^{*(2)\nu}\epsilon_j^{*(1)\mu'}\epsilon_{j'}^{(2)\nu'}\,, \qquad \text{(C.4.2)}$$

where the amplitudes for the different s, t, st channels $\left(M_{\mu\nu} M^*_{\mu'\nu'}\right)_{s,t,st}$ are equal to

$$\begin{aligned}
\left(M_{\mu\nu}\, M^*_{\mu'\nu'}\right)_s &= g_{\nu\nu'} g_{\mu\mu'}\,, \\
\left(M_{\mu\nu}\, M^*_{\mu'\nu'}\right)_t &= g_{\nu\nu'} g_{\mu\mu'}\,, \\
\left(M_{\mu\nu}\, M^*_{\mu'\nu'}\right)_{st} &= 2\,\left(2 g_{\mu\nu} g_{\mu'\nu'} - g_{\nu\nu'} g_{\mu\mu'}\right). \qquad \text{(C.4.3)}
\end{aligned}$$

Using these definitions together with $\mathbf{A}_{i'ij'j} \equiv \mathbf{W} M_{i'i} M^*_{j'j} \mathbf{W}^{-1}$ and $\mathbf{P} = \mathbf{C}\mathbf{A}_{i'ij'j}\mathbf{C}^{-1}$, one finds that the Stokes parameters after Thomson scattering are given by

$$\begin{bmatrix} \hat{I}_l \\ \hat{I}_r \\ \hat{U} \\ \hat{V} \end{bmatrix}^{(2)} = \begin{bmatrix} |\epsilon_l^{(2)} \cdot \epsilon_l^{(1)}|^2 & |\epsilon_l^{(2)} \cdot \epsilon_r^{(1)}|^2 & (\epsilon_l^{(2)} \cdot \epsilon_r^{(1)})(\epsilon_l^{(2)} \cdot \epsilon_l^{(1)}) & 0 \\ |\epsilon_r^{(2)} \cdot \epsilon_l^{(1)}|^2 & |\epsilon_r^{(2)} \cdot \epsilon_r^{(1)}|^2 & (\epsilon_r^{(2)} \cdot \epsilon_r^{(1)})(\epsilon_r^{(2)} \cdot \epsilon_l^{(1)}) & 0 \\ (\epsilon_r^{(2)} \cdot \epsilon_l^{(1)})(\epsilon_l^{(2)} \cdot \epsilon_l^{(1)}) & (\epsilon_r^{(2)} \cdot \epsilon_r^{(1)})(\epsilon_l^{(2)} \cdot \epsilon_r^{(1)}) & \mathbf{P}_{33} & 0 \\ 0 & 0 & 0 & \mathbf{P}_{44} \end{bmatrix} \begin{bmatrix} \hat{I}_l \\ \hat{I}_r \\ \hat{U} \\ \hat{V} \end{bmatrix}^{(1)} \text{(C.4.4)}$$

with

$$\begin{aligned}
\mathbf{P}_{33} &= \left[(\epsilon_r^{(2)} \cdot\ \epsilon_r^{(1)})(\epsilon_l^{(2)} \cdot\ \epsilon_l^{(1)}) + (\epsilon_r^{(2)} \cdot\ \epsilon_l^{(1)})(\epsilon_l^{(2)} \cdot\ \epsilon_r^{(1)})\right]\,, \\
\mathbf{P}_{44} &= \left[(\epsilon_r^{(2)} \cdot\ \epsilon_r^{(1)})(\epsilon_l^{(2)} \cdot\ \epsilon_l^{(1)}) - (\epsilon_r^{(2)} \cdot\ \epsilon_l^{(1)})(\epsilon_l^{(2)} \cdot\ \epsilon_r^{(1)})\right]\,, \qquad \text{(C.4.5)}
\end{aligned}$$

which indeed agrees with Chandrasekhar's results as displayed in Eq. (C.1.2). Using the Thomson kinematics in the fix frame, we obtain Eq. (2.3.19), as expected. Therefore, In the low energy limit of the incoming photon, the two formalisms are equivalent.

Appendix D

Kinematics and results in the different frames of reference

D.1 Reference frames

To compare the polarisation of light in processes with relativistic electrons from those with non-relativistic electrons we consider some frames of reference. Such frames are the centre of mass (COM) frame, the rest frame, the fixed frame and the spin frame; each of them is good for describing different physics aspects of the process.

The COM frame is a good approximation for describing thermal photon scattering with thermal electron. The rest frame can be treated as a limit of an energetic photon scattering with electron with a small momentum. The spin frame specifies the electron spin $J_z = \pm 1/2$ in the z direction. The fixed frame can be applied to an energetic electron scattering with a soft photon.

For every frame of reference shown in Fig. D.1 the four-momenta p_1 and p_2 correspond to the incoming and outgoing electrons as well as the four-momenta k_1 and k_2 correspond to the incoming and outgoing photons respectively. In the following we give the explicit kinematics for each of the frames.

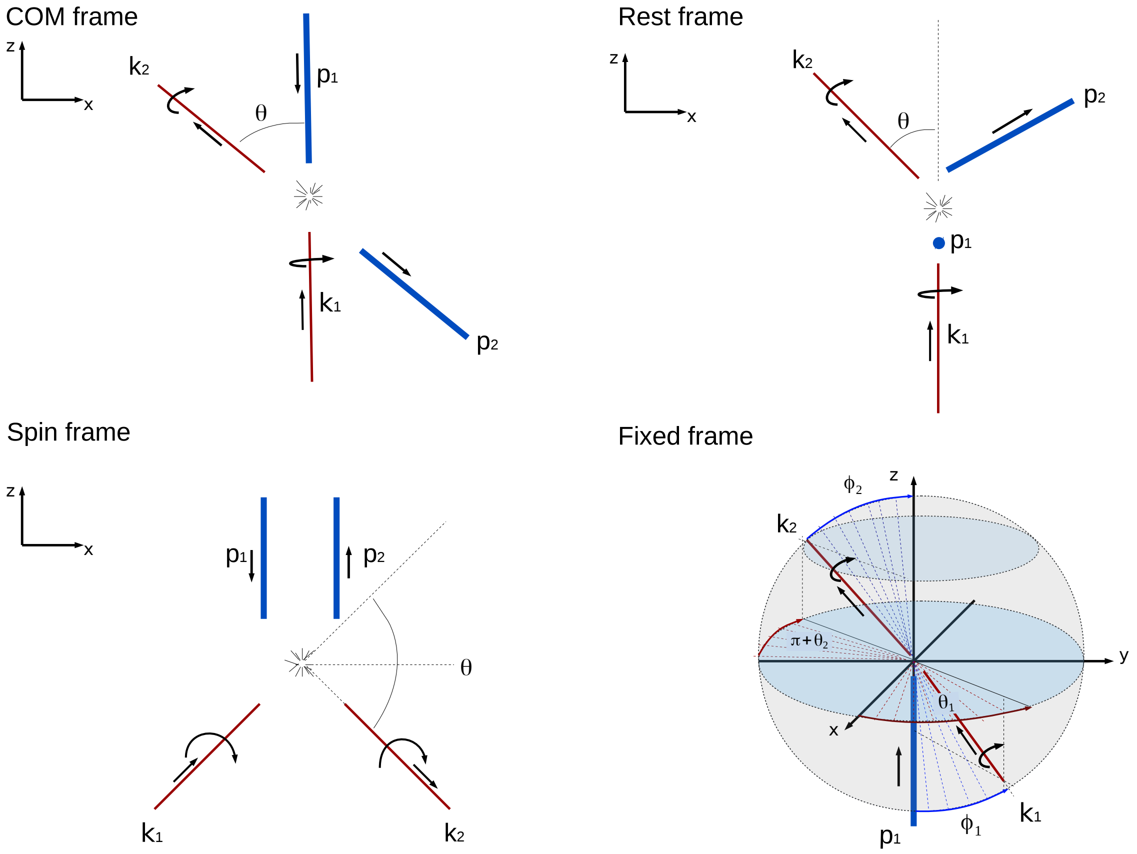

Figure D.1: Frame of references for the photon-electron scattering. For all four frames, the blue bold line refers to the incoming (outgoing) electron, the red line refers to the incoming (outgoing) photon. The straight arrows indicate the momentum direction for each particle while the deflect arrows indicate the helicity of the photons. In the upper-left corner we have the centre of mass (COM) frame, upper-right corner shows the rest frame, and lower-left corner shows the spin frame, where both the incoming and outgoing electrons are on the z directions. In each frame, the θ angle always corresponds to the angle between the outgoing and incoming photon. Finally, the lower-right corner shows the general fixed frame which contains four parameters, θ_1, θ_2, ϕ_1 and ϕ_2.

Centre of mass frame

In this frame the incoming photon and electron move in opposite directions with the same momentum $|\mathbf{p_1}| = E_\gamma$, which is the photon energy. The outgoing photon and electron do not change energies but only directions. We assume the angle between incoming photon and outgoing photon is θ. Finally, in this frame the energy for the incoming electron is $E_e^2 = E_\gamma^2 + m_e^2$ and the four momenta reads as follows,

$$\begin{aligned} p_1 &= (E_e, 0, 0, -E_\gamma)\,, \\ k_1 &= (E_\gamma, 0, 0, E_\gamma)\,, \\ k_2 &= (E_\gamma, E_\gamma \sin\theta, 0, E_\gamma \cos\theta)\,, \\ p_2 &= p_1 + k_1 - k_2\,. \end{aligned} \tag{D.1.1}$$

Rest frame

In this frame the electron is initially at rest and the photon has energy $E_{\gamma,1}$ and momentum $\mathbf{k}_1 = E_{\gamma,1}$ on the z direction. After the scattering the photon acquires an energy $E_{\gamma,2}$ and goes to a direction θ respect to the z–axis with momentum $\mathbf{p}_2$. The four-momenta are defined as,

$$\begin{aligned} p_1 &= (m_e, 0, 0, 0)\,, \\ k_1 &= (E_{\gamma,1}, 0, 0, E_{\gamma,1})\,, \\ k_2 &= (E_{\gamma,2}, E_{\gamma,2} \sin\theta, 0, E_{\gamma,2} \cos\theta)\,, \\ p_2 &= p_1 + k_1 - k_2\,. \end{aligned} \tag{D.1.2}$$

We present the squared matrix element for different polarisation transitions in terms of the initial and final photon energies since it simplifies our results drastically. For this we use

$$\begin{aligned} \cos\theta &= 1 - \frac{m_e(E_{\gamma,1} - E_{\gamma,2})}{E_{\gamma,1}E_{\gamma,2}}\,, \\ \sin\theta &= \frac{\sqrt{m_e(E_{\gamma,1} - E_{\gamma,2})(2E_{\gamma,1}E_{\gamma,2} - m_e E_{\gamma,1} + m_e E_{\gamma,2})}}{E_{\gamma,1}E_{\gamma,2}}\,. \end{aligned} \tag{D.1.3}$$

Spin frame

In this frame of reference the incoming and outgoing electrons are moving along the ±z direction respectively, and the incoming and outgoing photons are moving in the

$x - z$ plane. The four-momentum of the particles in this frame are given by,

$$\begin{aligned} p_1 &= (E_e, 0, 0, -k_z) \,, \\ k_1 &= (E_\gamma, k_x, 0, k_z) \,, \\ k_2 &= (E_\gamma, k_x, 0, -k_z) \,, \\ p_2 &= (E_e, 0, 0, k_z) \,. \end{aligned} \tag{D.1.4}$$

where $E_e = \sqrt{k_z^2 + m_e^2}$ and $E_\gamma = \sqrt{k_x^2 + k_z^2}$. Without of generality, $k_x, k_z > 0$ are assumed. Note that $k_z = E_\gamma \sin \frac{\theta}{2}$, and $k_x = E_\gamma \cos \frac{\theta}{2}$, with θ being the angle between the incoming and outgoing photon.

Fixed frame

In the fixed frame, we chose the incoming electron of energy $E_{e,1}$ and momentum $\mathbf{p}_1$ moving purely along the z direction. The photon in the initial state is coming from any direction with an energy $E_{\gamma,1}$ and momentum $\mathbf{k}_1$. The outgoing photon gets energy $E_{\gamma,2}$ and momentum $\mathbf{k}_2$ changing its directions with respect to the initial states. We define the four-momentum particles as,

$$\begin{aligned} p_1 &= (E_{e,1}, 0, 0, p_1) \,, \\ k_1 &= (E_{\gamma,1}, E_{\gamma,1} \cos\theta_1 \sin\phi_1, E_{\gamma,1} \sin\theta_1 \sin\phi_1, E_{\gamma,1} \cos\phi_1) \,, \\ k_2 &= (E_{\gamma,2}, E_{\gamma,2} \cos\theta_2 \sin\phi_2, E_{\gamma,2} \sin\theta_2 \sin\phi_2, E_{\gamma,2} \cos\phi_2) \,, \\ p_2 &= p_1 + k_1 - k_2 \,, \end{aligned} \tag{D.1.5}$$

where ϕ_1 is the angle between the incident photon and the incoming electron, ϕ_2 is the angle between the incident electron and the outgoing photon. Additional θ_1 and θ_2 are the angles between the incoming electron and the incoming photon, and the angle between the direction of the incoming electron and the outgoing photon in the $x - y$ plane respectively. In the fixed frame we require that $p_2^2 = p_1^2$ which leads to

$$E_{\gamma,2} = \frac{E_{\gamma,1}(E_{e,1} - p_1 \cos\phi_1)}{E_{e,1} - p_1 \cos\phi_2 - E_{\gamma,1}(\sin\phi_1 \sin\phi_2 \cos(\theta_2 - \theta_1) + \cos\phi_1 \cos\phi_2 - 1)}$$

$$= \frac{E_{\gamma,1}(E_{e,1} - p_1\mu_1)}{E_{e,1} - p_1\mu_2 - E_{\gamma,1}(\sqrt{1-\mu_1^2}\sqrt{1-\mu_2^2}\cos(\theta_2-\theta_1) + \mu_1\mu_2 - 1)}\,, \quad \text{(D.1.6)}$$

where we have used $\cos\phi_1 = \mu_1$ and $\cos\phi_2 = \mu_2$. In the above, one may use the angle between incoming photon and outgoing photon θ, which is given by

$$\cos\theta = \sin\phi_1 \sin\phi_2 \cos(\theta_2 - \theta_1) + \cos\phi_1 \cos\phi_2\,, \quad \text{(D.1.7)}$$

to simplify the formula.

D.1.1 Polarised squared amplitudes for the different frames

Using the general result of the squared amplitude in Eq. (5.3.11), we have calculated the amplitudes of photon-electron scattering with specified polarisations $e\gamma_\pm \to e\gamma_\pm$ and $e\gamma_\pm \to e\gamma_\mp$ in our four different frames. In the non-relativistic limit ($m_e \gg E_\gamma, \sqrt{E_e^2 - m_e^2}$), all four frames approximate to Thomson scattering. However, in the relativistic limit, different frames can be applied to different physical contexts.

Centre of mass frame

Amplitudes for the photon-electron scattering in this frame of reference with specified polarisations are given by

$$\begin{aligned}
\frac{1}{2}\sum_{\text{spins}} |\mathcal{M}(e\gamma_- \to e\gamma_-)|^2 =& \frac{1}{2}\sum_{\mathrm{S_e}} |\mathcal{M}(e\gamma_+ \to e\gamma_+)|^2 \\
=& (1+\cos\theta)\frac{\left(E_\gamma^2(1-\cos\theta)^2 + (E_\gamma + E_e)^2(\cos\theta + 1)\right)}{(E_e + E_\gamma\cos\theta)^2}\,, \\
[.5cm]\frac{1}{2}\sum_{\text{spins}} |\mathcal{M}(e\gamma_+ \to e\gamma_-)|^2 =& \frac{1}{2}\sum_{\mathrm{S_e}} |\mathcal{M}(e\gamma_- \to e\gamma_+)|^2 \\
=& (1-\cos\theta)^2\frac{(E_e - E_\gamma)\left(E_e^2 - E_\gamma^2\cos\theta\right)}{(E_e + E_\gamma)(E_e + E_\gamma\cos\theta)^2}\,. \quad \text{(D.1.8)}
\end{aligned}$$

In the high energy limit, i.e., the ultra-relativistic limit, they approximate to

$$\frac{1}{2}\sum_{\text{spins}} |\mathcal{M}(e\gamma_\pm \to e\gamma_\pm)|^2 = 1 + \cos\theta + \frac{4}{1+\cos\theta}\,,$$

$$\frac{1}{2}\sum_{\text{spins}}|\mathcal{M}(e\gamma_\pm \to e\gamma_\mp)|^2 = \frac{m_e^2(1-\cos\theta)^3}{4E_\gamma^2(1+\cos\theta)^2}\,. \tag{D.1.9}$$

Here, we have dropped the small mass in the denominator. These formulas are not valid if θ is close to π.

Rest frame

Working in the rest frame of reference, the corresponding squared amplitudes for processes where the photon helicity is preserved and changed are, respectively

$$\begin{aligned}\frac{1}{2}\sum_{\text{spins}}|\mathcal{M}(e\gamma_\pm \to e\gamma_\pm)|^2 &= \frac{(2E_{\gamma,1}E_{\gamma,2} - E_{\gamma,1}m_e + E_{\gamma,2}m_e)(E_{\gamma,1}^2 + E_{\gamma,2}^2 - E_{\gamma,1}m_e + E_{\gamma,2}m_e)}{E_{\gamma,1}^2E_{\gamma,2}^2}\,,\\ \frac{1}{2}\sum_{\text{spins}}|\mathcal{M}(e\gamma_\pm \to e\gamma_\mp)|^2 &= \frac{m_e(E_{\gamma,1} - E_{\gamma,2})^2(E_{\gamma,1} - E_{\gamma,2} + m_e)}{E_{\gamma,1}^2E_{\gamma,2}^2}\,.\end{aligned} \tag{D.1.10}$$

In the ultra relativistic limit ($E_{\gamma,1} \to \infty$), we get

$$\begin{aligned}\frac{1}{2}\sum_{\text{spins}}|\mathcal{M}(e\gamma_\pm \to e\gamma_\pm)|^2 &= 2\frac{E_{\gamma,1}^2 + E_{\gamma,2}^2}{E_{\gamma,1}E_{\gamma,2}}\,,\\ \frac{1}{2}\sum_{\text{spins}}|\mathcal{M}(e\gamma_\pm \to e\gamma_\mp)|^2 &= \frac{m_e(E_{\gamma,1} - E_{\gamma,2})^3}{E_{\gamma,1}^2E_{\gamma,2}^2}\,.\end{aligned} \tag{D.1.11}$$

Spin frame

Based on this frame, the amplitudes for the different polarisation transitions are

$$\begin{aligned}\frac{1}{2}\sum_{\text{spins}}|\mathcal{M}(e\gamma_\pm \to e\gamma_\pm)|^2 &= \frac{4E_e^2\sin^2\theta\left(E_\gamma^2\cos^2\theta\left(1+\cos^2\theta\right) + m_e^2\sin^2\theta\right)}{\left(E_e^2 - E_\gamma^2\cos^4\theta\right)^2}\,,\\ \frac{1}{2}\sum_{\text{spins}}|\mathcal{M}(e\gamma_\pm \to e\gamma_\mp)|^2 &= \frac{4m_e^2\cos^4\theta\left(E_e^2 + E_\gamma^2\cos^2\theta\right)}{\left(E_e^2 - E_\gamma^2\cos^4\theta\right)^2}\,.\end{aligned} \tag{D.1.12}$$

Fixed frame

When we sum/average over final/initial spins, the different polarisation transitions in the fixed frame are:

$$\frac{1}{2}\sum_{\text{spins}}|\mathcal{M}(e\gamma_\pm \to e\gamma_\pm)|^2 =$$

$$\frac{\Big(m_e^2 E_{\gamma,2}(E_{e,1}-p_{e,z}\mu_2) - E_{\gamma,1}(E_{e,1}-p_{e,z}\mu_1)(m_e^2 - 2E_{\gamma,2}(E_{e,1}-p_{e,z}\mu_2))\Big)}{E_{\gamma,1}^2 E_{k_2}^2 (E_{e,1}-p_{e,z}\mu_1)^2 (E_{e,1}-p_{e,z}\mu_2)^2}$$
$$\times \Big(E_{k_1}^2 (E_{e,1}-p_{e,z}\mu_1)^2 - m_e^2 E_{\gamma,1}(E_{e,1}-p_{e,z}\mu_1)$$
$$+ E_{\gamma,2}(E_{e,1}-p_{e,z}\mu_2)(m_e^2 + E_{\gamma,2}(E_{e,1}-p_{e,z}\mu_2))\Big)\,,$$

$$\frac{1}{2}\sum_{\text{spins}}|\mathcal{M}(e\gamma_\pm \to e\gamma_\mp)|^2 = \frac{m_e^2(\Delta-1)^2\Big(m_e^2 + E_{\gamma,1}E_{\gamma,2}(1-\Delta)\Big)}{(E_{e,1}-p_{e,z}\mu_1)^2(E_{e,1}-p_{e,z}\mu_2)^2}, \tag{D.1.13}$$

where $\Delta \equiv \cos\theta = \sqrt{1-\mu_1^2}\sqrt{1-\mu_2^2}\cos(\theta_1-\theta_2)+\mu_1\mu_2$, $\mu_1 = \cos\phi_1$ and $\mu_2 = \cos\phi_2$. In the ultra ($E_{\gamma,1}\to\infty$) relativistic limit we obtain

$$\begin{aligned}
\frac{1}{2}\sum_{\text{spins}}|\mathcal{M}(e\gamma_\pm \to e\gamma_\pm)|^2 =& \frac{\Big(E_{e,1}-\mu_1 p_{e,z}\Big)\Big(1-\Delta^2\Big)}{m_e^2}E_{\gamma,1}\,,\\
\frac{1}{2}\sum_{\text{spins}}|\mathcal{M}(e\gamma_\pm \to e\gamma_\mp)|^2 =& \frac{\Big(E_{e,1}-\mu_1 p_{e,z}\Big)\Big(1-\Delta\Big)^2}{m_e^2}E_{\gamma,1}\,.
\end{aligned} \tag{D.1.14}$$

Appendix E

Second Approach

In section 5.3.1 we have calculated the **A**–matrix elements given in Eq. (5.2.7), by directly substituting the explicit form of the electron spinors $u(p)_{\pm\frac{1}{2}}$, into the matrix element $\mathcal{M}$ accordingly to the chosen frame of reference. However, for the case of unpolarised electrons there is another way to get explicit form of these elements. Nonetheless the form of the general expression is not simple until applying the kinematics.

In the second approach instead of replacing all the elements in the amplitude, we sum/average over the electron spin as usual and use trace technology. Therefore, this approach can only be applied to the case of unpolarised electrons. Normally, if we do not care about the polarisation of the photons during the scattering process, we also sum/average over their helicity states. However, in order to find the polarised amplitude of polarised photon scattering, we assume definite helicity states for each polarisation vector in the initial and final states.

The calculation of the squared polarised amplitude using this approach starts from Eq. (5.3.1), which can be written as

$$\frac{1}{2}\sum_{\alpha,\beta=\pm}\mathcal{M}(e_\alpha\gamma_i \to e_\beta\gamma_{i'})\mathcal{M}^*(e_\alpha\gamma_j \to e_\beta\gamma_{j'}) \equiv$$

$$\Big(M_{i'i}\,M^*_{j'j}\Big)_s + \Big(M_{i'i}M^*_{j'j}\Big)_t + 2\,\mathrm{Re}[M_{i'i}M^*_{j'j}]_{st}\,, \qquad \text{(E.0.1)}$$

where we have summed/averaged over electron spin, but not photon helicity. The sub indices correspond to the s and u–channel contributions and i', i, j', j indicates the polarisation. More explicitly, each term in the equation above is given by,

$$\begin{aligned}
\left(M_{i'i}M^{*}_{j'j}\right)_{s} =& \frac{e^{4}}{(s-m_e^2)^2}\left(M_{\mu\nu}M^{*}_{\mu'\nu'}\right)_{s}\ \epsilon_{i}^{(1)\mu}\epsilon_{i'}^{*(2)\nu}\epsilon_{j}^{*(1)\mu'}\epsilon_{j'}^{(2)\ \nu'}\ ,\\
\left(M_{i'i}M^{*}_{j'j}\right)_{t} =& \frac{e^{4}}{(t-m_e^2)^2}\left(M_{\mu\nu}M^{*}_{\mu'\nu'}\right)_{t}\ \epsilon_{i}^{(1)\mu}\epsilon_{i'}^{*(2)\nu}\epsilon_{j}^{*(1)\mu'}\epsilon_{j'}^{(2)\ \nu'}\ ,\\
\left(M_{i'i}M^{*}_{j'j}\right)_{st} =& \frac{e^{4}}{(s-m_e^2)(t-m_e^2)}\left(M_{\mu\nu}M^{*}_{\mu'\nu'}\right)_{st}\ \epsilon_{i}^{(1)\mu}\epsilon_{i'}^{*(2)\nu}\epsilon_{j}^{*(1)\mu'}\epsilon_{j'}^{(2)\ \nu'}\ .
\end{aligned} \tag{E.0.2}$$

$\left(M_{\mu\nu}M^{*}_{\mu'\nu'}\right)_{s,t,st}$ are the squared polarisation vector–independent amplitude corresponding to each channel. This is the most general expression for the polarised squared amplitude of photon–scattering.

For simplicity, and comparison with Eq. (5.3.4) in section 5.3.1, we apply the rest frame kinematics. Therefore, the polarised squared amplitude takes the form,

$$\begin{aligned}
&\frac{1}{2}\sum_{\alpha,\beta}\mathcal{M}(e_\alpha\gamma_i\to e_\beta\gamma_{i'})\mathcal{M}(e_\alpha\gamma_j\to e_\beta\gamma_{j'})^{*} = \frac{1}{2m_eE_{\gamma,1}^2E_{\gamma,2}}\times\\
&\times\Big[2E_{\gamma,1}k_1\cdot\epsilon_i^{*(2)}\Big[(E_{\gamma,2}-E_{\gamma,1})\epsilon_{i'}^{(1)}\cdot\epsilon_j^{(2)}k_2\cdot\epsilon_{j'}^{*(1)}+(E_{\gamma,1}+E_{\gamma,2})k_2\cdot\epsilon_{i'}^{(1)}\epsilon_{j'}^{(1)}\cdot\epsilon_j^{(2)}\Big]\\
&+2E_{\gamma,1}k_1\cdot\epsilon_j^{(2)}\Big[(E_{\gamma,1}-E_{\gamma,2})k_2\cdot\epsilon_{i'}^{(1)}\epsilon_{j'}^{*(1)}\cdot\epsilon_i^{*(2)}-(E_{\gamma,1}+E_{\gamma,2})k_2\cdot\epsilon_{j'}^{*(1)}\epsilon_{i'}^{(1)}\cdot\epsilon_i^{*(2)}\Big]\\
&+E_{\gamma,2}\Big[\epsilon_{j'}^{*(1)}\cdot\epsilon_j^{(2)}\epsilon_{i'}^{(1)}\cdot\epsilon_i^{*(2)}\Big(2E_{\gamma,1}^2\Big[(E_{\gamma,2}-E_{\gamma,1})(\cos\theta-1)+4m_e\Big]+m_e^3\Big)\\
&-\Big(\epsilon_{j'}^{*(1)}\cdot\epsilon_j^{*(2)}\epsilon_{i'}^{(1)}\cdot\epsilon^{i}(k_2)-\epsilon_{j'}^{*(1)}\cdot\epsilon_{i'}^{(1)}\epsilon_i^{*(2)}\cdot\epsilon_j^{(2)}\Big)\left(2E_{\gamma,1}^2(\cos\theta-1)(E_{\gamma,2}-E_{\gamma,1})+m_e^3\right)\Big]\Big]\ ,
\end{aligned} \tag{E.0.3}$$

where we have neither specified the photon polarisation in the initial nor final state.

Considering the case where polarisation is conserved (changed), i.e., $e\gamma_\pm\to e\gamma_\pm$ ($e\gamma_\pm\to e\gamma_\mp$), the expression for the polarised squared amplitude simplifies even more and leads to the same result as in (D.1.10). Furthermore, the result in Eq. (E.0.3) allows to calculate the **A**–matrix by just doing every combination of $M_{i'i}M^{*}_{j'j}$ required in Eq. (5.3.1). In here, we have done it for the rest frame. However, is possible to do all this process for any frame of reference in Appendix D.

Appendix F

Cross section calculations

The cross section for the process preserving circular polarisation ($e\gamma_\pm \to e\gamma_\pm$) and the process changing it ($e\gamma_\pm \to e\gamma_\mp$) can be calculated by following the procedure described in Appendix B of [227], by which we express the amplitude in terms of the variables χ and η, where $\chi = (p_1 \cdot k_1)/m_e^2$ and $\omega = (p_1 \cdot k_2)/m_e^2$ and perform the integral over ω:

$$\sigma = \int_{\frac{2\chi}{2\chi+1}}^{2\chi} \frac{1}{32\pi m_e^2 \chi^2} |\mathcal{M}(\chi,\omega)|^2 d\omega\,. \tag{F.0.1}$$

We can then use the Lorentz invariant amplitudes in Eq. (5.3.11) to find the corresponding cross sections

$$\begin{aligned}
\sigma(e\gamma_\pm \to e\gamma_\pm) &= \frac{3\sigma_\mathrm{T}}{8}\left(\frac{2+3\chi-\chi^2}{\chi^2(1+2\chi)} - \frac{2+\chi-2\chi^2}{2\chi^3}\log(1+2\chi)\right),\\
\sigma(e\gamma_\pm \to e\gamma_\mp) &= \frac{3\sigma_\mathrm{T}}{8}\left(\frac{2+9\chi+13\chi^2+4\chi^3}{\chi^2(1+2\chi)^2} - \frac{2+3\chi}{2\chi^3}\log(1+2\chi)\right),
\end{aligned} \tag{F.0.2}$$

where $\sigma_\mathrm{T} = \frac{1}{6\pi m_e^2}$.The same method can be used to calculate the cross sections for the photon scattering off polarised electrons.

The summation of both photon and electron polarisations gives the standard Compton scattering amplitude

$$\begin{aligned}
|\mathcal{M}_\mathrm{C}|^2 &= \frac{1}{4}\sum_{k,l=\pm}\sum_{\alpha,\beta=\pm} |\mathcal{M}(e_\alpha\gamma_k \to e_\beta\gamma_l)|^2\\
&= 2\left(\frac{p_1{\cdot}k_1}{p_1{\cdot}k_2} + \frac{p_1{\cdot}k_2}{p_1{\cdot}k_1}\right) + 4m_e^2\left(\frac{1}{p_1{\cdot}k_1} - \frac{1}{p_1{\cdot}k_2}\right) + 2m_e^4\left(\frac{1}{p_1{\cdot}k_1} - \frac{1}{p_1{\cdot}k_2}\right)^2
\end{aligned} \tag{F.0.3}$$

and the total Compton scattering cross section is

$$\sigma_{\mathrm{C}} = \frac{3\sigma_{\mathrm{T}}}{4}\left(\frac{2+8\chi+9\chi^2+\chi^3}{\chi^2(1+2\chi)^2} + \frac{-2-2\chi+\chi^2}{2\chi^3}\log(1+2\chi)\right), \tag{F.0.4}$$

which is consistent with former result in [228]. It is useful to define the “summed” asymmetry between the two photon helicity states at the cross section level,

$$\begin{aligned}\Delta_V^{\sigma} &= \frac{\sigma(e\gamma_+ \to e\gamma_+) + \sigma(e\gamma_- \to e\gamma_-) - \sigma(e\gamma_+ \to e\gamma_-) - \sigma(e\gamma_- \to e\gamma_+)}{\sigma(e\gamma_+ \to e\gamma_+) + \sigma(e\gamma_- \to e\gamma_-) + \sigma(e\gamma_+ \to e\gamma_-) + \sigma(e\gamma_- \to e\gamma_+)} \\ &= \frac{\chi(1+\chi)\left(-2\chi(1+3\chi)+(1+2\chi)^2\log(1+2\chi)\right)}{2\chi\left(2+8\chi+9\chi^2+\chi^3\right)+\left(-2-2\chi+\chi^2\right)(1+2\chi)^2\log(1+2\chi)} \end{aligned} \tag{F.0.5}$$

which is the ratio of total conserved circular polarisation after integrating over phase space. Its behaviour as a function of χ is numerically shown in Fig. F.1. The Thomson scattering refers to the limit $\chi \to 0$. In this case, only $\Delta_V^{\sigma} = 0$, which is well-known [81]. The circular polarisation is likely to be preserved with larger χ, which corresponds to larger energy momentum transfer between photon and electron. For $\chi \gtrsim 10^4$ (corresponding to $E_{\gamma,1} \gtrsim 0.361$ GeV in the COM frame, or $E_{\gamma,1} \gtrsim 511$ GeV in the rest frame), Δ_V^{σ} can reach 0.8.

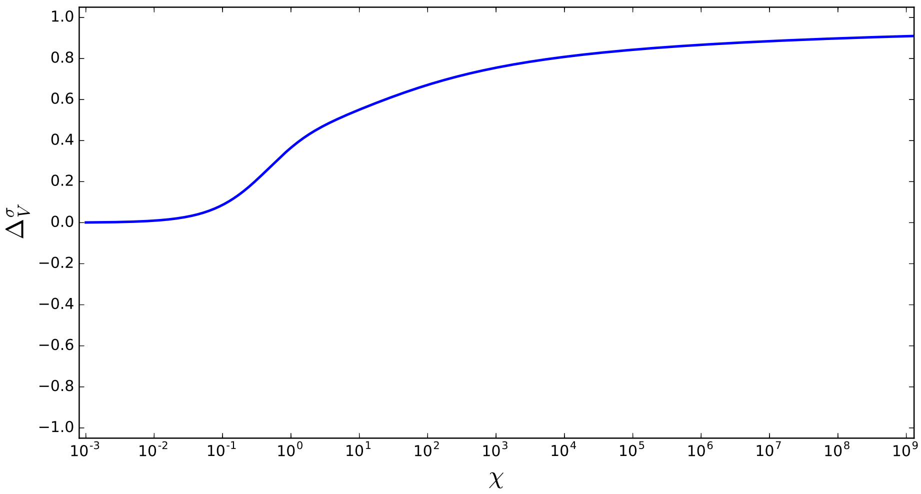

Figure F.1: The change of the net circular polarisation at the cross section level, Δ_V^{σ}, as a function of the Lorentz invariant parameter $\chi = p_1{\cdot}k_1/m_e^2$.

F.1 More plots in the fixed frame

The fixed frame is the most generic frame of reference we consider and consequently, has more kinematic parameters that can be changed. For the scattering with high energy incoming electron, circular polarisation is conserved for any angular distribution and any energy of the incoming photon, which agrees with the results in the spin and COM frames. However, for low energy incoming electrons, taking different kinematic configurations from the one shown in the main text (Fig. 5.1d), the plot in the fixed frame changes dramatically. Here, we show two sets of plots (Fig. F.2 and F.3) where we vary the energy of the incoming electron and the angular configuration of the scattering process. In every set of plots, the vertical axis corresponds to the energy of the photon in the initial state and the horizontal axis corresponds to $\cos\phi_2$ which is the angle between outgoing photon and incoming electron as discussed in section 5.3.1.

In Fig. F.2, we fixed the incident angle of the photon, ϕ_1, i.e., the angle between the incoming photon and electron, with its cosine value fixed at $\cos\phi_1 = 1$, 0.5 and 0 in the left, middle and right panels, respectively. For each row, we fix the kinetic energy of the incoming electron $p_1 = 1$ keV, 0.1 MeV, 1 MeV, 5 MeV, respectively. $\theta_1 - \theta_2$ is the difference between incoming and outgoing photons projected on the $x - y$ plane at $\pi/3$. The influence of $\theta_1 - \theta_2$ is less important, so we fix its cosine value at 0.5 for all plots. As shown in the left-top corner, by setting the incident angle $\phi_1 = 0$, the result for photon scattering with low energy electron is almost the same as that in the rest frame. But this behaviour changes largely once the incident angle increases. Increasing the energy of the incoming electron in general lead to larger Δ_V, i.e., less change of the net circular polarisation after scattering. Once $p_1 \gg m_e$, the circular polarisation is more likely to be preserved for large incident angles. In Fig. F.3, we fixed $p_1 = 1$ GeV, and see that the $\Delta_V < 0.9$ only for very small ϕ_1, noting that $\cos\phi_1 = 0.99999999$ and 0.999999 correspond to $\phi_1 \approx 0.0081^\circ$ and 0.081°, respectively. Only for $\phi_1 \gtrsim 0.1^\circ$, $\Delta_V > 0.9$ is satisfied.

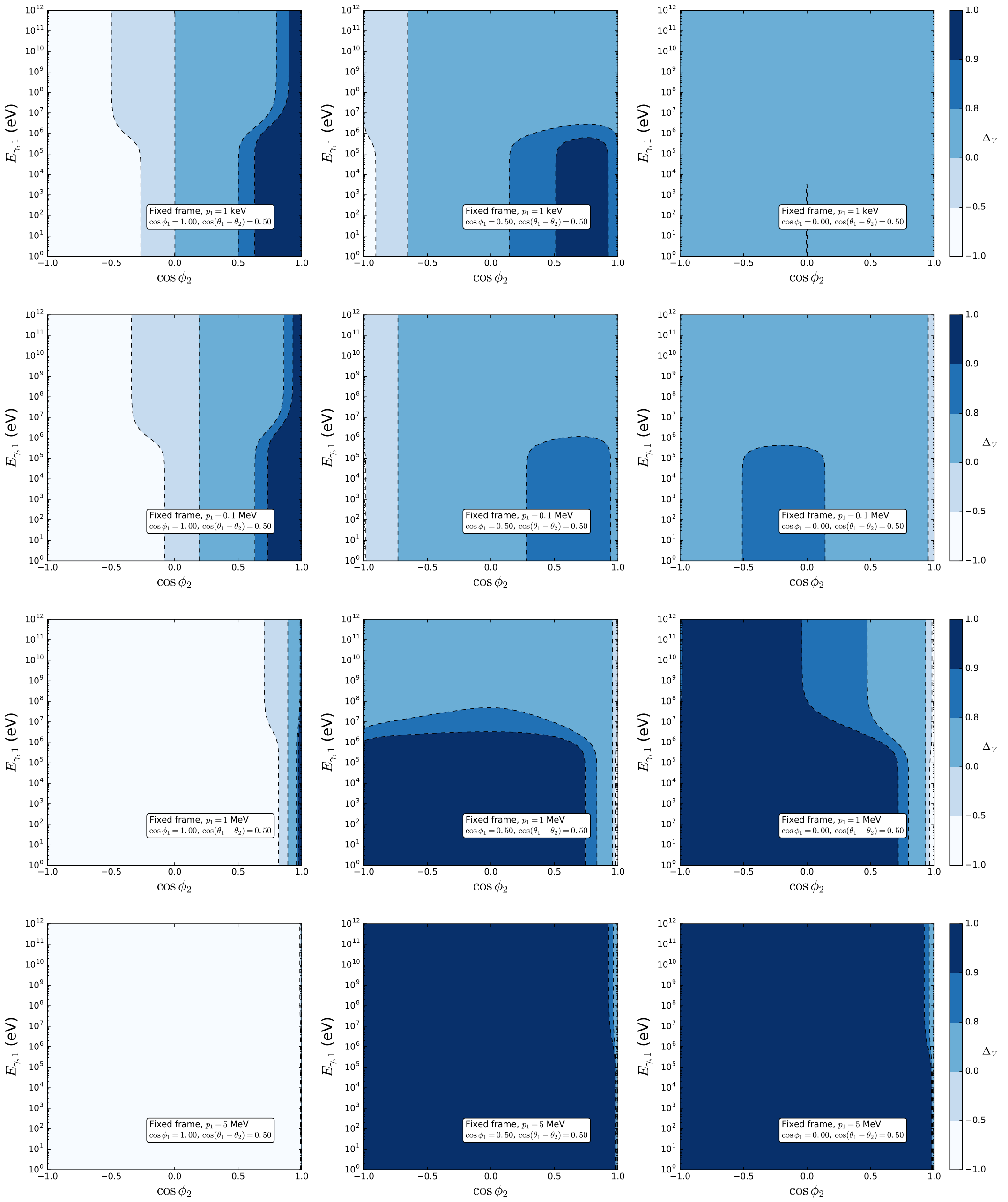

Figure F.2: The asymmetry of photon helicity states Δ_V in fixed frames with respect to different direction and energy information. For each row, we fix incoming electron kinetic energy $p_1 = 1$ keV, 0.1 MeV, 1 MeV and 5 MeV, respectively and for each column, we fix the angle ϕ_1 between incoming photon and electron with $\cos\phi_1 = 1$, 0.5 and 0, respectively. The angle difference between incoming and outgoing photons projected on the $x-y$ plane is fixed $\cos(\theta_1-\theta_2) = 0.5$.

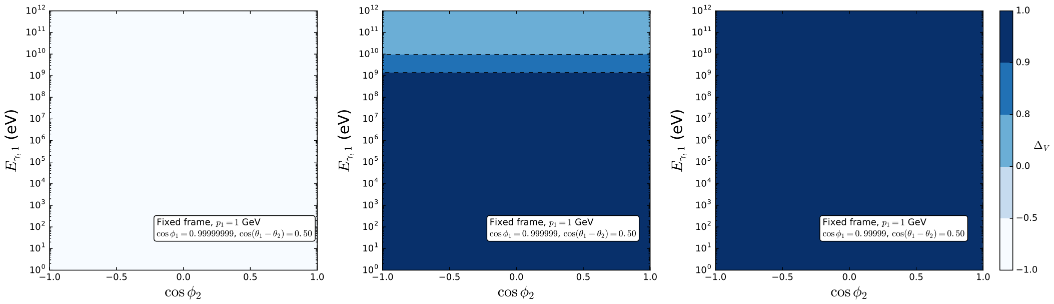

Figure F.3: The asymmetry of photon helicity states Δ_V for photon scattering with energetic electron in the fixed frame. The kinetic energy of incoming electron is fixed at 1 GeV, $\cos(\theta_1 - \theta_2) = 0.5$ is used as in Fig. F.2, and $\cos\phi_1 = 0.99999999$, 0.999999, 0.99999 respectively in each subfigure.

Appendix G

Relationship between T_{eff} and T_c in a WD

The photon diffusion equation is (with T given in K)

$$L = -4\pi r^2 \frac{c}{3\kappa\epsilon}\frac{d}{dr}(aT^4), \tag{G.0.1}$$

where L is the luminosity, (aT^4) is the black body energy density and κ is the opacity of the stellar material. In this expression, $1/\kappa\epsilon$ is an estimation of he photon mean free path. This leads to the energy transformation which determines the temperature gradient,

$$\frac{dT}{dr} = -\frac{3\kappa\epsilon}{4acT^3}\frac{L}{4\pi r^2}. \tag{G.0.2}$$

The aim is to find the luminosity surface L in terms of the temperature of the core T_c. This will lead us to a relation between the observed temperate T_{eff} of the star and T_c. To do so we start from the equation of hydrostatic equilibrium

$$\frac{dP}{dT} = \frac{GM(r)\epsilon}{c^2 r^2}\frac{4acT^3}{3\kappa\epsilon}\frac{4\pi r^2}{L}. \tag{G.0.3}$$

At high densities, the appropriate approximation to the opacity is Kramer's opacity which is $\kappa = \kappa_0 \epsilon \left(\frac{T}{K}\right)^{-3.5}$ with $\kappa_0 = 4.34 \times 10^{24} Z(1 + X_h)\,\mathrm{cm}^2\,\mathrm{g}^{-1}$. In the latter expression, Z stands for fractional abundance of elements heavier than hydrogen and

X_h is the fractional abundance of hydrogen [198]. Introducing the non-degenerate pressure given by the ideal gas law as $P = \epsilon K_B T/(M_u \mu)$, we obtain

$$PdP = \frac{4n\, a\, c 4\pi M(r) G}{3\kappa_0 \mu L} T^{7.5} dT \tag{G.0.4}$$

where μ is the mean molecular weight. In the surface layers, we can set $M(r) = M_\star$. We then integrate, with the boundary condition $P = 0$ at $T = 0$ and obtain

$$\epsilon = \sqrt{\frac{2}{8.5} \frac{4\, a\, c 4\pi M_\star G}{3\kappa_0 L} \frac{\mu M_u}{K_B K^{3.5}}} T^{3.25}. \tag{G.0.5}$$

We just have obtain ϵ in terms of the temperature in the outer region of the star. Kelvins (K) in red comes from the definition of κ. The surface approximation breaks down at some point in the interior layers when matter becomes degenerate. This occurs when the non-degenerate pressure equals the degenerate pressure at radius R_c. In this case, the core energy density is defined as

$$\epsilon_c = 0.5 \times 10^{-8} g\, cm^{-3} Y_e^{-1} \left(\frac{T_c}{K}\right)^{1.5}, \tag{G.0.6}$$

where Y_e is the mean number of electrons per baryon and T_c is the core temperature. Matching expressions Eq. (G.0.5) and Eq. (G.0.6) and solving for L leads to

$$L = 5.7 \times 10^6 \mathrm{erg\, s}^{-1} \mu Y_e^2 \frac{1}{Z(1+X_h)} \frac{M_\star}{M\odot} \left(\frac{T_c}{K}\right)^{3.5}, \tag{G.0.7}$$

where the gravitational constant G has been written in terms of the solar mass for convenience. Notice that this result is similar to $L = 4\pi\sigma_B R_\star^2 T_{eff}^4$[1] which is luminosity for a black body, but involves the temperature of the core T_c instead of the observable temperature of the surface T_{eff}. This suggest that the effective temperature is related to the core temperature as $T_{eff} \propto T_c^{7/8}$.

---

[1] σ_B has units of$[erg\, cm^{-2}\, s^{-1}\, K^{-4}]$ which gives the correct units for the luminosity.

Bibliography

[1] S. Balaji, M. Ramirez-Quezada and Y.-L. Zhou, *CP violation and circular polarisation in neutrino radiative decay*, *JHEP* **04** (2020) 178, [`1910.08558`].

[2] S. Balaji, M. Ramirez-Quezada and Y.-L. Zhou, *CP violation in the neutrino dipole moment*, *JHEP* **12** (2020) 090, [`2008.12795`].

[3] C. Boehm, A. O.-D. Campo, M. Ramirez-Quezada and Y.-L. Zhou, *Polarisation of high energy gamma-rays after scattering*, *Journal of Cosmology and Astroparticle Physics* **2019** (dec, 2019) 041–041.

[4] P. A. M. Dirac, *The quantum theory of the electron*, *Proceedings of the Royal Society of London. Series A, Containing Papers of a Mathematical and Physical Character* **117** (1928) 610–624.

[5] S. Tomonaga, *On a Relativistically Invariant Formulation of the Quantum Theory of Wave Fields**, *Progress of Theoretical Physics* **1** (08, 1946) 27–42.

[6] J. Schwinger, *On quantum-electrodynamics and the magnetic moment of the electron*, *Phys. Rev.* **73** (Feb, 1948) 416–417.

[7] J. Schwinger, *Quantum electrodynamics. i. a covariant formulation*, *Phys. Rev.* **74** (Nov, 1948) 1439–1461.

[8] R. P. Feynman, *Space-time approach to quantum electrodynamics*, *Phys. Rev.* **76** (Sep, 1949) 769–789.

[9] R. P. Feynman, *The theory of positrons*, *Phys. Rev.* **76** (Sep, 1949) 749–759.

[10] R. P. Feynman, *Mathematical formulation of the quantum theory of electromagnetic interaction*, *Phys. Rev.* **80** (Nov, 1950) 440–457.

[11] S. L. Glashow, *Partial-symmetries of weak interactions*, *Nuclear Physics* **22** (1961) 579 – 588.

[12] S. Weinberg, *A model of leptons*, *Phys. Rev. Lett.* **19** (Nov, 1967) 1264–1266.

[13] A. Salam, *Weak and Electromagnetic Interactions*, *Conf. Proc.* **C680519** (1968) 367–377.

[14] A. Pich, *Aspects of quantum chromodynamics*, in *Proceedings, Summer School in Particle Physics: Trieste, Italy, June 21-July 9, 1999*, pp. 53–102, 1999, `hep-ph/0001118`.

[15] G. Arnison, A. Astbury, B. Aubert, C. Bacci, G. Bauer, A. Bézaguet et al., *Experimental observation of isolated large transverse energy electrons with associated missing energy at s=540 gev*, *Physics Letters B* **122** (1983) 103 – 116.

[16] M. Banner, R. Battiston, P. Bloch, F. Bonaudi, K. Borer, M. Borghini et al., *Observation of single isolated electrons of high transverse momentum in events with missing transverse energy at the cern pp collider*, *Physics Letters B* **122** (1983) 476 – 485.

[17] G. Arnison, A. Astbury, B. Aubert, C. Bacci, G. Bauer, A. Bézaguet et al., *Experimental observation of lepton pairs of invariant mass around 95 gev/c2 at the cern sps collider*, *Physics Letters B* **126** (1983) 398 – 410.

[18] P. Bagnaia, M. Banner, R. Battiston, P. Bloch, F. Bonaudi, K. Borer et al., *Evidence for z0→e+e at the cern pp collider*, *Physics Letters B* **129** (1983) 130 – 140.

[19] G. S. Guralnik, C. R. Hagen and T. W. B. Kibble, *Global conservation laws and massless particles*, *Phys. Rev. Lett.* **13** (Nov, 1964) 585–587.

[20] F. Englert and R. Brout, *Broken symmetry and the mass of gauge vector mesons*, *Phys. Rev. Lett.* **13** (Aug, 1964) 321–323.

[21] P. W. Higgs, *Broken symmetries and the masses of gauge bosons*, *Phys. Rev. Lett.* **13** (Oct, 1964) 508–509.

[22] N. Cabibbo, *Unitary Symmetry and Leptonic Decays*, *Phys. Rev. Lett.* **10** (1963) 531–533.

[23] L.-L. Chau and W.-Y. Keung, *Comments on the parametrization of the kobayashi-maskawa matrix*, *Phys. Rev. Lett.* **53** (Nov, 1984) 1802–1805.

[24] R. Brown, U. Camerini, P. H. Fowler, H. Muirhead, C. F. Powell and D. M. Ritson, *Observations With Electron Sensitive Plates Exposed to Cosmic Radiation*, *Nature* **163** (1949) 82.

[25] R. H. Dalitz, *Decay of tau mesons of known charge*, *Phys. Rev.* **94** (1954) 1046–1051.

[26] T. D. Lee and C. N. Yang, *Question of parity conservation in weak interactions*, *Phys. Rev.* **104** (Oct, 1956) 254–258.

[27] J. H. Christenson, J. W. Cronin, V. L. Fitch and R. Turlay, *Evidence for the* 2π *decay of the* k_2^0 *meson*, *Phys. Rev. Lett.* **13** (Jul, 1964) 138–140.

[28] Belle collaboration, K. Abe et al., *Observation of large CP violation in the neutral* B *meson system*, *Phys. Rev. Lett.* **87** (2001) 091802, [`hep-ex/0107061`].

[29] BaBar collaboration, B. Aubert et al., *Observation of CP violation in the* B^0 *meson system*, *Phys. Rev. Lett.* **87** (2001) 091801, [`hep-ex/0107013`].

[30] T. L. Collaboration, A. A. Alves, L. M. A. Filho, A. F. Barbosa, I. Bediaga, G. Cernicchiaro et al., *The LHCb detector at the LHC*, *Journal of Instrumentation* **3** (aug, 2008) S08005–S08005.

[31] SNO COLLABORATION collaboration, Q. R. Ahmad, R. C. Allen, T. C. Andersen, J. D. Anglin, G. Bühler, J. C. Barton et al., *Measurement of the rate of* $\nu_e + d \rightarrow p + p + e^-$ *interactions produced by* ^8b *solar neutrinos at the sudbury neutrino observatory*, *Phys. Rev. Lett.* **87** (Jul, 2001) 071301.

[32] SUPER-KAMIOKANDE COLLABORATION collaboration, Y. Fukuda, T. Hayakawa, E. Ichihara, K. Inoue, K. Ishihara, H. Ishino et al., *Evidence for oscillation of atmospheric neutrinos*, *Phys. Rev. Lett.* **81** (Aug, 1998) 1562–1567.

[33] PARTICLE DATA GROUP collaboration, M. Tanabashi, K. Hagiwara, K. Hikasa, K. Nakamura, Y. Sumino, F. Takahashi et al., *Review of particle physics*, *Phys. Rev. D* **98** (Aug, 2018) 030001.

[34] W. Hu and S. Dodelson, *Cosmic Microwave Background Anisotropies*, *Ann. Rev. Astron. Astrophys.* **40** (2002) 171–216, [`astro-ph/0110414`].

[35] F. Zwicky, *Republication of: The redshift of extragalactic nebulae*, *General Relativity and Gravitation* **41** (Jan., 2009) 207–224.

[36] F. Zwicky, *On the Masses of Nebulae and of Clusters of Nebulae*, *Astrophys. J.* **86** (1937) 217–246.

[37] A. Bosma, *21-cm line studies of spiral galaxies. 2. The distribution and kinematics of neutral hydrogen in spiral galaxies of various morphological types.*, *Astron. J.* **86** (1981) 1825.

[38] V. C. Rubin and J. Ford, W.Kent, *Rotation of the Andromeda Nebula from a Spectroscopic Survey of Emission Regions*, *Astrophys. J.* **159** (1970) 379–403.

[39] H. Baer and X. Tata, *Dark matter and the LHC*, pp. 179–203. 2009. `0805.1905`. 10.1007/978-81-8489-295-6_12.

[40] F. Ruppin, J. Billard, E. Figueroa-Feliciano and L. Strigari, *Complementarity*

of dark matter detectors in light of the neutrino background, *Phys. Rev. D* **90** (2014) 083510, [1408.3581].

[41] XENON collaboration, E. Aprile et al., *Dark Matter Search Results from a One Ton-Year Exposure of XENON1T*, *Phys. Rev. Lett.* **121** (2018) 111302, [1805.12562].

[42] DarkSide collaboration, P. Agnes et al., *Low-Mass Dark Matter Search with the DarkSide-50 Experiment*, *Phys. Rev. Lett.* **121** (2018) 081307, [1802.06994].

[43] S. De and H. Tashiro, *Circular polarization of the cmb: A probe of the first stars*, 1401.1371.

[44] C. Boehm, C. Degrande, O. Mattelaer and A. C. Vincent, *Circular polarisation: a new probe of dark matter and neutrinos in the sky*, *JCAP* **1705** (2017) 043, [1701.02754].

[45] Z. Maki, M. Nakagawa and S. Sakata, *Remarks on the Unified Model of Elementary Particles*, *Progress of Theoretical Physics* **28** (11, 1962) 870–880.

[46] B. Pontecorvo, *Inverse beta processes and nonconservation of lepton charge*, *Zhur. Ekspt'l. i Teoret. Fiz.* **Vol: 34** (1, 1958) .

[47] Particle Data Group collaboration, M. Tanabashi et al., *Review of Particle Physics*, *Phys. Rev.* **D98** (2018) 030001.

[48] E. Majorana, *Teoria simmetrica dell'elettrone e del positrone*, *Il Nuovo Cimento* **14** (Apr., 1937) 171–184.

[49] V. Gribov and B. Pontecorvo, *Neutrino astronomy and lepton charge*, *Physics Letters B* **28** (1969) 493 – 496.

[50] C. Giunti and C. W. Kim, *Fundamentals of Neutrino Physics and Astrophysics*. 4, 2007.

[51] P. Minkowski, *→e at a rate of one out of 109 muon decays?*, *Physics Letters B* **67** (1977) 421 – 428.

[52] T. Yanagida, *Horizontal Symmetry and Masses of Neutrinos*, *Progress of Theoretical Physics* **64** (09, 1980) 1103–1105.

[53] M. Gell-Mann, P. Ramond and R. Slansky, *Complex Spinors and Unified Theories*, *Conf. Proc.* **C790927** (1979) 315–321, [`1306.4669`].

[54] R. N. Mohapatra and G. Senjanović, *Neutrino mass and spontaneous parity nonconservation*, *Phys. Rev. Lett.* **44** (Apr, 1980) 912–915.

[55] Z.-z. Xing and Z.-h. Zhao, *The minimal seesaw and leptogenesis models*, `2008.12090`.

[56] V. Brdar, A. J. Helmboldt, S. Iwamoto and K. Schmitz, *Type-I Seesaw as the Common Origin of Neutrino Mass, Baryon Asymmetry, and the Electroweak Scale*, *Phys. Rev. D* **100** (2019) 075029, [`1905.12634`].

[57] A. Boyarsky, M. Drewes, T. Lasserre, S. Mertens and O. Ruchayskiy, *Sterile neutrino Dark Matter*, *Prog. Part. Nucl. Phys.* **104** (2019) 1–45, [`1807.07938`].

[58] XENON collaboration, E. Aprile et al., *Observation of Excess Electronic Recoil Events in XENON1T*, `2006.09721`.

[59] C. Boehm, D. G. Cerdeno, M. Fairbairn, P. A. Machado and A. C. Vincent, *Light new physics in XENON1T*, `2006.11250`.

[60] N. F. Bell, G. Busoni, S. Robles and M. Virgato, *Improved Treatment of Dark Matter Capture in Neutron Stars*, *JCAP* **09** (2020) 028, [`2004.14888`].

[61] Planck collaboration, N. Aghanim et al., *Planck 2018 results. VI. Cosmological parameters*, `1807.06209`.

[62] Planck collaboration, Y. Akrami et al., *Planck 2018 results. I. Overview and the cosmological legacy of Planck*, `1807.06205`.

[63] G. Bertone, D. Hooper and J. Silk, *Particle dark matter: Evidence, candidates and constraints*, *Phys. Rept.* **405** (2005) 279–390, [`hep-ph/0404175`].

[64] C. Frenk and S. D. White, *Dark matter and cosmic structure*, *Annalen Phys.* **524** (2012) 507–534, [`1210.0544`].

[65] M. Boylan-Kolchin, J. S. Bullock and M. Kaplinghat, *Too big to fail? The puzzling darkness of massive Milky Way subhaloes*, *Mon.Not.Roy.Astron.Soc* **415** (July, 2011) L40–L44, [`1103.0007`].

[66] S. Dodelson and L. M. Widrow, *Sterile-neutrinos as dark matter*, *Phys. Rev. Lett.* **72** (1994) 17–20, [`hep-ph/9303287`].

[67] K. N. Abazajian, *Sterile neutrinos in cosmology*, *Phys. Rept.* **711-712** (2017) 1–28, [`1705.01837`].

[68] V. Barger, R. Phillips and S. Sarkar, *Remarks on the karmen anomaly*, *Physics Letters B* **352** (1995) 365 – 371.

[69] P. B. Pal and L. Wolfenstein, *Radiative Decays of Massive Neutrinos*, *Phys. Rev.* **D25** (1982) 766.

[70] L. Roszkowski, E. M. Sessolo and S. Trojanowski, *WIMP dark matter candidates and searches—current status and future prospects*, *Rept. Prog. Phys.* **81** (2018) 066201, [`1707.06277`].

[71] XENON collaboration, E. Aprile et al., *Light Dark Matter Search with Ionization Signals in XENON1T*, *Phys. Rev. Lett.* **123** (2019) 251801, [`1907.11485`].

[72] XENON collaboration, E. Aprile et al., *Search for Light Dark Matter Interactions Enhanced by the Migdal Effect or Bremsstrahlung in XENON1T*, *Phys. Rev. Lett.* **123** (2019) 241803, [`1907.12771`].

[73] LZ collaboration, D. Akerib et al., *The LUX-ZEPLIN (LZ) Experiment*, *Nucl. Instrum. Meth. A* **953** (2020) 163047, [`1910.09124`].

[74] PandaX-II collaboration, X. Cui et al., *Dark Matter Results From 54-Ton-Day Exposure of PandaX-II Experiment*, *Phys. Rev. Lett.* **119** (2017) 181302, [`1708.06917`].

[75] CRESST collaboration, A. Abdelhameed et al., *First results from the CRESST-III low-mass dark matter program*, *Phys. Rev. D* **100** (2019) 102002, [`1904.00498`].

[76] CTA Consortium collaboration, M. Actis et al., *Design concepts for the Cherenkov Telescope Array CTA: An advanced facility for ground-based high-energy gamma-ray astronomy*, *Exper. Astron.* **32** (2011) 193–316, [`1008.3703`].

[77] IceCube collaboration, M. Aartsen et al., *Search for Neutrinos from Dark Matter Self-Annihilations in the center of the Milky Way with 3 years of IceCube/DeepCore*, *Eur. Phys. J. C* **77** (2017) 627, [`1705.08103`].

[78] AMS collaboration, W. Xu, *The Latest Results from AMS on the Searches for Dark Matter*, pp. 205–220. WSP, Singapur, 2020. 10.1142/9789811207402_0014.

[79] Fermi-LAT collaboration, M. Ackermann et al., *Searching for Dark Matter Annihilation from Milky Way Dwarf Spheroidal Galaxies with Six Years of Fermi Large Area Telescope Data*, *Phys. Rev. Lett.* **115** (2015) 231301, [`1503.02641`].

[80] A. Boveia and C. Doglioni, *Dark Matter Searches at Colliders*, *Ann. Rev. Nucl. Part. Sci.* **68** (2018) 429–459, [`1810.12238`].

[81] S. Chandrasekhar, *Radiative Transfer*. Dover Books on Intermediate and Advanced Mathematics. Dover Publications, 1960.

[82] A. Kosowsky, *Cosmic microwave background polarization*, *Annals Phys.* **246** (1996) 49–85, [`astro-ph/9501045`].

[83] K. Hagiwara and D. Zeppenfeld, *Helicity amplitudes for heavy lepton production in e+e- annihilation*, *Nuclear Physics B* **274** (1986) 1 – 32.

[84] Berestetskii, Lifshitz and Pitaevskii, *Relativistic Quantum Theory*, vol. 4 of *Course of Theoretical Physics*. Pergamon, 1971.

[85] P. Montero-Camacho and C. M. Hirata, *Exploring circular polarization in the CMB due to conventional sources of cosmic birefringence*, `1803.04505`.

[86] R. L. White, *Polarization in reflection nebulae. I - Scattering properties of interstellar grains*, *Astrophysical Journal* **229** (may, 1979) 954–961.

[87] H. Zhang and M. Bttcher, *X-Ray and Gamma-Ray Polarization in Leptonic and Hadronic Jet Models of Blazars*, *Astrophys. J.* **774** (2013) 18, [`1307.4187`].

[88] H. Zhang, X. Chen and M. Bttcher, *Synchrotron Polarization in Blazars*, *Astrophys. J.* **789** (2014) 66, [`1401.7138`].

[89] T. Beckert and H. Falcke, *Circular polarization of radio emission from relativistic jets*, *Astron. Astrophys.* **388** (2002) 1106, [`astro-ph/0112398`].

[90] T. A. Ensslin, *Does circular polarisation reveal the rotation of quasar engines?*, *Astron. Astrophys.* **401** (2003) 499–504, [`astro-ph/0212387`].

[91] D. C. Homan, J. M. Attridge and J. F. C. Wardle, *Parsec-scale circular polarization observations of 40 blazars*, *The Astrophysical Journal* **556** (2001) 113.

[92] D. Homan, R. Ojha, D. Roberts and J. Wardle, *Electron–positron jets associated with the quasar 3c279*, .

[93] G. C. Bower, D. C. Backer, J.-H. Zhao, M. Goss and H. Falcke, *The linear polarization of sagittarius a*. i. vla spectropolarimetry at 4.8 and 8.4 ghz*, *The Astrophysical Journal* **521** (1999) 582.

[94] G. C. Bower, H. Falcke and D. C. Backer, *Detection of circular polarization in the galactic center black hole candidate sagittarius a**, *The Astrophysical Journal Letters* **523** (1999) L29.

[95] R. J. Sault and J.-P. Macquart, *Confirmation and analysis of circular polarization from sagittarius a**, *The Astrophysical Journal Letters* **526** (1999) L85.

[96] G. C. Bower, H. Falcke, R. J. Sault and D. C. Backer, *The spectrum and variability of circular polarization in sagittarius a* from 1.4 to 15 ghz*, *The Astrophysical Journal* **571** (2002) 843.

[97] K. C. Westfold, *The polarization of synchrotron radiation.*, *The Astrophysical Journal* **130** (Jul, 1959) 241.

[98] M. P. C. Legg and K. C. Westfold, *Elliptic polarization of synchrotron radiation*, *The Astrophysical Journal* **154** (Nov, 1968) 499.

[99] D. de Brca and A. Shearer, *Circular polarization of synchrotron radiation in high magnetic fields*, *Mon. Not. Roy. Astron. Soc.* **450** (2015) 533–540, [`1503.04722`].

[100] T. Jones and S. O'Dell, *Transfer of polarized radiation in self-absorbed synchrotron sources. i. results for a homogeneous source*, *Astrophys. J.; (United States)* **214:2** (6, 1977) .

[101] T. W. Jones and S. Odell, *Transfer of polarized radiation in self-absorbed synchrotron sources. ii. treatment of inhomogeneous media and calculation of emergent polarization*, *Astrophys. J.; (United States)* **215** (July, 1977) 236–246.

[102] R. Fender, D. Rayner, R. Norris, R. J. Sault and G. Pooley, *Discovery of circularly polarized radio emission from ss 433*, *The Astrophysical Journal Letters* **530** (2000) L29.

[103] A. Brunthaler, G. C. Bower, H. Falcke and R. R. Mellon, *Detection of circular polarization in m81**, *Astrophys. J.* **560** (2001) L123, [astro-ph/0109170].

[104] C. Boehm, C. Degrande, J. Scholtz and A. C. Vincent, *Using Circular Polarisation to Test the Composition and Dynamics of Astrophysical Particle Accelerators*, 1901.05462.

[105] R. Mohammadi, *Evidence for cosmic neutrino background form CMB circular polarization*, *Eur. Phys. J.* **C74** (2014) 3102, [1312.2199].

[106] S. Alexander, J. Ochoa and A. Kosowsky, *Generation of Circular Polarization of the Cosmic Microwave Background*, *Phys. Rev.* **D79** (2009) 063524, [0810.2355].

[107] S. Shakeri, S. Z. Kalantari and S.-S. Xue, *Polarization of a probe laser beam due to nonlinear QED effects*, *Phys. Rev.* **A95** (2017) 012108, [1703.10965].

[108] M. Sadegh, R. Mohammadi and I. Motie, *Generation of circular polarization in CMB radiation via nonlinear photon-photon interaction*, *Phys. Rev.* **D97** (2018) 023023, [1711.06997].

[109] M. Giovannini, *The v-mode polarization of the cosmic microwave background*, 0909.3629.

[110] W. Bonivento, D. Gorbunov, M. Shaposhnikov and A. Tokareva, *Polarization of photons emitted by decaying dark matter*, *Phys. Lett.* **B765** (2017) 127–131, [1610.04532].

[111] A. Elagin, J. Kumar, P. Sandick and F. Teng, *Prospects for detecting a net photon circular polarization produced by decaying dark matter*, *Phys. Rev.* **D96** (2017) 096008, [1709.03058].

[112] W.-C. Huang and K.-W. Ng, *Polarized gamma rays from dark matter annihilations*, `1804.08310`.

[113] J. Kumar, P. Sandick, F. Teng and T. Yamamoto, *Gamma-ray Signals from Dark Matter Annihilation Via Charged Mediators*, *Phys. Rev.* **D94** (2016) 015022, [`1605.03224`].

[114] C. M. Hirata, A. Mishra and T. Venumadhav, *Detecting primordial gravitational waves with circular polarization of the redshifted 21 cm line. I. Formalism*, *Phys. Rev.* **D97** (2018) 103521, [`1707.03513`].

[115] A. Mishra and C. M. Hirata, *Detecting primordial gravitational waves with circular polarization of the redshifted 21 cm line. II. Forecasts*, *Phys. Rev.* **D97** (2018) 103522, [`1707.03514`].

[116] J. Schechter and J. W. F. Valle, *Majorana Neutrinos and Magnetic Fields*, *Phys. Rev.* **D24** (1981) 1883–1889.

[117] J. Schechter and J. W. F. Valle, *Neutrino Decay and Spontaneous Violation of Lepton Number*, *Phys. Rev.* **D25** (1982) 774.

[118] R. E. Shrock, *Electromagnetic Properties and Decays of Dirac and Majorana Neutrinos in a General Class of Gauge Theories*, *Nucl. Phys.* **B206** (1982) 359–379.

[119] J. F. Nieves, *Electromagnetic Properties of Majorana Neutrinos*, *Phys. Rev.* **D26** (1982) 3152.

[120] B. Kayser, *Majorana Neutrinos and their Electromagnetic Properties*, *Phys. Rev.* **D26** (1982) 1662.

[121] M. Dvornikov and A. Studenikin, *Electric charge and magnetic moment of massive neutrino*, *Phys. Rev.* **D69** (2004) 073001, [`hep-ph/0305206`].

[122] M. S. Dvornikov and A. I. Studenikin, *Electromagnetic form-factors of a massive neutrino*, *J. Exp. Theor. Phys.* **99** (2004) 254–269, [`hep-ph/0411085`].

[123] N. F. Bell, B. Kayser and S. S. C. Law, *Electromagnetic Leptogenesis*, *Phys. Rev.* **D78** (2008) 085024, [`0806.3307`].

[124] C. Giunti and A. Studenikin, *Neutrino electromagnetic interactions: a window to new physics*, *Rev. Mod. Phys.* **87** (2015) 531, [`1403.6344`].

[125] P. Minkowski, *$\mu \to e\gamma$ at a Rate of One Out of 10^9 Muon Decays?*, *Phys. Lett.* **67B** (1977) 421–428.

[126] T. Yanagida, *Horizontal gauge symmetry and masses of neutrinos*, *Conf. Proc.* **C7902131** (1979) 95–99.

[127] S. L. Glashow, *The Future of Elementary Particle Physics*, *NATO Sci. Ser. B* **61** (1980) 687.

[128] R. N. Mohapatra and G. Senjanovic, *Neutrino Mass and Spontaneous Parity Nonconservation*, *Phys. Rev. Lett.* **44** (1980) 912.

[129] J. Schechter and J. W. F. Valle, *Neutrino Masses in SU(2) x U(1) Theories*, *Phys. Rev.* **D22** (1980) 2227.

[130] E. Bulbul, M. Markevitch, A. Foster, R. K. Smith, M. Loewenstein and S. W. Randall, *Detection of An Unidentified Emission Line in the Stacked X-ray spectrum of Galaxy Clusters*, *Astrophys. J.* **789** (2014) 13, [`1402.2301`].

[131] A. Boyarsky, O. Ruchayskiy, D. Iakubovskyi and J. Franse, *Unidentified Line in X-Ray Spectra of the Andromeda Galaxy and Perseus Galaxy Cluster*, *Phys. Rev. Lett.* **113** (2014) 251301, [`1402.4119`].

[132] S. Gariazzo, C. Giunti, M. Laveder, Y. F. Li and E. M. Zavanin, *Light sterile neutrinos*, *J. Phys.* **G43** (2016) 033001, [`1507.08204`].

[133] M. Drewes et al., *A White Paper on keV Sterile Neutrino Dark Matter*, *JCAP* **1701** (2017) 025, [`1602.04816`].

[134] Z.-z. Xing, *Flavor structures of charged fermions and massive neutrinos*, `1909.09610`.

[135] M. Chianese, G. Miele, S. Morisi and E. Vitagliano, *Low energy IceCube data and a possible Dark Matter related excess*, *Phys. Lett.* **B757** (2016) 251–256, [`1601.02934`].

[136] IceCube collaboration, M. G. Aartsen et al., *Search for neutrinos from decaying dark matter with IceCube*, *Eur. Phys. J.* **C78** (2018) 831, [`1804.03848`].

[137] IceCube collaboration, M. G. Aartsen et al., *First observation of PeV-energy neutrinos with IceCube*, *Phys. Rev. Lett.* **111** (2013) 021103, [`1304.5356`].

[138] IceCube collaboration, M. G. Aartsen et al., *Observation and Characterization of a Cosmic Muon Neutrino Flux from the Northern Hemisphere using six years of IceCube data*, *Astrophys. J.* **833** (2016) 3, [`1607.08006`].

[139] T2K collaboration, K. Abe et al., *Search for CP Violation in Neutrino and Antineutrino Oscillations by the T2K Experiment with* 2.2×10^{21} *Protons on Target*, *Phys. Rev. Lett.* **121** (2018) 171802, [`1807.07891`].

[140] T2K collaboration, K. Abe et al., *Combined Analysis of Neutrino and Antineutrino Oscillations at T2K*, *Phys. Rev. Lett.* **118** (2017) 151801, [`1701.00432`].

[141] NOvA collaboration, P. Adamson et al., *Constraints on Oscillation Parameters from* ν_e *Appearance and* ν_μ *Disappearance in NOvA*, *Phys. Rev. Lett.* **118** (2017) 231801, [`1703.03328`].

[142] DUNE collaboration, B. Abi et al., *The DUNE Far Detector Interim Design Report, Volume 2: Single-Phase Module*, `1807.10327`.

[143] Hyper-Kamiokande Proto-Collaboration collaboration, K. Abe et al., *Physics potential of a long-baseline neutrino oscillation experiment using a J-PARC neutrino beam and Hyper-Kamiokande*, *PTEP* **2015** (2015) 053C02, [`1502.05199`].

[144] Hyper-Kamiokande collaboration, K. Abe et al., *Physics potentials with the second Hyper-Kamiokande detector in Korea*, *PTEP* **2018** (2018) 063C01, [`1611.06118`].

[145] M. Fukugita and T. Yanagida, *Baryogenesis Without Grand Unification (leptogenesis)*, *Phys. Lett.* **B174** (1986) 45–47.

[146] E. K. Akhmedov, V. A. Rubakov and A. Yu. Smirnov, *Baryogenesis via neutrino oscillations*, *Phys. Rev. Lett.* **81** (1998) 1359–1362, [`hep-ph/9803255`].

[147] W. Buchmuller, P. Di Bari and M. Plumacher, *Leptogenesis for pedestrians*, *Annals Phys.* **315** (2005) 305–351, [`hep-ph/0401240`].

[148] S. Davidson, E. Nardi and Y. Nir, *Leptogenesis*, *Phys. Rept.* **466** (2008) 105–177, [`0802.2962`].

[149] B. Kayser, *CPT, CP, and c Phases and their Effects in Majorana Particle Processes*, *Phys. Rev.* **D30** (1984) 1023.

[150] C. Broggini, C. Giunti and A. Studenikin, *Electromagnetic Properties of Neutrinos*, *Adv. High Energy Phys.* **2012** (2012) 459526, [`1207.3980`].

[151] X. Shi and G. Sigl, *A Type II supernovae constraint on electron-neutrino - sterile-neutrino mixing*, *Phys. Lett. B* **323** (1994) 360–366, [`hep-ph/9312247`].

[152] G. G. Raffelt and S. Zhou, *Supernova bound on keV-mass sterile neutrinos reexamined*, *Phys. Rev. D* **83** (2011) 093014, [`1102.5124`].

[153] M. E. Peskin and D. V. Schroeder, *An Introduction to quantum field theory*. Addison-Wesley, Reading, USA, 1995.

[154] Z.-z. Xing and Y.-L. Zhou, *Enhanced Electromagnetic Transition Dipole Moments and Radiative Decays of Massive Neutrinos due to the Seesaw-induced Non-unitary Effects*, *Phys. Lett.* **B715** (2012) 178–182, [1201.2543].

[155] P. Frampton, S. Glashow and T. Yanagida, *Cosmological sign of neutrino CP violation*, *Phys. Lett. B* **548** (2002) 119–121, [hep-ph/0208157].

[156] Z.-z. Xing and S. Zhou, *Neutrinos in particle physics, astronomy and cosmology*. 5, 2011.

[157] J. Neukammer, H. Rinneberg, G. Jönsson, W. E. Cooke, H. Hieronymus, A. König et al., *Autoionization inhibited by internal interferences*, *Phys. Rev. Lett.* **55** (Nov, 1985) 1979–1982.

[158] D.-d. Wu, *Rephasing invariants and cp violation*, *Phys. Rev. D* **33** (Feb, 1986) 860–863.

[159] I. Esteban, M. Gonzalez-Garcia, A. Hernandez-Cabezudo, M. Maltoni and T. Schwetz, *Global analysis of three-flavour neutrino oscillations: synergies and tensions in the determination of θ_{23}, δ_{CP}, and the mass ordering*, *JHEP* **01** (2019) 106, [1811.05487].

[160] E. Fernandez-Martinez, J. Hernandez-Garcia and J. Lopez-Pavon, *Global constraints on heavy neutrino mixing*, *JHEP* **08** (2016) 033, [1605.08774].

[161] A. Ibarra and G. G. Ross, *Neutrino phenomenology: The Case of two right-handed neutrinos*, *Phys. Lett. B* **591** (2004) 285–296, [hep-ph/0312138].

[162] J. Casas and A. Ibarra, *Oscillating neutrinos and $\mu \to e, \gamma$*, *Nucl. Phys. B* **618** (2001) 171–204, [hep-ph/0103065].

[163] S. Antusch, P. Di Bari, D. Jones and S. King, *Leptogenesis in the Two Right-Handed Neutrino Model Revisited*, *Phys. Rev. D* **86** (2012) 023516, [1107.6002].

[164] P. Di Bari, K. Farrag, R. Samanta and Y. L. Zhou, *Density matrix calculation of the dark matter abundance in the Higgs induced right-handed neutrino mixing model*, `1908.00521`.

[165] A. Atre, T. Han, S. Pascoli and B. Zhang, *The Search for Heavy Majorana Neutrinos*, *JHEP* **05** (2009) 030, [`0901.3589`].

[166] S. King and P. Lubin, *Circular polarization of the cmb: Foregrounds and detection prospects*, `1606.04112`.

[167] M. M. Komesaroff, J. A. Roberts, D. K. Milne, P. T. Rayner and D. J. Cooke, *Circular and linear polarization variations of compact radio sources*, *Monthly Notices of the Royal Astronomical Society* **208** (1984) 409–425.

[168] J. Fernández, J. Hubbell, A. Hanson and L. Spencer, *Polarization effects on multiple scattering gamma transport*, *Radiation Physics and Chemistry* **41** (1993) 579 – 630.

[169] W. H. McMaster, *Matrix representation of polarization*, *Rev. Mod. Phys.* **33** (Jan, 1961) 8–28.

[170] J. Mao and J. Wang, *Linear polarization, circular polarization, and depolarization of gamma-ray bursts: A simple case of jitter radiation*, *The Astrophysical Journal* **838** (mar, 2017) 78.

[171] V. Petrillo, A. Bacci, C. Curatolo, I. Drebot, A. Giribono, C. Maroli et al., *Polarization of x-gamma radiation produced by a thomson and compton inverse scattering*, *Phys. Rev. ST Accel. Beams* **18** (Nov, 2015) 110701.

[172] S. Stock, A. Surzhykov, S. Fritzsche and D. Seipt, *Compton scattering of twisted light: angular distribution and polarization of scattered photons*, *Phys. Rev.* **A92** (2015) 013401, [`1505.00313`].

[173] G. Sigl and G. Raffelt, *General kinetic description of relativistic mixed neutrinos*, *Nucl. Phys.* **B406** (1993) 423–451.

[174] N. Bartolo, A. Hoseinpour, S. Matarrese, G. Orlando and M. Zarei, *CMB Circular and B-mode Polarization from New Interactions*, `1903.04578`.

[175] W. H. Press and D. N. Spergel, *Capture by the sun of a galactic population of weakly interacting, massive particles*, *Astrophys. J.* **296** (Sept., 1985) 679–684.

[176] A. Gould, *WIMP Distribution in and Evaporation From the Sun*, *Astrophys. J.* **321** (1987) 560.

[177] A. Gould, *Resonant Enhancements in WIMP Capture by the Earth*, *Astrophys. J.* **321** (1987) 571.

[178] I. Goldman and S. Nussinov, *Weakly interacting massive particles and neutron stars*, **40** (Nov., 1989) 3221–3230.

[179] C. Kouvaris, *WIMP Annihilation and Cooling of Neutron Stars*, *Phys. Rev. D* **77** (2008) 023006, [`0708.2362`].

[180] A. de Lavallaz and M. Fairbairn, *Neutron Stars as Dark Matter Probes*, *Phys. Rev.* **D81** (2010) 123521, [`1004.0629`].

[181] M. Baryakhtar, J. Bramante, S. W. Li, T. Linden and N. Raj, *Dark Kinetic Heating of Neutron Stars and An Infrared Window On WIMPs, SIMPs, and Pure Higgsinos*, *Phys. Rev. Lett.* **119** (2017) 131801, [`1704.01577`].

[182] J. Bramante, A. Delgado and A. Martin, *Multiscatter stellar capture of dark matter*, *Phys. Rev.* **D96** (2017) 063002, [`1703.04043`].

[183] B. Dasgupta, A. Gupta and A. Ray, *Dark matter capture in celestial objects: Improved treatment of multiple scattering and updated constraints from white dwarfs*, *JCAP* **1908** (2019) 018, [`1906.04204`].

[184] G. Busoni, A. De Simone, P. Scott and A. C. Vincent, *Evaporation and scattering of momentum- and velocity-dependent dark matter in the Sun*, *JCAP* **1710** (2017) 037, [`1703.07784`].

[185] S. O. Kepler, S. J. Kleinman, A. Nitta, D. Koester, B. G. Castanheira, O. Giovannini et al., *White Dwarf Mass Distribution in the SDSS*, *Mon. Not. Roy. Astron. Soc.* **375** (2007) 1315–1324, [`astro-ph/0612277`].

[186] P.-E. Tremblay, J. Cummings, J. S. Kalirai, B. T. Gänsicke, N. Gentile-Fusillo and R. Raddi, *The field white dwarf mass distribution*, *Monthly Notices of the Royal Astronomical Society* **461** (Jun, 2016) 2100–2114, [`1606.05292`].

[187] S. O. Kepler, I. Pelisoli, D. Koester, N. Reindl, S. Geier, A. D. Romero et al., *White dwarf and subdwarf stars in the Sloan Digital Sky Survey Data Release 14*, *Monthly Notices of the Royal Astronomical Society* **486** (04, 2019) 2169–2183.

[188] R. H. Fowler, *On Dense Matter*, *Monthly Notices of the Royal Astronomical Society* **87** (12, 1926) 114–122.

[189] S. Chandrasekhar, *The maximum mass of ideal white dwarfs*, *Journal of Astrophysics and Astronomy* **15** (Jun, 1994) 115–116.

[190] S. O. Kepler, D. Koester, A. D. Romero, G. Ourique and I. Pelisoli, *White Dwarf Mass Distribution*, vol. 509 of *Astronomical Society of the Pacific Conference Series*, p. 421. 2017. `1610.00371`.

[191] G. Fontaine, P. Brassard and P. Bergeron, *The Potential of White Dwarf Cosmochronology*, **113** (Apr., 2001) 409–435.

[192] E. E. Salpeter, *Energy and Pressure of a Zero-Temperature Plasma.*, *ApJ* **134** (Nov., 1961) 669.

[193] A. Mathew and M. K. Nandy, *General relativistic calculations for white dwarfs*, *Research in Astronomy and Astrophysics* **17** (May, 2017) 061, [`1401.0819`].

[194] L. Mestel, *On the theory of white dwarf stars. I. The energy sources of white*

dwarfs, *Monthly Notices of the Royal Academical Society* **112** (Jan., 1952) 583.

[195] F. D'Antona and I. Mazzitelli, *Cooling of white dwarfs*, *Annual Review of Astronomy and Astrophysics* **28** (1990) 139–181, [`https://doi.org/10.1146/annurev.aa.28.090190.001035`].

[196] S. L. Shapiro and S. A. Teukolsky, *Black holes, white dwarfs, and neutron stars : the physics of compact objects.* 1983.

[197] S. M. de Carvalho, M. Rotondo, J. A. Rueda and R. Ruffini, *Relativistic Feynman-Metropolis-Teller treatment at finite temperatures*, *Int. J. Mod. Phys. Conf. Ser.* **23** (2013) 244, [`1312.2434`].

[198] A. Phillips, *The Physics of Stars.* Manchester Physics Series. Wiley, 1999.

[199] D. Koester and G. Chanmugam, *REVIEW: Physics of white dwarf stars*, *Reports on Progress in Physics* **53** (July, 1990) 837–915.

[200] G. P. McCook and E. M. Sion, *A Catalog of Spectroscopically Identified White Dwarfs*, *THE ASTROPHYSICAL JOURNAL SUPPLEMENT SERIES* **121** (Mar., 1999) 1–130.

[201] E. M. Sion, J. L. Greenstein, J. D. Landstreet, J. Liebert, H. L. Shipman and G. A. Wegner, *A proposed new white dwarf spectral classification system.*, *Astroparticle J.* **269** (June, 1983) 253–257.

[202] M. A. Hollands, P. E. Tremblay, B. T. Gänsicke, N. P. Gentile-Fusillo and S. Toonen, *The Gaia 20 pc white dwarf sample*, *Monthly Notices of the Royal Astronomical Society* **480** (Nov., 2018) 3942–3961, [`1805.12590`].

[203] N. P. Gentile Fusillo, P.-E. Tremblay, B. T. Gänsicke, C. J. Manser, T. Cunningham, E. Cukanovaite et al., *A Gaia Data Release 2 catalogue of white dwarfs and a comparison with SDSS*, *Monthly Notices of the Royal Academical Society* **482** (Feb., 2019) 4570–4591, [`1807.03315`].

[204] A. Gould, *Weakly interacting massive particle distribution in and evaporation from the sun*, *ApJ* (1987) 560–570.

[205] A. Fitzpatrick, W. Haxton, E. Katz, N. Lubbers and Y. Xu, *The Effective Field Theory of Dark Matter Direct Detection*, *JCAP* **02** (2013) 004, [`1203.3542`].

[206] J. Goodman, M. Ibe, A. Rajaraman, W. Shepherd, T. M. Tait and H.-B. Yu, *Constraints on Dark Matter from Colliders*, *Phys. Rev. D* **82** (2010) 116010, [`1008.1783`].

[207] N. F. Bell, G. Busoni and S. Robles, *Heating up Neutron Stars with Inelastic Dark Matter*, *JCAP* **1809** (2018) 018, [`1807.02840`].

[208] M. Cirelli, E. Del Nobile and P. Panci, *Tools for model-independent bounds in direct dark matter searches*, *JCAP* **10** (2013) 019, [`1307.5955`].

[209] G. Belanger, F. Boudjema, A. Pukhov and A. Semenov, *micrOMEGAs3: A program for calculating dark matter observables*, *Comput. Phys. Commun.* **185** (2014) 960–985, [`1305.0237`].

[210] R. Catena and B. Schwabe, *Form factors for dark matter capture by the Sun in effective theories*, *JCAP* **04** (2015) 042, [`1501.03729`].

[211] A. Gould, *Weakly Interacting Massive Particle Distribution in and Evaporation from the Sun*, *Astrophysical Journal* **321** (Oct., 1987) 560.

[212] M. Nauenberg, *Energy transport and evaporation of weakly interacting particles in the sun*, *Phys. Rev. D* **36** (Aug, 1987) 1080–1087.

[213] A. Bottino, G. Fiorentini, N. Fornengo, B. Ricci, S. Scopel and F. Villante, *Does solar physics provide constraints to weakly interacting massive particles?*, *Phys. Rev. D* **66** (2002) 053005, [`hep-ph/0206211`].

[214] A. C. Vincent and P. Scott, *Thermal conduction by dark matter with velocity and momentum-dependent cross-sections*, *JCAP* **04** (2014) 019, [`1311.2074`].

[215] A. C. Vincent, A. Serenelli and P. Scott, *Generalised form factor dark matter in the Sun*, *JCAP* **08** (2015) 040, [`1504.04378`].

[216] L. R. Bedin, M. Salaris, G. Piotto, J. Anderson, I. R. King and S. Cassisi, *The End of the White Dwarf Cooling Sequence in M4: An Efficient Approach*, *Astrophys. J.* **697** (June, 2009) 965–979, [`0903.2839`].

[217] G. Bertone and M. Fairbairn, *Compact Stars as Dark Matter Probes*, *Phys. Rev.* **D77** (2008) 043515, [`0709.1485`].

[218] P. Scott, M. Fairbairn and J. Edsjo, *Dark stars at the Galactic centre - the main sequence*, *Mon. Not. Roy. Astron. Soc.* **394** (2009) 82, [`0809.1871`].

[219] M. McCullough and M. Fairbairn, *Capture of Inelastic Dark Matter in White Dwarves*, *Phys. Rev.* **D81** (2010) 083520, [`1001.2737`].

[220] J. R. Neeley, M. Marengo, G. Bono, V. F. Braga, M. Dall'Ora, P. B. Stetson et al., *On the Distance of the Globular Cluster M4 (NGC 6121) Using RR Lyrae Stars. II. Mid-infrared Period-luminosity Relations.*, *Astrophys. J.* **808** (July, 2015) 11, [`1505.07858`].

[221] SuperCDMS collaboration, R. Agnese et al., *Projected Sensitivity of the SuperCDMS SNOLAB experiment*, *Phys. Rev. D* **95** (2017) 082002, [`1610.00006`].

[222] Q. Yue, K. Kang, J. Li and H. T. Wong, *The CDEX Dark Matter Program at the China Jinping Underground Laboratory*, *J. Phys. Conf. Ser.* **718** (2016) 042066, [`1602.02462`].

[223] DARWIN collaboration, J. Aalbers et al., *DARWIN: towards the ultimate dark matter detector*, *JCAP* **11** (2016) 017, [`1606.07001`].

[224] N. F. Bell, G. Busoni and S. Robles, *Capture of Leptophilic Dark Matter in Neutron Stars*, *JCAP* **06** (2019) 054, [`1904.09803`].

[225] N. F. Bell, G. Busoni, S. Robles and M. Virgato, *Improved Treatment of Dark Matter Capture in Neutron Stars II: Leptonic Targets*, `2010.13257`.

[226] Y. Minami and E. Komatsu, *New Extraction of the Cosmic Birefringence from the Planck 2018 Polarization Data*, *Phys. Rev. Lett.* **125** (2020) 221301, [`2011.11254`].

[227] A. Olivares-Del Campo, C. Bœhm, S. Palomares-Ruiz and S. Pascoli, *Dark matter-neutrino interactions through the lens of their cosmological implications*, *Phys. Rev.* **D97** (2018) 075039, [`1711.05283`].

[228] C. Boehm and J. Lavalle, *Clarifying the covariant formalism for the SZ effect due to relativistic non-thermal electrons*, *Phys. Rev.* **D79** (2009) 083505, [`0812.3282`].